PHASE EQUILIBRIA BETWEEN IRON AND SLAG IN $CO/CO_2/H_2/H_2O$ ATMOSPHERES RELEVANT TO A NOVEL FLASH IRONMAKING TECHNOLOGY

by

Mohassab Yousef Mohassab Ahmed

A dissertation submitted to the faculty of
The University of Utah
in partial fulfillment of the requirements for the degree of

Doctor of Philosophy

Department of Metallurgical Engineering

University of Utah

August 2013

The University of Utah Graduate School

STATEMENT OF DISSERTATION APPROVAL

The dissertation of **Mohassab Yousef Mohassab Ahmed**

has been approved by the following supervisory committee members:

Hong Yong Sohn	, Chair	**03/25/2013** Date Approved
Joann Lighty	, Member	**03/25/2013** Date Approved
Sivaraman Guruswamy	, Member	**03/25/2013** Date Approved
Michael S. Moats	, Member	**03/25/2013** Date Approved
Moo Eob Choi	, Member	**03/25/2013** Date Approved

and by **Jan D. Miller**, Chair of the Department of **Metallurgical Engineering**

and by Donna M. White, Interim Dean of The Graduate School.

ABSTRACT

In an effort to develop a novel flash ironmaking process, to be called the Sohn process in this dissertation, with the potential of steelmaking in a single continuous process, the phase equilibria involved and the chemistry of selected slag systems were investigated. The Sohn process is an ecofriendly flash ironmaking process for producing iron from iron oxide concentrates in a flash reactor using fuels and reductants that help reduce energy consumption and minimize greenhouse gas emissions. Amongst the proposed reductants and fuels are H_2, natural gas, and coal gas. The molten bath (iron-slag bath) is expected to equilibrate with gas atmospheres of mainly H_2/H_2O, $CO/CO_2/H_2/H_2O$, and CO/CO_2 corresponding to H_2, natural gas/coal gas (NG/CG), and coke/coal (blast furnace, BF), respectively. The latter was investigated to allow comparison with the blast-furnace conditions. The slag composition was selected to resemble that of the blast furnace, which consisted of the CaO-MgO-SiO_2-Al_2O_3-FeO-MnO-P_2O_5 system with CaO/SiO_2 in the range 0.8 to 1.4. The temperature range was 1550 to 1650°C encompassing a wide range of expected ironmaking temperatures for the Sohn process. The oxygen partial pressure was maintained in the reducing range 10^{-10} to 10^{-9} atm in the three gas atmospheres.

It was found that H_2O dramatically affects the chemistry of the slag and strongly affects the phase equilibria in the slag as well as the equilibrium distribution of elements between slag and molten metal.

It was found that the slags under H_2O-containing (H_2 and NG/CG) atmospheres had a moderately higher degree of polymerization as compared to that under the blast furnace conditions. H_2O in the gas atmosphere also increased the activity coefficient of FeO in the slag and accordingly lowered the FeO content. The FeO content in the slag of H_2 (FeO wt% = 10) and NG/CG (11) was significantly less than under the BF (16) conditions. On the other hand, the average MgO solubility (22 wt%) under the NG/CG was higher than under the BF (18%) conditions, whereas MgO solubility showed no change under H_2 (18 wt%) relative to the BF. Moreover, H_2O causes the highest L_S in the case of H_2 as compared with all the other reducing agents. H_2 showed 400% (L_S = 5.0) enhancement in L_S, whereas NG/CG exhibited 130% (L_S = 2.3) improvement compared with the BF (L_S = 1.0). Under H_2 (L_P = 9) and NG/CG (L_P = 17), L_P was 50 and 6 % lower than under the BF (18) conditions, respectively. In addition, H_2O in the gas atmosphere depressed L_{Mn}. L_{Mn} under H_2 (L_{Mn} = 5) and NG/CG (4) conditions was, respectively, 29 and 43% lower than under the BF (7) conditions.

The findings from this work suggest that the Sohn process will produce high quality iron with lower impurity levels and less FeO in the slag than the blast furnace.

TABLE OF CONTENTS

LIST OF TABLES

LIST OF FIGURES

NOMENCLATURE

Symbol	Unit	Definition
a	-	Slag-to-metal ratio in eqs 4-16, 5-13, and 8-6
a_M	-	Activity of species M
B′	-	Basicity index, eq 7-6
BO	-	Bridging oxygen
C_M	-	Slag capacity of species M
f_M	-	Henrian activity coefficient of species M
g	-	Gas phase
ΔG°	J/mol	Standard Gibbs free energy
j	-	Number of cycles in silicate anion
K_i	-	Equilibrium constant of reaction i
L_M	-	Distribution ratio of element M between slag and molten iron
M	-	Dissolved M in the molten iron
[wt% M]	%	Weight percent of M in iron
(wt% M)	%	Weight percent of M in slag
MW_M	g/mol	Molar molecular weight
n_M	mol	Amount of species M
NBO/Si	-	Nonbridging oxygen per tetrahedral silicon
NBO/T	-	Nonbridging oxygen per tetrahedra
$n_{H_2,\min}$	mol	Minimum amount of hydrogen to reduce iron oxide to metallic iron including the amount to overcome the equilibrium barrier

$n_{H_2,\text{red}}$	mol	Amount of hydrogen used for reaction 2-3
$n_{H_2,\text{sup}}$	mol	Total amount of hydrogen fed into the reactor
pM	atm	Partial pressure of species M
pO_2°	atm	Equilibrium oxygen partial pressure for a mixture of solid Fe + pure liquid FeO
P_T	atm	Total pressure inside the reactor tube
Q^n	-	Silicate anion (Q-species), n = 0,1,2,3, 4
R	J/mol.K	Universal gas constant
r^2	-	Correlation coefficient
Rxx	-	Sample designation for samples containing Mn
s	-	Solid phase
Sxx	-	Sample designation for samples without Mn
T	°C, K	Temperature
w_{NB}	-	Net charge on the total network-breaking cations
X_M	-	Mole fraction of M
x_T	-	Sum of network formers

Greek Symbol

γ	-	Raultian activity coefficient
$\varepsilon_{FeO}^{H_2O}$	-	Interaction coefficient between water vapor and FeO in the slag
θ	degree	Diffraction angel
λ	Å	Wave length
Λ_{th_i}	-	Optical basicity of pure oxide *i*
v_{NB}	-	Total charge of the total network-breaking cations
τ_a	10^{-12}s	Amplitude correlation time
τ_c	10^{-12}s	Coherence lifetime

χ^2	-	Weighted sum of squared residuals
ψ	-	Measure of silicate polymerization degree

ACKNOWLEDGMENTS

I would like to express my deep gratitude to my supervisor, Professor H. Y. Sohn, whose expertise, understanding, and patience added considerably to my graduate experience and most effectively, his openness and encouragement for new ideas and research avenues. My beloved Professor, if I happen to be a professor, I hope I can treat my students the way you treated me. Without your help and directions, this work would not have been completed.

I would like to thank the excellent supervisory committee members, Professors JoAnn Lighty, Sivaraman Guruswamy, Michael S. Moats, and Moo Eob Choi, for their priceless time and effort to review my work.

This research would not have been possible without the financial assistance of American Iron and Steel Institute (AISI) through a Research Service Agreement with the University of Utah under AISI's CO_2 Breakthrough Program.

I am grateful to my parents, parents-in-law, my brother, and my sisters for the support they provided me through my entire life. Special appreciation goes to my father and my brother, Emad, without whose help and countless support I would not have finished my PhD.

Sincere appreciation and thanks go to my beloved wife and best friend, Eman, without whose love, encouragement, and assistance I would not have finished this dissertation. Eman, without your tireless effort to secure a quiet and productive lifestyle

and above all taking care of me and our sweet daughter, Noor, it would have been impossible to run my 15-hour experiments and accordingly finish my PhD.

Special thanks go to the light of my life, my daughter. I would love to record the unforgettable moment of my nephew, Aliaa's, birth who was born at the time I was reviewing my first draft of this dissertation.

I dedicate this work to my grandmother, my first teacher, who passed away at the beginning of my PhD study.

CHAPTER 1

INTRODUCTION

1. 1. Background

Iron, steel's precursor, fueled the industrial revolution starting in 1750, enabling manufacturing equipment in factories and rail transport. Modern steelmaking was developed 150 years ago with the invention of the Bessemer process, allowing for the affordable mass-production of steel, which is an iron alloy.[1] This set off a second industrial revolution, and sustained economic growth. Iron has, in fact, been a vital material in technology for well over three thousand years. World iron production has increased from 625 million tons (Mt) in 2001 to 1,175 Mt in 2011 (it was 382 Mt in 1968).[2-4] Iron is used predominantly in modern industrial societies where it approximately accounts for 95% of the metals used.[5] Therefore, the production of iron is by far the largest metal production industry in the world.

Currently, steelmaking processes are dominated by two major routes, as shown in Figure 1-1:[6]

(1) the primary steelmaking or integrated steelmaking through:

- blast furnace (BF) - basic oxygen furnace (BOF) producing 66% of world steel

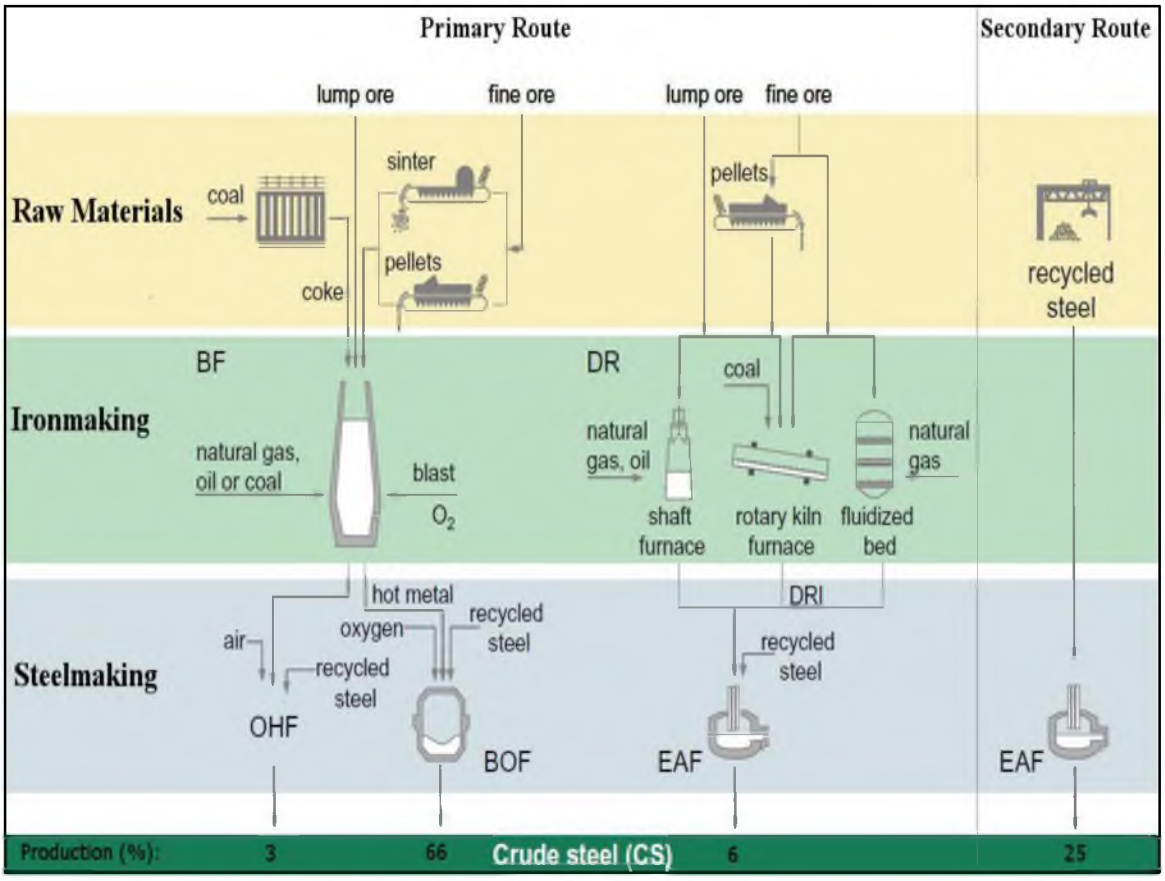

Figure 1-1. Schematic diagrams of the steelmaking routes and their contribution to world steel production as well as their energy intensities.[6]

- BF - open hearth furnace (OHF) accounting for 3% of global steel production
- Direct reduction (DR) – electric arc furnace (EAF) which produces 6 % of world steel.

(2) the secondary or mini steelmaking using EAF, mostly recycling steel scrap, which accounts for 25% of world steel production.

Globally, the primary steelmaking route produces around 75% of steel and the remaining 25% is made by the secondary route. In the primary steelmaking route, most of the metal is produced by the BF, which utilizes iron ore, coke, and flux to produce hot metal (pig iron) for BOF/OHF to produce steel, and the rest is produced through the direct reduction process. The DRI is produced by reduction of the ore (lump, pellet, or fine) below the melting point where coke is not used. The DRI is produced in relatively small scales (< 1 Mt/year) and has different properties than pig iron. It serves as a high quality scrap substitute for EAF.[7] In the secondary steelmaking process, steel scrap is used to make steel by melting in the EAF using electricity.

Although the primary steelmaking process is energy intensive compared to the secondary steelmaking using EAF, as shown in Figure 1-1, the primary route will continue to be the major steel producer. This is attributed to the fact that most steel products remain in use for decades before they can be recycled, unlike plastics and paper. Therefore, there is not enough scrap steel to meet the exponentially growing steel demand. [6, 8] World demand is met by integrating the two routes; primary and secondary.

In this chapter, the current ironmaking processes will be discussed as well as the technologies and processes under development across the globe.

1. 2. Iromaking Processes

Iron is produced worldwide via blast furnace (BF), direct reduction (DR), and recently smelting reduction (SR), with the BF as the main means to make iron, after which comes DR. Nowadays, smelting reduction shares only around 1% of global iron production; however, increasing attention is being paid to this process as a competitor to the BF process. The BF technology is well established and commercially dominating the ironmaking industry. Some DR and SR processes, however, have already been adopted in iromaking plants. In addition to these three technologies, there are electrolysis-based technologies to produce iron, which are currently under research; we will refer to it as EI in this text. These ironmaking processes will be discussed in some details in the following sections.

The main subject of the present work, however, is a novel flash ironmaking process, the Sohn process, which is under development at the University of Utah and will be discussed and compared with the current processes as well as with some of those that are under research.

1. 2. 1. Blast Furnace (BF)

The blast furnace process has been the major producer of iron from its ores for over 600 years.[9] The BF brings to the market approximately 94% of the iron, also known as pig iron.[2] The smallest blast furnaces have a capacity of 0.550 Mt pig iron per year; however, state-of-the-art ones produce 2-4 Mt pig iron per year.

The blast furnace ironmaking is a countercurrent process occurring in a shaft furnace. Where iron-bearing ores (sinter, pellets, or lump of mostly magnetite, Fe_3O_4,

hematite, Fe_2O_3, and goethite, $Fe_2O_3.H_2O$),[5] coke, and flux are fed into a shaft furnace from the top, and preheated air (blast) is blown into the bottom through tuyeres to burn and provide the heat required for the smelting process. Coke is made by carburizing the coal (i.e., heating in the absence of oxygen at high temperatures). In the BF, coke functions as: (1) the main chemical reductant of iron ore to iron, (2) fuel, (3) strong and permeable support for the burden, allowing an adequate flow of gases through the furnace. Coke retains its strength at high temperatures in contrast to coal, which tends to soften at elevated temperatures. Because of the latter function, coke must be used in the blast furnace rather than coal or any other fuel. Similarly fine ores cannot be directly charged to the blast furnace; rather, they have to be sintered/pelletized. The purpose of sintering and pelletizing is to render the fine charge into strong but porous clinker and agglomerated balls (pellets) with a size of ~1.5 cm to enhance the burden permeability and facilitates the reduction.[7] Supplementary fuels, such as pulverized coal, natural gas (NG), and oil, are also injected into the furnace through the tuyeres to reduce the use of coke, which is expensive. The hot air reacts with coke and injected fuels, forming 2,000 – 2,500°C hot gas. This hot gas rises and passes through raw materials that are descending from the top to the bottom of the furnace. When the hot gases (mostly N_2, CO, and CO_2) are ascending, their sensible heat is transferred to the descending materials as a result the offgas temperature decreases, while the descending charge receives heat from the hot gas and experiences a series of physiochemical changes, most importantly the partial reduction of iron oxides. The final reduction to iron, the desulfurization, and silica reduction occurs in the lower part of the bosh and the crucible where the temperature is higher. The reduction takes place by CO and H_2 in the gas and solid carbon in coke.

Liquid hot metal (pig iron) and molten slag are formed in the hearth of the furnace. Based on the above discussion, the blast furnace is considered to be chemically and thermally efficient reactor. Moreover, there have been efforts to improve the BF processes such as increasing productivity and energy efficiency, decreasing coke consumption, developing better cokemaking processes, reducing CO_2 emissions, increasing pulverized coal injection, and injecting more natural gas and plastics. Many of these technologies to improve the BF process have been already commercialized. Furthermore, the R&D efforts continue to enhance the BF process. Examples of technologies under research are reforming coke oven gas with the aid of catalysts (Course 50), top gas recycling, CO_2 capture and storage, avoiding gas flaring, and heat recovery from slag.[10]

Despite aforementioned merits and improvements, the blast furnace process still suffers from drawbacks. As long as the blast furnace is used, the needs for sintering/ pelletizing of the ore and high-grade coking coal cannot be avoided. Other materials preparation contributes significantly to the energy consumption as well as CO_2 emissions in the blast furnace process. Figure 1-2 indicates that ore and coke preparation emits ~ 20% of the total CO_2 in the BF-BOF route and the BF contributes ~70%, whereas the steelmaking step adds only ~11% of the total emissions.[11] Moreover, the BF process is energy intensive and requires a high capital cost as it entails large infrastructure. Table 1-1 compares the primary energy intensity, defined as the energy used for the production facility as well as to generate the electricity consumed at the facility, to produce a metric ton of mild steel for three steelmaking technologies.[12] It is seen that the BF consumes around 78% of the total energy consumed in the BF-BOF route.[12]

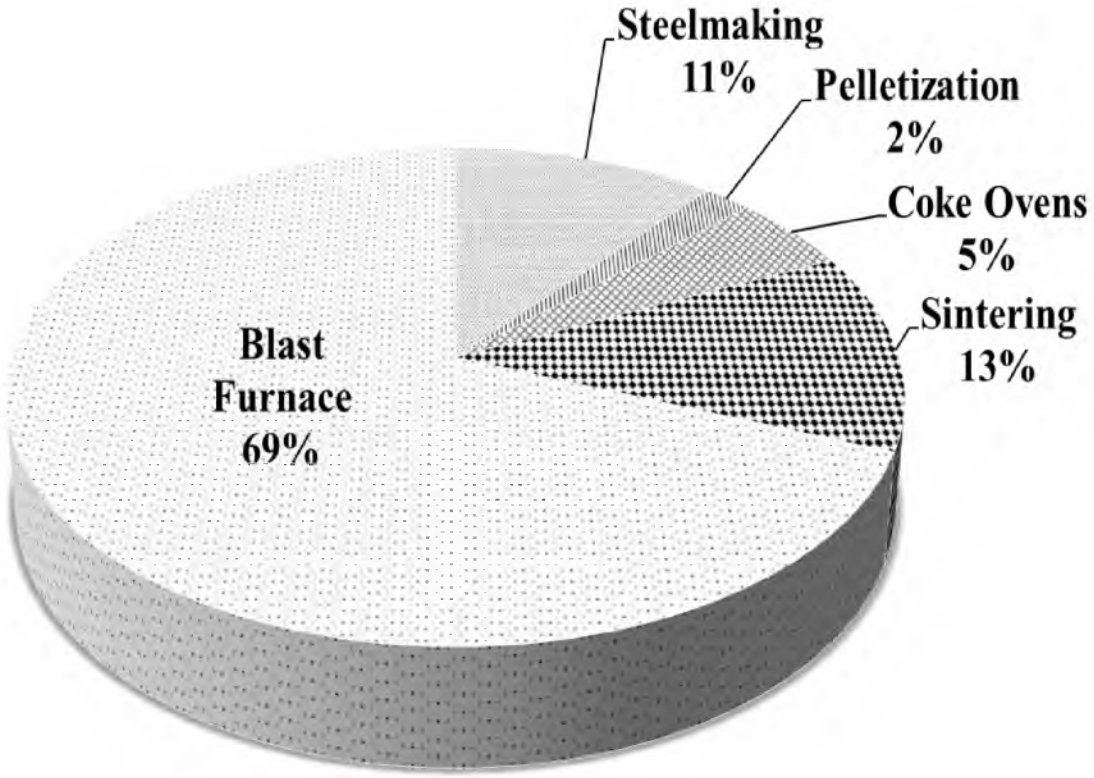

Figure 1-2. The CO_2 emissions in primary steelmaking (BF-BOF), (total = 2227 kg CO_2/ton steel).[11]

Table 1-1. World best practice primary energy intensity values for iron and steel (values are GJ per metric ton of steel and the primary energy includes electricity generation, transmission, and distribution losses of 67%)[12]

Production step	Process	**BF-BOF**	**SR-BOF**	**DRI-EAF**	**Scrap-EAF**
Material preparation	Sintering	2.2		2.2	
	Pelletizing		0.8	0.8	
	Coking	1.1			
Iron making	BF	12.4			
	SR		17.9		
	DRI			9.2	
Steelmaking	BOF	-0.3	-0.3		
	EAF			5.9	5.5
	Refining	0.4	0.4		
Total (GJ/t)		**15.8**	**18.8**	**18.1**	**5.5**

Since the Kyoto protocol (38 nations agreed in 1997 to reduce greenhouse gas emissions on average by 5.2% by 2012) was announced, greenhouse gases (GHG) emissions and the resulting climate change have continued to be a significant environmental issue for the steel industry and, in particular, the BF process, as will be discussed later.

1. 2. 2. Direct Reduction (DR)

Direct reduction processes are mostly gas-based, which are globally dominated by MIDREX technology (63% of world DR).[13] Ore (fines, pellets, or lumps) is reduced in solid state – unlike BF process where a liquid metal is produced. Direct reduced iron (DRI) or sponge iron offers an alternative steel production route to BF-BOF and Scrap-EAF routes. DRI production is common in the Middle East, South America, India, and Mexico. DR offers an attractive route due to its low capital investment and its suitability to local raw material situations.[14] Despite the aforementioned advantages, the DR route suffers from drawbacks such as the small scale of operations, which acts as a barrier for energy efficiency investments. Also, the DRI is prone to reoxidation unless passivated or briquetted. The energy requirement of the DR-EAF route is compared with the BF-BOF route in Table 1-1, which shows that the former route requires ~2 GJ per metric ton of steel more than the latter.[12] Also, the quality of the DRI is highly dependent on the feed quality unlike hot metal produced by the BF with stable and dependable quality.[13] In DR, natural gas and coal are the two primary fuels. More than 90% of the global DRI plants use (lower grade) natural gas, whereas production in India is mainly coal based.

DRI processes can be grouped according to the type of reactor used, namely:[10]

- Shaft furnaces (Midrex, Energiron)
- Rotary kilns (SL/RN process)
- Rotary hearth furnaces (Fastmet/Fastmelt, and ITmk3)
- Fluidized bed reactors (Circored)

In DR, iron oxide is reduced below iron melting point, resulting in no slag phase. Therefore, all gangue elements of the iron ores remain in the DRI and need to be separated via the slag in the EAF. This increases the electrical energy and electrode consumption of the EAF compared to steel scrap melting (secondary steelmaking). This energy consumption can be reduced by immediate transfer of hot DRI to the EAF melt shop. By doing this, the heat from the direct reduction process lowers the cost of melting the DRI in the EAF, considerably cutting the energy costs and electrode consumption.[10]

The most common technologies used for DRI production are MIDREX and Energiron, both using natural gas. The energy consumption in natural-gas-based DRI production is well known and established to be 10.4 GJ/t-DRI. Natural gas-based DRI production also leads to lower CO_2 emissions, with emissions ranging from 0.77 to 0.92 ton of CO_2 per ton of steel (compared with ~ 1.9 ton of CO_2 per ton of steel for the BF-BOF route), [8] depending on the type of electricity used.[10] Presently, this process is more expensive than the BF process and it also demands better quality iron ore, which increases the cost and limits it flexibility. The amount of electricity required for melting DRI in EAF also makes the process less efficient in terms of energy use (18 GJ/t of crude steel compared with 16 GJ/t in the BF-BOF route, as shown in Table 1-1). The clear potential of this proven technology is, however, the removal of the need for coke ovens and reducing CO_2 emissions.

1. 2. 3. Smelting Reduction (SR)

Smelting reduction processes (SR) are the latest development in pig iron production. The SR emerged during the 1990s. In SR, iron ore and coal are added directly to a metal-slag bath where the ore can be reduced. The SR combines the gasification of coal with the melt reduction of iron ore. Energy intensity of smelting reduction is lower than that of blast furnace, as coking step is avoided and the need for ore preparation is reduced. Examples of this process are Finex and Hismelt. Although SR reduces GHG emissions, the process demands higher energy for ironmaking step (18.7 GJ/t of crude steel) that exceeds the total energy required for the entire steelmaking process through the BF-BOF route (15.8 GJ/t).

In 2003, Birat *et al.*[15] made an interesting benchmarking study that was based on process calculations. This study was aimed to visualize the future scenarios of steelmaking technologies beyond Kyoto protocol. Based on their study, the results of which are presented in Figure 1-3, the share of different ironmaking technologies which could be in place in 2050 was forecasted with a total steel make in excess of 2300 Mt (compared with 1518 Mt in 2011).[2, 16] The BF is expected still to be the largest process for iron production; however, it is expected to drop from 94% (in 2011) to 60% (in 2050). Based on the same study, GHG emission is expected to be 39% less than that of 2003. Also, they presented examples of these future processes such as those based on the increased use of hydrogen for reduction, low carbon fuels such as natural gas, and smelting processes.

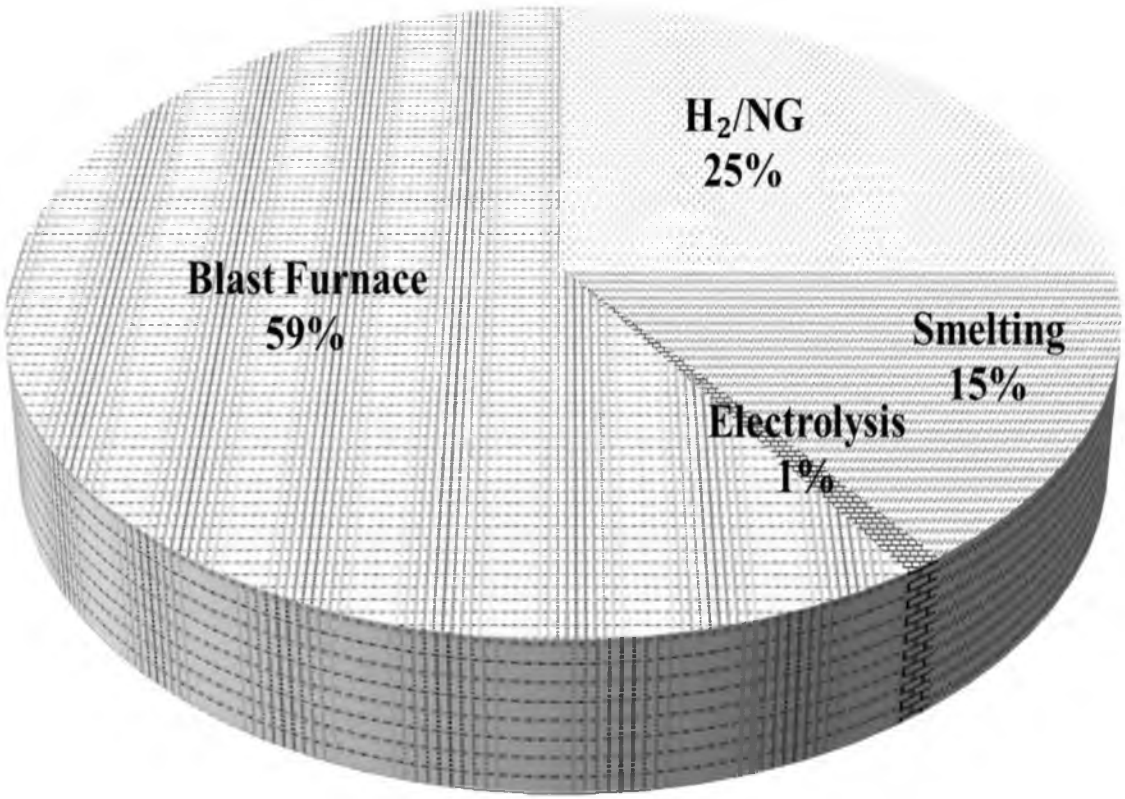

Figure 1-3. Predicted share of ironmaking routes in 2050.[15]

1. 2. 4. Electrolytic Ironmaking (EI)

In principle, iron oxide can be reduced by aqueous or molten electrolysis. There are two processes that are currently under research: (1) molten oxide electrolysis (MOE) and (2) aqueous elelctrolysis.

ULCOLYSIS[17] and the Sadoway process[18] are the two molten electrolysis processes under research to reduce iron from iron oxide in a molten bath. In MOE processes, iron ore is dissolved in a molten oxide mixture at 1550-1700°C. The anode, made of a material inert towards the oxide mixture, is dipped in this solution. The electrical current is passed between this anode and a liquid iron pool connected to the circuit as the cathode. Oxygen evolves as a gas at the anode and iron is produced as a liquid metal at the cathode.

ULCOWIN is an example of a research project to study the aqueous electrolysis, often referred to as electowinning, as a means to produce iron on a large scale. Unlike MOE, aqueous electrolysis uses an alkaline solution (mostly aqueous NaOH) as the electrolyte. In addition, two inert electrodes are used instead of only one in MOE. On the cathode, the iron cations get reduced and iron is plated, whereas on the anode, oxygen evolves similarly to MOE.

In electrolysis, CO_2 created during these processes would also be eradicated. However, electrolysis still might produce CO_2 as the process relies intensively on electrical energy which is produced by the consumption of carbon-based fuels. Also, there are other obstacles to be overcome in MOE, such as the high temperature required to maintain the electrolyte liquid as well as the electrode material for large scale. For aqueous electrolysis, in addition to the above-mentioned, the major challenge is the large-

scale solution treatment and purification as well as the other problems associated with hydrometallurgical processes.

1. 3. A Novel Ironmaking Technology

According to the International Energy Association (IEA), the iron and steel sector accounts for 6.7% of the world CO_2 emissions.[19] Also, the iron and steel industry is the second-largest industrial user of energy, consuming 2.58×10^7 TJ in 2007 and the largest industrial source of CO_2 emissions (30%).[8] On average, 1.9 tons of CO_2 are emitted for every ton of steel produced coming mostly from the BF process as mentioned earlier.[8]

Reduction in energy use and CO_2 emissions in the steel industry is rapidly reaching the limits defined by the laws of physics and chemistry. In order to make major reductions in future energy consumption and CO_2 emissions, new methods of making steel will require completely fresh and innovative thinking. According to Birat *et al.*,[15] breakthrough technologies based on radically new routes will be required in order to fulfill the environmental regulations and energy consumption reduction plans. Given the limited efficiency potential inherent in existing best technologies and based on the driving force discussed above, a flash ironmaking technology was conceived as a novel ironmaking technology by Sohn[20] at the University of Utah. This technology is based on fine particle reduction using a reductant gas such as hydrogen, natural gas, coal gas, or a combination thereof. It is the first flash-type ironmaking process converting iron ore concentrate directly to metallic iron in-flight, which would be suitable for an industrial-scale operation. This process will produce iron directly from concentrate without requiring pelletization or sintering and thus avoids the need for coke. In addition, this

process concept allows an intensive operation, unlike other alternate ironmaking routes, taking a full advantage of the fine particle size of the concentrate with a large surface area which permits rapid reduction by a gas. Another potential benefit of this process is the possibility of steelmaking in a single continuous process, as shown in Figure 1-4.[21] Kinetic feasibility tests have been carried out on the reduction of magnetite concentrate particles by hydrogen in the temperature range 1150-1400°C.[22-24] Most importantly, these tests have revealed that high reduction degrees above 90% could be achieved within several seconds. It was found that the reduction rate has 1/2-order dependence with respect to hydrogen partial pressure. The effect of particle size changed with temperature. Also, the study declared that the reduction rate increased with particle size at 1150°C and 1200°C, but the effect of particle size was negligible when reduction temperature was above 1300°C. In addition to the kinetics study, process simulation for the flash ironmaking process was carried out, using the METSIM software, to assess the economic feasibility using different process configurations.[25-28] Major results are summarized in Figures 1-5 and 1-6. Figure 1-5 shows potential higher energy savings, lower carbon footprint, and economic feasibility (except H_2-based 1-step process (H1S) and H_2-based 2-step process (H2S) configurations) relative to the BF. However, application of a $50 per ton of CO_2 credit should make the use of hydrogen economically feasible at the 2010 price of hydrogen, as Figure 1-6 suggests.[25-28]

Currently, the Sohn process is going to be tested on a larger bench scale to investigate different process variables mostly using natural gas as fuel and reductant; the experimental system is exhibited in Figure 1-7.[29] During this phase, the kinetics of reduction with natural gas is going to be explored in parallel with the slag chemistry and

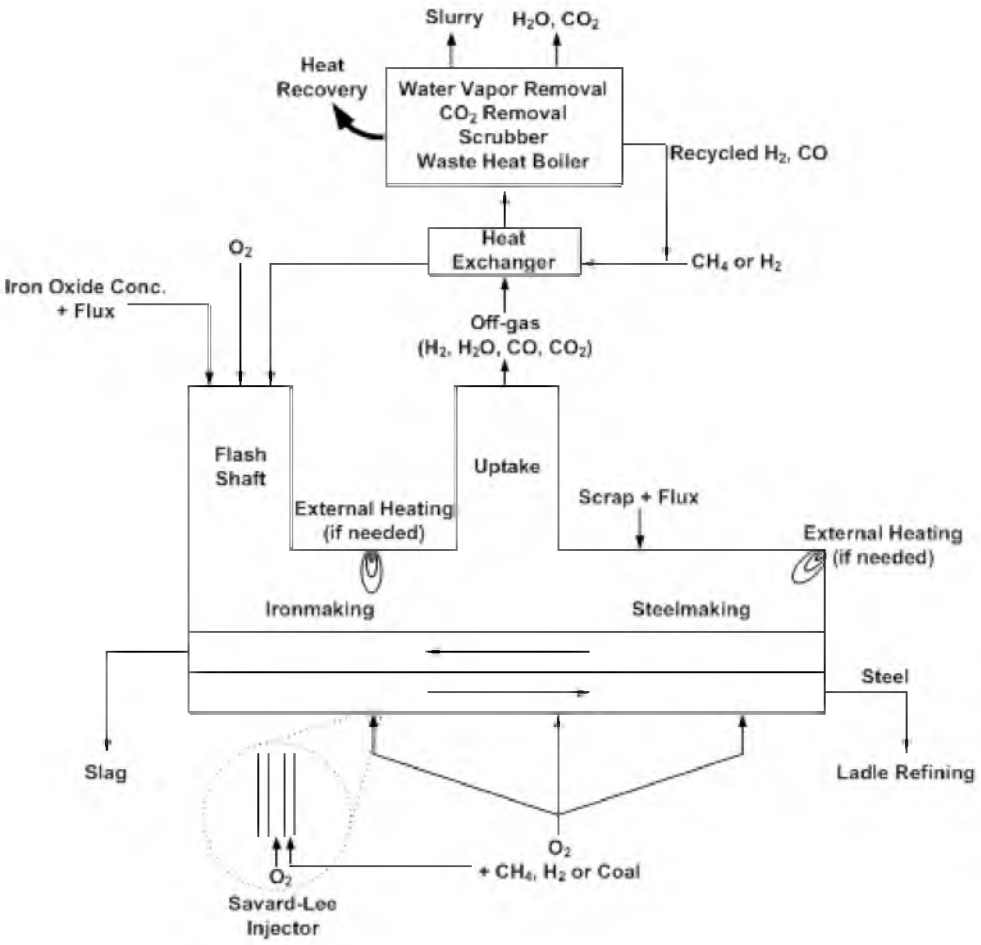

Figure 1-4. A schematic diagram of the Sohn process.[21]

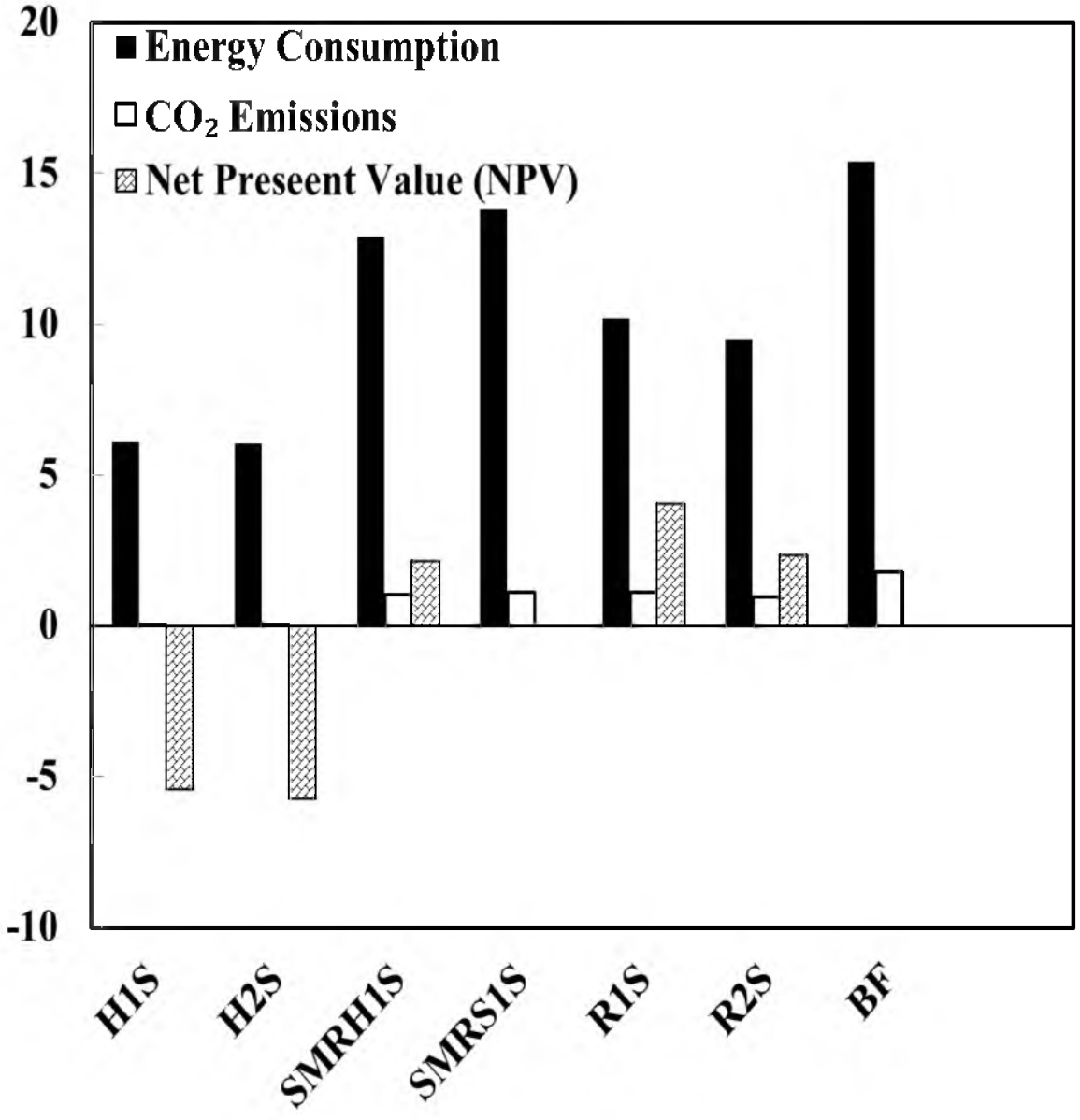

Figure 1-5. The energy consumption (GJ/ton of iron), CO_2 emission (tons/ton of iron), and NPV for 1 Mt/ year plant of the different configurations of the flash ironmaking (Sohn) process in addition to the BF applying \$0 CO_2 credit. [H1S: H_2-based 1-step process, H2S: H_2-based 2-step process, SMRH1S: 1-step process with hydrogen production from SMR (Steam-Methane Reforming), SMRS1S: 1-step process with syngas production from SMR, R1S: Reformerless1-step process, R2S: Reformerless 2-step process].[25-28]

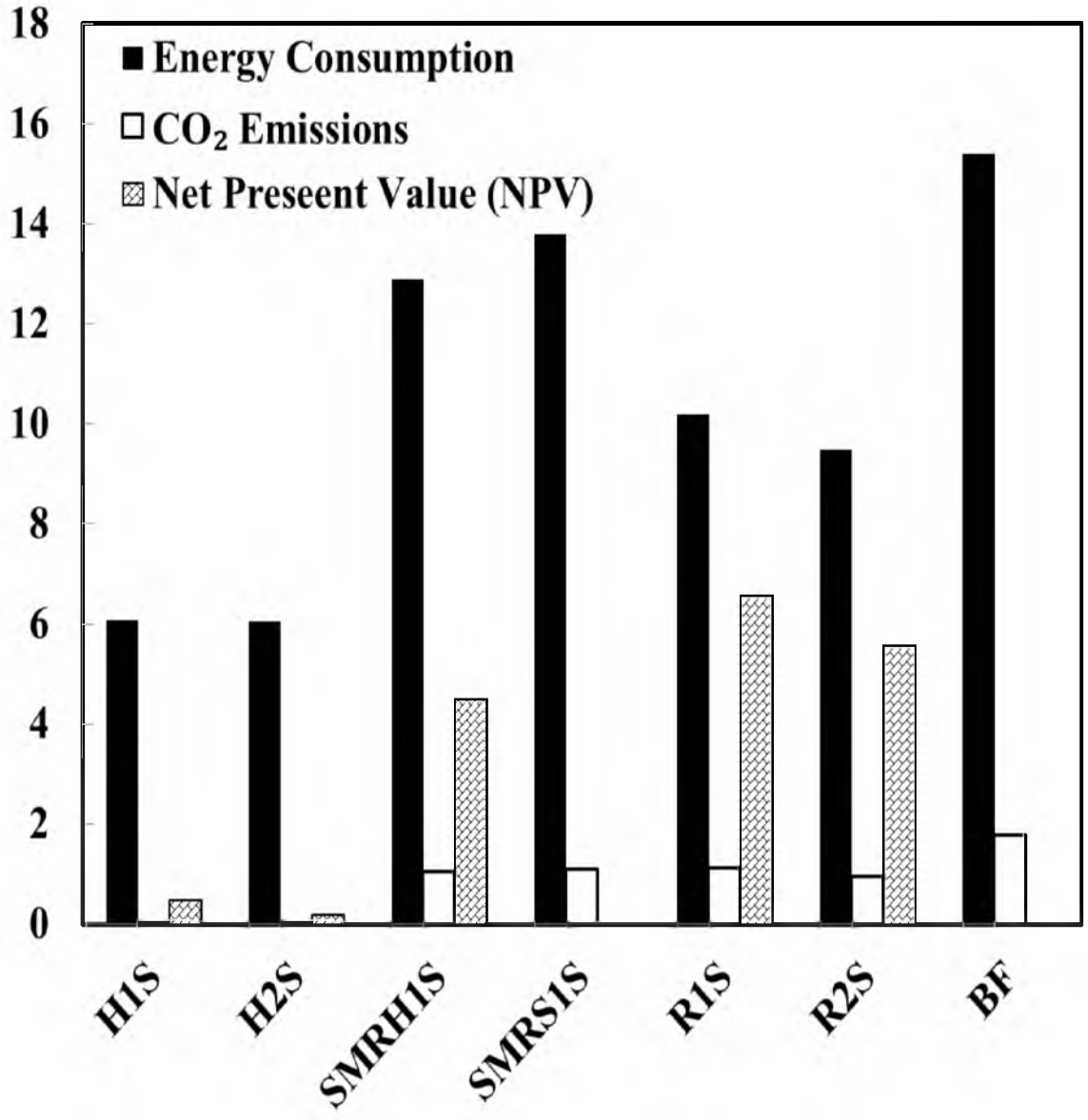

Figure 1-6. The energy consumption (GJ/ton of iron), CO_2 emission (tons/ton of iron), and NPV of the different configurations of the Flash ironmaking process in addition to the BF applying \$50 CO_2 credit.[25-28]

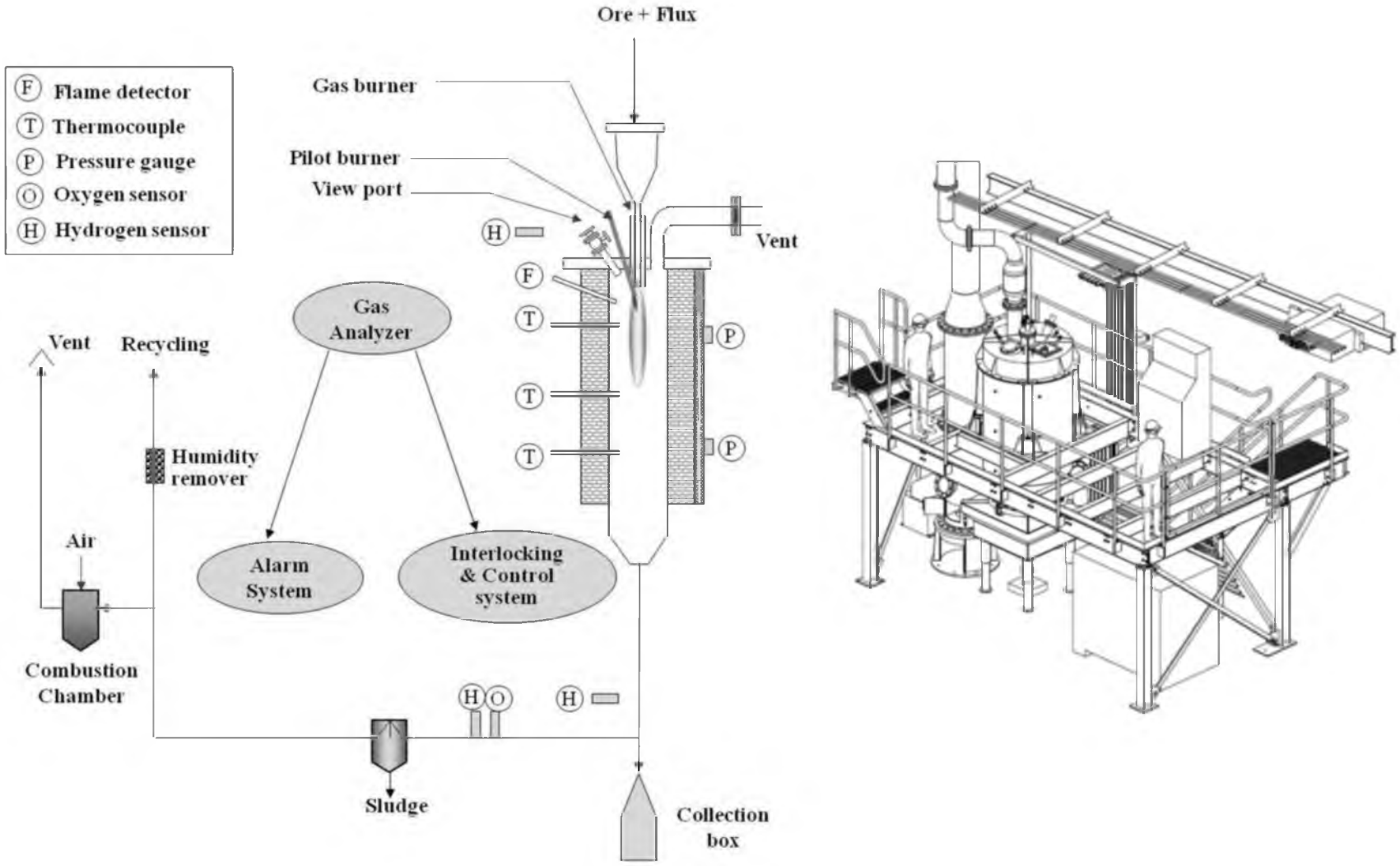

Figure 1-7. Bench-scale test facility: conceptual diagram (on the left), preliminary facility layout (on the right).[29]

phase equilibria studies.

1. 4. Scope of the Work

The hot metal produced by the blast furnace has to go through desulfurization, dephosphorization, and demanganization treatments to bring the levels of these impurities down to acceptable levels. FeO in the slag represents iron loss, which might require slag recycling if it exceeds certain limits. Thus, it is critical to determine the levels of these elements as well as the chemistry of the slag in the iron produced by the Flash ironmaking process. In addition, the fact that the linings of high-temperature furnaces are Mg-based makes it crucial to investigate MgO activity in the slag. This will help with lining lifetime assessment and maintenance requirements.

The effect of gas atmosphere on the slag chemistry has been investigated using various spectroscopic and characterization techniques. Most of the tests have been carried out under the proposed process conditions, and the distribution of S, P, and Mn between metal and slag has been determined. The behavior of FeO and MgO in the slag was also investigated.

The CaO-MgO-SiO_2-Al_2O_3-FeO-MnO (<1.0 wt%)-P_2O_5 (<0.5 wt%) slag was used in the study. The slag composition was chosen to simulate that of a typical ironmaking process. The experimental temperature range was 1550-1650°C, which is wide enough to encompass the expected operating temperatures of the novel ironmaking process. Equilibrium experiments were conducted under $CO/CO_2/H_2/H_2O$, H_2/H_2O and CO/CO_2. The first gas mixture was used to represent the conditions of using natural gas or coal gas in the reduction process, whereas the second mixture was used to represent

the case of using H_2 gas and CO/CO_2 was used to compare results with the blast furnace conditions.

This research is the first of its type because previous researchers only focused on the BF conditions where oxygen partial pressure was controlled by the CO/CO_2 equilibrium. This research is expected to answer important questions about the flash ironmaking technology, the Sohn process, such as those of the quality of the produced iron, the iron loss into the slag, and the lining erosion.

1. 5. References

(1) World Steel Association. Sustainable steel: At the core of a green economy. http://www.worldsteel.org/dms/internetDocumentList/bookshop/Sustainable-steel-at-the-core-of-a-green-economy/document/Sustainable-steel-at-the-core-of-a-green-economy.pdf (accessed 10/08/2012).

(2) World Steel Association. World Steel in Figures 2012. http://www.worldsteel.org/dms/internetDocumentList/bookshop/WSIF_2012/document/World%20Steel%20in%20Figures%202012.pdf (accessed 10/08/2012).

(3) World Steel Association. Steel statistical yearbook 2011. http://www.worldsteel.org/dms/internetDocumentList/statistics-archive/yearbook-archive/Steel-statistical-yearbook 2011/document/Steel%20statistical%20yearbook%202011.pdf (accessed 10/08/2012).

(4) World Steel Association. Steel statistical yearbook 1978. http://www.worldsteel.org/dms/internetDocumentList/statistics-archive/yearbook-archive/A-handbook-of-world-steel-statistics-1978/document/A%20handbook%20of%20world%20steel%20statistics%201978.pdf (accessed 10/08/2012).

(5) Yellishetty, M.; Ranjith, P. G.; Tharumarajah, A., Iron ore and steel production trends and material flows in the world: Is this really sustainable? *Resources, Conservation and Recycling* **2010,** *54*, 1084-1094.

(6) World Steel Association. Steel and energy. http://www.worldsteel.org/dms/internetDocumentList/fact-sheets/Fact-sheet_Energy/document/Fact%20sheet_Energy.pdf (accessed 10/08/2012).

(7) Worrell, E.; Blinde, P.; Neelis, M.; Blomen, E.; Masanet, E. Energy efficiency improvement and cost saving opportunities for the U.S. iron and steel industry: An energy star® guide for energy and plant managers. http://ies.lbl.gov/drupal.files/ies.lbl.gov.sandbox/4779E.pdf (accessed 10/08/2012).

(8) World Steel Association. Steel's contribution to a low carbon future. http://www.worldsteel.org/publications/bookshop?bookID=26c4d914-f159-4468-8933-94404015861b (accessed 10/08/2012).

(9) Strassburger, J. H.; Brown, D. C.; Dancy, T. E.; Stephenson, R. L., *Blast furnace-theory and practice*. Gordon and Breach Science: New York, USA, 1969.

(10) Industerial Effeciency Technology Database (IETD). Iron and steel. http://www.ietd.iipnetwork.org/content/iron-and-steel (accessed 10/08/2012).

(11) Orth, A.; Anastasijevic, N.; Eichberger, H. Low CO_2 emission technologies for iron and steelmaking as well as titania slag production. *Miner. Eng.* **2007,** *20*, 854-861.

(12) Worrell, E.; Price, L.; Neelis, M.; Galitsky, C.; Nan, Z. World best practice energy intensity values for selected industrial sectors. http://ies.lbl.gov/iespubs/62806.pdf (accessed 10/08/2012).

(13) European IPPC Bureau. Best available techniques for the production of iron and steel. http://old.vpvb.gov.lv/ippc/bat/bat_ES1/EdzelzsTerauds_Pr200907.pdf (accessed 10/08/2012).

(14) Industerial Effeciency Technology Database (IETD). Direct reduced iron. http://www.ietd.iipnetwork.org/content/direct-reduced-iron.

(15) Birat, J.-P.; Hanrot, F.; Danloy, G. *CO_2 mitigation technologies in the steel industry: A benchmarking study based on process calculation*, CIM. **2004**, 17-25.

(16) Gupta, S.; Sahajwalla, V. The Scope for fuel rate reduction in ironmaking. http://www.ccsd.biz/publications/files/TN/TN16%20New%20Report%20Working%20Final.pdf (accessed 10/10/2012).

(17) ULCOS. http://www.ulcos.org/en/research/electrolysis.php (accessed 10/10/2012).

(18) Kim, H.; Paramore, J.; Allanore, A.; Sadoway, D. R., Electrolysis of molten iron oxide with an iridium anode: The role of electrolyte basicity. *J. Electrochem. Soc.* **2011,** *158*, E101-E105.

(19) International Energy Association Statistics 2012. CO_2 emissions from fuel combustion. (accessed 01/18/2013).

(20) Sohn, H. Y.; Choi, M. E.; Zhang, Y.; Ramos, J. E. Suspension reduction technology for ironmaking with low CO_2 emission and energy requirement. *Iron Steel Technol. (AIST Trans.)* **2009**, *6*, 158-165.

(21) Sohn, H. Y.; Choi, M. E. Steel industry and carbon dioxide emissions - A novel ironmaking process with greatly reduced carbon footprint. In *Carbon dioxide emissions: New research*, ed. by M. Carpenter and E. J. Shelton, Nova Science Publishers, Hauppauge, NY, 2012.

(22) Wang, H.; Sohn, H., Hydrogen reduction kinetics of magnetite concentrate particles relevant to a novel flash ironmaking process. *Metall. Mater. Trans. B* **2013**, *44B*, 133-145. DOI: 10.1007/s11663-012-9754-z.

(23) Choi, M. E. *Suspension hydrogen reduction of iron ore concentrate*. PhD Dissertation, University of Utah, Salt Lake City, Utah, USA, **2010**.

(24) Zhang, Y. *Bench-scale flash reduction on iron ore concentrate.* M.S. Thesis, University of Utah, Salt Lake City, Utah, USA, **2008**.

(25) Pinegar, H. K.; Moats, M. S.; Sohn, H. Y. Flowsheet development, process simulation and economic feasibility analysis for novel suspension ironmaking technology based on natural gas: Part 3 - Economic feasibility analysis. *Ironmaking Steelmaking* **2012**, *40*, 44-49.

(26) Pinegar, H. K.; Moats, M. S.; Sohn, H. Y. Process simulation and economic feasibility analysis for a hydrogen-based novel suspension ironmaking technology. *Steel Res. Int.* **2011**, *82*, 951-963.

(27) Pinegar, H.; Moats, M.; Sohn, H. Y. Flowsheet development, process simulation and economic feasibility analysis for novel suspension ironmaking technology based on natural gas: Part 2 - Flowsheet and simulation for ironmaking combined with steam methane reforming. *Ironmaking Steelmaking* **2013,** *40*, 32-43.

(28) Pinegar, H.; Moats, M.; Sohn, H., Flowsheet development, process simulation and economic feasibility analysis for novel suspension ironmaking technology based on natural gas: Part 1-flowsheet and simulation for ironmaking with reformerless natural gas. *Ironmaking Steelmaking* **2012,** *39*, 398-408.

(29) Vehec, J.; Sohn, H. Y.; Kim, H.G.; Choi, M.E. Hydrogen flash smelting, *Proceedings of EECRsteel-METEC*, Session 13: 1-6, Dusseldorf, Germany, June 26-July 1; Dusseldorf, Germany, 2011.

CHAPTER 2

EXPERIMENTAL WORK

The distribution of sulfur, phosphorus, and manganese and the activity coefficient of FeO (γ_{FeO}) and γ_{MgO} in the slag and the dissolution behavior of MgO under three different sets of gas atmospheres (H_2/H_2O, CO/CO_2, $H_2/H_2O/CO/CO_2$) were studied.

2. 1. Materials

Table 2-1 presents a list of the chemicals used in the study, their purity, and their suppliers. CaO was calcined in platinum crucibles at 1200°C for 12 h to decompose any hydroxide and carbonate present. It was then stored in a desiccator with dry powders of SiO_2, Al_2O_3, MgO, MnO, FeO, $Ca_2P_2O_7$, FeS, and Fe. Pure water (99.9997%) was used to prevent any scale formation in the system. A small amount of $Ca_2P_2O_7$ was added to determine phosphorus distribution from the same equilibration experiment.

2. 2. Experimental Conditions Determination

The experimental conditions *viz.* slag compositions, temperature, and oxygen partial pressure are carefully selected to encompass the conditions of the proposed novel ironmaking process. The details of these conditions will be discussed below.

Table 2-1. Materials used in the present study

Material	Purity	Supplier
Aluminum Oxide (Al_2O_3)	99.99%	Acros Organics (Morris Plains,NJ)
Calcium Oxide (CaO)	99.95%	Alfa Aesar (Ward Hill, MA)
Silicon(IV) Oxide (SiO_2)	99.995%	Alfa Aesar (Ward Hill, MA)
Magnesium Oxide (MgO)	99.99%	Acros Organics (Morris Plains,NJ)
Iron(II) Oxide (FeO)	99.95%	Sigma-Aldrich (St Louis, MO)
Manganese(II) Oxide (MnO)	99%	Sigma-Aldrich (St Louis, MO)
Ferrophosphorus	P(22.0-28.0%)	Miller and Company (Rosemont,IL)
Ferromanganese	Mn(80.0-95.0%)	Miller and Company (Rosemont,IL)
Calcium Pyrophosphate ($Ca_2P_2O_7$)	≥99.9%	Sigma-Aldrich (St Louis, MO)
Iron (Fe)	≥99.99%	Sigma-Aldrich (St Louis, MO)
Iron(II) Sulfide (FeS)	99.98	Alfa Aesar (Ward Hill, MA)
Water (H_2O)	99.9997	Sigma-Aldrich (St Louis, MO)
Hydrogen (H_2)	99.999%	Airgas (Denver, CO)
Carbon Monoxide (CO)	99.999%	Airgas (Denver, CO)
Carbon Dioxide (CO_2)	99.999%	Airgas (Denver, CO)
Nitrogen (N_2)	99.999%	Airgas (Denver, CO)

2. 2. 1. Slag Composition

The slag compositional range was selected to cover the major components in the blast furnace slag. Table 2-2 presents the blast furnace slag compositions obtained from the National Slag Association database. Also, Table 2-3 provides the starting slag composition. Slags without Mn (slags # 1-4 in Table 2-3) will be referred to as Slag I, whereas those containing Mn (slags # 5-7 in Table 2-3) will be referred to as Slag II.

2. 2. 2. Oxygen Partial Pressure (pO_2)

To determine the range of the working pO_2, two steps were employed. First, the "% Excess Hydrogen" was used to calculate the ratio of H_2 to H_2O in the gas atmosphere and accordingly, pO_2 was calculated. To further explain the % Excess Hydrogen definition, its derivation will be shown starting with the reduction of magnetite with H_2, as follows:

$$Fe_3O_4(s) + H_2(g) = 3FeO(s) + H_2O(g) \qquad (2\text{-}1)$$

$$FeO(s) + H_2(g) = Fe(s) + H_2O(g) \qquad (2\text{-}2)$$

$$Fe_3O_4(s) + 4H_2(g) = 3Fe(s) + 4H_2O(g)\ (\text{overall}) \qquad (2\text{-}3)$$

$$K_2 = \left[\frac{pH_2O}{pH_2}\right]_{eq} = \left[\frac{n_{H_2O}}{n_{H_2}}\right]_{eq} \qquad (2\text{-}4)$$

The last step of the reduction, reaction 2-2, is significantly limited by equilibrium. On the other hand, the first stage, reaction 2-1, has a larger equilibrium constant than wustite reduction, reaction 2-2. For instance, the equilibrium constant of the final stage,

Table 2-2. Blast Furnace slag compositions in weight percent

Slag	Limits	CaO	SiO_2	MgO	Al_2O_3	MnO	Fe_tO	CaO/SiO_2	Reference
1	Low	32	32	5	7	0.2	1	1.0	BF Brochure[3]
	High	45	42	15	16	1	1.5	1.1	
2	Low	34	32	5	9	0.2	0.3	1.1	Slag & Corrosion[4]
	High	44	40	18	17	1.5	1.5	1.1	
3	Low	34	31	1	10	0.1	0.1	1.1	1949[5]
	High	48	45	15	17	1.4	1	1.1	
4	Low	31	31	2	8	0.2	0.2	1.0	1957[5]
	High	47	41	16	18	2.3	0.9	1.1	
5	Low	32	32	2	8	0.2	0.2	1.0	1968[5]
	High	44	40	19	20	2	0.9	1.1	
6	Low	34	27	7	7	0.15	0.2	1.3	1985[5]
	High	43	38	15	12	0.76	1.6	1.1	

Table 2-3. The starting slag composition in weight percent

Slag	CaO	SiO_2	MgO	Al_2O_3	MnO	FeO	FeS	$Ca_2P_2O_7$	CaO/SiO_2
1	29	36	10	10	0	15	0.3	0.3	0.8
2	33	33	10	10	0	15	0.3	0.3	1
3	35	30	10	10	0	15	0.3	0.3	1.2
4	38	27	10	10	0	15	0.3	0.3	1.4
5	26	32	10	15	2	15	0.9	1.5	0.8
6	29	29	10	15	2	15	0.9	1.5	1
7	32	26	10	15	2	15	0.9	1.5	1.2

eq 2-4, is ~1 at 1400°C, producing an equilibrium gas mixture of H_2/H_2O ratio of ~1/1. It is worth noting that the equilibrium constant, K_2, does not change much at higher temperatures until iron starts volatilizing.

Based on the above discussion, the minimum molar amount of hydrogen required to complete the reduction of magnetite in the reactor is the stoichiometric hydrogen for the reduction of magnetite to iron plus the hydrogen needed to overcome the wustite/iron equilibrium. This minimum required hydrogen is approximately twice the stoichiometric hydrogen because the stoichiometric hydrogen is the same molar amount as water vapor generated by the reduction. Thus,

$$n_{H_2,\min} = n_{H_2,red} + \frac{n_{H_2,red}}{K_2} = n_{H_2,red}\left[1 + \frac{1}{K_2}\right] \qquad (2\text{-}5)$$

In this equation, $n_{H_2,red}$ is the molar amount of hydrogen used for reaction 2-3, $n_{H_2,min}$ is the minimum molar amount of hydrogen required to remove oxygen in iron oxide, including the hydrogen needed to overcome the equilibrium barrier. The ratio of excess amount of hydrogen compared to the minimum required hydrogen was used to define "% Excess Hydrogen" as follows:

$$\%\ Excess\ H_2 = \frac{n_{H_2,\sup} - n_{H_2,\min}}{n_{H_2,\min}} \times 100 \qquad (2\text{-}6)$$

where $n_{H_2,sup}$ is the molar amount of hydrogen supplied in the reactor. To study the kinetics of the process, which was carried out by other members of our group, this ratio

was varied as one of the parameters. It is worth mentioning that with excess H_2 of only 40%, complete reduction was accomplished in about 7 seconds at temperatures above 1300°C. The initial pO_2 range was selected to encompass the %Excess H_2 in the expected range of operation of the Sohn process. Therefore, pO_2 was initially selected in the range 10^{-10} to 10^{-8} atm.

The second step in determining the experimental pO_2 range was to ensure that under this range of pO_2, the amount of FeO will not be excessive. This condition is an obvious requisite in the slag-metal equilibration technique. In order to assess that pO_2 range under which the three-phase equilibrium (gas-slag-metal equilibrium) could be maintained, HSC 5.11 software (Outokumpu Oyj, Riihitontuntie 7, Finland) was used. The objective of these calculations was to determine the highest pO_2 under which the iron/wustite equilibrium exists. The HSC software contains a handy tool to calculate the phase stability diagrams, namely Lpp-Diagrams. The Lpp-Diagram module was used to calculate the phase stability boundaries as lines based on the reaction equations. It is worth noting that this module calculates these boundaries based on pure FeO in equilibrium with molten Fe compared to the actual conditions where the FeO is not in the pure form in the slag. The Lpp-Diagrams of the Fe-O system was generated by HSC 5.11 for the systems Fe-C-O and Fe-H-O in the temperature range 1550 to 1650°C. Figures 2-1 and 2-2 show only two examples of the predominance area diagrams and the rest are not shown here. It is notable that these calculations acted as guidelines for determining iron/wustite boundaries, which was found to be $pO_2 \leq 10^{-8}$ atm in the temperature range 1550 to 1650°C. In order to precisely determine pO_2 range for the equilibrium experiments, a set of preliminary experiments were conducted at different temperatures

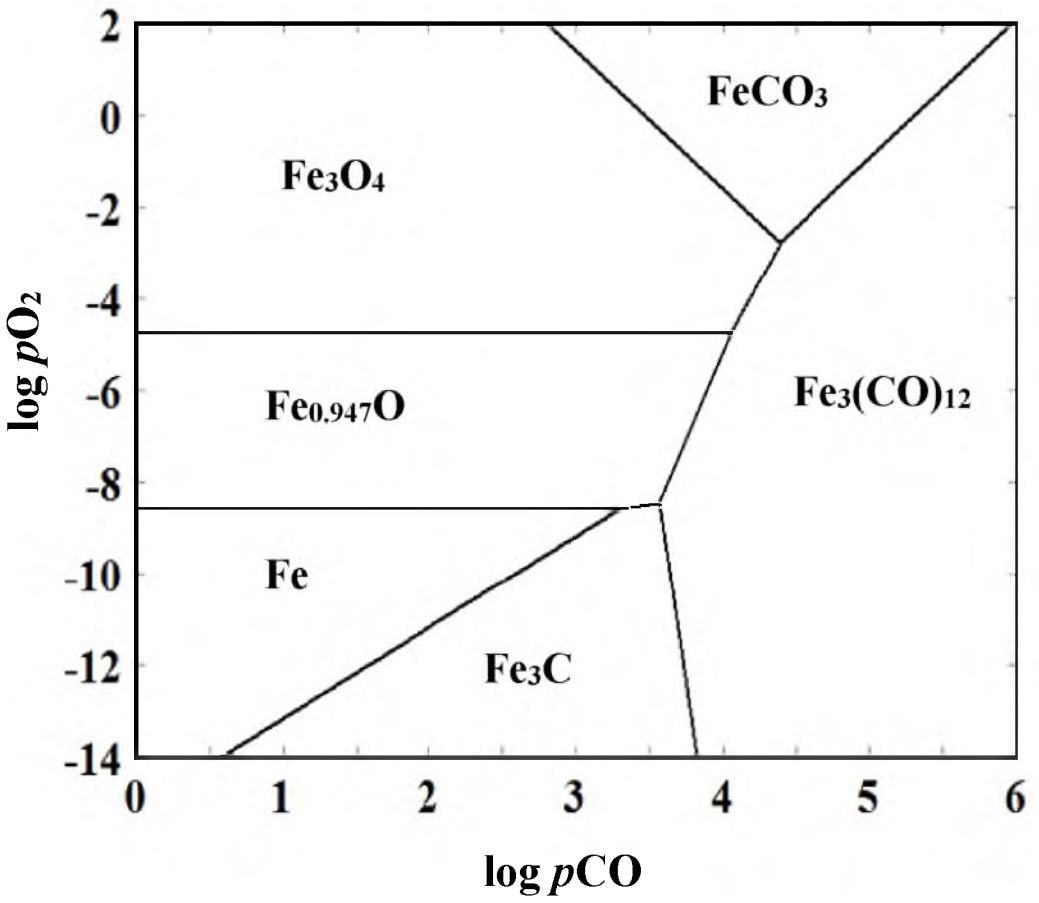

Figure 2-1. The phase stability diagram for Fe-C-O system at 1550°C.

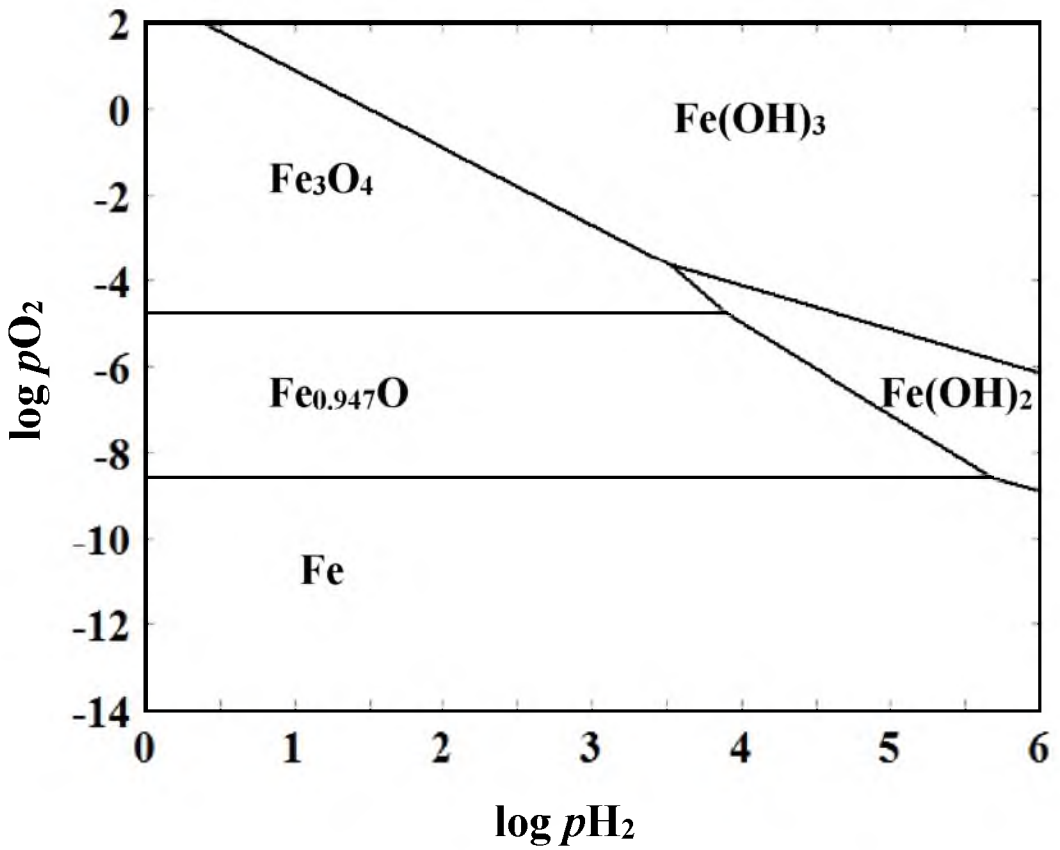

Figure 2-2. The phase stability diagram for Fe-H-O system at 1550°C.

with various slag compositions. It was found that the highest pO_2 should be less than 10^{-8} atm within the temperature range of 1550-1650°C to prevent complete oxidation of iron.

To sum up, the preliminary determination of the pO_2 range was done based on the process feasibility research (% Excess H_2) along with the predominance area diagrams (calculated by HSC) and finally the experimental verification. Using the previous feasibility research results, we determined the pO_2 range of interest to be 10^{-10}-10^{-8} atm. Using HSC equilibrium calculations, it was found that the maximum pO_2 should be 10^{-8} atm for the 3-phase equilibrium to be maintained, which was verified by the preliminary experiments. Therefore, the experimental pO_2 was selected to be in the range 10^{-10}-10^{-9} atm and was controlled by the molar ratio of H_2/H_2O, $CO/CO_2/H_2/H_2O$, or CO/CO_2.

2. 2. 3. Temperature

The experimental temperature range was selected to be from 1550°C to 1650°C. The lowest experimental temperature was selected to maintain the iron in molten state, i.e., higher than iron melting point: 1538°C. Although 1650°C is considered high for ironmaking, it was selected as the maximum temperature to study the effect of temperature over a wide range.

2. 3. Equilibrium Calculations

The equilibrium gas composition was calculated using HSC 5.11 (Outokumpu Oyj, Riihitontuntie 7, Finland) built-in module; called Equilibrium Compositions. For experiments with SO_2 in the gas mixture, the input used in the HSC equilibrium compositions module was 2.8 mol% SO_2(g), constant for all experiments, and 97.2 mol%

was split between H_2 and H_2O according to the ratio of H_2/H_2O that varied from 1.7 to 10. For experiments without SO_2 in the gas mixture, there were three equilibrium gas mixtures. For the first mixture ($CO/CO_2/H_2/H_2O$), which represent the cases of using natural gas or coal gas as the fuel and reductant, we calculated the equilibrium gas composition of the partial combustion of CH_4 with O_2 using the input of molar ratios (CH_4/O_2) of 1/1 and 1/0.5, which produce enough reducing atmosphere with pO_2 ranging from 10^{-10} to 10^{-9} atm. Since our input gases were CO, CO_2, H_2, and H_2O, the output of this partial combustion process was used as the input to maintain pO_2 within the above-mentioned range. The equilibrium calculation results are shown in Table 2-4.

Since the purpose of carrying out the experiments under three different gas atmospheres was to investigate the effect of gas atmosphere on the variables under study, it was necessary to fix all the parameters such as slag composition, temperature, and pO_2. The $CO/CO_2/H_2/H_2O$ gas mixture was used as the reference with respect to pO_2. Using the following reactions and relations, the required amounts were calculated for the target pO_2 (based on the $CO/CO_2/H_2/H_2O$ gas mixture) and temperature. For a CO/CO_2 equilibrium mixture:

$$2CO_2(g) = 2CO(g) + O_2(g) \qquad (2\text{-}7)$$

$$\frac{pCO}{pCO_2} = \left(\frac{K}{pO_2}\right)^{\frac{1}{2}} \qquad (2\text{-}8)$$

where K = 6.77×10^{-8}, 1.81×10^{-7}, and 4.57×10^{-7} at 1550°C, 1600°C, and 1650°C, respectively.

Table 2-4. Calculated gas partial pressures at the experimental temperatures and P_T = 0.85 atm using $CO/CO_2/H_2O/H_2$ gas mixtures (1 atm = 101.3 kPa; Rxx, Sample Designation)

		CH_4/O_2 (molar ratio)			
		1.0/1.0		1.0/0.70	
pO_2 (atm)	1550°C	1.9×10^{-09}	R10-R12	1.6×10^{-10}	R19-R21
	1600°C	4.8×10^{-09}	R13-R15	3.6×10^{-10}	R22-R24
	1630°C	8.0×10^{-09}	R16-R18	6.1×10^{-10}	R25-R27
pCO (atm)	1550°C	2.4×10^{-01}	R10-R12	2.7×10^{-01}	R19-R21
	1600°C	2.4×10^{-01}	R13-R15	2.7×10^{-01}	R22-R24
	1630°C	2.4×10^{-01}	R16-R18	2.7×10^{-01}	R25-R27
pCO_2 (atm)	1550°C	4.4×10^{-02}	R10-R12	1.4×10^{-02}	R19-R21
	1600°C	4.2×10^{-02}	R13-R15	1.4×10^{-02}	R22-R24
	1630°C	4.2×10^{-02}	R16-R18	1.4×10^{-02}	R25-R27
pH_2O (atm)	1550°C	2.4×10^{-01}	R10-R12	1.0×10^{-01}	R19-R21
	1600°C	2.4×10^{-01}	R13-R15	1.0×10^{-01}	R22-R24
	1630°C	2.4×10^{-01}	R16-R18	1.0×10^{-01}	R25-R27
pH_2 (atm)	1550°C	3.3×10^{-01}	R10-R12	4.7×10^{-01}	R19-R21
	1600°C	3.3×10^{-01}	R13-R15	4.7×10^{-01}	R22-R24
	1630°C	3.2×10^{-01}	R16-R18	4.7×10^{-01}	R25-R27
Flow Rates (mL/min)*	H_2	90	R10-R18	128	R19-R27
	H_2O	0.054		0.022	
	CO	69		77	
	CO_2	13		5	

*Flow rates are calculated at 0.85 atm (atmospheric pressure at Salt Lake City) and 25°C.

For a H_2/H_2O equilibrium mixture:

$$2H_2O(g) = 2H_2(g) + O_2(g) \qquad (2\text{-}9)$$

$$\frac{pH_2}{pH_2O} = \left(\frac{K}{pO_2}\right)^{\frac{1}{2}} \qquad (2\text{-}10)$$

where K = 4.23×10^{-9}, 1.02×10^{-8}, and 2.37×10^{-8} at 1550°C, 1600°C, and 1650°C, respectively. By solving eqs 2-8 and 2-10, using a known pO_2 and the total flow, the flow rate of each component gas can be calculated as listed in Tables 2-5 – 2-7. The calculated molar amounts at 1550°C were used as the input amounts for HSC to calculate the equilibrium gas composition at the other temperatures.

2. 4. Experimental Apparatus

The experimental apparatus was composed of two horizontal furnaces connected in series. The first furnace was used as part of a water vapor generator shown in Figure 2-3. The second furnace was the main reactor shown in Figure 2-4.

2. 4. 1. Water Vapor Generator

To add water vapor to the gas mixture, tubes for gases and a tube for water were connected to a cross connection the outlet from which was a 1/8 inch (0.318 cm) ID tube leading into the first furnace kept at 400°C. Water was injected as liquid using a MASTERFLEX digital peristaltic pump drive (Cole-Parmer Instrument, Vernon Hills, IL), which provided flow rates from 0.001 mL/min to 3400 mL/min with an accuracy of

Table 2-5. Calculated gas partial pressures at the experimental temperatures and P_T = 0.85 atm using $H_2/H_2O/SO_2$ gas mixtures (Sxx, Sample Designation)

		H_2/ H_2O (molar ratio)			
		1.7		3	
pO_2	1550°C	2.2×10^{-09}	S1-S4	7.0×10^{-10}	S5-S8
	1600°C	4.8×10^{-09}	S17-S20	1.8×10^{-09}	S21-S24
	1650°C	-	-	4.2×10^{-09}	S37-S38
pH_2	1550°C	4.7×10^{-10}	S1-S4	1.2×10^{-03}	S5-S8
	1600°C	4.1×10^{-04}	S17-S20	1.3×10^{-03}	S21-S24
	1650°C	4.3×10^{-04}	-	1.3×10^{-03}	S37-S38
pS_2	1550°C	1.4×10^{-03}	S1-S4	1.0×10^{-03}	S5-S8
	1600°C	1.7×10^{-03}	S17-S20	1.3×10^{-03}	S21-S24
	1650°C	2.0×10^{-03}	-	1.6×10^{-03}	S37-S38
pH_2O	1550°C	3.6×10^{-01}	S1-S4	2.6×10^{-01}	S5-S8
	1600°C	3.6×10^{-01}	S17-S20	2.6×10^{-01}	S21-S24
	1650°C	3.6×10^{-01}	-	2.6×10^{-01}	S37-S38
Flow Rates (mL/min)*	H_2	125		149	
	H_2O (liq.)	0.047		0.032	

* Flow rates are calculated at 25°C and 0.85 atm (atmospheric pressure at Salt Lake City).

Table 2-5. Continued

		H_2/ H_2O (molar ratio)			
		6		10	
pO_2	1550°C	2.4×10^{-10}	S13-S16	1.1×10^{-10}	S9-S12
	1600°C	5.3×10^{-10}	S29-S32	2.7×10^{-10}	S25-S28
	1650°C	-	-	-	-
pH_2	1550°C	1.3×10^{-03}	S13-S16	1.3×10^{-03}	S9-S12
	1600°C	1.3×10^{-03}	S29-S32	1.4×10^{-03}	S25-S28
	1650°C	1.4×10^{-03}	-	1.4×10^{-03}	-
pS_2	1550°C	8.3×10^{-04}	S13-S16	7.3×10^{-04}	S9-S12
	1600°C	1.0×10^{-03}	S29-S32	9.5×10^{-04}	S25-S28
	1650°C	1.3×10^{-03}	-	1.2×10^{-03}	-
pH_2O	1550°C	1.7×10^{-01}	S13-S16	1.3×10^{-01}	S9-S12
	1600°C	1.7×10^{-01}	S29-S32	1.3×10^{-01}	S25-S28
	1650°C	1.7×10^{-01}	-	1.3×10^{-01}	-
Flow Rates (mL/min)*	H_2	170		181	
	H_2O (liq.)	0.018		0.011	

*Flow rates are calculated at 0.85 atm (atmospheric pressure at Salt Lake City) and 25°C.

Table 2-6. Calculated gas partial pressures at the experimental temperatures and P_T = 0.85 atm using CO/CO_2 gas mixtures (Rxx, Sample Designation)

		CH_4/ O_2 (molar ratio)			
		1.0/1.0		1.0/0.70	
pO_2	1550°C	3.49×10^{-08}	R37-R39	1.37×10^{-10}	R46-R48
	1600°C	9.31×10^{-08}	R40-R42	3.67×10^{-10}	R49-R51
	1630°C	1.63×10^{-07}	R43-R45	6.44×10^{-10}	R52-R54
pCO	1550°C	4.78×10^{-01}	R37-R39	8.10×10^{-01}	R46-R48
	1600°C	4.78×10^{-01}	R40-R42	8.10×10^{-01}	R49-R51
	1630°C	4.78×10^{-01}	R43-R45	8.10×10^{-01}	R52-R54
pCO_2	1550°C	3.72×10^{-01}	R37-R39	3.96×10^{-02}	R46-R48
	1600°C	3.72×10^{-01}	R40-R42	3.96×10^{-02}	R49-R51
	1630°C	3.72×10^{-01}	R43-R45	3.96×10^{-02}	R52-R54
Flow Rates (mL/min)*	CO	103	R37-R45	66	R46-R54
	CO_2	30		7	

*Flow rates are calculated at 0.85 atm (atmospheric pressure at Salt Lake City) and 25°C.

Table 2-7. Calculated gas partial pressures at the experimental temperatures and P_T = 0.85 atm using H_2/H_2O gas mixtures

		CH_4/O_2 (molar ratio)			
		1.0/1.0		1.0/0.70	
pO_2	1550°C	3.49×10^{-08}	R64-R66	1.39×10^{-10}	R73-R75
	1600°C	8.46×10^{-08}	R67-R69	3.35×10^{-10}	R76-R78
pH_2O	1550°C	6.43×10^{-01}	R64-R66	1.39×10^{-01}	R73-R75
	1600°C	6.43×10^{-01}	R67-R69	1.39×10^{-01}	R76-R78
pH_2	1550°C	2.06×10^{-01}	R64-R66	7.10×10^{-01}	R73-R75
	1600°C	2.06×10^{-01}	R67-R69	7.10×10^{-01}	R76-R78
Flow Rates (mL/min)*	H_2	68	R64-R72	97	R73-R81
	H_2O	0.04		0.017	

*Flow rates are calculated at 0.85 atm (atmospheric pressure at Salt Lake City) and 25°C.

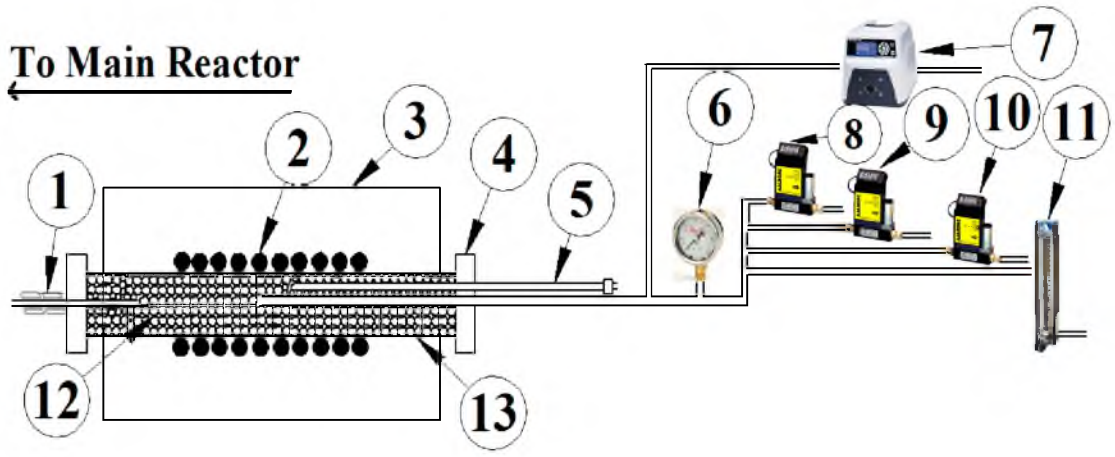

Figure 2-3. Water vapor generator: (1) Heating Tape (2) Heating elements, (3) Furnace body, (4) Stainless steel flange, (5) K-type thermocouple, (6) Pressure gauge, (7) Digital water pump, (8) CO_2 mass flow controller (MFC), (9) H_2 MFC, (10) CO/SO_2 MFC, (11) N_2 flow meter, (12) Ceramic rings, (13) Stainless steel tube.

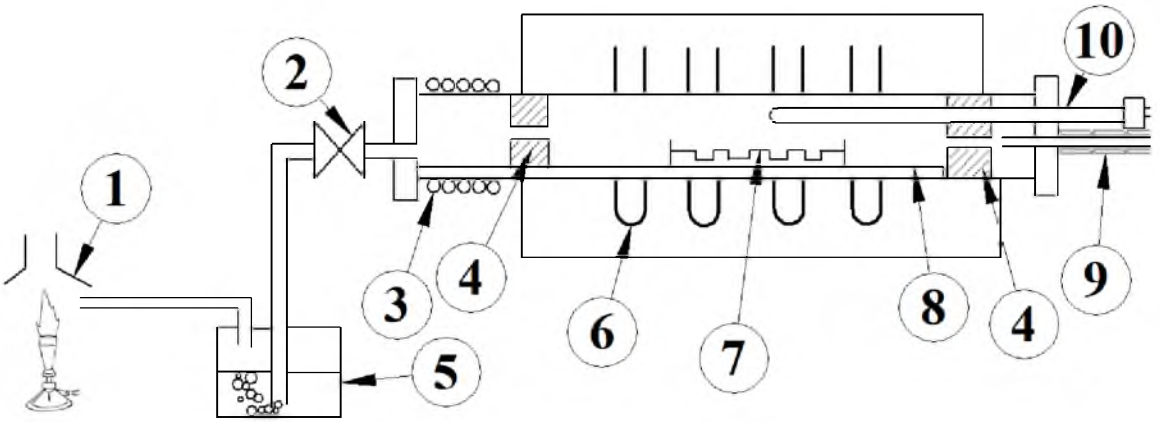

Figure 2-4. Main reactor: (1) Fume hood, (2) Valve, (3) Water cooling jacket, (4) Alumina shield, (5) NaOH scrubber, (6) $MoSi_2$ heating elements, (7) Alumina sample holder, (8) Alumina gutter, (9) Heating tape, (10) B-type thermocouple.

± 0.1%. The furnace had a 304 stainless steel tube (42 cm/length and 3 cm/ID) packed with Raschig rings to enhance gases mixing and heat transfer for rapid vaporization of water. Then, the gas mixture was delivered to the main reactor. The temperature was controlled using a K-type thermocouple and digital temperature controller with PID (Proportional Integral Derivative) adjustment (Nanmac Corporation, Framingham, MA) to an accuracy of ±2°C. The gases flow rates were controlled by Aalborg mass flow controllers (MFC) (AALBORG, Orangeburg, NY) with an accuracy of ±0.1, ±2, ±1.5, ±1.5 mL/min for SO_2, H_2, CO, and CO_2 gases, respectively.

2. 4. 2. Main Reactor

A horizontal electrical resistant furnace heated by $MoSi_2$ heating elements with an alumina reaction tube (8 cm OD, 7 cm ID, 120 cm length) was employed. Temperature was controlled and monitored inside the tube by two B-type thermocouples (Pt6%Rh/Pt30%Rh). One thermocouple was connected to a 708P temperature controller (MTI Corporation, Richmond, CA) with an advanced PID adjustment to control the supplied power with an accuracy of ±1°C. The other monitored the experimental temperature in the vicinity of the samples with a temperature deviation of 0.2 - 0.5°C. The samples holder was placed in the even temperature zone of the furnace, which was about 15 cm in length around the center of the reaction tube.

2. 5. Slag Preparation

For some experiments, the required amounts of CaO, SiO_2, Al_2O_3, and MgO were mixed in an alumina agate mortar to obtain the desired compositions and transferred to a

graphite crucible (5 cm OD, 6.6 cm height, 0.8 cm wall thickness), supplied by GraphiteStore.com, Inc. (Buffalo Grove, IL), to be premelted at 1600°C for 1 h under a N_2 flow. MgO was added as a slag component to minimize the consumption of the magnesia crucible used in this work for the reasons explained in Section 2.6. Thus, all the slags tested in this work were MgO-saturated. The premelted slag was crushed into fine powder in the alumina agate mortar. Premelting was confirmed by X-ray diffraction (XRD) and scanning electron microscope-energy dispersive spectroscopy (SEM-EDS). Figure 2-5 shows the XRD patterns of two premelted Slag I and Slag II with CaO/SiO_2 = 1. It indicates the presence of akermanite ($Ca_2MgSi_2O_7$), gehlenite ($Ca_2Al_2SiO_7$), spinel ($MgAl_2O_4$), and monticilite ($CaMgSiO_4$). The presence of these phases and the absence of phase such as priclase (MgO) or any other single oxide phase assures the homogeneity of the synthesized slag (according to the phase diagram[6]) and most importantly, the avoidance of MgO supersaturation. Figure 2-6 shows the uniform melting as evidenced by SEM. Another higher magnification SEM image is shown in Figure 2-7 where EDS was adopted to recognize all the existing phases. It indicates that the oxides are present as the following complex oxides: akermanite ($Ca_2MgSi_2O_7$) and gehlenite ($Ca_2Al_2SiO_7$), spinel ($MgAl_2O_4$), montcillite ($MgCaSiO_4$), ($CaMg_{0.3}AlSi_2Mn_2O_{10}$), ($CaMg_{0.3}AlSi_2Mn_{0.5}O_8$), ($Ca_2AlSi_3MnO_{12}$), ($Ca_{0.2}MgSi_{0.7}Mn_{0.1}O_3$), and ($Ca_{0.1}MgSi_{0.7}Mn_{0.1}O_3$). No evidence of periclase (MgO) or any other simple oxide phase was observed. That observation confirms that the adopted premelting conditions achieved slag homogeneity in Slags I and II. It also presaturated Slag II with magnesia without reaching undesired supersaturation, which might have been evidenced by the presence of periclase.

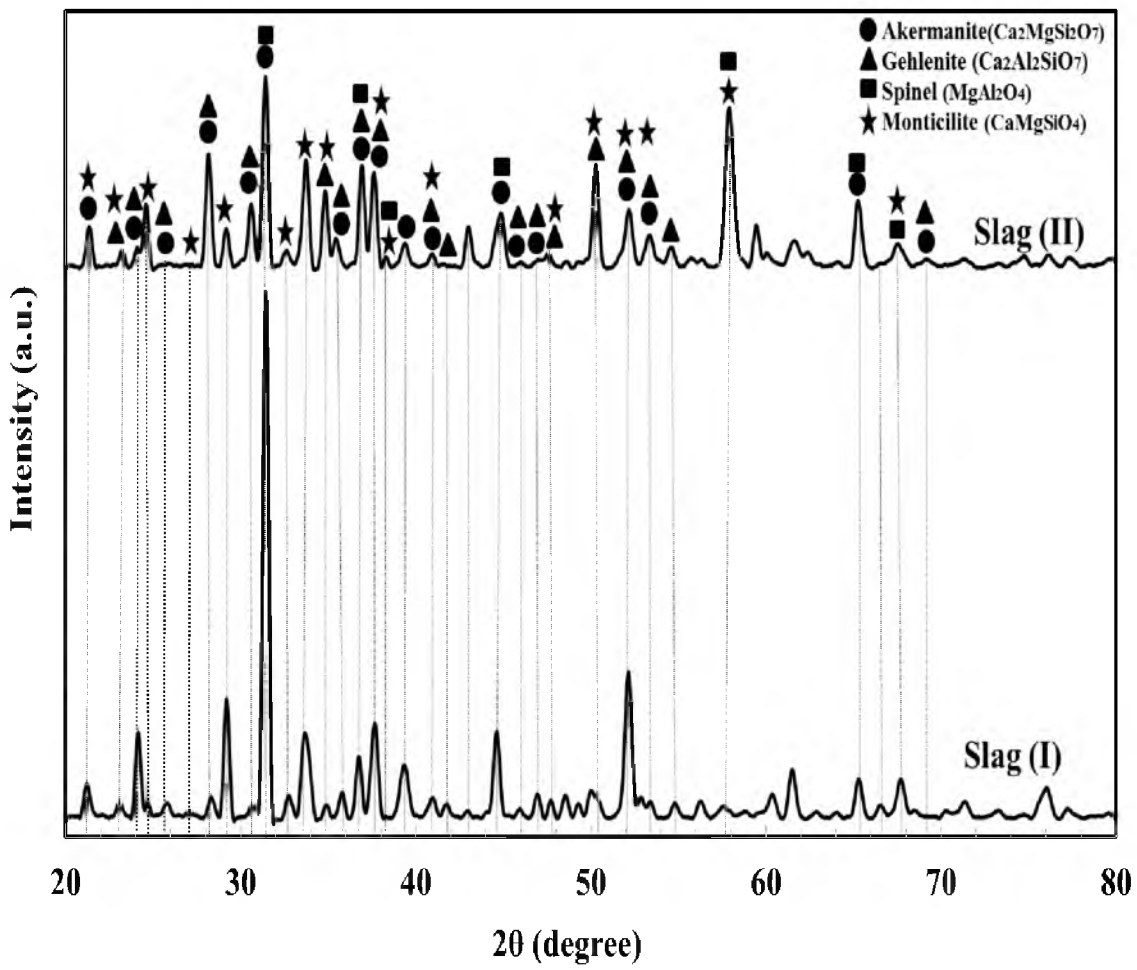

Figure 2-5. XRD pattern showing the peaks for akermanite, gehlenite, spinel, and monticilite, the presence of which verifies uniform slag melting for Slag I and Slag II with $CaO/SiO_2 = 1$.

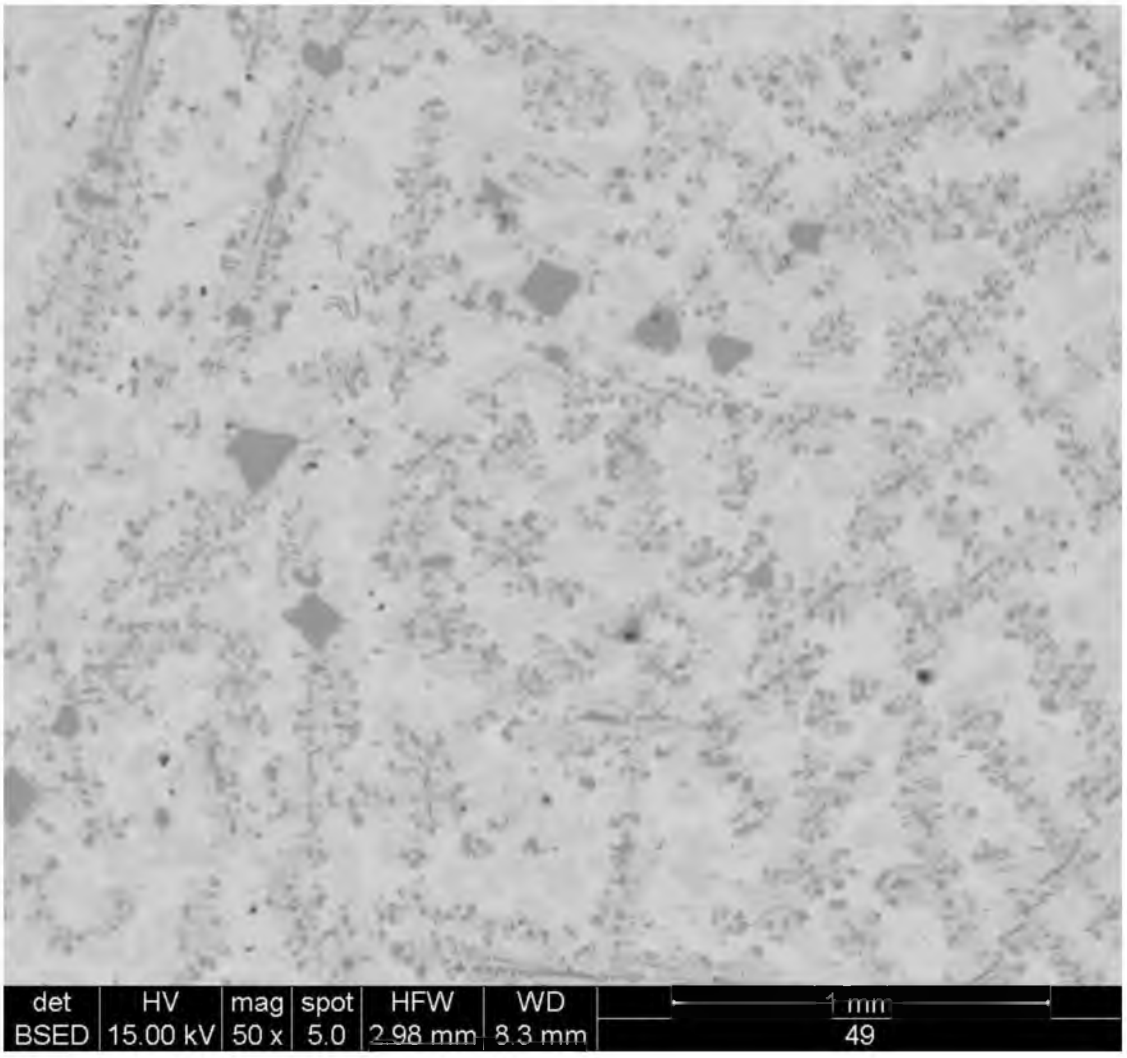

Figure 2-6. Premelted Slag II sample (CaO/SiO_2 = 1) showing complete and uniform melting.

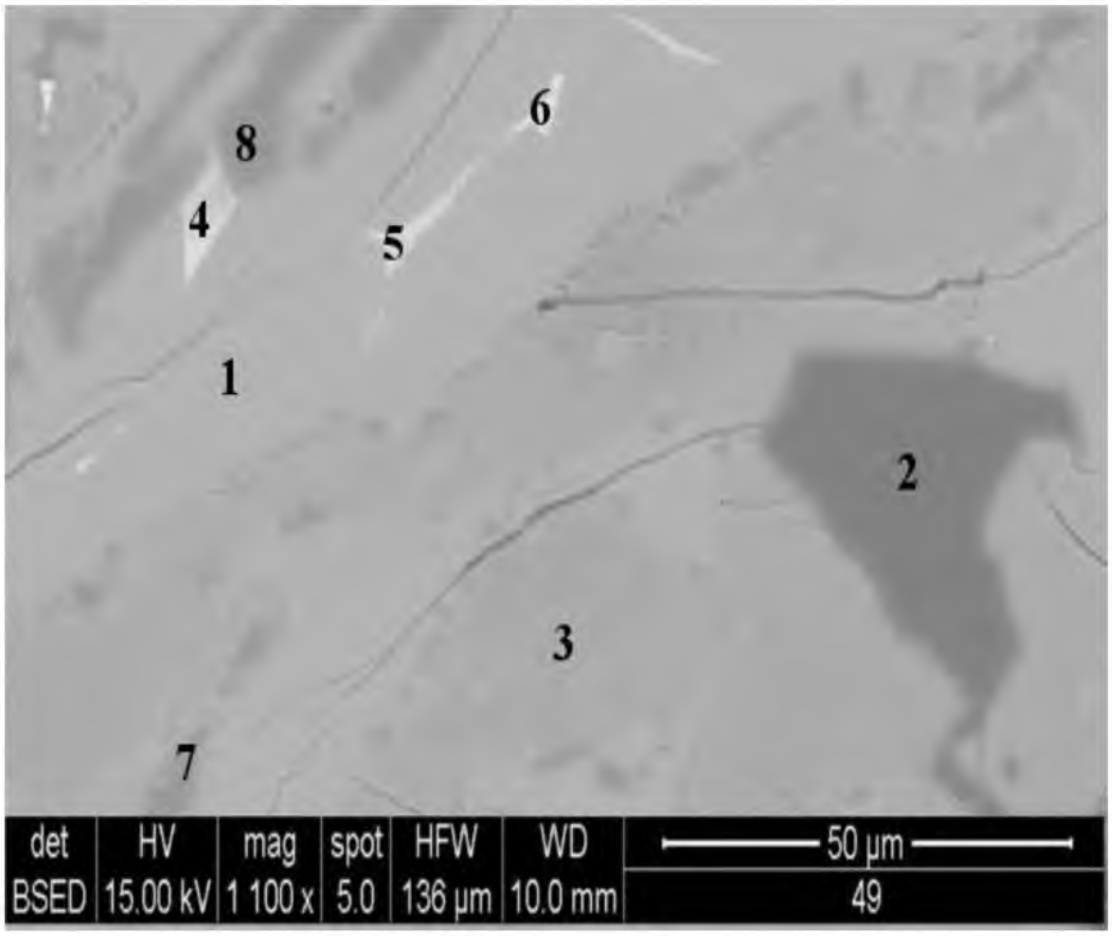

Figure 2-7. Magnified SEM micrograph of the same sample in Figure 2-6 showing the absence of any separate periclase phase (MgO) and the presence of akermanite ($Ca_2MgSi_2O_7$) and gehlenite ($Ca_2Al_2SiO_7$) [1], spinel ($MgAl_2O_4$) [2], montcillite ($MgCaSiO_4$) [3], ($CaMg_{0.3}AlSi_2Mn_2O_{10}$) [4], ($CaMg_{0.3}AlSi_2Mn_{0.5}O_8$) [5], ($Ca_2AlSi_3MnO_{12}$) [6], ($Ca_{0.2}MgSi_{0.7}Mn_{0.1}O_3$) [7], and ($Ca_{0.1}MgSi_{0.7}Mn_{0.1}O_3$) [8].

The Slag I powder, premelted in a graphite crucible, was transferred to a 99.8% pure alumina boat to be decarburized[6] at 1200°C for 24 h under an air flow. Dry FeO, $Ca_2P_2O_7$, and FeS powders were added and mixed well in an agate mortar. To ensure the uniform distribution of major slag components and verify composition consistency of the slag powders amongst the different equilibrium experiments, the slag powder was mapped by EDS, as shown in Figures 2-8 – 2-11, which confirmed the good mixing of major slag components. Each of the $Ca_2P_2O_7$ and FeS powders was added at 0.9 wt% and 1.5 wt% of the total slag and the resulting synthetic slag was stored in a desiccator to be used in the experiments.

To prepare the master Slag II, predetermined amounts of CaO, SiO_2, Al_2O_3, MgO and MnO dry powders were added into magnesia crucibles (4 cm OD, 7.6 cm height, 0.3 cm wall thickness) supplied by Ozark Technical Ceramics, Inc. (Webb City, MO) for premelting and magnesia presaturation at 1600°C for 5 h. The synthetic slag was then ground to a particle size of less than 40 μm. Then dry FeO, $Ca_2P_2O_7$, and FeS powders were added as in Slag I and mixed for 36 h in tumbler mixer supplied by Bioengineering Inc. (Cambridge, MA). Figures 2-12 – 2-14 show the uniform mixing as evidenced by the distribution of the elements of the major components in the slag powder. The master slag powders were then kept under vacuum in a desiccator for use in the equilibrium experiments.

2. 6. Experimental Procedure

The initial slag composition other than FeO was chosen to be similar to that of the blast furnace slag to enable the comparison with the blast furnace conditions. The FeO

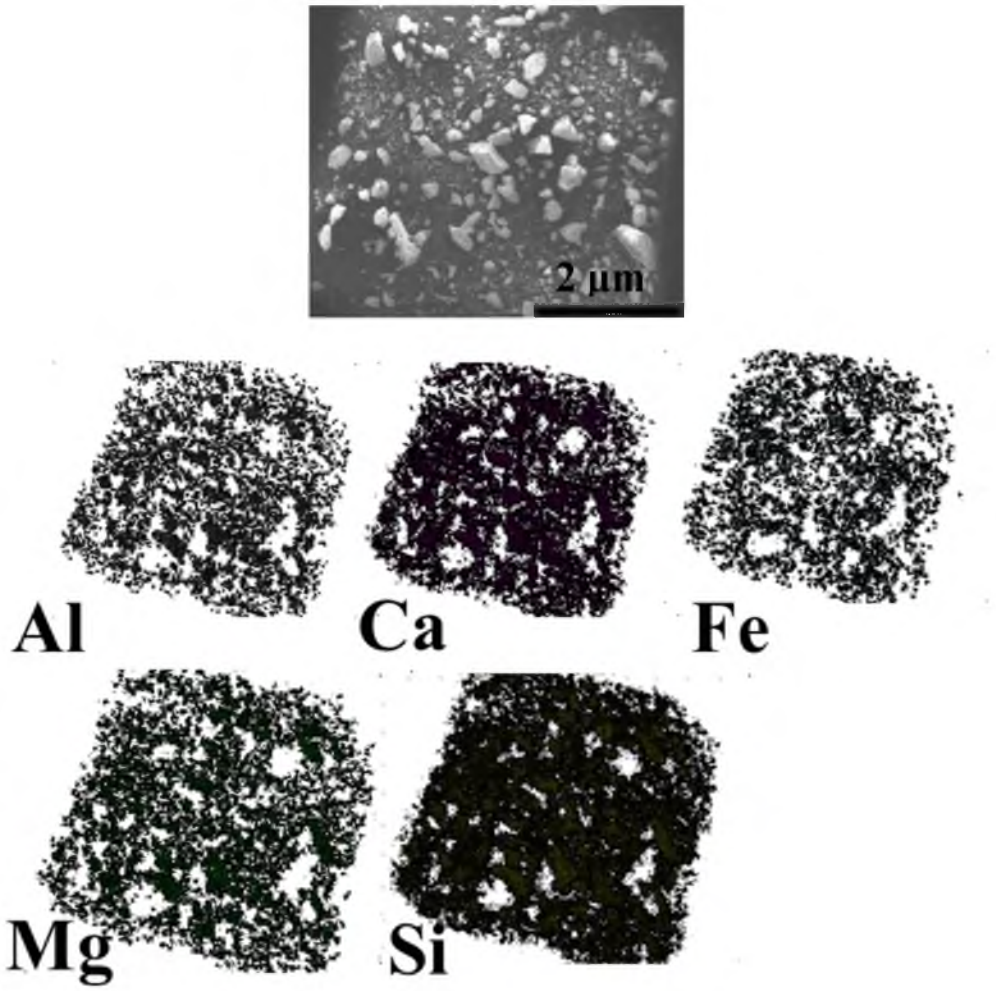

Figure 2-8. EDS elemental maps of Slag I of %CaO/%SiO_2 = 0.8, premelted in a graphite crucible at 1600°C and decarburized at 1200°C.

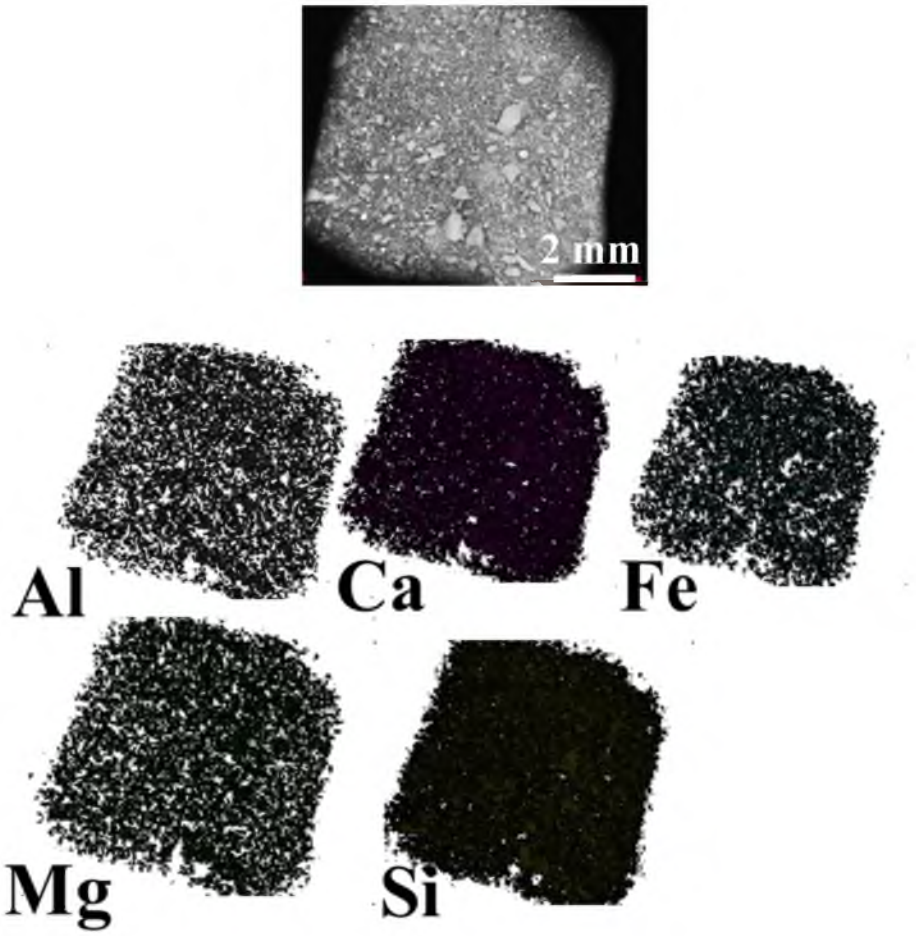

Figure 2-9. EDS elemental maps of Slag I of %CaO/%SiO_2 = 1.0, premelted in a graphite crucible at 1600°C and decarburized at 1200°C.

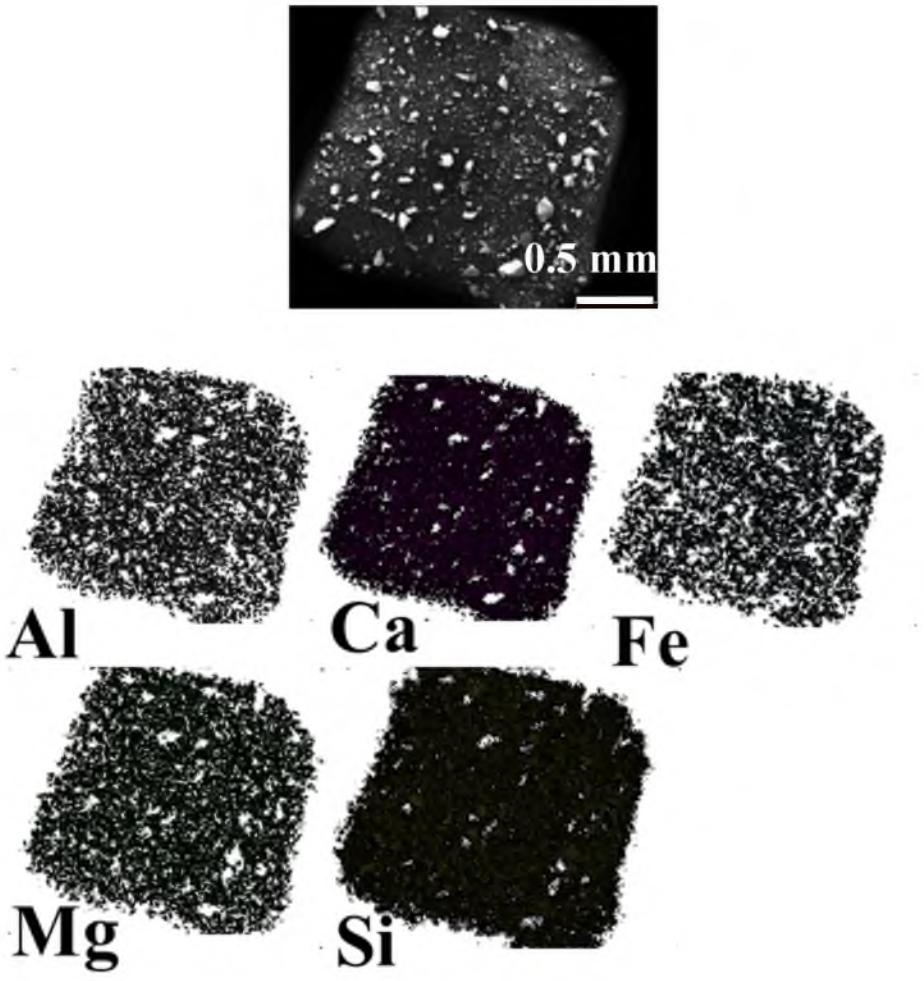

Figure 2-10. EDS elemental maps of Slag I of %CaO/%SiO_2 = 1.2, premelted in a graphite crucible at 1600°C and decarburized at 1200°C.

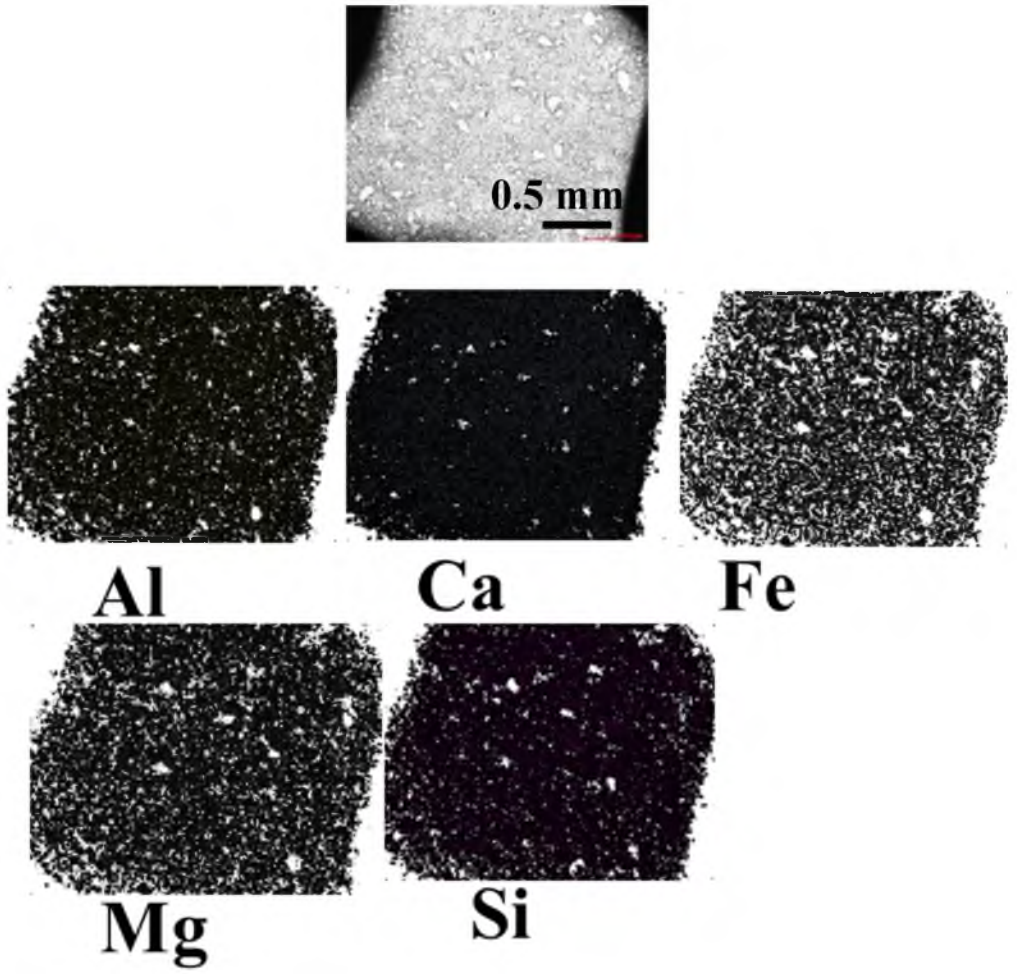

Figure 2-11. EDS elemental maps of Slag I of %CaO/%SiO_2 = 1.4, premelted in a graphite crucible at 1600°C and decarburized at 1200°C.

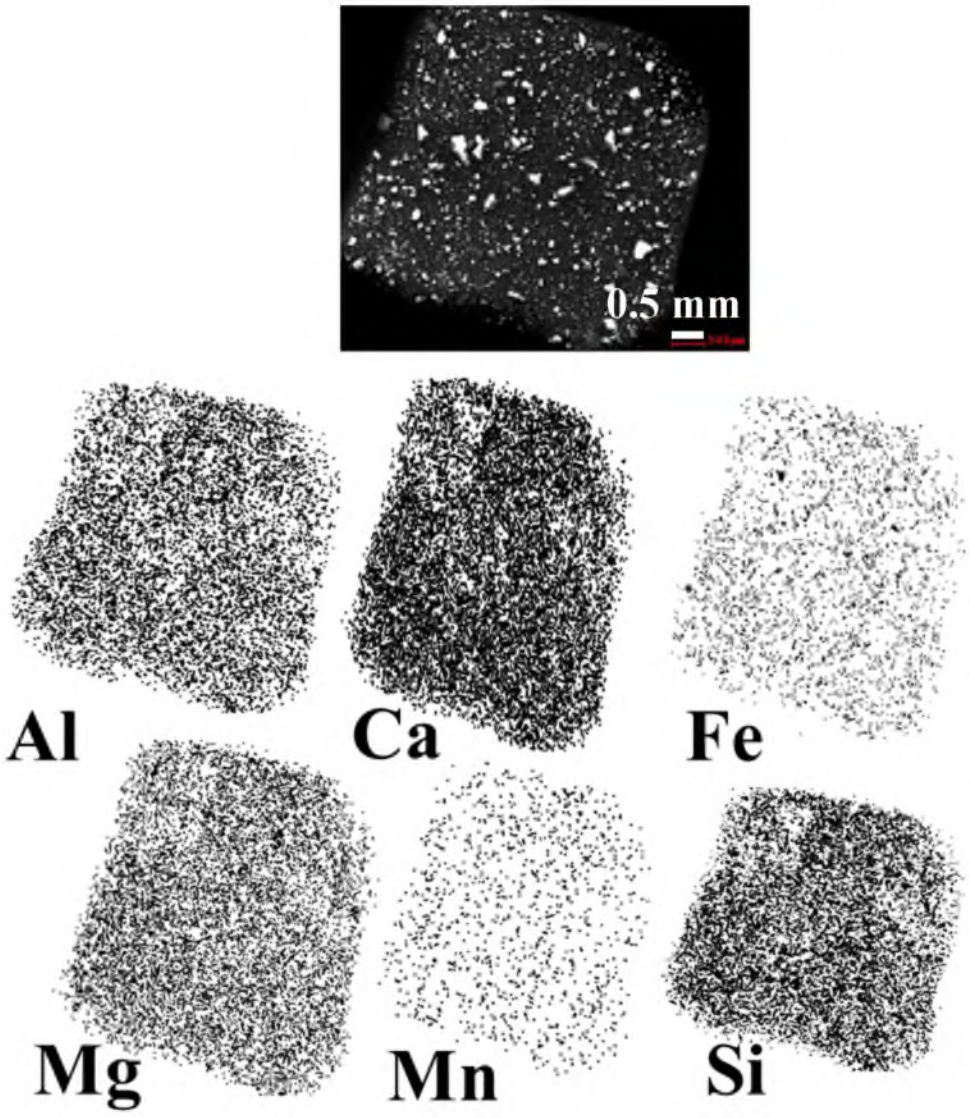

Figure 2-12. EDS elemental maps of Slag II of $\%CaO/\%SiO_2$ = 0.8, premelted in a magnesia crucible at 1600°C.

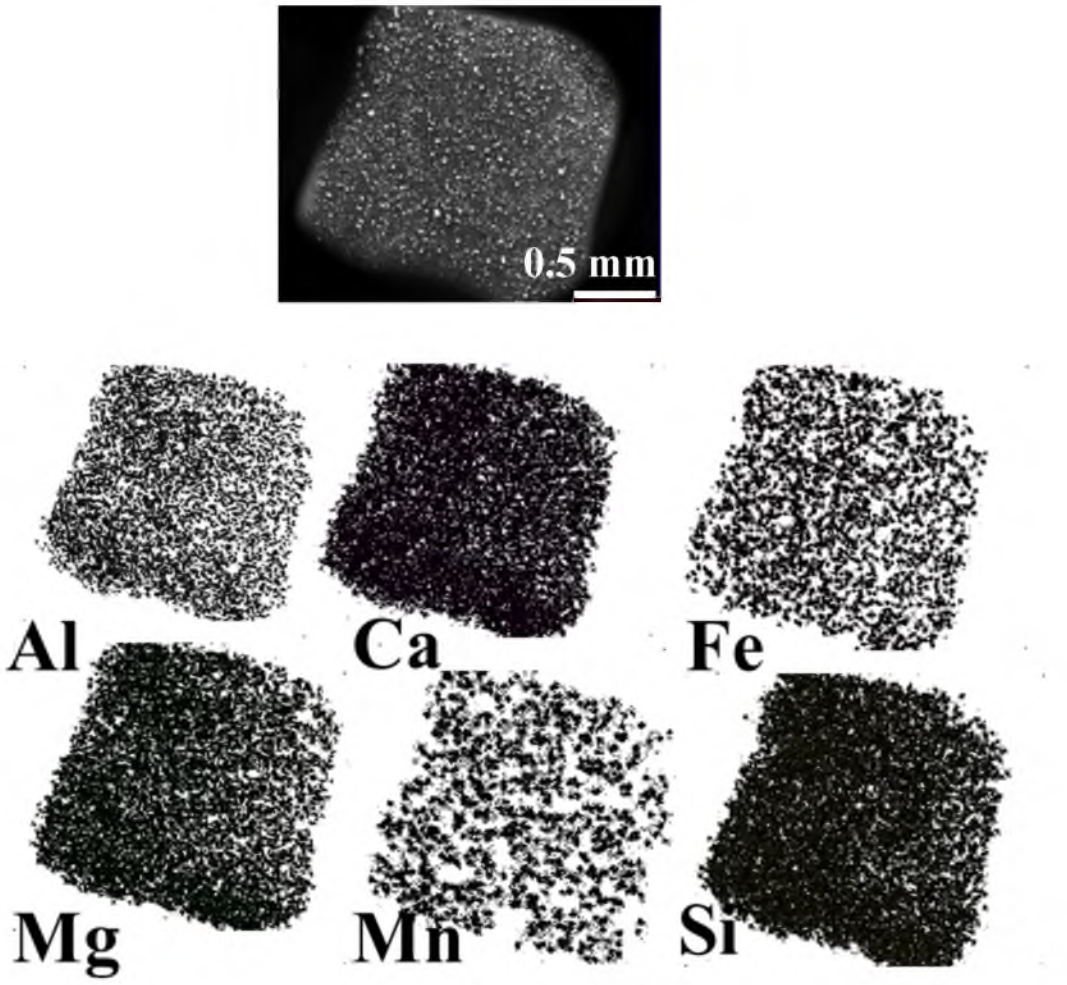

Figure 2-13. EDS elemental maps of Slag II of %CaO/%SiO_2 = 1.0, premelted in a magnesia crucible at 1600°C.

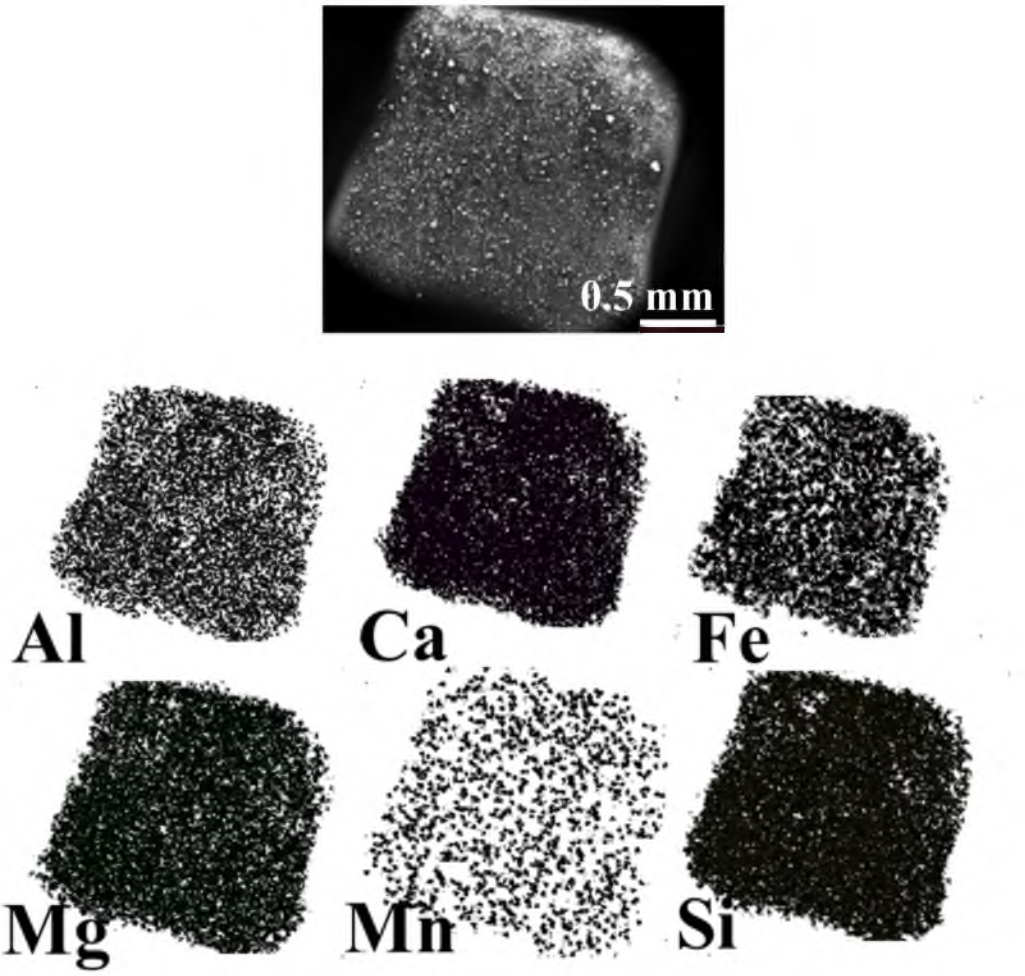

Figure 2-14. EDS elemental maps of Slag II of %CaO/%SiO_2 = 1.2, premelted in a magnesia crucible at 1600°C.

content in the slag was fixed by the equilibrium of molten iron with the gas phase affected by the contents of other slag constituents. For one portion of the experiments, the samples were prepared as 2.5 g of slag mixed with 2.5 g of iron powder. They were mixed well to reduce the time to reach equilibrium in magnesia crucibles (1.8 cm OD, 4 cm height, 0.25 cm wall thickness) supplied by Ozark Technical Ceramics, Inc. (Webb City, MO). Several materials, such as calcia (CaO), magnesia (MgO), platinum (Pt), and alumina (Al_2O_3), were carefully examined as the crucible material. Each of these materials was evaluated in terms of mechanical strength, high-temperature stability, and resistance to thermal shock, inertness toward molten slag, corrosion, or wettability by liquid iron, cost, and availability. After careful consideration of the different parameters and on the basis of the trials conducted with different materials, dense-sintered magnesia crucibles were selected. For the rest of the experiments, the samples were prepared as mentioned above but 1 g of slag mixed with 1 g of iron powder in smaller magnesia crucibles (1.3 cm OD, 2.5 cm height, 0.2 cm wall thickness).

The furnace was heated to the target temperature under a flow of N_2. At the target temperature, the furnace was opened to introduce the four-sample alumina holder to the even temperature zone within less than 5 minutes. Then, N_2 was switched to the experimental gas mixture. After 10 or 15 h, time to attain equilibrium which will be discussed in Section 2.5.2, the experimental gases were switched back to N_2 by stopping the water pump and gradually decreasing the experimental gases flows while increasing the N_2 flow. After 5 minutes of purging, the furnace was opened, the holder was pulled out within 5 minutes, and the samples were quenched in water or ice bath. The crucible

itself together with the sample was crushed, and iron was separated from the slag. Then, the iron was shredded and the slag finely ground.

Reproducibility of the experiments was confirmed by the consistency of the ICP and EDS quantitative analysis results of repeated experiments under the same conditions and it was found to be ±10%.

2. 6. 1. Analysis Methods

A number of quantitative and qualitative methods were employed in this work. Inductively coupled plasma optical emission spectrometry (ICP-OES) was employed to quantitatively analyze for S, P, and Mn as well as all the oxides in the slag. Also, energy dispersive spectroscopy (EDS) was used to map the distribution of phases in the slag. Scanning electron microscopy (SEM), X-ray diffraction (XRD), Fourier transform infrared spectroscopy (FTIR) along with Raman spectroscopy, and X-ray photon spectroscopy (XPS) were used to explore the different phases, the different chemical bonds, and the binding energies of different species, respectively. In the next sections, details will be presented for each of these techniques.

2. 6. 1. 1. *Scanning Electron Microscope (SEM) and Energy Dispersive Spectroscopy (EDS)*

An FEI Quanta 600 FEG SEM supplied by FEI (Hillsboro, Oregon) was used. The SEM was equipped with an EDAX tool (Genesis X-ray microanalysis system) for EDS analysis, which was supplied by EDAX Inc. (Mahwah, NJ). The accelerating voltage was selected to be 15 kV to enable the quantitative analysis of all the elements of interest.

Parts of the crushed crucible walls with slag pieces sticking to them were carefully mounted into epoxy, polished, and coated with a thin layer of carbon since the samples were nonconductive using carbon coater (Desk II, Denton Vacuum, Denton Vacuum, LLC, Moorestown, NJ). Also, the synthetic slag fine powder was scanned to confirm their homogeneity before use in the experiment. The high vacuum mode was employed to get high resolution and accurate EDS results. The working distance was selected to be within the analytical working distance specified by EDAX. The tilting was set to zero in all the samples.

2. 6. 1. 2. *X-Ray Diffraction (XRD)*

To identify the different phases in the slag, the fine powder was introduced into a Siemens D5000 X-ray diffractometer supplied by Bruker Cooperation (Wisconsin, MI) and equipped with Ni-filtered Cu Kα radiation (λ = 1.5406 Å). The X-ray intensity was measured over 2θ (θ: diffraction angel) from 10 to 100° with a scanning rate of 0.05°/s.

2. 6. 1. 3. *Fourier Transform Infrared Spectroscopy (FTIR)*

Infrared spectra were collected with a Continuum IR Microscope coupled to a Nicolet 6700 FTIR Spectrometer supplied by Thermo Scientific (Waltham, MA). The microscope was outfitted with a 250 μm MCT-A detector and 15X Reflechromat objective with apertures of 25 and 50 μm. The Happ-Genzel apodization function with 2 levels of zero filling was used to omit the noise peaks before spectra were Fourier transformed. A small amount of powder was placed on an aluminum mirror slide and flattened with a roller knife. Thinly flattened particles were examined by IR reflection

absorption spectroscopy (RAS) where 256 scans were coadded. All spectra were acquired at 4 cm^{-1} resolution and data points spacing of 0.48 cm^{-1}.

2. 6. 1. 4. *Raman Spectroscopy*

Raman spectra were collected via a DXR Raman Microscope, supplied by Thermo Scientific (Waltham, MA), applying a 532 nm laser, a full-range grating, 2 mW power, 50X objective, 50 mm pinhole, and collection time of 10 s. A small amount of sample powder was placed on a glass slide and pressed with another slide to make a flat surface for analysis. The glass slides containing the sample were placed on the microscope stage and single spot Raman collection or Raman point-mapping was performed.

2. 6. 1. 5. *X-Ray Photon Spectroscopy (XPS)*

All XPS measurements were made using a Kratos™ Axis Ultra DLD multi-technique surface analysis instrument, which was supplied by Kratos Analytical Inc. (Spring Valley, NY). The base pressure of the analysis chamber during these experiments was 3×10^{-10} Torr, with operating pressures around 1×10^{-9} Torr. Spectra were collected using the monochromatic Al Kα source (1486.7 eV) and a 300×700 micron spot size. Both low resolution survey scans, and high resolution scans of energy ranges of interest were done. Significant charging artifacts were seen for all samples, resulting in peak shifts and broadening. The peak widths were minimized by flooding the sample with low-energy electrons and ions from the charge neutralizer system. To determine the absolute energy shift, spectra were referenced to the C1s peak from adventitious carbon, which is a minute amount of carbonaceous contaminants usually adsorbed on the surface

of most samples exposed to air during handling. The mono Al source was operated at 12 mA of emission current with the target anode set to 15 kV, for a resulting power of 180 W. For survey spectra, the data were collected using a pass energy of 160 eV, a step size of 1 eV, and a dwell time of 200 ms. High resolution regional spectra were collected using a pass energy of 40 eV, a step size of 0.1 eV, and a dwell time of 300 ms. Each high resolution scan was averaged over 3 sweeps to improve signal to noise.

XPS spectra were deconvoluted using Gaussian/Lorentzian functions to represent distinct oxidation states. Where appropriate, these functions were combined with polynomials to aid in deconvolution to identify and eliminate excessive differential surface charge build-up, satellite peaks, and multiplet splitting.

Constraints were placed on the full width at half maximum (FWHM) and position of each peak, and a least squares-based fitting algorithm was employed until the lowest mean squared error was achieved.

2. 6. 1. 6. *Inductively Coupled Plasma Optical Emission Spectrometry (ICP-OES)*

The compositions of the iron and the slag phases were analyzed by ICP-OES for their sulfur, phosphorus, and manganese contents in addition to the complete oxides content in the slag. Spectro Genesis SOP spectrometer supplied by SPECTRO Analytical Instruments Inc. (Mahwah, NJ) was used. Prior to analysis, the samples were digested in closed Savillex® vessels made of a translucent and chemical resistant material (Teflon PFA®), which can withstand temperatures up to 240°C, were used as the digestion vessels, which were supplied by Savillex (Eden Prairie, MN).

The digestion method was developed in this laboratory and a provisional application has been filed with the United States Patent and Trademark Office (USPTO).[7] Mixtures of acids used in the digestion method are strongly dependent on the composition of the samples. Therefore, the digestion solution adopted for the slag is different from the one used in the iron samples. Also, the mixture and digestion method are different in samples without Mn and those with Mn. The digestion and analysis procedure was as follows:

Samples without Mn:

The iron samples were analyzed for P and S contents as follows:

1- A mixture of 6 mL HCl (38 %, Fisher Scientific, Pittsburgh, PA), 2 mL HNO_3 (70 %, EMD Chemicals, Philadelphia, PA), and 2 mL H_2O_2 (40 %, Sigma-Aldrich, St Louis, MO) was poured into a 60 mL digestion vessel.

2- Very quickly, a cleaned piece of iron sample of 0.2 g was dropped in the mixture and the vessel was closed tightly using a wrench set. The weight of the iron was rounded to nearest milligram.

3- Six to ten sample vessels were placed on the microwave plate. A countertop microwave (2.0 cu. ft., General Electric, Fairfield, CT) with 100% power (1200 W) and 3 rev./s was set for 3 min at a frequency of 2450 MHz.

4- The vessels were taken outside the oven and cooled to room temperature and each vessel was opened and the solutions were analytically transferred into a 100 mL volumetric flask, which was then diluted to the mark.

5- A sample of 50 mL was taken for ICP-AES analysis.

The slag samples were finely ground, dried for more than 24 h at 125°C, and kept in a desiccator under vacuum and dririte to be analyzed for Al_2O_3, CaO, MgO, SiO_2, FeO, S, and P contents as follows:

1- A mixture of 6 mL HCl (38 %), 2 mL HNO_3 (70 %), 2 mL HF (48 %, Mallinckrodt Chemicals, Phillipsburg, NJ), and 2 mL H_2O_2 (40 %) was poured into a digestion vessel.

2- A slag sample of 0.2 g was added into the vessel, which was then rapidly and tightly closed.

3- Six to ten sample vessels were placed in the microwave oven applying 100% power (1200 W) and 3 rev./s for 5 min.

4- The vessels were taken outside the microwave oven and cooled to room temperature and opened, and 4 mL boric acid (10 wt%, Mallinckrodt Chemicals, Phillipsburg, NJ) was added to mask excess fluoride ions in the solution. The vessel was then closed tightly and microwaved for additional 3 min.

5- After the vessel cooled down, it was opened and the solution was analytically transferred into 100 mL volumetric flask which was then diluted to the mark.

6- A sample of 50 mL was taken for ICP-AES analysis.

Samples with Mn:

Iron samples were analyzed for P, S, and Mn contents as follows:

1- A mixture of 4 mL HCl (38 %), 4 mL HNO_3 (70 %), 1 mL HF (48 %), and 1 mL H_2O_2 (40 %) was poured into a digestion vessel.

2- Very quickly, a piece of iron sample of 0.1g was dropped in the mixture and the vessel was closed tightly.

3- Six to ten sample vessels were placed in the microwave plate applying 50% power (600 W) and 3 rev./s for 10 min.

4- The vessels were taken outside the microwave oven and cooled to room temperature and each vessel was opened and the solutions were analytically transferred into 100 mL, which was then diluted to the mark volumetric flask for ICP analysis.

The slag samples were finely ground, dried for more than 24 h at 125°C, and kept in a desiccator under vacuum and dririte to be analyzed for Al_2O_3, CaO, MgO, SiO_2, FeO, MnO, S, and P contents as follows:

1- A slag sample of 0.1 g was placed in a Savillex® vessel.

2- A mixture of 4 mL HCl (38 %), 4 mL HNO_3 (70 %), 4 mL HF (48 %), and 2 mL H_2O_2 (40 %) was then added in the Savillex® vessel and the vessel was rapidly and tightly closed.

3- Six to ten sample vessels were placed in the microwave oven with 20% power (240 W) and 3 rev./s for 15 min.

4- The vessels were taken outside the microwave oven, cooled to room temperature, opened, and the solution was analytically transferred into 100 mL volumetric, which was then diluted to the mark flask and then taken for ICP-AES analysis.

After the digestion of the samples was completed, the samples were analyzed by a Spectro Genesis® SOP ICP-AES. The ICP was equipped with an autosampler and controlled by Smart Analyzer Vision software. The ICP operational conditions are given in Table 2-8. For calibration, sets of multielement standards supplied by Inorganic Ventures (Christiansburg, VA) containing all the analytes of interest at eight different

Table 2-8. Instrumental operating condition for Spectro Genesis® SOP (ICP-AES)

Parameter	Instrument operating conditions
Plasma power	1400 W
Plasma (coolant) gas flow	12 $Lmin^{-1}$
Auxiliary gas flow	1 $Lmin^{-1}$
Nebulizer gas flow	1 $Lmin^{-1}$
Optic flush	0.5 $Lmin^{-1}$
Pump speed	2 step (normal) 4 step (fast)
Wash time	25 s
Read delay	25 s
Replicate readings	3

levels of concentration were prepared and measured at the suitable wavelengths. The emission lines used are shown in Table 2-9. For S and P, multiple wavelengths were selected to assure the accuracy of quantitative analysis. After the analysis of all the samples were completed, a single wavelength was selected for each element, which gave the best quantitative results compared with reference samples. The analysis reproducibility was maintained in the range of ±2 to ±10%.

2. 6. 2. Equilibrium Time Determination

In order to determine the equilibrium time, two sets of experiments were designed. The first was to reach equilibrium form the lower side, where the desired element is mostly concentrated on the metal side. The second set was designed so that the equilibrium could be reached from the higher side, which is the slag. When equilibrium is reached, the values of the distribution ratios should be the same regardless of the element source whether it comes from the slag or the metal side. Sulfur, phosphorus, and manganese ferroalloys were prepared by mixing the commercial alloys, see Table 2-1 for details, with iron powder to bring their S, P, or Mn contents to 0.3 wt%. The mixture was then melted under a flow of N_2 (99.999%) for 7 h at 1600°C in alumina crucibles (99.6%) supplied by AdValue Technology (Tucson, AZ). Then, the furnace was cooled to room temperature under a continuous flow of N_2 (99.999%). In some experiments, equilibrium time was determined from the slag side, whereas in the majority of the experiments, it was determined from metal and slag sides as presented in Figures 2-15 – 2-18 and 2-19 – 2-23, respectively. Essentially the same equilibrium condition was attained regardless of

Table 2-9. Wavelengths and analytical details used for each element

Element	Wavelength (nm)	Method detection limit (ppm)	Standard Error (ppm)	Correlation coefficient
Al	309.271	0.113	0.716	0.99826
Ca	183.801	0.331	0.446	0.99799
Fe	238.204	8.00	0.579	0.99805
Mg	280.270	0.003	0.713	0.99828
Mn	259.373	0.006	0.913	0.99718
P	178.287 213.618 214.914	0.319 0.373 0.400	0.420 0.488 0.386	0.99822 0.99878 0.99936
S	180.731 182.034	0.800 0.202	0.659 0.594	0.99903 0.99911
Si	251.612	0.800	0.369	0.99987

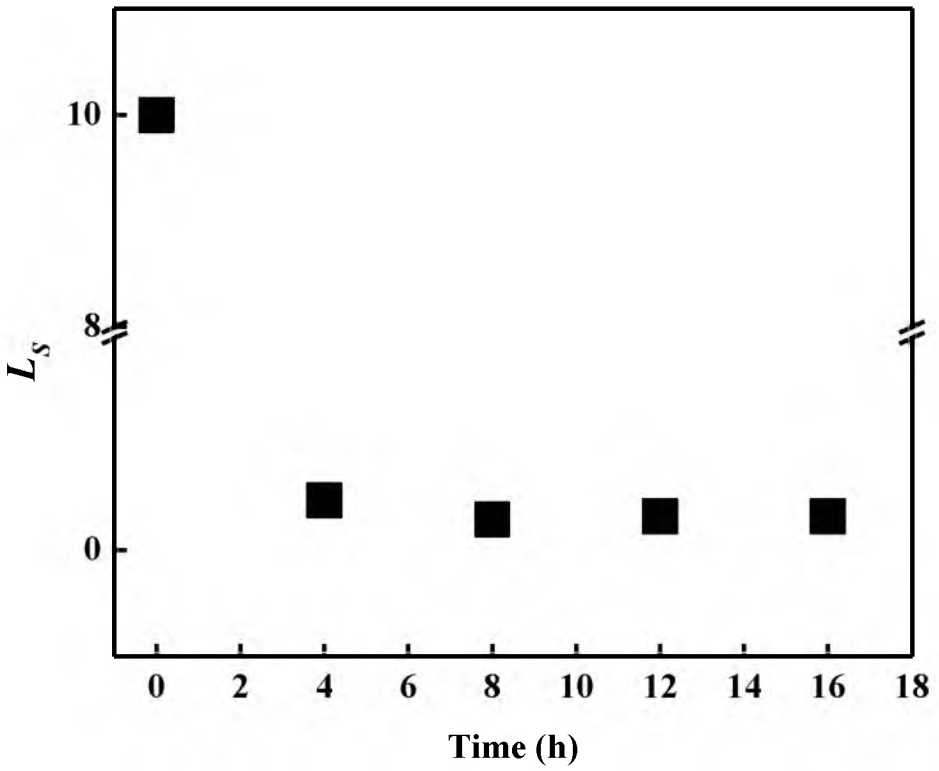

Figure 2-15. The variation of sulfur distribution ratio with time from the slag side in experiments without Mn.

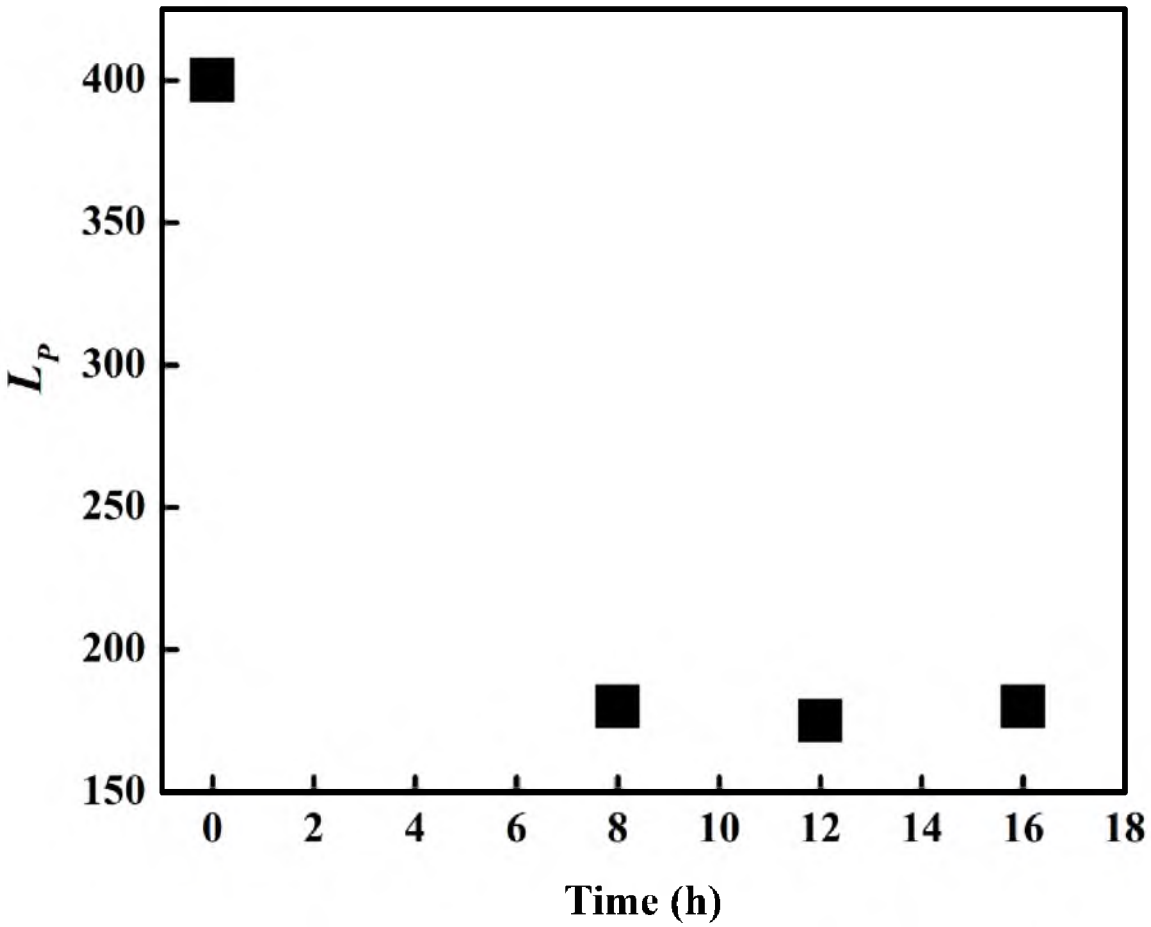

Figure 2-16. The variation of phosphorus distribution ratio with time from the slag side in experiments without Mn.

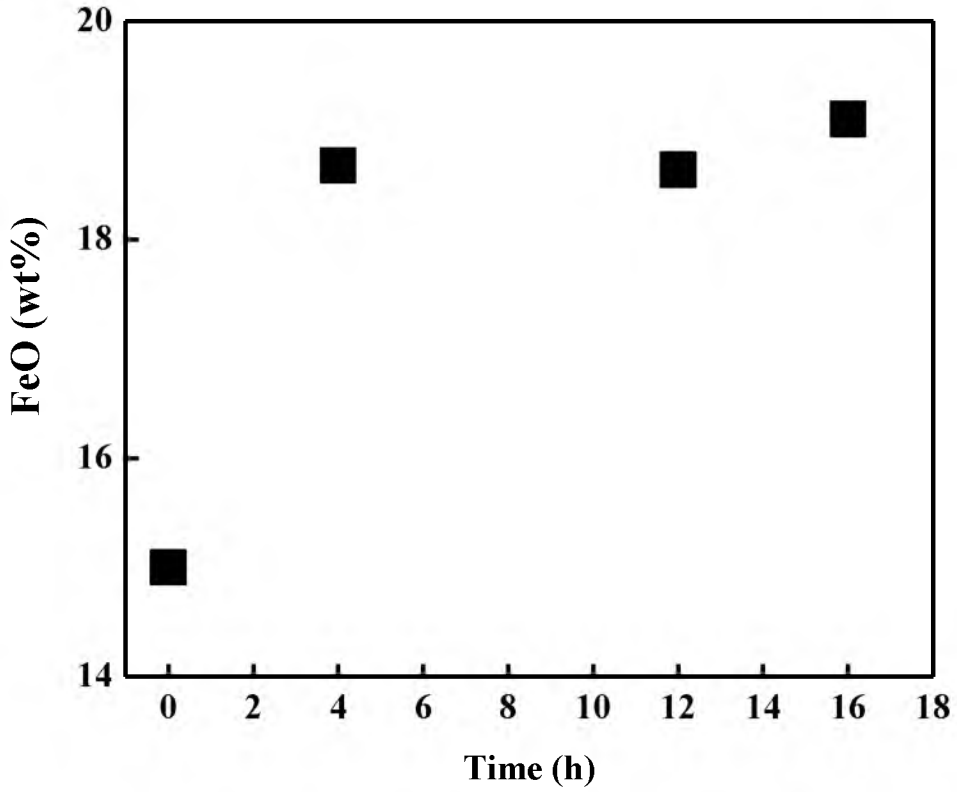

Figure 2-17. The variation of FeO content with time in experiments without Mn.

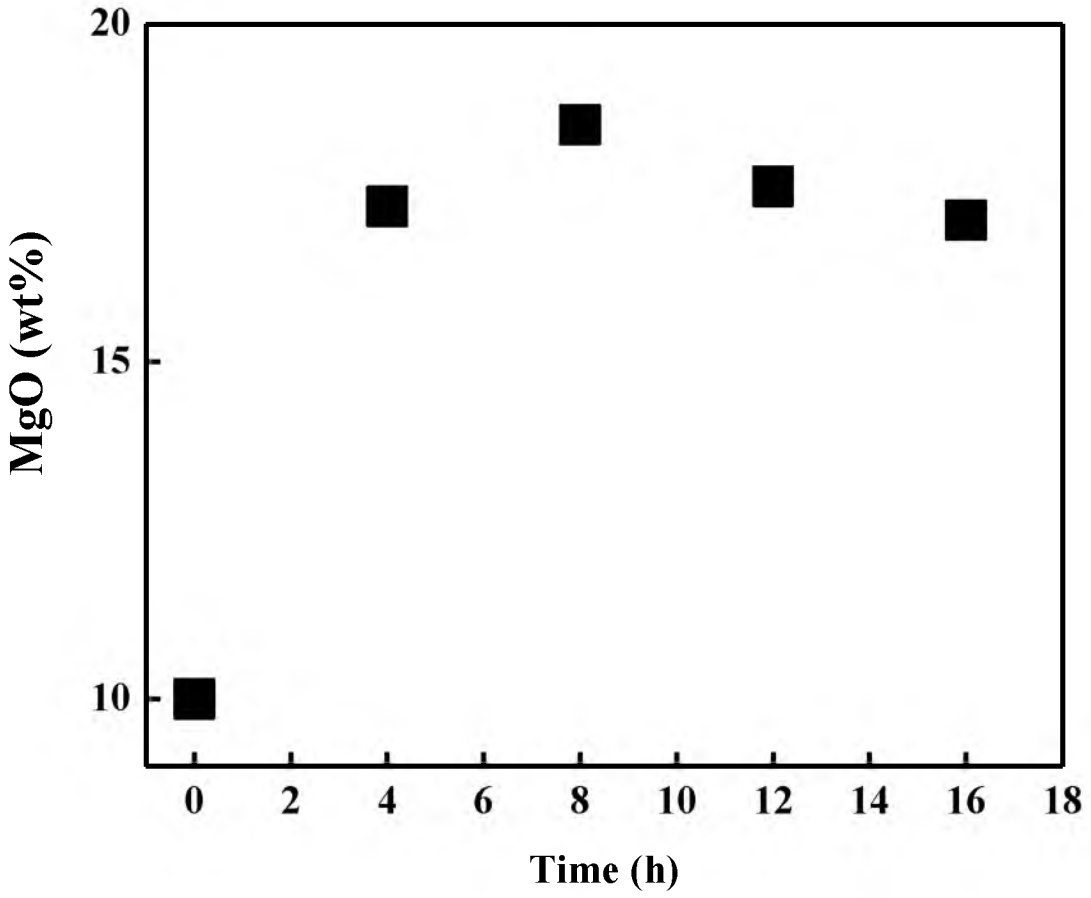

Figure 2-18. The variation of MgO content with time in experiments without Mn.

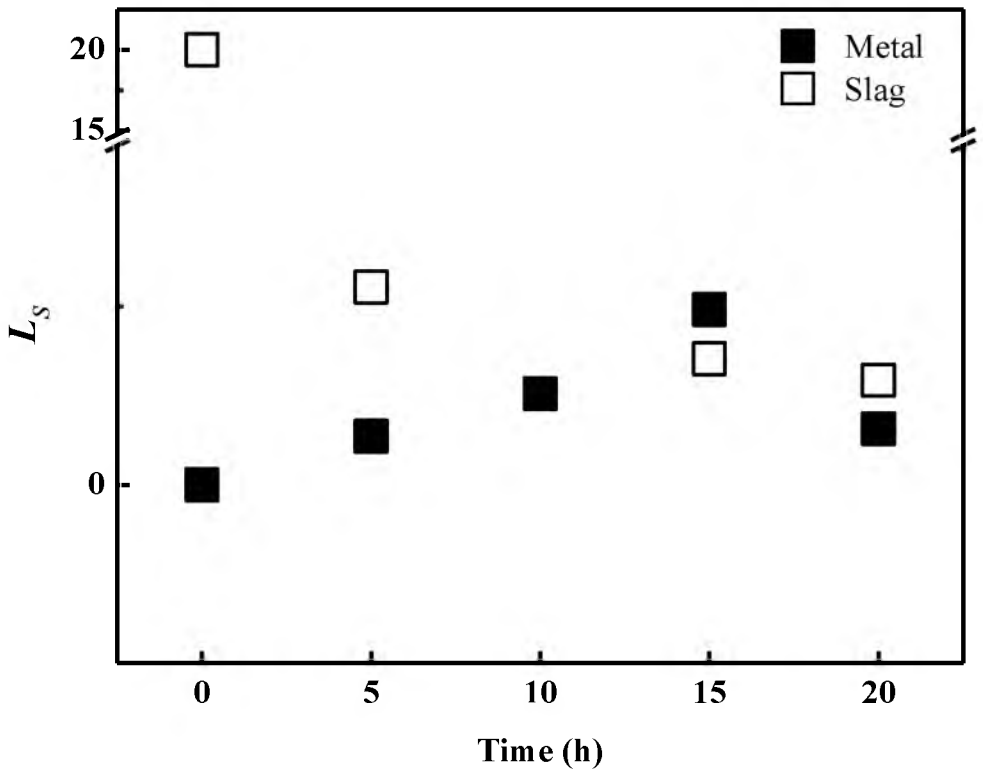

Figure 2-19. The variation of sulfur distribution ratio with time from both metal and slag sides in experiments with Mn.

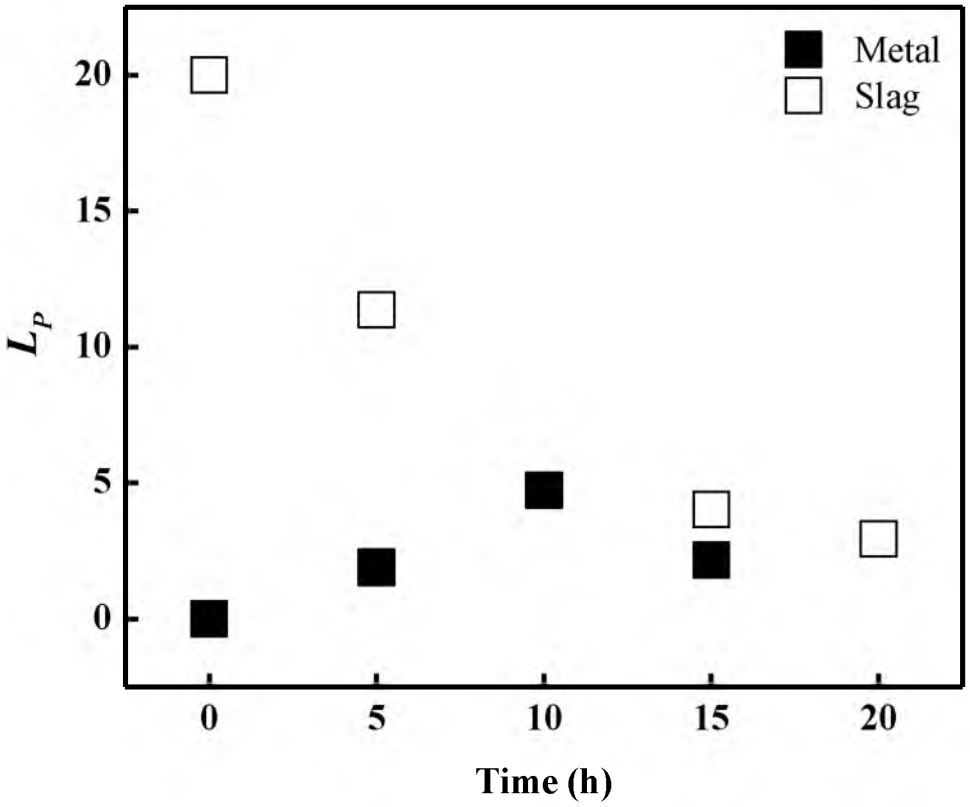

Figure 2-20. The variation of phosphorus distribution ratio with time from both metal and slag sides in experiments with Mn.

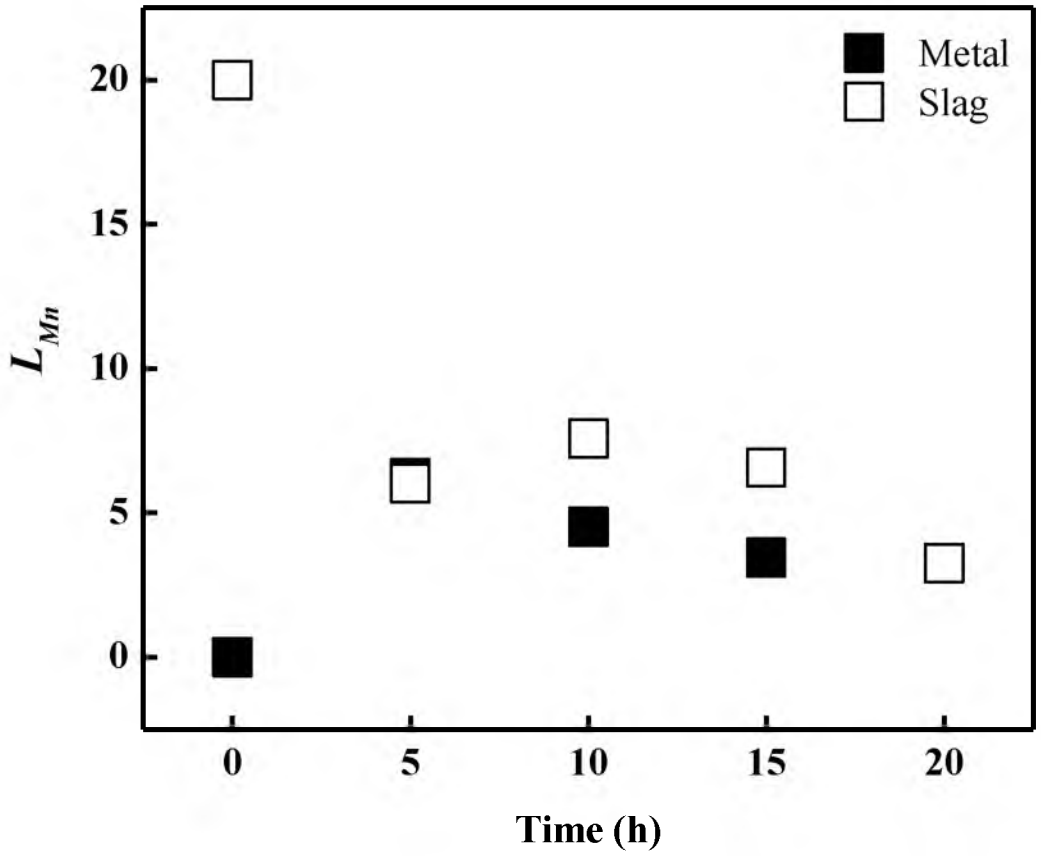

Figure 2-21. The variation of Manganese distribution ratio with time from both metal and slag sides in experiments with Mn.

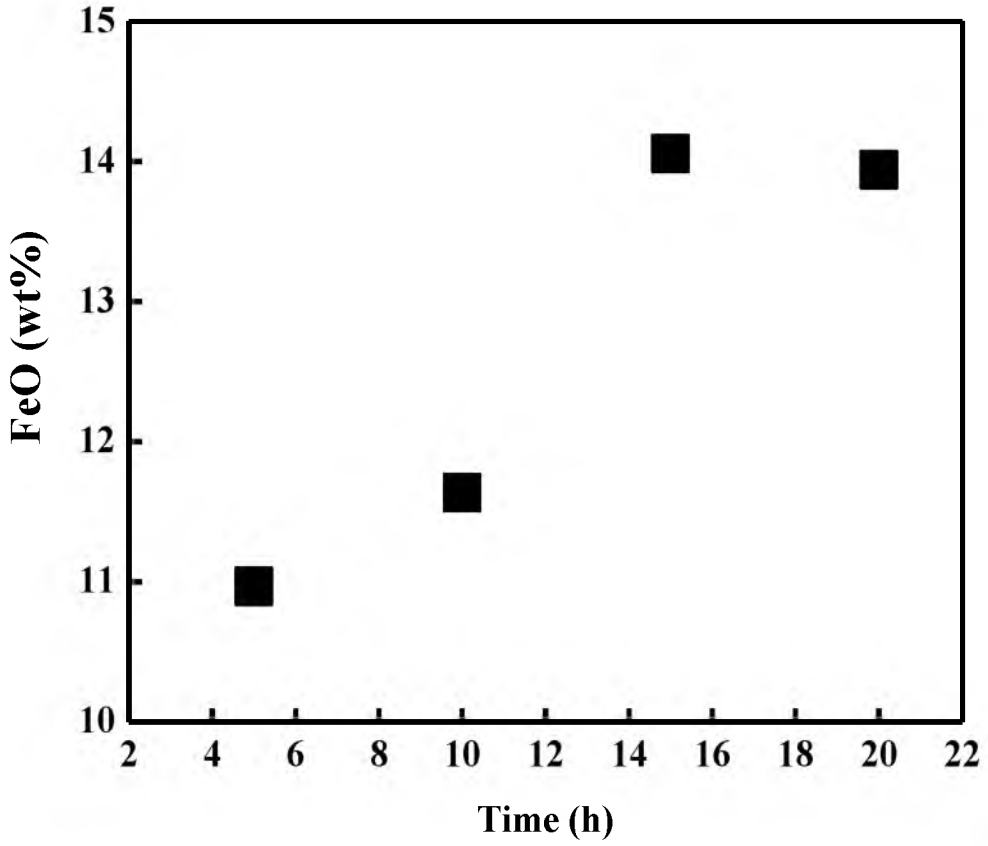

Figure 2-22. The variation of FeO with time in experiments with Mn.

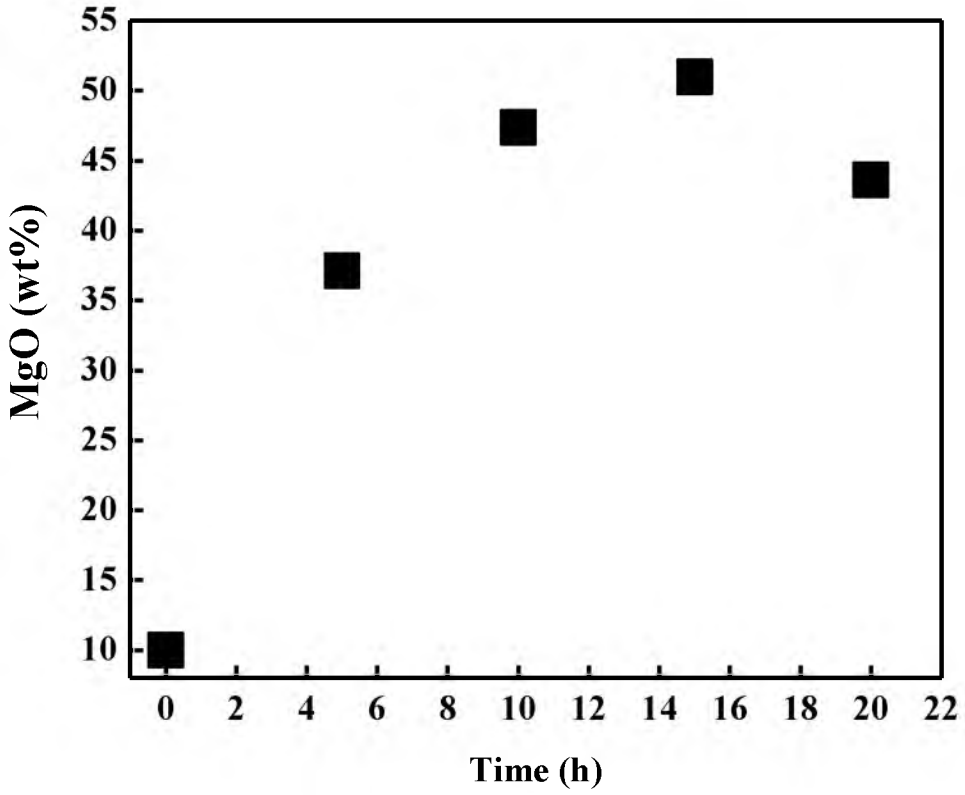

Figure 2-23. The variation of MgO with time in experiments with Mn.

the side from which equilibrium was reached, and the time required to attain equilibrium was the same.

From preliminary experiments, it was found that equilibrium was attained after 8 and 10 h for experiments without Mn and those with Mn, respectively, as shown in Figures 2-15 – 2-18 and 2-19 – 2-23. To ensure complete 3-phase (gas-slag-metal) equilibrium, 10 and 15 h were chosen in this work.

Comparing our gas rate/reactor volume to the previous work,[8-10] this ratio in our system was smaller. Thus, the gaseous species were also assumed to be in equilibrium with each other.

2. 7. References

(1) Kimura, H. *Material and energy flow simulation and economic analysis for a novel suspension ironmaking techonology*. M.S. Thesis, University of Utah, Salt Lake City, Utah, USA, **2010**.

(2) Zhang, Y. *Bench-scale flash reduction of iron ore concentrate*. M.S. Thesis, University of Utah, Salt Lake City, Utah, USA, **2008**.

(3) National Slag Association. Blast Furnace Slag: The Construction Material of Choice. http://www.nationalslag.org/archive/nsa_blast_furnace_brochure.pdf (accessed 05/01/2012).

(4) National Slag Association. Slag and its relation to the corrosion characteristics of ferrous metals . http://www.nationalslag.org/archive/legacy/nsa_172-13_slag_and_corrosion.pdf (accessed 05/01/2012).

(5) US Department of Transportation, Federal Highway Adminstration. User guidelines for waste and byproduct materials in pavement construction. http://www.fhwa.dot.gov/publications/research/.../pavements/.../research/infrastructure/structures/97148/bfs1.cfm (accessed 05/01/2012).

(6) Osborn, E. F.; DeVries, R. C.; Gee, K. H.; Kraner, H. M., Optimum composition of blast-furnace slag as deduced from liquidus data for the quaternary system CaO-MgO-Al_2O_3-SiO_2. *J. Met.* **1954,** *6*, 33-45.

(7) Mohassab-Ahmed, M. Y.; Sohn, H. Y. (University of Utah). Method and device for digestion of materials in a microwave oven. U.S. Patent Application No. 61/651, 789, Unpublished (filing date May 25, 2012).

CHAPTER 3

SLAG CHEMISTRY

3. 1. Introduction

Slag plays a crucial role in determining the quality of the produced hot metal. The slag acts as the undesirable elements absorber that takes up elements such as sulfur, phosphorus, silicon, as well as others from the hot metal. The capacity of the slag towards each of these elements is mainly controlled by its composition. For instance, the higher the basicity of the slag, the higher its sulfide capacity. Most importantly, the slag chemistry has a huge impact on the activity of FeO in the slag and accordingly, the product loss into the slag. Thus, the knowledge of the slag chemistry is essential for interpreting equilibria in slag-metal reactions as well as understanding properties such as viscosity, density, and conductivity. Ironmaking slags contain silica and other complex forming components. Therefore, the structure of the silicate is crucial to understanding of the structure and behavior of the slag. In order to interpret and correlate the aforementioned properties with the slag composition, it is indispensable to understand the structure of the slag. In this chapter, we will discuss the effect of CO/CO_2, H_2/H_2O, and $CO/CO_2/H_2/H_2O$ gas atmospheres on the chemistry of ironmaking slag.

3. 2. Slag Structure

In ironmaking, silica is the major component in the slag with the content in the range of 27 to 45 wt%, as shown in Table 2-1 (Chapter 2), depending on the type and origin of the iron ore. Silica is the independent variable based on which the flux amount and slag composition are determined to control the physicochemical properties of the slag. Therefore, these properties of slags are controlled by the structure of silicate melts.

Molecular and ionic theories are the two theories put forward to interpret the structure of silicate melts and their properties. The molecular theory, the stoichiometric approach, is based on the assumption that a liquid slag is composed of individual oxides, fluorides, etc., such as SiO_2, CaO, Al_2O_3, and CaF_2, and that these components can combine to form $CaSiO_3$ (for instance) and other more complex compounds. This theory led to the use of the activity of a component such as SiO_2 to characterize the effects of the addition of other components. This theory has been used widely in the study of metallurgical slags (for example, the work done by Liu *et al.*,[1] Basu *et al.*,[2] and others[3, 4]). However, earlier electrical conductivity studies have shown that the conduction mechanism is predominantly ionic in nature rather than electronic, where the latter becomes significant only in slags with more than 70 wt% FeO or MnO.[5] That result led Herasymenko[6] to formulate the basics of the ionic theory. This finding has been supported by the chromatographic separation of different polymeric silicate anions.[7, 8] According to that theory, liquid slags are composed of: (1) cations such as Ca^{2+}, Fe^{2+} etc., (2) anions such as O^{2-}, S^{2-}, and (3) anion complexes such as SiO_4^{4-}, AlO_4^{5-}, PO_4^{3-}.[5] Therefore, unlike silicate minerals, which usually contain only a single type of anion (monodisperse) (e.g., SiO_4^{4-} in olivine), silicate melts are composed of a distribution of

different polymeric silicate anions of different molecular weights. Consequently, silicate melts are polydisperse systems with statistical distribution of various molecular weights.[9]

Silicate anions are comprised of silicon cations surrounded by 4 oxygen anions forming tetrahedral units. These tetrahedra are joined together in chains or rings by bridging oxygens (BO), as shown in Figure 3-1. Cations are classified into two categories with respect to their impact on the silicate chains or rings (silicate polymer); the first type is the network breaker where these cations tend to break the BO bond and render it to nonbridging oxygen (NBO), O^-, and free oxygens, O^{2-}. This process is called depolymerization of silicate melt, which is usually expressed by the ratio of (nonbridging oxygen atoms/number of tetrahedrally-coordinated atoms), usually denoted as the (NBO/T) ratio (that ratio was first introduced as X by Stevels[10]). It is worth noting that the rates and equilibria in slag-metal reactions as well as the physical properties are strongly dependent upon the NBO/T ratio.[11, 12] Examples of the network breaker cations are Ca^{2+}, Mg^{2+}, and Fe^{2+}. In addition to that ratio, Si anions are frequently classified using the term structon or Q-notation (Q^n where n = 0,1,2,3,4), which was defined as single atom (or ion or molecule) surrounded by others in a specified manner.[13, 14] Figure 3-1 shows examples of silicate ions with their Q-notation and NBO/T ratios in addition to other distinguishing features. A Si polyanion may have more than one isomer with different Q values, as will be shown later in the text.

The second type of cations is the network former, such as Al^{3+} and P^{5+}, which form AlO_4^{5-}, PO_4^{3-}units. To balance the electrical charge, cations such as Ca^{2+}, Mg^{2+}, or Fe^{2+} are required. The cations involved in charge-balancing duties do not participate in network breaking. Thus, Al_2O_3 increases the polymerization of the silicate melt.[12] Like

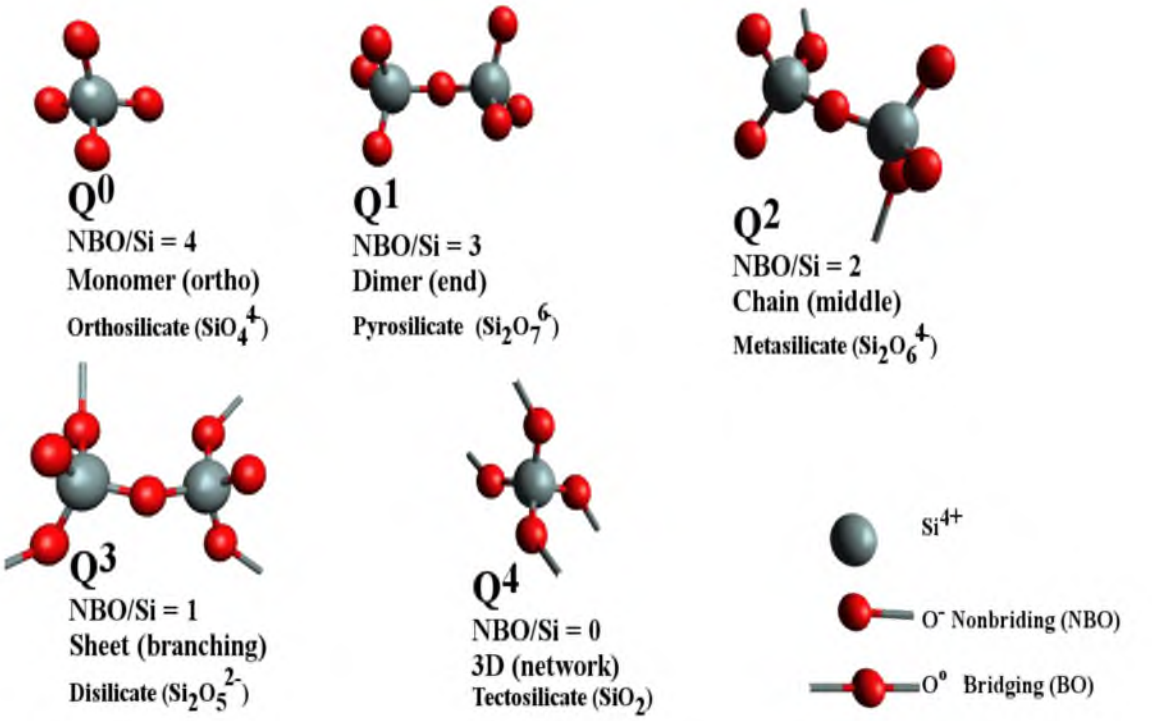

Figure 3-1. Models of silicate melt structural entities with their Q-notation, NBO/Si ratios, and structural units in addition to showing the bridging and nonbridging oxygens, BO and NBO, respectively.

Al_2O_3, P_2O_5 increases polymerization since it forms phosphate complexes which have greater affinity for cations, which are mostly of the network modifier type, than silicate ions. This higher tendency towards cations accounts for phosphate ability to increase silica polymerization since phosphate consumes the silicate network modifiers and hence decreases the attack of these cations on the silicate polymers. It is noted that P_2O_5 is less likely to form P—O—Si bonds compared to the aforementioned phosphate complexes, which are based on the PO_4^{3-} units.[12] Throughout the course of this work, we will focus on Si as the predominant network forming element due to the relatively high abundance of SiO_2 compared with the other network formers, Al_2O_3 and P_2O_5.

The silicate melts comprise of various 3-dimensionally, interconnected units such as SiO_2, $Si_2O_5^{2-}$, $Si_2O_6^{4-}$, $Si_2O_7^{2-}$, SiO_4^{4-} coexisting in the melt.[12] The portion of these units is affected by the nature of the cation in the silicate melt. The SiO_2 and SiO_4^{4-} units are favored by small cations of high valences, e.g., $Mg^{2+}>Ca^{2+}>Na^{+}$. In presence of these basic metal oxides, silicate polymers are broken according to the following pattern: $Si_6O_{18}^{12-}\rightarrow Si_4O_{12}^{8-}\rightarrow Si_3O_9^{6-}\rightarrow Si_2O_7^{6-}\rightarrow SiO_4^{-4}$. This explains the absence of isolated SiO_2 molecules in industrial slags. Instead, SiO_2-based slags are known to consist of polymers of tetrahedral units (SiO_4^{-4}).[5, 11, 15]

In summary, the ionic theory can be mainly presented through the following equilibria:

$$M_nO = nM^{(2/n)+} + O^{2-} \qquad \text{[Oxide dissociation in the slag]} \quad (3\text{-}1)$$

$$i(SiO_4)^{4-} = (Si_iO_{3i+1-j})^{2(i+1-j)-} + (i-1+j)O^{2-} \qquad \text{[Si anion polymerization]} \quad (3\text{-}2)$$

where i is the number of Si atoms in the polyanion, j is the number of cycles. When $j = 0$ or ≥ 1, reaction 3-2 produces chain or cyclic polyanions, respectively.[16]

3. 3. Experimental Details

In order to determine the effect of gas composition on the chemistry of the slag, three experiments were conducted under the following conditions:

a) Initial (before MgO presaturation) slag composition (in wt%) was the same in the three experiments [CaO (29), SiO_2 (29), MgO (10), Al_2O_3 (15), MnO (2), FeO (15), FeS (0.9), $Ca_2P_2O_7$ (1.5), CaO/SiO_2 = 1.0].

b) pO_2 was ~ 1.5×10^{-10} atm in the three experiments which was controlled by CO/CO_2, H_2/H_2O, and $H_2/H_2O/CO/CO_2$ in the first, second, and third experiments, respectively.

c) Temperature was controlled at 1550°C.

Tables 3-1 and 3-2 show the final chemical composition of the three slags after the equilibrium experiment (15 hr) as determined by ICP-OES and the equilibrium gas partial pressures as calculated by HSC, respectively. Several methods have been adopted to investigate the structure of slags such as vibration spectroscopic techniques, X-ray emission spectroscopy, and X-ray diffraction. Vibrational excitations in the slag samples can be studied in the infrared and the visible spectrum region via IR and Raman spectroscopy, respectively. In the case of Raman, it has been used intensively in slag and molten silicates research because of the fact that the detection methods in the visible region are well developed. Much of the recent advances in the slag structure field have

Table 3-1. Final chemical composition of the three slags as determined by ICP-OES

Gas Mixture	FeO (wt%)	MnO (wt%)	CaO (wt%)	Al_2O_3 (wt%)	MgO (wt%)	SiO_2 (wt%)	P_2O_5 (wt%)	S (wt%)	CaO/ SiO_2
$H_2/H_2O/CO/CO_2$	10.8	0.6	33.5	18.5	16.8	29.8	0.73	0.04	1.1
CO/CO_2	16.9	0.6	26.3	15.0	26.2	23.6	0.69	0.07	1.1
H_2/H_2O	9.6	0.7	31.2	17.1	19.7	32.1	0.89	0.05	1.0

Table 3-2. The gases partial pressures as calculated by HSC at 1550°C

Gas Mixture	pH_2 (atm)	pH_2O (atm)	pCO (atm)	pCO_2 (atm)	pO_2 (atm)
$H_2/H_2O/CO/CO_2$	0.47	0.1	0.27	0.01	1.5×10^{-10}
CO/CO_2	0	0	0.81	0.04	
H_2/H_2O	0.71	0.14	0	0	

come from magmas and natural minerals research done by geological laboratories.[17]

In this study, Fourier transform infrared spectroscopy (FTIR), Raman spectroscopy, and X-ray photon spectroscopy (XPS), X-ray diffraction (XRD), and scanning electron microscope equipped with energy dispersive spectrometer (SEM-EDS) were adopted in this study to explore the effect of gas composition on the chemistry of the ironmaking slag.

3. 3. 1. FTIR and Raman Peak Deconvolution

In crystalline materials, the spectral peaks are sharp and have well-defined patterns. However in quenched slags, these peaks are broad bands and must be deconvoluted. Based on Mysen and coworkers[17, 18] and McMillan[19, 20] in addition to others, the characteristic symmetric stretching bands for SiO_4 tetrahedra are a convoluted spectrum of sheets with an NBO/Si ratio of 1 ($Si_2O_5^{2-}$), chains with an NBO/Si ratio of 2 ($Si_2O_6^{4-}$), dimers with an NBO/Si ratio of 3 ($Si_2O_7^{6-}$), and monomers with an NBO/Si ratio of 4 (SiO_4^{4-}).[21] Therefore, FTIR, Raman, and XPS spectra were deconvoluted. This deconvolution allows the peak assigning and more importantly, the quantitative determination of the different silicate species in the slag. In this section, the curve fitting algorithm used for FTIR and Raman spectra will be discussed. The fitting for XPS was carried out with a different method that will be briefly described in the XPS section.

Slag samples are powder (solid) where $\tau_c >> \tau_a$ [τ_c is the coherence lifetime, which is the time a coherent vibration (the initial stage of vibration where all the molecules vibrates together "coherently") takes to fade and become incoherent, and τ_a is the amplitude correlation time, which is the time required for an excited molecule to return to

its ground state. For vibrations, τ_a is a few picoseconds (10^{-12} s)].[22] In other words, the excited molecule relaxes before incoherence becomes severe. This happens in solids because the environment is not in motion. The various molecules of the solid experience a statistical distribution of environments and the line shape takes on the bell curve or Gaussian profile.[22] Hence, the following Gaussian function is used in peak fitting for FTIR and Raman spectra:

$$y = a_{\circ} \exp\left[-(\ln 2)\cdot\left(\frac{x-a_1}{a_2}\right)^2\right] \qquad (3\text{-}3)$$

where $a_{\circ}$, a_1, and a_2 are the peak height, center, and HWHM (half width at half-maximum), respectively. Before peak deconvolution, the data were base-line corrected. The spline base line was subtracted carefully considering the interfering factors that affect the shape of the spectrum. Following the baseline correction performed using linear interpolation and selection of zero values at minima in peak intensities, all spectra were corrected to zero.[18, 23] After normalization of the spectra to enable the comparison of individual samples, peak deconvolution using Gaussian peak fitting was applied. None of the peak parameters were preassigned in the fitting process. The maximum number of peaks was selected such that adding more peaks had no significant improvements in the goodness-of-fit including χ^2 (the weighted sum of squared residuals, WSSR) and R^2 (the correlation coefficient) expressed as:

$$\chi^2(a)=\sum_{i=1}^{N}\left[\frac{y_i - y(x_i;a)}{\sigma_i}\right]^2 = \sum_{i=1}^{N} w_i[y_i - y(x_i;a)]^2 \qquad (3\text{-}4),$$

$$R^2 \equiv 1 - \frac{\sum_i (y_i - f_i)^2}{\sum_i (y_i - \bar{y})^2} \qquad (3\text{-}5)$$

where σ, w, and f are the standard deviation, weight $(1/\sigma^2)$, and calculated y, respectively. Peaks were deconvoluted by fityk 0.9.8 software.[24] It is worth noting that in this work, the residual was used to refer to the weighted residual, [y-f(x)]/σ which will be plotted along with the fitted peaks at the lower part of the graph as will be shown later.

Although FTIR and Raman specra were recorded over the range of 4000-500 cm^{-1}, the spectra were concentrated between 1200 and 650 cm^{-1}. This range represents the symmetric stretching vibration bands of the [SiO_4], [AlO_4] tetradedra, the symmetric Si–O bending vibration bands, and Si–OH vibrations.[25] Moreover, other wavenumbers outside that range are dominated by a high noise to signal ratio.[23] Therefore, the curve fitting was only applied to that range. Most of the peaks with area less than 1% of the total area of all the peaks, which do not have any physical meaning, have been omitted from the tables of peak parameters although they might show in the fitted graphs.

3. 3. 1. 1. FTIR and Raman Peak Assignment

Identifying the vibrational modes and assigning the peaks of silica is complex. Furthermore, the effort increases for any addition of another component such as CaO, FeO, or other oxide. The addition of a network modifier, for example, changes the bonding arrangements as a function of the composition. The higher concentration of

network modifiers produce more Q^n (with n = 3; 2; 1; 0) Si atoms.[17] Each network modifier adds one nonbridging oxygen (NBO). Thus, the addition of a network modifier adds new vibrational modes, Si–O–[metal] bending and stretching, and it breaks up the network, altering modes associated with the silica network as a result.[26] This scenario was for adding only one type of network modifiers; however, the addition of other network modifiers such as hydrogen in the form of water, or hydroxyls, adds further complexity and different vibrational modes. The different network modifiers create different bending and stretching modes. These modifiers also affect the network modes differently. The assignment of modes to peaks is, therefore, strongly dependent on the concentration and the type of the network modifier. Different network modifiers may have peaks in neighboring or overlapping regions of the spectrum.[26] Major vibrational modes found in silicate melts are symmetric and asymmetric stretching and bending modes. The assigned peaks of these modes found in the literature are listed in Table 3-3 based on which FTIR and Raman peaks were assigned, as will be shown later. Most of the discrepancies were resolved considering the differences in composition between the samples used in this study and those in the literature.

Similar to fused silica, the SiO_4 stretching vibration modes give rise to a sharp band at 1100 cm^{-1}. When a network modifier oxide is added, that peak shifts towards lower wavenumbers and broadens, which is attributed to the buildup of SiO_4 tetrahedra with higher number of nonbridging oxygen. These changes in the spectrum depend clearly on the type and concentration of the modifying cation in addition to the strength of their bonds with oxygen.[30]

Table 3-3. Raman and IR peak assignment of silicate systems in the literature

IR band (cm^{-1})	Assignment (species)
800-600	Stretching vibrations Al–O[27]
678	Stretching vibrations Al–O[28, 29]
800-700	Asymmetric bending Si–O–Si[30]
726	Symmetric stretching of Al−O−Si and Si−O−Si[28]
756	vibration of Si−O−Si[28]
780	Bending of bridged SiO4 tetrahedral group[21, 26, 31]
800	Bending mode of bridging oxygen perpendicular to Si–Si axis and within Si–O–Si plane and Network structure of SiO2 glass[26, 31, 32]
805	Si–O–Si asymmetric stretching between tetrahedra[26, 33, 34]
880-850	Si–O–[NB], $[Q_0]$[26, 32, 35]

Table 3-3. Continued.

IR band (cm^{-1})	Assignment (species)
875, 935	symmetric stretching of Al−O−M[28]
920-900	Si–O–[NB], $[Q_1]$[26, 35] (dimer)
930	Si–O–[NB], $[Q_1]$[36, 37]
935	symmetric stretching of Al−O−M[28]
940	Si–OH[26, 34, 38]
990-950	Si–O–[NB], $[Q_2]$[25, 26, 30, 32, 35, 37] (chain)
986-950	asymmetric stretching of Si−O−M[28]
952	Si–OH[26, 39]
960-930, 850	Si–OH[34, 40]
980	Si–OH[26, 38]

Table 3-3. Continued.

IR band (cm^{-1})	Assignment (species)
1000	SiO_4 tetrahedra stretching[26, 31]
1120-1050	Si–O–[NB], $[Q_3]$[25, 34] (sheets)
1080-1050	asymmetric stretching of Al−O−Si and Si−O−Si[28]
1065-1060	Si–O–Si Stretching within the tetrahedra[26, 33]
1100	Si–O–[NB], $[Q_3]$[26, 32, 35]
1150	asymmetric stretching of Al−O−Al or Al−O−Si[28]
1162−1201	asymmetric stretching of Si−O−Si[28]
1200-1060	Si–O–, $[Q_4]$[5, 26, 32]

3. 3. 1. 2. FTIR Spectroscopy

With the ability to distort the dipole moment in a molecule, IR induces certain molecular vibrations (IR vibrational modes), which are characteristic of the chemical environment of the molecule (fingerprint). FTIR has been used to qualitatively determine the structure of silicate melts by many researchers.[21, 23] For qualitative/ semiquantitaive determination of silicate species in the melt, a careful peak deconvolution should be done, as will be shown next in this chapter. Infrared spectra were collected with a Continuum IR Microscope coupled to a Nicolet 6700 FTIR Spectrometer supplied by Thermo Scientific (Waltham, MA). The microscope was outfitted with a 250 μm MCT-A detector and 15X Reflechromat objective with apertures of 25 and 50 μm. Happ-Genzel apodization with 2 levels of zero filling was used. A small amount of powder was placed on an aluminum mirror slide and flattened with a roller knife. Thinly flattened particles were examined by IR reflection absorption technique (RA) where 256 scans were coadded. All spectra were acquired at 4 cm^{-1} resolution and data points spacing of 0.48 cm^{-1}.

While the topography of the three spectra is different, as shown in Figure 3-2, it is difficult to distinguish these differences before deconvolution. Figures 3-3 – 3-5 show the deconvoluted peaks along with the measures of goodness-of-fit expressed as the minimum χ^2 and the maximum R^2 values in addition to the maximum randomness in residual distributions. No constraints were applied in the fitting. The vibrational peaks in the silicate region can be primarily classified into two types of peaks: (1) the stretching and bending modes of A–O–B (A: Si, Al, M; B: Si, Al) and (2) the stretching vibrations of NBO ($Si–O^-$) which distinguishes the Q-species. Vibrations that belong to the first

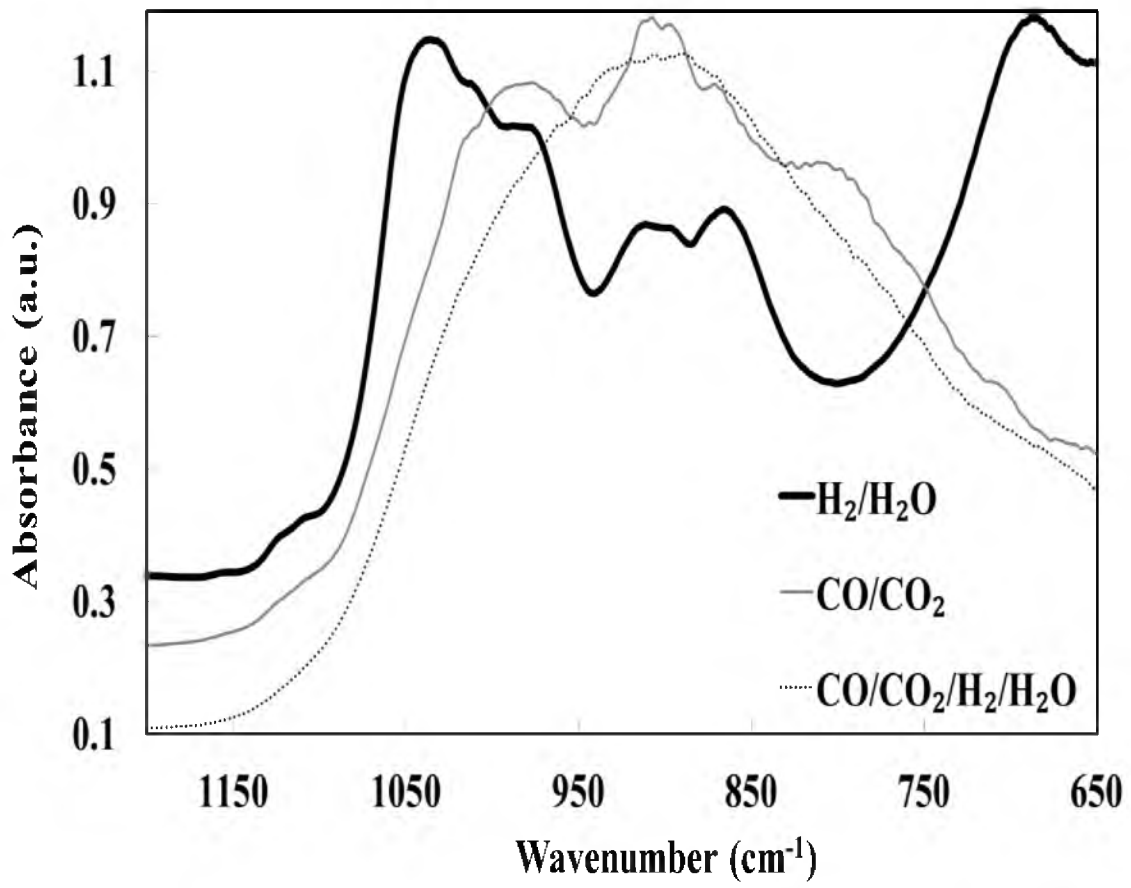

Figure 3-2. The FTIR-RAS under the three different gas mixtures.

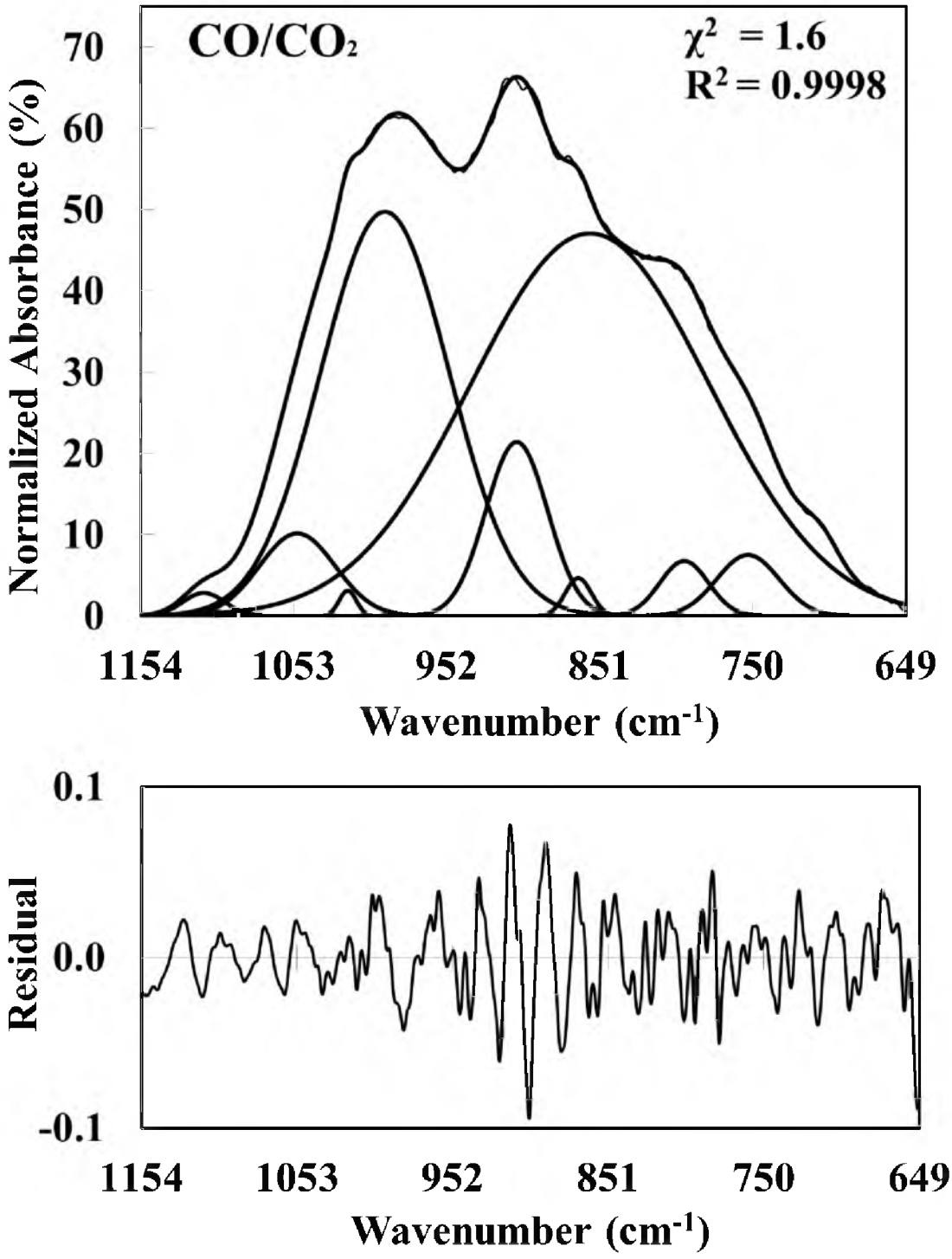

Figure 3-3. The fitted FTIR-RAS under CO/CO_2 atmosphere.

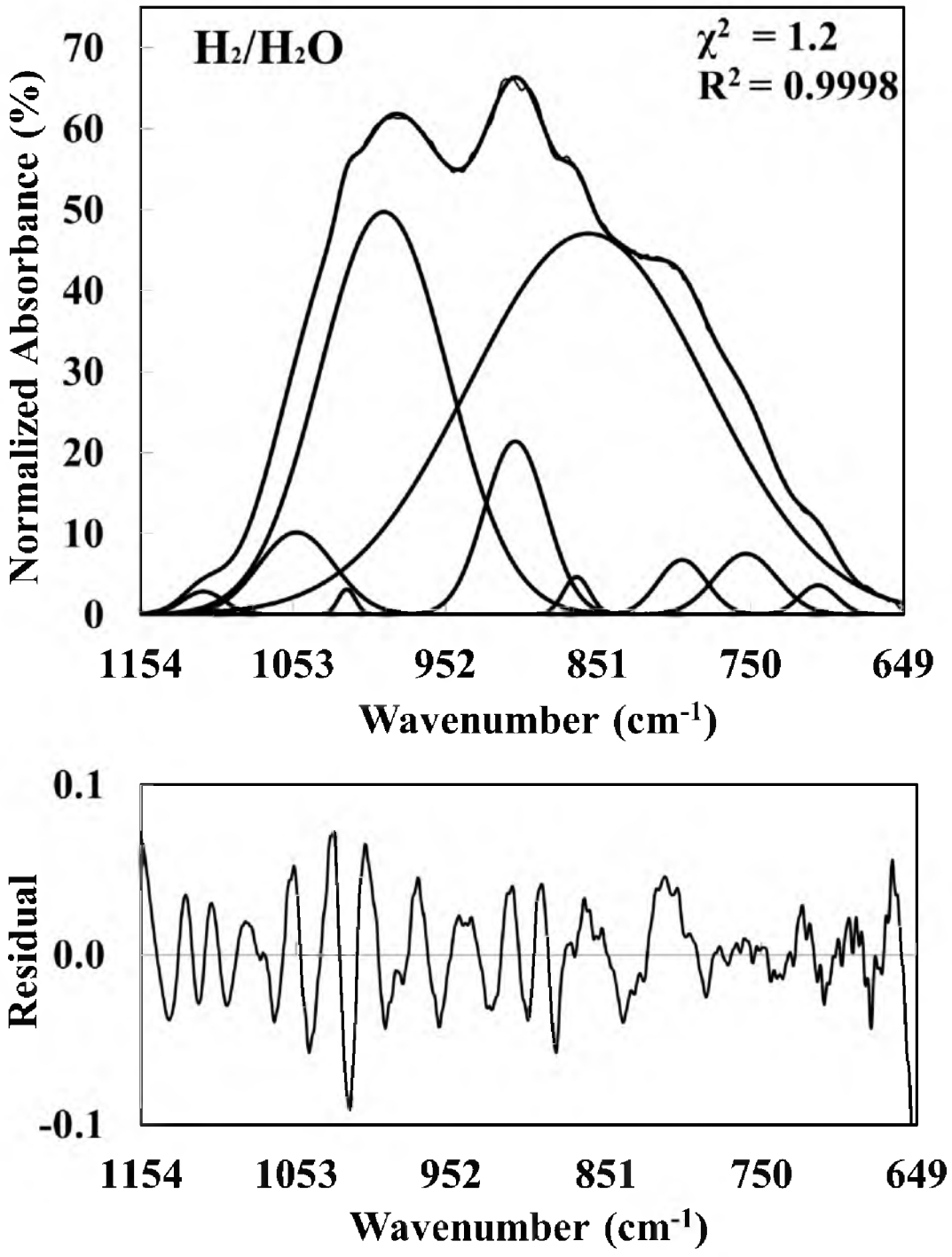

Figure 3-4. The fitted FTIR-RAS spectrum under H_2/H_2O atmosphere.

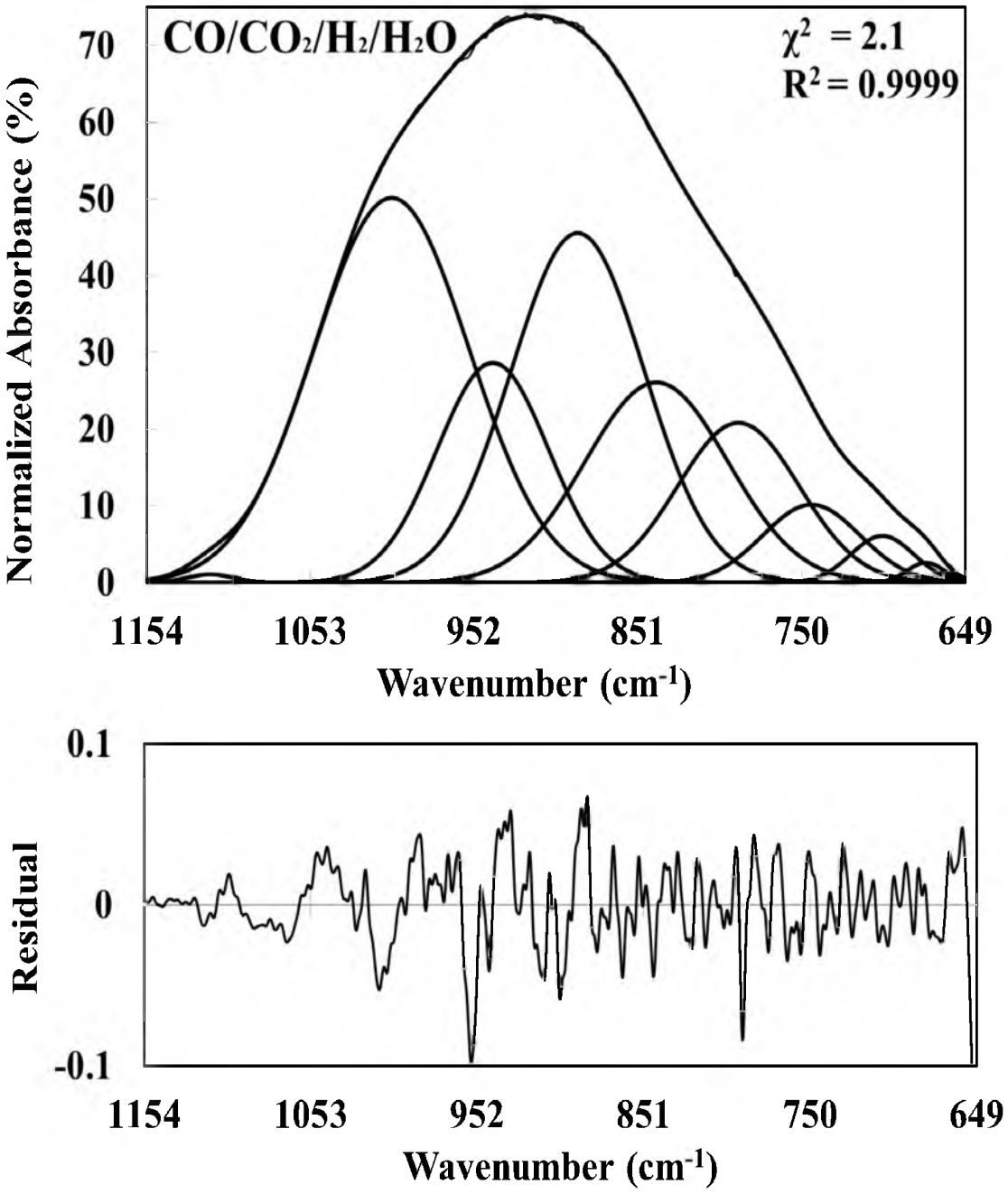

Figure 3-5. The fitted FTIR-RAS spectrum under $CO/CO_2/H_2/H_2O$ atmosphere.

category are the asymmetric bending of Si–O–Si (siloxane) at ~ 700 cm^{-1}, symmetric stretching of Si–O–Si and Al–O–Si at ~ 750 cm^{-1}, asymmetric stretching of Si–O–Si at ~ 800 cm^{-1}, asymmetric stretching of Si–O–Si and Al–O–Si at ~ 1050 cm^{-1}. The second category contains Q^0 vibrations within ~870-840 cm^{-1}, Q^1 within ~920-890 cm^{-1}, Q^2 within ~970-940 cm^{-1}, and Q^3 within ~1025-1000 cm^{-1}. All peak assignments were carefully selected considering the composition effect on shifting their position and these assignments were consistent with the published literature, as shown in Table 3-3. All the peak parameters of these assigned peaks are listed in Table 3-4 along with the relative abundance of each species expressed in their area percentage.

From the results shown in Figures 3-3–3-5 and Table 3-4, it is seen that the asymmetric bending peak of Si–O–Si at ~700 cm^{-1} exists in the case of two atmospheres with H_2O while absent in CO/CO_2. Also, the relative abundance of Si–O–Si and Al–O–Si bonds, which could be calculated by area % of the symmetric stretching of these bonds, is 5.3, 2.2, and 4% in the case of H_2/H_2O, CO/CO_2, and $CO/CO_2/H_2/H_2O$, respectively. The areas % associated with the asymmetric stretching of Si–O–Si in the case of CO/CO_2 and $CO/CO_2/H_2/H_2O$ are 1.6 and 10.2, respectively. The more polymerized the silicate melt, the more pronounced Si–O–Si and Al–O–Si vibrations. Therefore, the melt under CO/CO_2 should be more depolymerized than the other two cases.

The previous observation is supported by the distribution of Q^n species under the different gas atmospheres as shown in Table 3-4 and Figures 3-3–3-5. The more polymerized the melt, the more the Q^n with higher n. It is noted that the slag under CO/CO_2 did not show any Q^3 peak while the others did. The area percentages of Q^0+Q^1 and Q^2+Q^3 are 60 and 31, respectively, in the case of CO/CO_2, 25 and 55 under H_2/H_2O,

Table 3-4. Peak parameters of the assigned peaks of FTIR-RAS

Species	Position (cm^{-1})	Height	Area	Area (%)	FWHM	$\Delta\bar{\upsilon}$ (cm^{-1})
CO/CO_2						
Asymmetric bending of Si–O–Si	~700.0	0.0	0.0	0.0	0.0	
Symmetric stretching of Si–O–Si and Al–O–Si	753.3	7.5	387	2.2	48.5	753.3
Asymmetric stretching of Si–O–Si	795.4	6.8	271	1.6	37.7	42.1
Q^0	857.6	47.1	9276	53.6	185.1	62.2
Q^1	906.0	21.4	1095	6.3	48.1	48.4
Q^2	993.0	49.7	5272	30.5	99.6	87.0
Asymmetric stretching of Si–O–Si and Al–O–Si	1050.8	10.1	636	3.7	58.8	57.8
H_2/H_2O						
Asymmetric bending of Si–O–Si	698.5	16.6	679	6.1	38.5	
Symmetric stretching of Si–O–Si and Al–O–Si	728.0	9.5	591	5.3	58.2	29.6
Q^0	867.3	27.3	1658	14.9	57.0	139.2
Q^1	919.5	25.3	1127	10.2	41.9	52.3
Q^2	969.7	28.8	1349	12.2	44.1	50.2
Q^3	1025.1	56.8	4757	42.9	78.7	55.4
Asymmetric stretching of Si–O–Si and Al–O–Si	1050.9	15.8	518	4.7	30.9	25.8
$CO/CO_2/H_2/H_2O$						
Asymmetric bending of Si–O–Si	700.2	6.1	298	1.6	45.7	
Symmetric stretching of Si–O–Si and Al–O–Si	743.9	10.2	768	4.0	70.9	43.7
Asymmetric stretching of Si–O–Si	789.0	20.8	1953	10.2	88.0	45.0
Q^0	839.6	26.1	2875	15.0	103.5	50.6
Q^1	888.1	45.6	4690	24.4	96.7	48.6
Q^2	940.5	28.7	2473	12.9	81.1	52.4
Q^3	1002.9	50.2	6023	31.4	112.8	62.4

and 39 and 44 in the case of $CO/CO_2/H_2/H_2O$. In other words, more depolymerized species appear in the following order: $CO/CO_2 > CO/CO_2/H_2/H_2O > H_2/H_2O$.

3. 3. 1. 3. Raman Spectroscopy

In Raman spectroscopy, the incident radiation induces polarization of the chemical bonds, causing them to re-emit energy characteristic of a series of vibrational modes similar to IR. Unlike IR, however, a chemical bond does not have to be a dipole in order to be Raman active. Raman analysis should provide both qualitative and quantitative measurements of the various chemical species involved in the silicate network structure or the structural units.[41] However, because Raman spectroscopy is based upon the polarizability of the silicates, whereas IR is based upon the dipole moment change, samples can be either Raman or IR active in certain cases, depending upon the chemical environment of the slag.[41] Therefore, Raman spectroscopy is used in this study to complement FTIR analysis.

Raman spectra were collected via a DXR Raman Microscope, supplied by Thermo Scientific (Waltham, MA), using a 532 nm laser, a full-range grating, 2 mW power, 50X objective, 50 mm pinhole, and collection time of 10 s. A small amount of sample powder was placed on a glass slide and pressed with another slide to make a flat surface for analysis. The glass slides containing the sample were placed on the microscope stage and single spot Raman collection was performed. All spectra were acquired at 4 cm^{-1} spectral resolution and data point spacing of 0.96 cm^{-1}.

Figure 3-6 presents Raman spectra of the slag samples obtained under the three gas atmospheres. Like FTIR spectra, no differences can be sorted out before

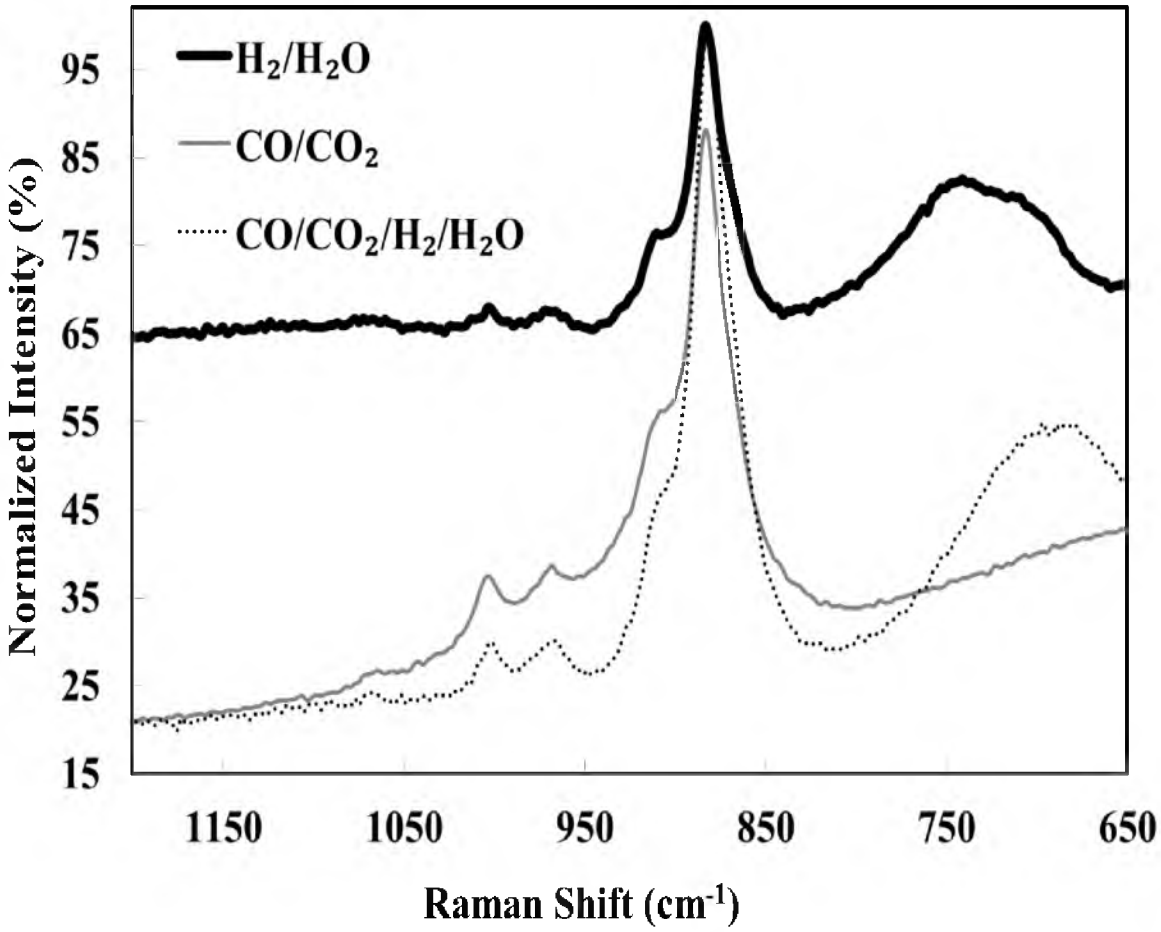

Figure 3-6. The Raman spectra under the three different gas mixtures.

deconvolution but one peak in the range of 750-650 cm^{-1} absent in the slag of CO/CO_2 appeared in the other slags. Following the algorithm used to fit FTIR spectra, Raman spectra were deconvoluted, as shown in Figures 3-7 – 3-9.

Symmetric stretching leads to intense Raman peaks, whereas asymmetric bending leads to weak peaks in amorphous phases, which explains the absence of bending vibrations in the assigned Raman peaks shown in Table 3-5. Raman peaks were assigned so that the symmetric stretching of Al–O is at ~ 700 cm^{-1}, symmetric stretching of Si–O–Si and Al–O–Si at ~ 750 cm^{-1} in the case of H_2/H_2O, while in $CO/CO_2/H_2/H_2O$ slag, the peak was shifted towards a lower frequency of 699 cm^{-1}. Also, the stretching of Si–OH was assigned to 850 cm^{-1} and that of Al–O–M (M: Ca, Fe, Mg) was assigned to ~870 and 910cm^{-1} depending on the type of M. The asymmetric stretching of Si–O–M has been assigned to ~1000 cm^{-1}. Moreover, Q^0, Q^1, and Q^2 were assigned to peaks at ~880, 900, and 970 cm^{-1}, respectively.

In comparing the Raman peaks for the three gas atmospheres, the absence of the Si–O–Si and Al–O–Si symmetric stretching peak was observed in the case of CO/CO_2 unlike the two other cases. This observation is similar to the FTIR result. It is worth noting that this peak was observed at 750 cm^{-1} in the case of H_2/H_2O while in the $CO/CO_2/H_2/H_2O$ slag, it was at 699 cm^{-1}. That shift towards the lower frequency is attributed to the fact that under $CO/CO_2/H_2/H_2O$, the SiO_2 content in the slag was diluted by the increase in the FeO content in the slag, whereas under H_2/H_2O, the FeO content was smaller, which led to a higher SiO_2 content, as shown in Table 3-1. It has been reported that the highest emission peak for silicate shifted towards higher frequency by increasing silica content.[42] It is also notable that each of these two peaks represents 38-

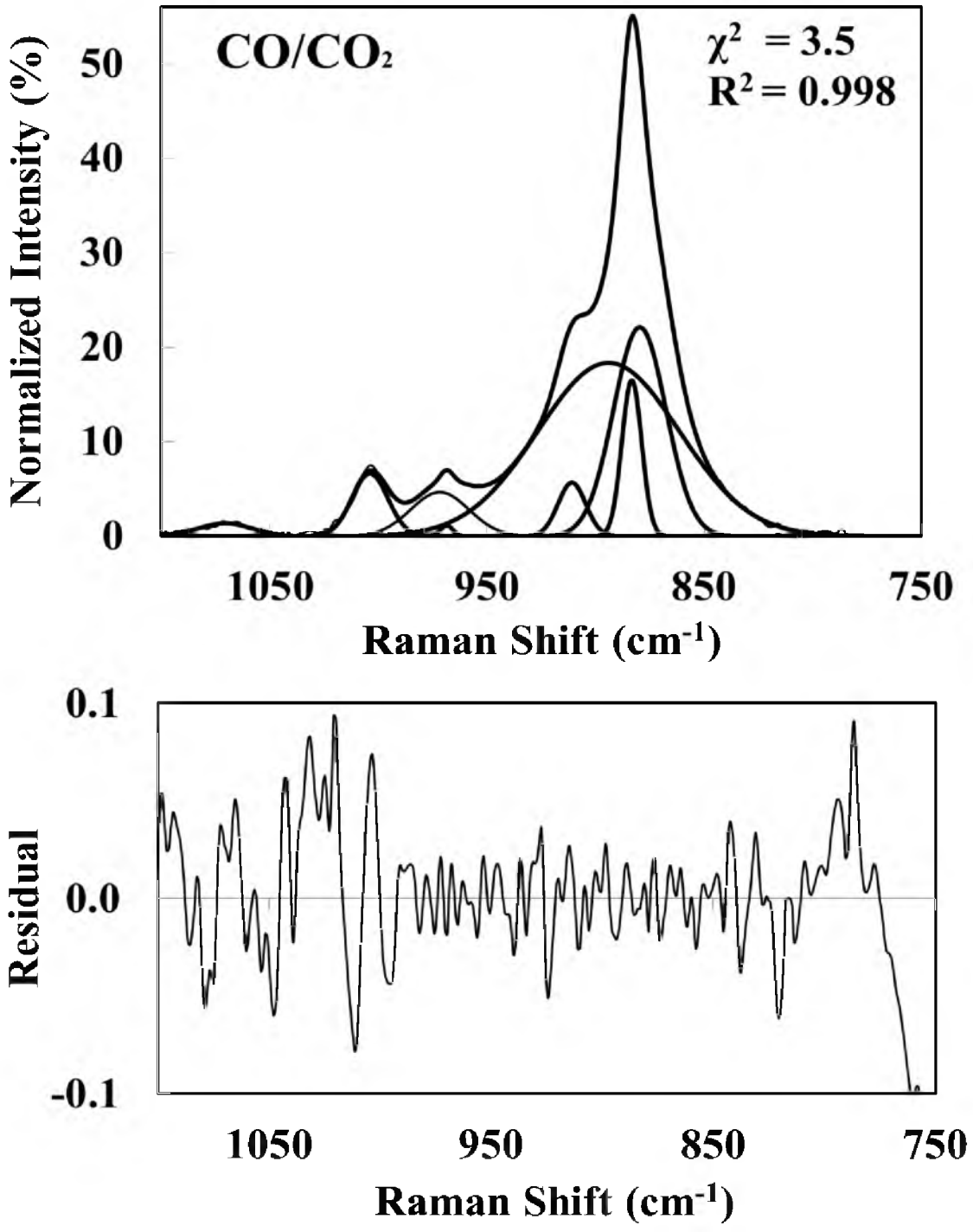

Figure 3-7. The fitted Raman spectrum under CO/CO_2 atmosphere.

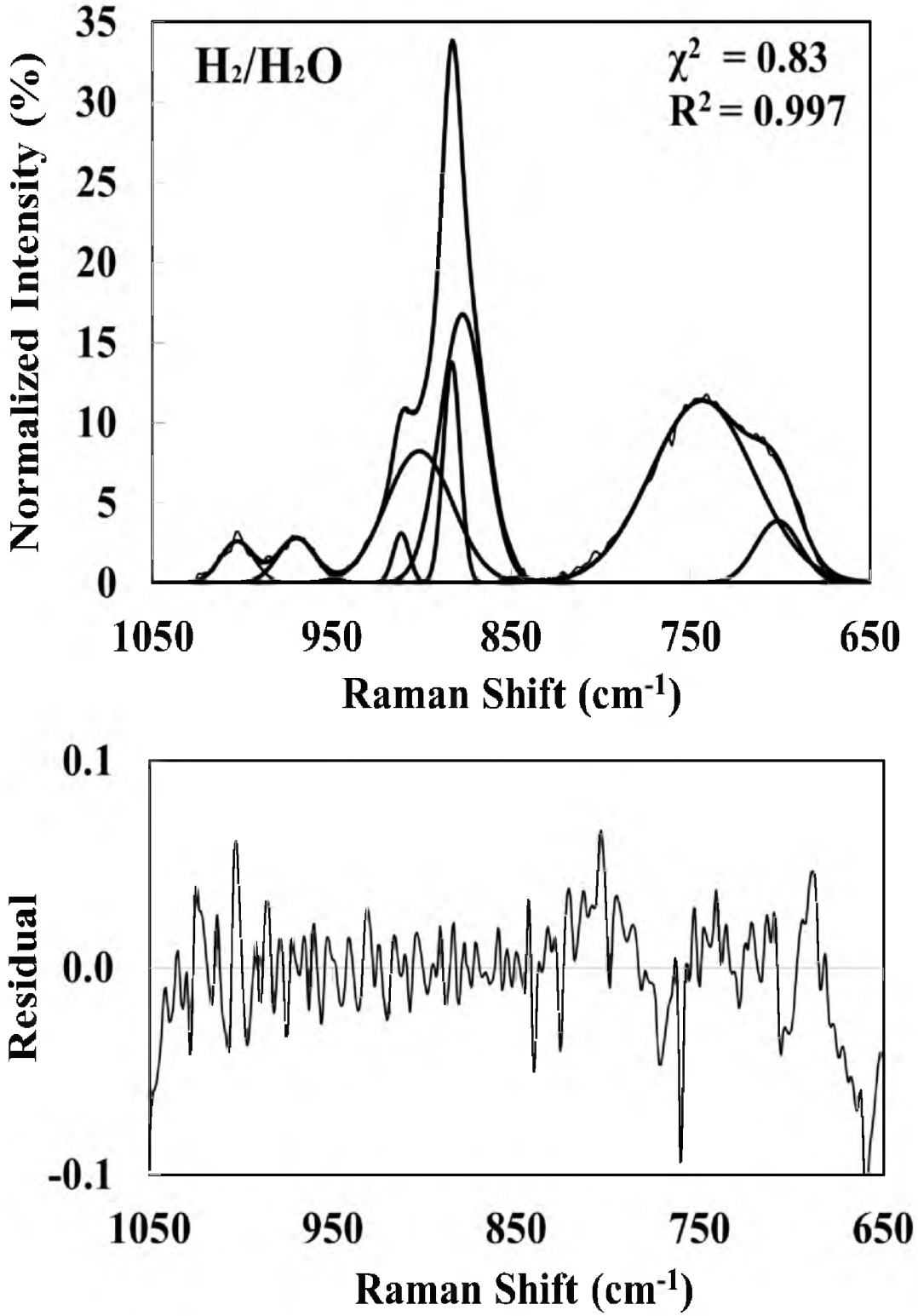

Figure 3-8. The fitted Raman spectrum under H_2/H_2O atmosphere.

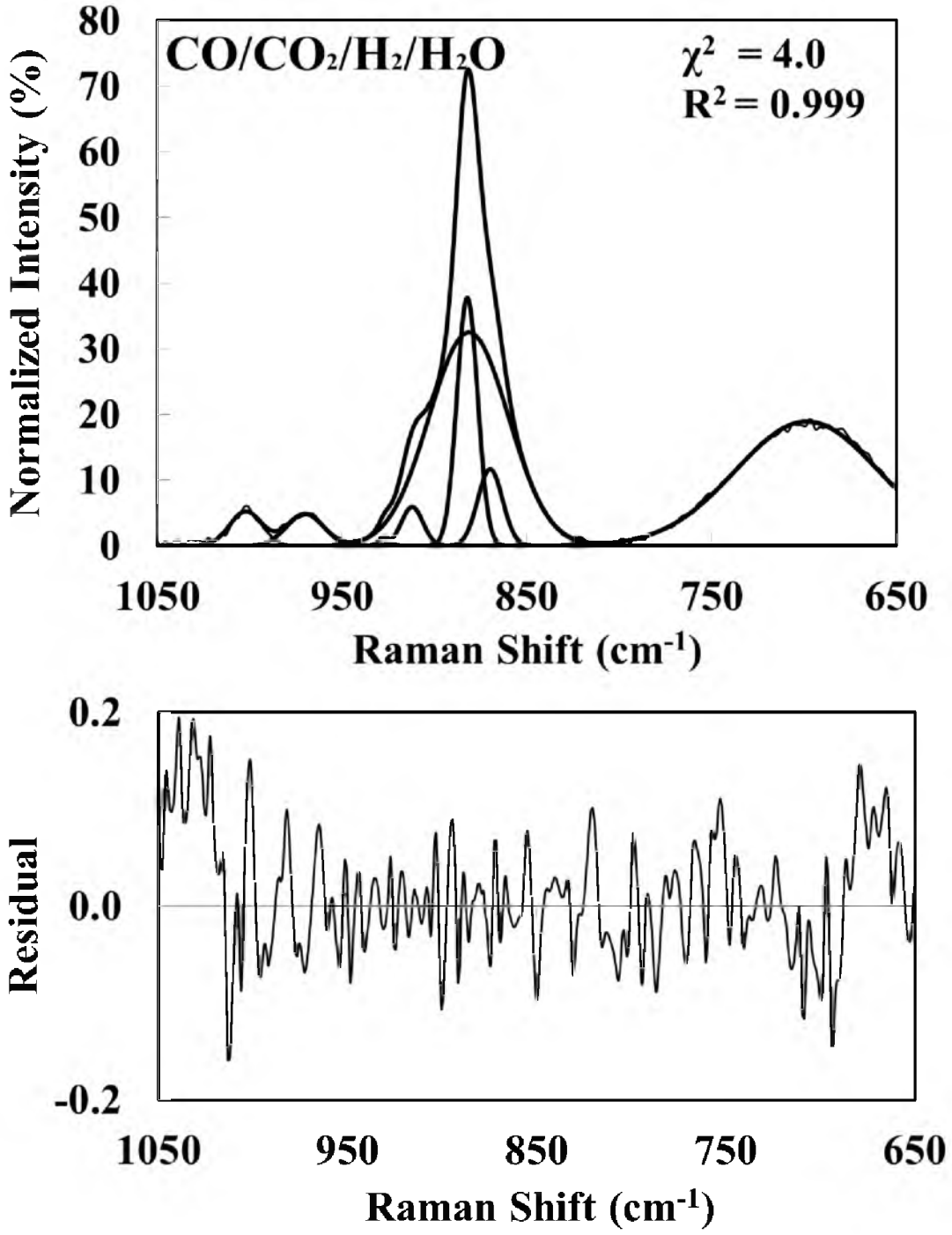

Figure 3-9. The fitted Raman spectrum under $CO/CO_2/H_2/H_2O$ atmosphere.

Table 3-5. Peak parameters of the assigned peaks of Raman spectra

Species	Position (cm^{-1})	Height	Area	Area (%)	FWHM	Δʊ (cm^{-1})
CO/CO_2						
Q^0	879.7	22.1	671	23.9	28.5	
Stretching of Al–O–M	883.4	16.5	189	6.7	10.7	3.7
Q^1	894.1	18.4	1498	53.3	76.6	10.7
Stretching of Al–O–M	911.0	5.7	91	3.2	15.0	16.9
Q^2	971.9	4.7	156	5.6	31.5	60.9
Asymmetric stretching of Si–O–M	1004.1	6.6	137	4.9	19.5	32.2
Asymmetric stretching of Si–O–Si/M and Al–O–Si/M	1070.8	1.4	42	1.5	29.0	66.8
H_2/H_2O						
Stretching of Al–O	701.4	3.9	120	5.5	29.1	
Symmetric stretching of Si–O–Si and Al–O–Si	743.6	11.4	822	37.5	67.8	42.1
Q^0	877.3	16.8	524	23.9	29.3	133.7
Stretching of Al–O–M	883.3	13.8	163	7.5	11.2	6.1
Q^1	901.4	8.2	382	17.4	43.7	18.1
Stretching of Al–O–M	911.5	3.1	35	1.6	10.6	10.1
Q^2	969.9	2.8	73	3.3	24.4	58.5
Asymmetric stretching of Si–O–M	1003.0	2.6	60	2.7	21.9	33.1
$CO/CO_2/H_2/H_2O$						
Symmetric stretching of Si–O–Si and Al–O–Si	698.6	18.9	1836	39.5	91.0	
Streching of Al–O–M	870.0	11.7	196	4.2	15.7	171.4
Q^0	881.5	32.5	1747	37.6	50.5	11.5
Not resolved	882.4	37.8	532	11.5	13.2	0.8
Stretching of Al–O–M	912.2	5.9	86	1.9	13.7	29.8
Q^2	970.1	4.9	121	2.6	23.3	58.0
Asymmetric stretching of Si–O–M	1002.3	5.2	114	2.5	20.4	32.1

40% of the total peak areas, which indicates the significantly relevant abundance of the associated species (the polymerized silicates). Also, another peak had appeared only under H_2/H_2O, which was assigned to the stretching of Al–O at ~700 cm^{-1}. The appearance of the aforementioned peaks under CO/CO_2 and the predominance or even the presence of them under the other two atmospheres indicates that the CO/CO_2 slag is more depolymerized than under the two other atmospheres. The sum of the area % of all the peaks that are attributed to Si–O–M depends on the atmospheres in the following order: CO/CO_2 (4.9%) > H_2/H_2O (2.7%) > $CO/CO_2/H_2/H_2O$ (2.5%). This also shows that the slag under CO/CO_2 tends to be less polymerized than the other two slags, consistent with the FTIR observations.

To complete that comparison, the distribution of the Q species was examined. The order of the atmospheres with respect to the sum of the area % of the most depolymerized species (Q^0+Q^1) is CO/CO_2 (77%) > H_2/H_2O (41%) > $CO/CO_2/H_2/H_2O$ (38%). That confirms the claim that the silicate melts show more dissociation in the presence CO/CO_2 gas mixture than under the other two atmospheres. That conclusion is in agreement with the FTIR results.

3. 3. 2. X-Ray Photon Spectroscopy (XPS)

XPS spectra are obtained by irradiating a material with X-rays and detecting the kinetic energy and the number of electrons escaping from the surface of the material within a depth of approximately 10 nm. Therefore, XPS technique is commonly used for surface analysis applications rather than for bulk analysis as IR and Raman. However, a deeper spectroscopic analysis can be obtained when the surface is etched with Ar-ion.

XPS is a valuable tool in detecting tiny changes in the chemical environments of ions in the slag. Moreover, XPS can be used to quantify the BO and NBO amounts through deconvolution of its spectra to distinctive peaks that could be assigned to O°, O^{-}, and O^{2-} in the slag system.[43]

All XPS measurements were made using a Kratos™ Axis Ultra DLD multi-technique surface analysis instrument, which was supplied by Kratos Analytical Inc. (Spring Valley, NY). The base pressure of the analysis chamber during these experiments was 3×10^{-10} Torr, with operating pressures around 1×10^{-9} Torr. Spectra were collected using a monochromatic Al Kα source (1486.7 eV) and a 300×700 micron spot size. Both low resolution survey scans and high-resolution scans of energy ranges of interest were done. Significant artifacts generated by charging were seen for all samples, resulting in peak shifts and broadening. The peaks were sharpened by flooding the sample with low-energy electrons and ions from the charge neutralizer system. To determining the absolute energy shift, spectra were referenced to the C1s peak from adventitious carbon, which is a thin layer of carbonaceous material usually adsorbed on the surface of most air exposed samples. The mono Al source was operated at an emission current of 12 mA with the target anode set to 15 kV for a resulting power of 180 W. For survey spectra, the data were collected using pass energy of 160 eV, a step size of 1 eV, and a dwell time of 200 ms. High resolution regional spectra were collected using pass energy of 40 eV, a step size of 0.1 eV, and a dwell time of 300 ms. Each high resolution scan was averaged over 3 sweeps to improve signal to noise.

Shirley-type background considers the change in the structure of XPS spectrum where the background cannot be linear with the same slope throughout the entire

spectrum; instead, it must be subtracted at higher values in the higher binding energy zone and *vice versa*. Shirley-type background was, therefore, subtracted from each spectrum to remove most of the extrinsic losses.[44] Then, XPS spectra were deconvoluted using Gaussian/Lorentzian functions to represent distinct oxidation states. Where appropriate, these functions were combined with polynomials to aid in deconvolution to identify and eliminate excessive differential surface charge build-up, satellite peaks, and multiplet splitting. Constraints were placed on the full width at half maximum (FWHM) and position of each peak, and a least squares-based fitting algorithm was employed until the lowest mean squared error was achieved.

Figure 3-10 shows the deconvoluted peaks of O 1s. The three atmospheres showed three states of oxygen assigned consistently with the literature as free oxygen (O^{2-}) at ~530 eV, NBO (O^{-}) at ~531.5 eV, and BO (O°) at ~533 eV, as listed in Table 3-6.[43, 45] The different slags follow the order H_2/H_2O (16.7%) > $CO/CO_2/H_2/H_2O$ (11.6) > CO/CO_2 (10.6%) with respect to the relative abundance of the BO, whereas the three slags exhibit a reverse order based on the free oxygen; CO/CO_2 (44%) > $CO/CO_2/H_2/H_2O$ (41%) > H_2/H_2O (37%). Moreover, the ratio of the NBO/BO orders the slags as: CO/CO_2 (4.3) > $CO/CO_2/H_2/H_2O$ (4.1) > H_2/H_2O (2.8). Based on XPS analysis, it is conclude that the studied slag is more depolymerized under CO/CO_2 and more polymerized under the H_2/H_2O atmosphere. These results are consistent with Q-species distribution provided by FTIR and Raman analyses.

Based on the general polymerization reaction, reaction 3-2, combined with the area % assigned to the free oxygen (O^{2-}) in the H_2/H_2O slag, the silicate anion should form ring and branched structures rather than chains. That explains the lower free oxygen

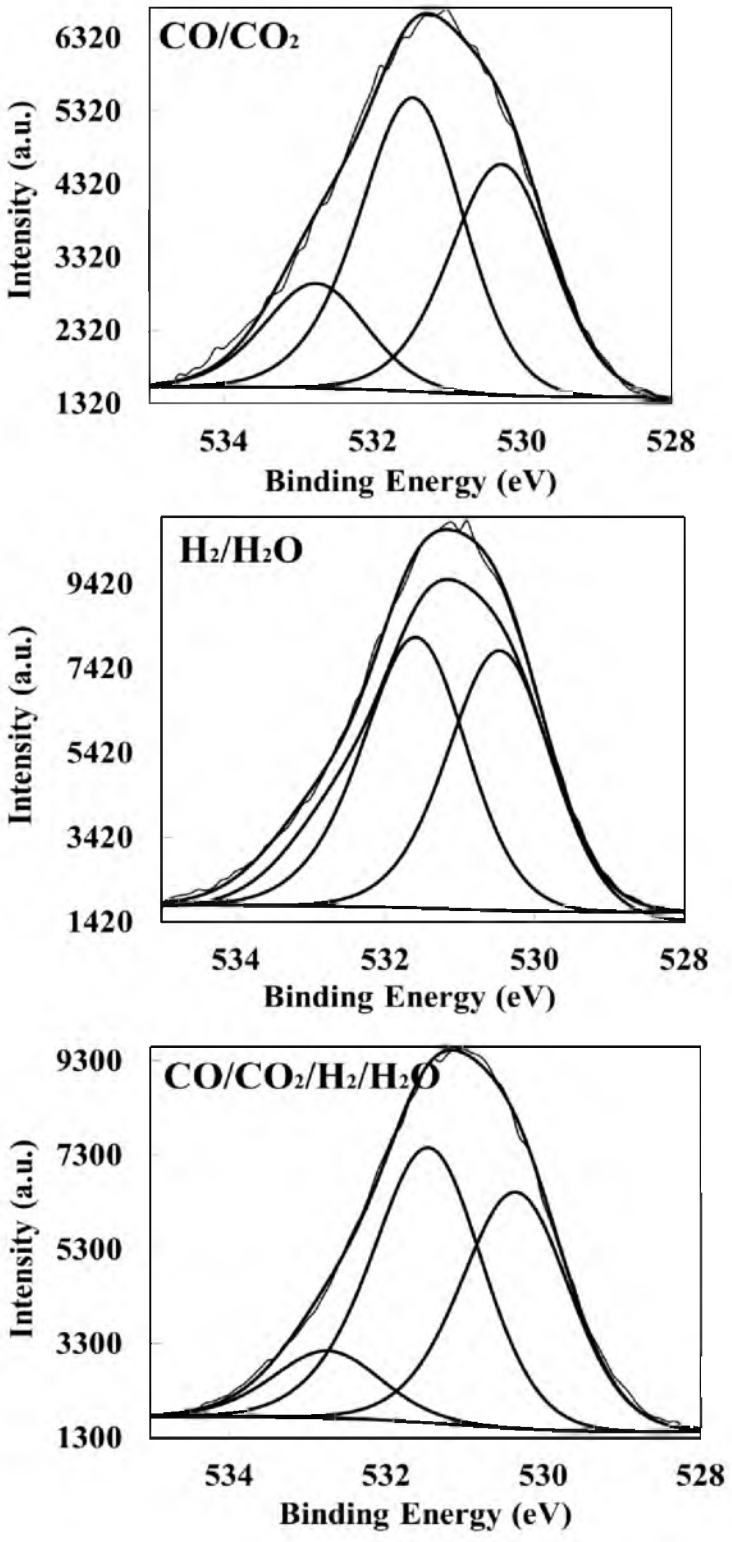

Figure 3-10. XPS spectra of O 1s under different gas atmospheres.

Table 3-6. Peak parameters used to fit O 1s XPS spectra

Peak	Position (eV)	Corrected Position[a] (eV)	FWHM	Area	Corrected Area[b]	Atomic %	ΔE[c] (eV)
CO/CO_2							
Free (O^{2-})	528.4	530.5	1.6	10659.7	6173.4	43.8	
NBO (O^-)	529.5	531.6	1.6	11102.2	6425.5	45.6	1.1
BO (O°)	530.9	533.0	1.6	2568.5	1485.3	10.6	1.4
H_2/H_2O							
Free (O^{2-})	528.7	530.3	1.6	5480.1	3173.1	36.7	
NBO (O^-)	529.9	531.5	1.6	6962.7	4028.8	46.6	1.2
BO (O°)	531.2	532.8	1.6	2488.1	1438.6	16.7	1.3
$CO/CO_2/H_2/H_2O$							
Free (O^{2-})	528.3	530.4	1.6	8693.6	5035.1	40.9	
NBO (O^-)	529.4	531.5	1.6	10119.9	5857.3	47.5	1.1
BO (O°)	530.6	532.7	1.6	2468.4	1427.6	11.6	1.3

[a]Corrected Position (eV) = Position (eV) + 2.1 (eV).

[b]Corrected Area = (Area/(RSF*T*MFP)); RSF: Relative Sensitivity Factor, T: Temperature in Kelvin, MFP: Mean Free Path.

[c]ΔE (eV) = $E_{(below)} - E_{(above)}$.

content in this slag with the high polymerization tendency.

3. 3. 3. X-Ray Diffraction (XRD)

To identify the major crystalline phases in the slag, the fine powder was analyzed by a Siemens D5000 X-ray diffractometer supplied by Bruker Cooperation (Wisconsin, MI) using Ni-filtered Cu Kα radiation (λ = 1.5406). The X-ray intensity was measured over 2θ (θ: diffraction angel) from 10 to 100° with a scanning rate of 0.05°/s. The XRD patterns were electronically compared with American Mineralogist Crystal Structure Database XRD files.[46]

No separate oxide phases, e.g., CaO, MgO, FeO, etc., were recognized. Three phases were identified: fayalite Fe_2SiO_4, merwinite $Ca_3Mg(SiO_4)_2$, and hedenbergite $CaFe(SiO_3)_2$. As Figure 3-11 shows, the three phases have the strongest characteristic peaks in the case of CO/CO_2. Moreover, the silicate anion of each of these phases is Q^0; the least polymerized silicate anion with NBO/T = 4, as shown in Figure 3-1. The more pronounced peaks of these phases under CO/CO_2 indicate the predominance of less polymerized species in it compared with the other two cases. This result is consistent with the spectroscopic analysis results.

3. 3. 4. Calculation of the Degree of Depolymerization (NBO/T)

The bulk NBO/T was calculated for the three slags according to the method adopted by Mills,[5, 12] the description of which can be summarized as follows:

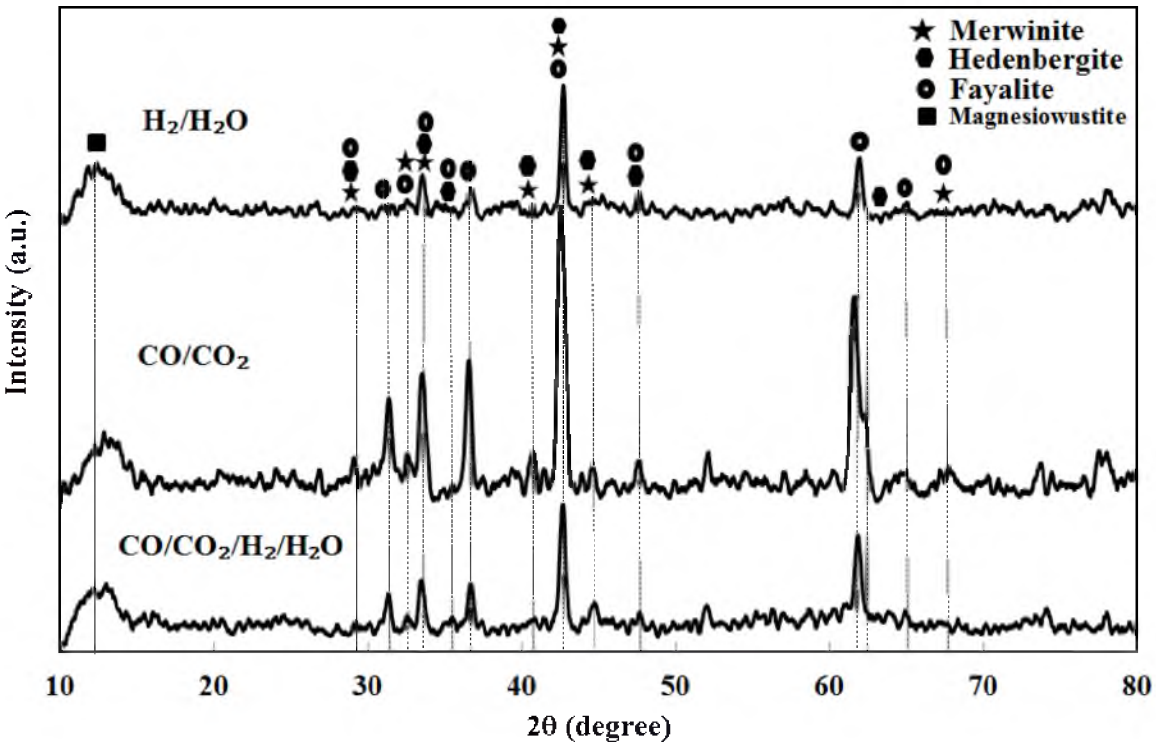

Figure 3-11. XRD patterns of slag under the three different gas mixtures.

$$NBO/T = w_{NB} / x_T \qquad (3\text{-}6)$$

$$x_T = \sum x_{SiO_2} + 2x_{Al_2O_3} + 2x_{P_2O_5} \qquad (3\text{-}7)$$

$$w_{NB} = v_{NB} - 2x_{Al_2O_3} \qquad (3\text{-}8)$$

$$v_{NB} = \sum 2\left(x_{CaO} + x_{MgO} + x_{FeO} + x_{MnO}\right) \qquad (3\text{-}9)$$

where w_{NB}, x_T, v_{NB} and x are the net charge on the total network-breaking cations, the sum of mole fractions of network forming cations, the total charge of the total network-breaking cations, and mole fraction of species, respectively.

The calculation results are shown in Table 3-7. Based on the bulk NBO/T ratio presented in this table, the silicate polymers tend to become more depolymerized under the CO/CO_2 atmosphere and more polymerized under atmospheres containing H_2O. It is noted that the depolymerization ratio did not change significantly when H_2/H_2O was replaced by the $CO/CO_2/H_2/H_2O$ atmosphere.

Table 3-8 summarizes most of the analysis results. It is notable that all the results consistently lead to the conclusion that the CO/CO_2 slag has the least polymerization degree of all the three, whereas the two other slags have approximately a similar degree of polymerization. This suggests that water affects the slag more significantly than CO_2 when they coexist in the gas mixture, as will be discussed later in Section 3.5.

Combining the analysis results, the equilibria among Q-species in the studied slags are represented by:

<u>CO/CO_2</u>

$$Q^1 + O^{2-} = 2Q^0 \qquad (3\text{-}10)$$

Table 3-7. The NBO/T values under the three different gas atmospheres

	CO/CO_2	H_2/H_2O	$H_2/H_2O/CO/CO_2$
x_{FeO}	0.123	0.071	0.079
x_{MnO}	0.004	0.005	0.004
x_{CaO}	0.246	0.293	0.315
x_{Al2O3}	0.077	0.088	0.096
x_{MgO}	0.341	0.257	0.219
x_{SiO2}	0.205	0.281	0.262
x_{P2O5}	0.003	0.003	0.003
x_S	0.001	0.001	0.001
x_T	0.360	0.460	0.460
v_{NB}	1.430	1.250	1.240
w_{NB}	1.270	1.080	1.040
NBO/T	3.490	2.320	2.280

Table 3-8. Comparison of some of the structure analysis results

Species	FTIR	Raman	XPS (BO, NBO)	NBO/T
CO/CO_2				
Q^0	59.3	28.9	11, 46	3.49
Q^1	7.0	64.4		
Q^2	33.7	6.7		
Q^3				
$(Q^0+ Q^1)/ (Q^2+ Q^3)$	2.0	13.9		
$(Q^2+ Q^3)/ (Q^0+ Q^1)$	0.5	0.07		
H_2/H_2O				
Q^0	18.6	53.5	17, 47	2.32
Q^1	12.7	39.0		
Q^2	15.2	7.5		
Q^3	53.5			
$(Q^0+ Q^1)/ (Q^2+ Q^3)$	0.5	12.4		
$(Q^2+ Q^3)/ (Q^0+ Q^1)$	2.2	0.08		
$CO/CO_2/H_2/H_2O$				
Q^0	17.9	93.5	12, 48	2.28
Q^1	29.2			
Q^2	15.4	6.5		
Q^3	37.5			
$(Q^0+ Q^1)/ (Q^2+ Q^3)$	0.9	14.4		
$(Q^2+ Q^3)/ (Q^0+ Q^1)$	1.1	0.07		

$$2Q^2 + Q^0 = 3Q^1 \qquad (3\text{-}11)$$

H_2/H_2O and $CO/CO_2/H_2/H_2O$

$$2Q^0 = Q^1 + O^{2-} \qquad (3\text{-}10)$$

$$3Q^1 = 2Q^2 + Q^0 \qquad (3\text{-}11)$$

$$3Q^2 = 2Q^3 + Q^0 \qquad (3\text{-}12)$$

$$2Q^2 = Q^1 + Q^3 \qquad (3\text{-}13)$$

where under CO/CO_2, the higher order Q-species tend to dissociate to form more stable lower-order species. On the other hand, under the two H_2O-containing atmospheres, the smaller Q-species tend to polymerize and form bigger silicate polymers.

3. 4. Slag Basicity

According to Brönsted and Lowry,[47] an acidic material is the one capable of furnishing hydrogen cations, whereas the basic material receives hydrogen cations in the aqueous systems, as follows:

$$\text{Acid} = \text{Base} + H^+ \qquad (3\text{-}14)$$

$$\text{e.g.,} \quad H_3PO_4 = H_2PO_4^- + H^+ \qquad (3\text{-}15)$$

while Flood and Förland,[48] after the work of Lux[49], defined the acid-base reaction in an oxide system as "the transfer of an oxygen from a state of polarization to another," which

is consistent with the Lewis acid-base definition. Therefore, in aprotic solvents (relevant to silicate melts), O^{2-} replaces H^{+}. Thus, a basic oxide is O^{2-}-donor and an acidic oxide is O^{2-}-acceptor.

$$\text{Acid} = \text{Base} + O^{2-} \qquad (3\text{-}16)$$

$$\text{e.g.,} \qquad SiO_4^{4-} = SiO_3^{2-} + O^{2-} \qquad (3\text{-}17)$$

The same authors also introduced the $pO^{2-} = -\log a_{O}^{2-}$ as a characteristic scale to measure the oxoacidity, which is analogous to pH scale in aqueous solutions.

Reaction 3-2 shows the silicate polymerization reaction where it evolves three oxygen types: singly bonded O^{-} (NBO), doubly bonded O^{0} (BO), and free oxygen.[50] Therefore, that reaction can be simplified as:

$$2O^{-} = O^{\circ} + O^{2-} \qquad (3\text{-}18)$$

Combined with reaction 3-1, the dissociation of metal oxide, one can expect the acid-base property of dissolved oxides to significantly affect the extent of silicate polymerization by producing or consuming free oxygen anions (O^{2-}).

As mentioned earlier, metal oxides are either network modifiers or formers, i.e., O^{2-}-acceptor or O^{2-}-donor, respectively. Therefore, the relative abundance of basic (network modifier) and acidic (network former) oxides should give a general indication of the extent of depolymerization of the melt, and consequently, should be a simple indicator of the trend of changes in oxide activities with slag composition. Hence, the

equilibrium constants for gas-slag-metal reaction and the elements distribution ratios expressed in terms of slag components are often functions of slag basicity.[51]

It is believed that Herty[51] was the first to introduce the concept of basicity for steelmaking slags as the V ratio (wt%CaO/wt%SiO_2). Since the definition of basicity is somewhat arbitrary and the V ratio does not account for other oxides in slags, many different basicity indices have been used in literature, as summarized in Table 3-9. The general theme of all these indices is that they are all dependent upon the slag type and composition range.

In addition to the mole or wt%-based indices presented in Table 3-9, Duffy and Ingram[56] introduced the concept of optical basicity (Λ), which is based on the different electronic configuration of the elements as observed by the frequency shift in UV absorption bands, which could be calculated from Pauling electronegativities. The optical basicity could be calculated using the following relation:

$$\Lambda = \frac{\sum_{i=1}^{n} x_i n_i \Lambda_{th_i}}{\sum_{i=1}^{n} x_i n_i} \qquad (3\text{-}19)$$

where x_i, n_i, and Λ_{th_i} are the mole fraction, number of oxygen atoms, and the optical basicity of pure oxide i. Using the optical basicity becomes challenging for slags containing transition metal oxides (FeO, MnO, TiO_2) due to the difficulty of experimental measurement of their Λ_{th} as they are strong UV absorbers. However Λ_{th} could be

Table 3-9. Slag basicity indices in the literature

Index	Notes	Reference
$\frac{wt\%CaO}{wt\%SiO_2}$	V ratio	12, 51, 52
$\frac{x\,CaO + xMgO}{xSiO_2}$	x is the mole fraction	12
$\frac{wt\%\,CaO}{wt\%SiO_2 + wt\%\,Al_2O_3}$	For slags with 10-20 wt% Al_2O_3	12, 53
$\frac{wt\%\,CaO}{wt\%SiO_2 + wt\%\,P_2O_5}$	For high P_2O_5 containing slags	12
$\frac{x\,MO - 3xP_2O_5}{xSiO_2}$	MO is the basic oxide(s)	12
$\frac{wt\%CaO + 1.4 \times wt\%MgO}{wt\%SiO_2 + 0.6\,wt\%Al_2O_3}$	MgO is equivalent to CaO and ½ P_2O_5 is equivalent to SiO_2 on molar basis	52
$\frac{wt\%\,CaO + 1.4\,wt\%MgO}{wt\%SiO_2 + 0.84wt\%\,P_2O_5}$	-MgO is equivalent to CaO and P_2O_5 is equivalent to SiO_2 on molar basis -that ratio = 1.17×(CaO/SiO_2) at P_2O_5 < 5wt% and MgO < 8wt%	12, 52, 53
$\frac{xMO}{xSiO_2 + 2xP_2O_5 + 0.5xAl_2O_3 + 0.5xFe_2O_3}$	MO is the basic oxide(s)	12
$\frac{CaO - 4\ P_2O_5}{SiO_2}$	In moles/100 grams slag	54
$\frac{CaO}{SiO_2 + 0.634P_2O_5}$	In moles/100 grams slag	54

Table 3-9. Continued.

Index	Notes	Reference
$\frac{CaO + MnO}{2SiO_2 + 4P_2O_5}$	In moles/100 grams slag	54
$\frac{x\,CaO - 4xP_2O_5}{xSiO_2}$		12
$\frac{wt\%CaO}{wt\%SiO_2 \times wt\%Al_2O_3}$	Not valid for slags with no Al_2O_3	52
$\frac{wt\%CaO' \times 100}{wt\%SiO_2 + wt\%CaO}$	$wt\%CaO' = wt\%CaO - 1.18wt\%P_2O_5$	54
$wt\%CaO - 1.86wt\%SiO_2 - 1.19wt\%P_2O_5$	The difference between basic and acidic oxides	12
$wt\%CaO - 0.93wt\%SiO_2 - 1.18wt\%P_2O_5$		54
$xMO - 2xSiO_2 - 4xP_2O_5 - 2xAl_2O_5 - xFe_2O_3$	For slags containing significant concentration of Fe_2O_3	12
$\frac{xCaO + 0.67xMgO}{xSiO_2 + xAl_2O_5}$		12
$\frac{xCaO + 0.5xMgO}{xSiO_2 + 0.33xAl_2O_5}$	Bell's ratio	12, 55
$(wt\%CaO + wt\%MgO + wt\%MnO) - (wt\%SiO_2 + wt\%P_2O_5 + wt\%TiO_2)$	The difference between basic and acidic oxides	12
$6.05x_{CaO} + 4.8x_{MnO} + 4.0x_{MgO} + 3.4x_{FeO} - 6.31x_{SiO_2} - 0.3x_{Al_2O_3} - 4.97x_{TiO_2}$	Referred to as excess base (B^{xs})	12

calculated from Pauling electronegativity, some researchers reported poor correlation of the sulfide and phosphide capacities with these values.[12]

Slag basicity has been also indexed by the solubility of gases like O_2, N_2, and CO_2 in the slag, which requires the knowledge of the solubility of these gases in the slags of interest under the experimental conditions. Moreover, there various attempts to define basicity with regard to numerous redox reactions such as Cr^{3+}/Cr^{3+}, Fe^{2+}/Fe^{3+}, and Mn^{2+}/Mn^{3+}, but this approach is associated with a number of problems.[12]

It is crucial that the aforementioned basicity definitions are for the compositions of molten slags; however, in practice, the slags often contain undissolved CaO and MgO. The chemical analyses of such slag samples without correction for undissolved CaO and MgO will give unrealistic basicities, which are much higher than those in the molten part of the slag. For this reason, the slags used in this study have been analyzed by SEM along with EDS. Figure 3-11 shows back scattered SEM image across sectioned magnesia crucible containing slag after the equilibrium experiment. The image was mapped for Ca. Mg, Fe, and Si elements by EDS (the colored images in Figure 3-12). No pure oxides (isolated islands) were registered even close to the crucible wall. The slag sample was homogeneous and dominated by a dark matrix with light dendritic structures embedded in it, as shown in Figure 3-12. The sample was further magnified (the inset in Figure 3-13) and an EDS spot analysis was carried out. The dark matrix was found to be mainly (Si,Mg,Al,Ca,Fe)O phase (silicate anions with network modifiers) and the dendritic structure was dominated by (Fe,Mg)O phase (magnesiowustite). This analysis has been carried out on most of the samples in this study, based on which the absence of any undissolved islands of any single oxide in the slag melt was confirmed. Although no

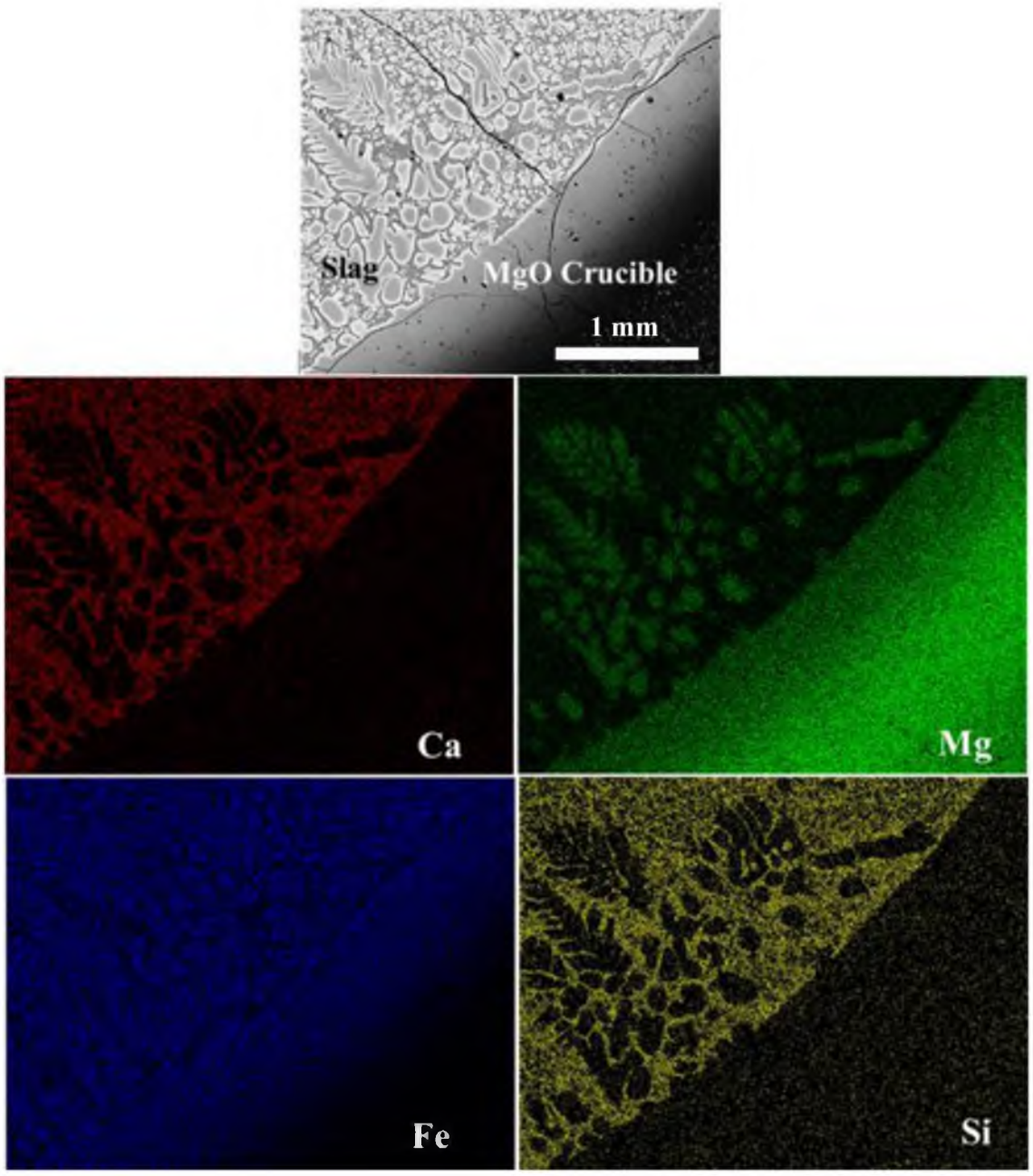

Figure 3-12. BSED-SEM micrograph of a cross-sectioned magnesia crucible containing slag (the top). The four colored images show the EDS elemental maps.

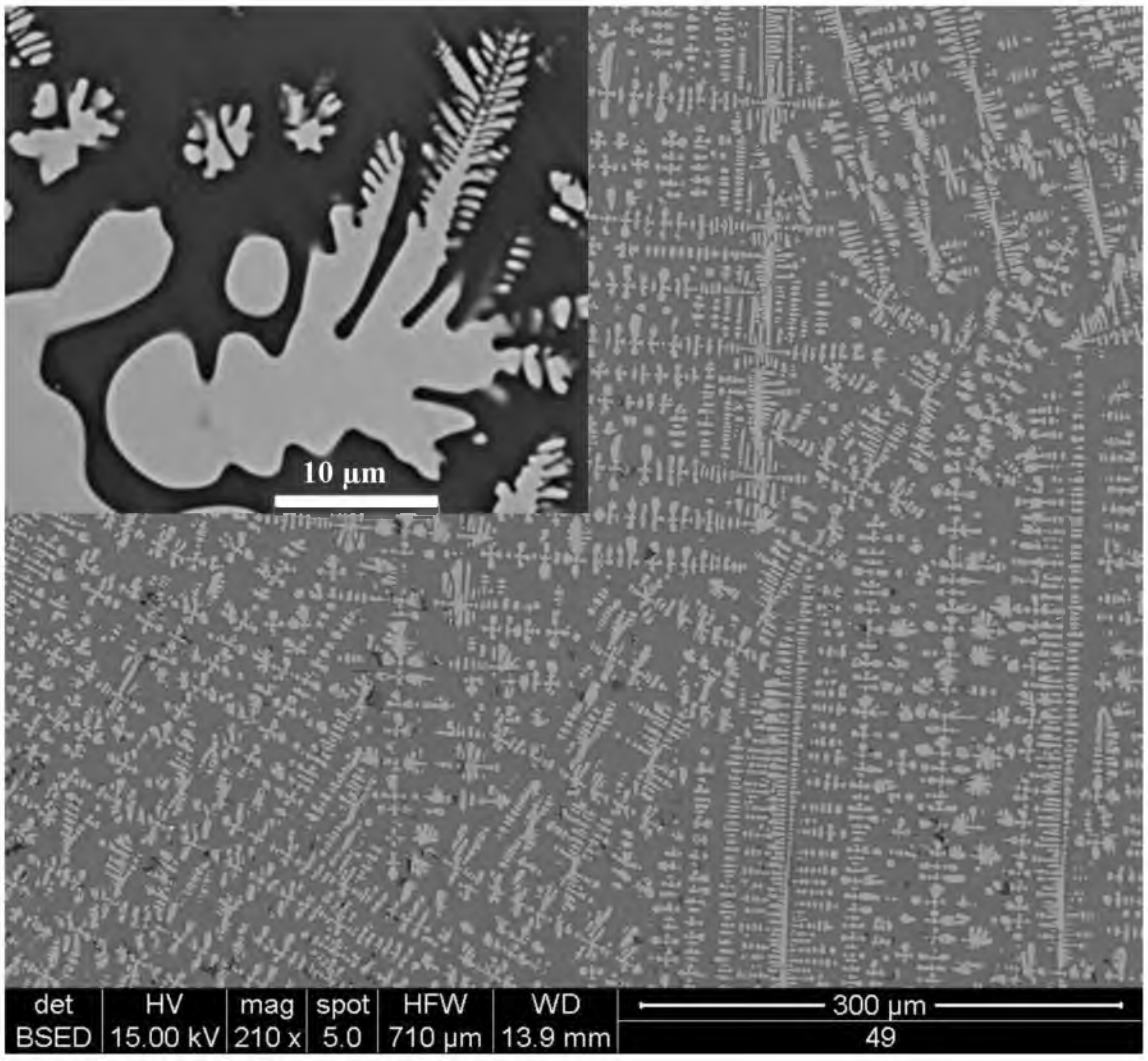

Figure 3-13. BSED-SEM micrograph showing the homogeneity of the slag with an inset with higher magnification showing the slag matrix with the floating dendritic structures.

separate MgO granules could be detected near the crucible wall, isolating the slag from the broken walls of crucible for analysis was still challenging as magnesia could crack and fall into the slag, causing analysis errors. To avoid that, a piece of the bulk slag far from the crucible walls was picked for grinding and further analyses.

It is notable that basicity according to any of the indices mentioned above, whether the ratio or the difference between basic and acidic slags, or even the optical basicity, is basically a measure of the free oxygen in the slag that can, for example, oxidize dissolved elements in the molten iron (e.g., S, P, Mn, Si,…etc), dissociate silicate polymers, or control the lining wear. Thus, any of the aforementioned basicity indices could be used based on the bulk chemical analysis results of the slag constituents. The basicity index that best correlates the property of interest will be used, as will be discussed later in the following chapters.

From O 1s XPS results, one can find that the order of the different atmospheres based on O^{2-}% is CO/CO_2 (44%) > $CO/CO_2/H_2/H_2O$ (41%) > H_2/H_2O (37%) as mentioned earlier. Based on that, it can be concluded that the type of gas atmosphere affects the real basicity of the slag. This is expected to have an impact on the distribution ratios of S, P, and Mn between slag and molten iron, as will be discussed later.

3. 5. Solubility of Gases in the Slag

Dissolved gases in the slag can exert measurable influence on slag properties, even at 10-ppm concentrations. The three gas atmospheres investigated in this study belong to the gas system C-O-H with different ratios. That system is composed of a large number of gaseous species, including hydrocarbons. However, most of these species have

very low thermodynamic stability at the experimental temperatures. We will restrict ourselves, therefore, to the following species in the C-O-H system: O_2, CO_2, H_2O, H_2, CO, and CH_4. Based on HSC calculations, these gases constitute over 99.5 mol% of the gas mixtures used in this study. Since O_2 has been fixed under the three gas atmosphere, the solubility of only the other five gases will be discussed here. The dissolved gases, which mostly react with structural species (especially with silicates) in the slag, perturb the balance of these species. Therefore, that solubility could change the physical as well as chemical properties (*vide infra*) of slag.

CO_2 dissolves in the slag as an acidic oxide reacting with oxo-species.[9] At $pO_2 > 10^{-10}$ atm, CO_2 reacts in the slag as follows:

$$CO_2 + O^{2-} = CO_3^{2-} \qquad (3\text{-}20)$$

The solubility is controlled by the oxygen partial pressure as well as the slag basicity. In lime-silicate slags, CO_2 solubility is very small in acidic and slightly basic slags.[57, 58]

Water, a very amphoteric oxide, exerts a dramatic influence on the slag, even at very low concentrations. Water affects phase equilibria, reaction kinetics, density, and viscosity. According to Mysen and Richet,[17] there is probably not a single gas with the impact of water on the silicate melts. Although there is some disaccord regarding the absolute value of the water dissolved in slag in the literature, all the results agree upon the following: (1) water dissolves mainly in two forms: hydroxyl ions and molecular water (mostly at elevated pressures), (2) water content in the slag increases proportionally

to the square root of water vapor partial pressure, and (3) the water content follows a parabolic shape as a function of basicity with a minimum around the metasilicate region. The latter observation is attributed to the amphoteric nature of H_2O, which determines the dissolution mechanism.[59-64] It is notable that at high pressure, water can also dissolve into silicate melts as individual molecules rather than liquid-like structure.[17]

The dissolution mechanism was proposed in the late 1950s.[59, 63, 65] Based on the experimental observations and correlations, it was suggested that water dissolves according to different mechanisms at different basicities, as shown in Figure 3-13. The overall reaction for both acidic and basic slags is represented by[66]:

$$H_2O(g) + O^* = 2OH^* \qquad (3\text{-}21)$$

where O* represents double or single bonded oxygen, or O^{2-}, and OH^* is single bonded to silicon or as a free ion.[67] Thus, H_2O can contribute to the silicate depolymerization or polymerization. These mechanisms have been substantiated by experimental correlations and spectroscopic investigations.[40, 68-70] The slags used in this studied can be classified as moderately basic slags. Therefore, water is expected to dissolve according to one of the mechanisms shown in eqs b and c in Figure 3-14. The former mechanism implies an increase in polymerization under H_2/H_2O compared with CO/CO_2 atmosphere. This is in accordance with FTIR and Raman results as well as the calculated NBO/T shown in Table 3-8. The XPS also indicated that the BO under H_2/H_2O is higher than CO/CO_2 atmosphere supporting mechanism b. Therefore, it is more likely that water dissolution follows the first mechanism, b, than the other one, c.

Acidic Slag

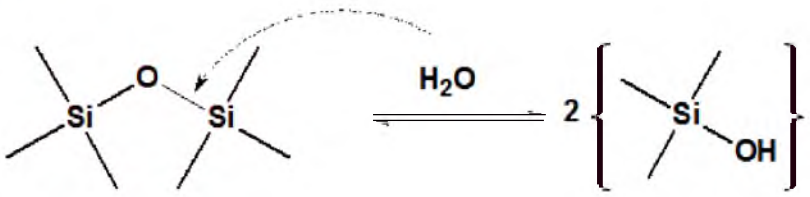

(a)

Depolymerization

Basic Slag

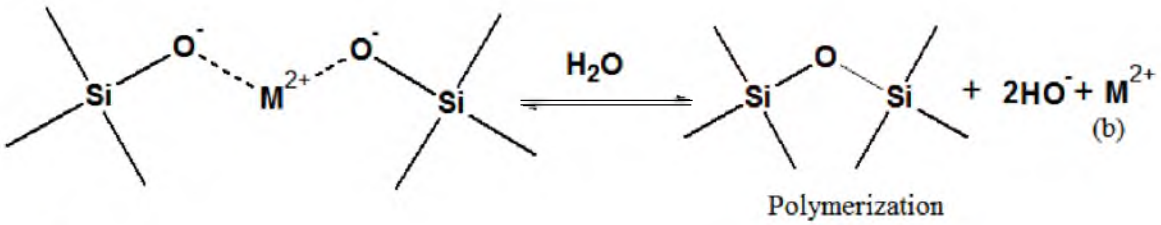

(b)

Polymerization

or

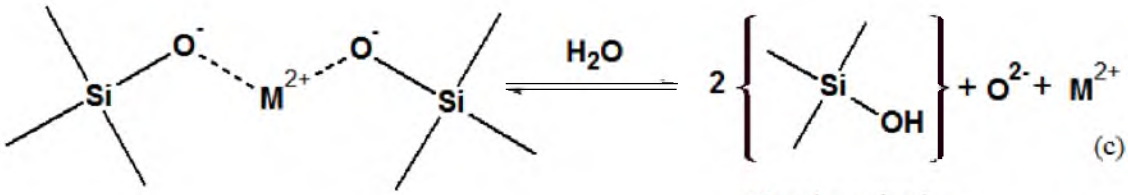

(c)

Depolymerization

Highly Basic Slag

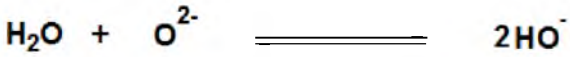

(d)

Figure 3-14. The potential mechanisms of water solubility in slags with different basicities.

It is notable that when CO_2 and H_2O coexist in the studied system, as in the case of $CO/CO_2/H_2/H_2O$ atmosphere, the impact of H_2O was more pronounced than CO_2, as shown in Table 3-8. That means that in the studied slags, H_2O dissolves more significantly than CO_2, which agrees with the literature.[57, 58]

The solubility of H_2 in silicate melts have not been reported at iron or steelmaking conditions. However, it has been reported that H_2 dissolves in silicate, forming OH groups, and hence depolymerizing the melt at high temperature and pressure, relevant to magma research.[17] For the last major gas in the gas mixtures used in the study, CO, it has reported that at lower pressures, CO acts as a diluent of the gas phase with no measurable solubility in the melt. Similarly H_2 could be treated as a simple diluent in the gas mixture in this work. Only high-pressure experiments were found in the literature relevant to CH_4 solubility in silicate melts. It was suggested that CH_4 might break the BO to form $Si–CH_3$ or Si–OH, indicating its depolymerization impact.[17] For the fact that CH_4 in this experiment constitutes < 1 mol% of the $CO/CO_2/H_2/H_2O$ mixture, its impact would have been negligible, even if it was presumably soluble under the conditions of this study. Hence, it is not discussed further in this work. All the discussions in the following chapters, therefore, will be limited to the H_2O solubility and pH_2O.

3. 6. Conclusions

The gas mixture of CO/CO_2, H_2/H_2O, and $CO/CO_2/H_2/H_2O$ is referred to as blast furnace (BF), hydrogen (H_2), and natural gas/coal gas (NG/CG), respectively.

Based on the spectroscopic and XRD analyses in addition to NBO/T calculations, H_2O stabilizes the more polymerized silicates anions rather than the depolymerized

monomers. It was found that for the investigated slags at 1550°C H_2 and NG/CG exhibits BO (bridging oxygen; the higher the BO, the higher the polymerization degree) of 55 and 9 % more than the BF, whereas for the ratio NBO/T of both showed ~ 35% less than in the BF. Moreover, slags under H_2 and NG/CG have values of $\psi = (Q^0+Q^1)/(Q^2+Q^3)$ (a measure of depolymerization) 75 and 55 less than slags under the BF conditions, as Figure 3-15 summarizes. Therefore, it can be concluded that the higher the water content in the gas atmosphere, the more polymerized the silicates in the slag. This difference in polymerization degrees plays a critical rule in the distribution of elements between slag and molten iron as well as the activity coefficients of oxides in the slag, as will be discussed in the following chapters. In addition, the degree of polymerization controls the physical properties of the slag such as the viscosity. Based on the spectroscopic, XRD, and chemical analyses, it is concluded that H_2O in the gas atmosphere increases the slag viscosity.

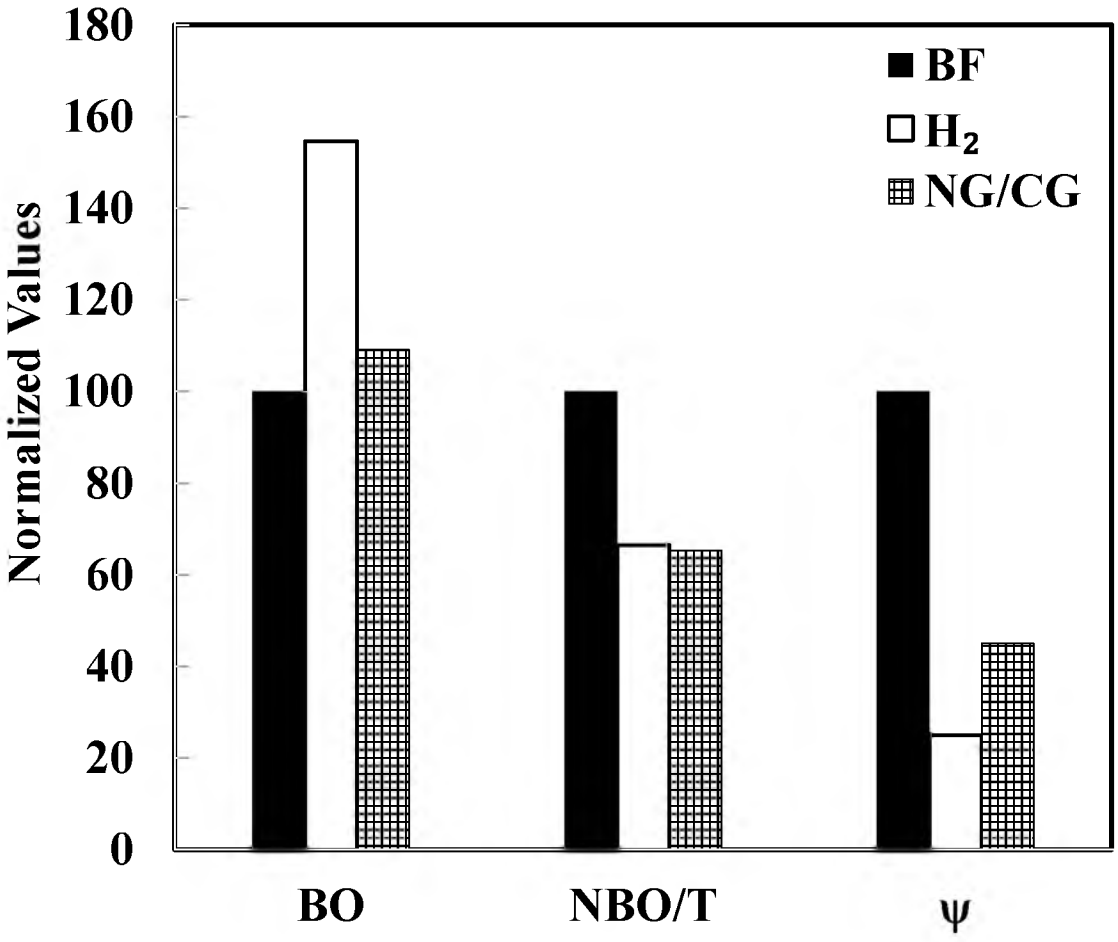

Figure 3-15. Effect of the type of reductant, relative to the BF gas composition, on the bridging oxygen (BO), nonbridging oxygen/tetrahedra (NBO/T), and the ratio $\psi = (Q^0+Q^1)/(Q^2+Q^3)$.

3. 7. References

(1) Liu, S. H.; Fruehan, R.; Morales, A.; Ozturk, B. Measurement of FeO activity and solubility of MgO in smelting slags. *Metall.Trans. B* **2001**, *32*, 31-36.

(2) Basu, S.; Lahiri, A. K.; Seetharaman, S. Activity of ferric oxide in steelmaking slag. *Metall.Trans. B* **2010,** *41*, 414-419.

(3) Mohassab-Ahmed, M. Y.; Sohn, H. Y.; Kim, H. G., Phosphorus distribution between liquid iron and magnesia-saturated slag in H_2/H_2O atmosphere relevant to a novel ironmaking technology. *Ind. Eng. Chem. Res.* **2012,** *51*, 7028-7034.

(4) Suito, H.; Inoue, R. Manganese equilibrium between molten iron and MgO-saturated CaO-Fe_tO-SiO_2-MnO slags. *Trans. Iron Steel Inst. Jpn.* **1984,** *24*, 257-265.

(5) Mills, K. *The structure of silicate melts*. National Physical Laboratory, Division of Materials Metrology. Teddington, England, **1991**.

(6) Herasymenko, P. Electrochemical theory of slag-metal equilibria. Part i.-reactions of manganese and silicon in acid open-heart furnace. *Trans. Faraday Soc.* **1938,** *34*, 1245-1254.

(7) Götz, J.; Masson, C. Trimethylsilyl derivatives for the study of silicate structures. Part i. A direct method of trimethylsilylation. *J. Chem. Soc. A* **1970**, 2683-2686.

(8) Lentz, C. W. Silicate minerals as sources of trimethylsilyl silicates and silicate structure analysis of sodium silicate solutions. *Inorg. Chem.* **1964,** *3*, 574-579.

(9) Fraser, D. G., Acid-base properties and structons: Towards a structural model for predicting the thermodynamic properties of silicate melts. *Ann. Geophys.* **2005**, 549-559.

(10) Stevels, J. M. Networks in glasses and other polymers. *Glass Ind.* **1954,** *35*, 657-662.

(11) Masson, C. The chemistry of slags-an overview. Metall. Slags Fluxes, Int. Symp., Proc., 2nd, **1984**, 3-44.

(12) Mills, K., *Slag atlas*. Second Edition ed.; Verlag Stahleisen GmbH: Düsseldorf, Germany, 1995.

(13) Huggins, M. L., The structure of amorphous materials. *J. Phys. Chem.* **1954,** *58*, 1141-1146.

(14) Fraser, D. G., Thermodynamic properties of silicate melts. *Thermodynamics Geology* **1977**, 301-325.

(15) Živković, Ž.; Mitevska, N.; Mihajlović, I.; Nikolić, Đ. The influence of the silicate slag composition on copper losses during smelting of the sulfide concentrates. *J. Mining Metall. B: Metall.* **2009,** *45*, 23-34.

(16) Ariskin, A. A.; Polyakov, V. B., Simulation of molecular mass distributions and evaluation of o 2- concentrations in polymerized silicate melts. *Geochem. Int.* **2008,** *46*, 429-447.

(17) Mysen, B. O.; Richet, P. *Silicate glasses and melts: Properties and structure*. Elsevier, **2005**.

(18) Mysen, B. O.; Finger, L. W.; Virgo, D.; Seifert, F. A. Curve-fitting of raman spectra of silicate glasses. *Am. Mineral.* **1982,** *67*, 686-695.

(19) McMillan, P., A raman spectroscopic study of glasses in the system CaO-MgO-SiO_2. *Am. Mineral.* **1984,** *69*, 645-659.

(20) McMillan, P. Structural studies of silicate glasses and melts-applications and limitations of raman spectroscopy. *Am. Mineral.* **1984,** *69*, 622-644.

(21) Park, J. Y.; Park, S. J.; Chang, W. S.; Sohn, I. Effect of feot content and CaO/SiO_2 ratio on hydrogen dissolution in CaF_2–CaO–SiO_2-based welding fluxes. *J. Am. Ceram. Soc.* **2012,** *95*, 1756-1763.

(22) Bradley, M. Curve fitting in raman and ir spectroscopy: Basic theory of line shapes and applications. *Thermo Fisher Scientific, Madison, USA, Application Note* **2007,** 50733.

(23) Swann, G.; Patwardhan, S. Application of Fourier transform infrared spectroscopy (FTIR) for assessing biogenic silica sample purity in geochemical analyses and palaeoenvironmental research. *Climate of the Past* **2010,** *7*, 65-74.

(24) Wojdyr, M. Fityk: A general-purpose peak fitting program. *J. Appl. Crystallogr.* **2010,** *43*, 1126-1128.

(25) Park, H.; Park, J. Y.; Kim, G. H.; Sohn, I. Effect of TiO_2 on the viscosity and slag structure in blast furnace type slags. *Steel Res. Int.* **2012,** *83*, 150-156.

(26) MacDonald, S. A.; Schardt, C. R.; Masiello, D. J.; Simmons, J. H., Dispersion analysis of FTIR reflection measurements in silicate glasses. *J. Non-Cryst. Solids* **2000,** *275*, 72-82.

(27) Branda, F.; Arcobello-Varlese, F.; Costantini, A.; Luciani, G., Tg and FTIR of $(2.5-x)CaO{\cdot}x/3M_2O_3{\cdot}2SiO_2$ (m=Y, La, In, Al, Ga) glasses. *J. Non-Cryst. Solids* **1999,** *246*, 27-33.

(28) Aronne, A.; Esposito, S.; Pernice, P. FTIR and dta study of lanthanum aluminosilicate glasses. *Mater. Chem. Phys.* **1997,** *51*, 163-168.

(29) Lin, X.; Ideta, K.; Miyawaki, J.; Takebe, H.; Yoon, S.-H.; Mochida, I. Correlation between fluidity properties and local structures of three typical asian coal ashes. *Energy Fuels* **2012,** *26*, 2136-2144.

(30) Genson, A.; Hanifi, A. R.; L'Helguen, A.; Trinel, B.; Pomeroy, M. J.; Hampshire, S. Structural features of Ca-Si-Al-$O_{100-x-y}F_xN_y$ glasses by FTIR spectroscopy, *Eur. Cer. Soc.*, **2008**.

(31) Burns, A.; Brack, H. P.; Risen, W. M. Dielectric and infrared reflectance studies of inorganic oxide glasses. *J. Non-Cryst. Solids* **1991,** *131*, 994-1000.

(32) Matson, D. W.; Sharma, S. K.; Philpotts, J. A., The structure of high-silica alkali-silicate glasses. A raman spectroscopic investigation. *J. Non-Cryst. Solids* **1983,** *58*, 323-352.

(33) Husung, R. D.; Doremus, R. H. The infrared transmission spectra of four silicate glasses before and after exposure to water. *J. Mater. Res.* **1990,** *5*, 2209-2217.

(34) Park, J. Y.; Park, J. G.; Lee, C. H.; Sohn, I. Hydrogen dissolution in the TiO_2–SiO_2–FeO and TiO_2–SiO_2–MnO based welding-type fluxes. *ISIJ Int.* **2011,** *51*, 889-894.

(35) Merzbacher, C. I.; White, W. B. The structure of alkaline earth aluminosilicate glasses as determined by vibrational spectroscopy. *J. Non-Cryst. Solids* **1991,** *130*, 18-34.

(36) Park, J. H.; Min, D. J.; Song, H. S. FT-IR spectroscopic study on structure of CaO-SiO_2 and CaO-SiO_2-CaF_2 slags. *ISIJ Int.* **2002,** *42*, 344-351.

(37) Lee, Y.; Kim, J.; Yi, S.; Min, D. Viscous behaviour of CaO-SiO_2-Al_2O_3-MgO-FeO slag, VII International Conference on Molten Slags Fluxes and Salts, The South African Institute of Mining and Metallurgy, **2004**, 225-230.

(38) Almeida, R.; Guiton, T.; Pantano, C. Characterization of silica gels by infrared reflection spectroscopy. *J. Non-Cryst. Solids* **1990,** *121*, 193-197.

(39) Gervais, F.; Blin, A.; Massiot, D.; Coutures, J.; Chopinet, M.; Naudin, F. Infrared reflectivity spectroscopy of silicate glasses. *J. Non-Cryst. Solids* **1987,** *89*, 384-401.

(40) Park, J. Y.; Han, J. S.; Sohn, I. Hydrogen dissolution in the CaF_2-CaO-SiO_2 system. *ISIJ Int.* **2011,** *51*, 1788-1794.

(41) Sohn, I.; Min, D. J. A review of the relationship between viscosity and the structure of calcium-silicate-based slags in ironmaking. *Steel Res. Int.* **2012,** *83*, 611-630.

(42) Ueda, S.; Koyo, H.; Ikeda, T.; Kariya, Y.; Maeda, M. Infrared emission spectra of CaF_2-CaO-SiO_2 melt. *ISIJ Int.* **2000,** *40*, 739-743.

(43) Park, J. H.; Rhee, P. C. H. Ionic properties of oxygen in slag. *J. Non-Cryst. Solids* **2001,** *282*, 7-14.

(44) Shirley, D. A. High-resolution X-ray photoemission spectrum of the valence bands of gold. *Phys. Rev. B* **1972,** *5*, 4709-4714.

(45) Kim, H.; Sohn, I., Effect of CaF_2 and Li_2O additives on the viscosity of CaO–SiO_2–Na_2O slags. *ISIJ Int.* **2011,** *51*, 1-8.

(46) Downs, R. T.; Hall-Wallace, M. The american mineralogist crystal structure database. *Am. Mineral.* **2003,** *88*, 247-250.

(47) Kauffman, G. B. The bronsted-lowry acid base concept. *J. Chem. Educ.* **1988,** *65*, 28-31.

(48) Lux, H., "Acids" and "bases" in a fused salt bath: The determination of oxygen-ion concentration. *Z. Elektrochem. Soc.* **1939,** 303-310.

(49) Flood, H.; Förland, T., The acidic and basic properties of oxides. *Acta Chem. Scand.* **1947,** *1*, 592-604.

(50) Fincham, C.; Richardson, F. The behaviour of sulphur in silicate and aluminate melts. *Proc. Royal Soc. Lond. A* **1954**, 40-62.

(51) Turkdogan, E. T., Physicochemical aspects of reactions in ironmaking and steelmaking processes. *Trans. Iron Steel Inst. Jpn.* **1984,** *24*, 591-611.

(52) Fruehan, R. *The making, shaping and treating of steel*, The AISE Steel Foundation, 11th edition: Pittsburgh, USA, **1998**.

(53) Turkdogan, E. T. *Physicochemical properties of molten slags and glasses. Metals Society* **1983.**

(54) Grant, N. J.; Chipman, J. Sulphur equilibria between liquid iron and slags. *Trans. AIME* **1946**, 134-149.

(55) Yang, X.; Liu, T.; Guo, Z.; Wang, D., Study on the correlation between phosphate capacity index and slag basicity. *Selected Papers Eng. Chem. and Metall.* **1996**, 8-21.

(56) Duffy, J. A.; Ingram, M. D., An interpretation of glass chemistry in terms of the optical basicity concept. *J. Non-Cryst. Solids* **1976,** *21*, 373-410.

(57) Suk, M. O.; Jo, S. K.; Kim, S. H.; Kim, J. S.; Shim, S. C. The effect of carbon in slag on steel reoxidation and carbon analysis by X-ray photoelectron spectroscopy in the CaO-SiO_2-Al_2O_3-MgO-MnO-Fe_tO system. *Metall. Trans. B* **2004,** *35*, 1087-1095.

(58) Rosenqvist, T. *Principles of extractive metallurgy*. Tapir Forlag: **2004**, 305.

(59) Tomlinson, J. W. A note on the solubility of water in a molten sodium silicate. *J. Soc. Glass Technol.* **1956,** *40*, 25T-31T.

(60) Mysen, B. O.; Virgo, D.; Harrison, W. J.; ScARFE, C. M. Solubility mechanisms of H_2O in silicate melts at high pressures and temperatures: A raman spectroscopic study. *Am. Mineral.* **1980,** *65*, 900-914.

(61) Schwerdtfeger, K.; Schubert, H. G. Solubility of water in CaO-Al_2O_3 melts at 1600°C. *Metall. Trans., B* **1978,** *9B*, 143-144.

(62) Iguchi, Y.; Ban-Ya, S.; Fuwa, T. Solubility of water in liquid CaO-SiO_2 with Al_2O_3, TiO_2, and FeO at 15500. *Trans. Iron Steel Inst. Jap.* **1969**, *9*, 189-195.

(63) Russell, L. E. Solubility of water in molten glass. *J. Soc. Glass Technol.* **1957,** *41*, 304T-317T.

(64) Zuliani, D. J.; Iwase, M.; McLean, A. The thermodynamics of water vapor dissolution in CaO-MgO-SiO_2 slags. *Trans. Iron Steel Soc. AIME* **1982,** *1*, 61-67.

(65) Walsh, J. H.; Chipman, J.; King, T. B.; Grant, N. J., Hydrogen in steelmaking slags. *J. Metals* **1956,** *8*, 1568-1576.

(66) Turkdogan, E.T. *Fundamentals of Steelmaking*, The Institute of Materials, London, **1996**.

(67) Jo, S. K.; Kim, S. H. The solubility of water vapour in CaO-SiO_2-Al_2O_3-MgO slag system. *Steel Res.*, **2000**, *71*, 15-21.

(68) Brandberg, J.; Sichen, D. Water vapor solubility in ladle-refining slags. *Metall. Trans. B,* **2006**, *37*, 389-393.

(69) Mysen, B. Water in peralkaline aluminosilicate melts to 2 GPa and 1400 °C. *Geochim. Cosmochim. Acta* **2002,** *66*, 2915-2928.

(70) Leekes, G.; Nowack, N.; Schlegelmilch, F., Dissolution of water vapor in ESR-slags of the systems CaO-Al_2O_3 and CaF_2-CaO-Al_2O_3 by application of Fourier-transform-infrared-spectroscopy. *Steel Res.* **1988,** *59*, 406-416.

CHAPTER 4

SULFUR DISTRIBUTION BETWEEN LIQUID IRON AND MAGNESIA-SATURATED SLAG IN $CO/CO_2/H_2/H_2O$ ATMOSPHERES RELEVANT TO A NOVEL FLASH IRONMAKING TECHNOLOGY

4. 1. Introduction

In recent years, there has been an increased demand for clean steels with low sulfur. It is known that sulfur contributes to drastic decrease of ductility and fracture toughness of steel. There has been much research done to study the distribution of sulfur and the sulfide capacities for various slag compositions, different temperatures, and oxygen potential.[1] Most previous work used CO/CO_2 gas mixture to control oxygen partial pressure (pO_2).[2-7] Others used only inert atmospheres,[8, 9] although Kor and Richardson[10] used a mixture of CO_2/H_2 to control pO_2. In our laboratory, we are developing a novel ironmaking process based on the reduction of iron oxide concentrates by hydrogen or natural gas in a suspension reduction process, with the ultimate goal of significantly reducing CO_2 emission, energy consumption, and environmental pollution in the steel industry.[11] Due to the fact that there are few articles published on sulfur distribution under an H_2/H_2O atmosphere, we conducted this research.

The sulfur partition reaction can be taken as an exchange reaction between sulfur in the metal and oxygen in the slag:

$$\underline{S}\,(\text{metal}) \;+\; O^{2-} \;=\; \underline{O}\,(\text{metal}) + S^{2-} \qquad (4\text{-}1)$$

The equilibrium constant for reaction 4-1, K_1, is given by the equation:

$$K_1 = \frac{a_{\underline{O}} \cdot a_{S^{2-}}}{a_{\underline{S}} \,.\, a_{O^{2-}}} \qquad (4\text{-}2)$$

where a is the thermodynamic activity relative to appropriate standard states. The activities of sulfur in the two phases can be expressed in terms of the concentrations, viz.

$$a_{\underline{S}} = (wt\%\,\underline{S}\,in\ metal).\, f_{\underline{S}} \qquad (4\text{-}3)$$

and

$$a_{S^{2-}} = (wt\%S^{2-}\ in\ slag).\, f_{S^{2-}} \qquad (4\text{-}4)$$

where $f_{\underline{S}}$ and $f_{S^{2-}}$ represent the Henrian activity coefficients of sulfur in the metal and the sulfide ion in the slag, respectively. The sulfur partition ratio (L_S) is then given by the relationship:

$$L_S = \frac{(wt\%S)_{slag}}{[wt\%\underline{S}]_{metal}} = K_1 \cdot \frac{a_{O^{2-}}}{a_{\underline{O}}} \cdot \frac{f_{\underline{S}}}{f_{S^{2-}}} \qquad (4\text{-}5)$$

As it is not realistic to attempt to measure these parameters, the problem is approached by considering the equilibrium between the slag and a gas phase where the chemical potentials of relevant species are known and fixed. This has resulted in the development of the concept of slag capacity.

The sulfide capacity of slag is expressed as[12]:

$$C_S = \exp\left(\frac{-\Delta G^{\circ}}{RT}\right)\left(\frac{a_{O^{2-}}}{f_{S^{2-}}}\right) \qquad (4\text{-}6)$$

where $a_{O^{2-}}$ is the activity of oxygen ion in the slag, $f_{S^{2-}}$ is the Henrian activity coefficient of sulfide ions in the slag, R is the gas constant, T is the temperature in K, and ΔG° is the standard Gibbs free energy change for the following reaction:

$$\frac{1}{2}S_2(g) + O^{2-}(slag) = S^{2-}(slag) + \frac{1}{2}O_2(g) \qquad \Delta G^{\circ} = 118500 - 58.82 \times T \ (J/mol) \qquad (4\text{-}7)$$

In terms of measurable quantities, the sulfide capacity can be expressed as:

$$C_S = (wt\%S_{slag})\left(\frac{p_{O_2}}{p_{S_2}}\right)^{1/2} \qquad (4\text{-}8)$$

While the exponential factor on the right side of eq 4-6 is system independent, the ratio $a_{O^{2-}} / f_{S^{2-}}$ is characterized by the specific system. Fincham and Richardson[12] assumed the constancy of the above ratio for a given slag. They justified that $a_{O^{2-}}$ can be considered constant due to polymerization/depolymerization reactions in silicate melts, but the $f_{S^{2-}}$ need not be constant. Any modeling of the sulfide capacities for complex slags must take into account this variation and thus the sulfide capacities are difficult to predict purely on the basis of the thermodynamics of the silicate melts alone, unless the activity coefficient of the sulfide ion is taken into consideration.

In the case of iron- and steelmaking processes, it is the sulfide capacity value of the slag that is of great relevance. The C_S values of a number of synthetic slags have been experimentally measured from the 1950s and have been periodically reviewed.[13-15] In general, as seen from eq 4-6, the sulfide capacity of a slag is a function of the activity of the oxygen in the slag, which in turn is dependent on the slag basicity. In this study, basicity defined as follows was used to explain its effect on the distribution ratio.

$$\frac{wt\%CaO + 1.4 \times wt\%MgO}{wt\%SiO_2 + 0.6\, wt\%Al_2O_3} \qquad (4\text{-}9)$$

which uses the assumption that one mole of CaO is equivalent to one mole of MgO and one mole of Al_2O_3 is equivalent to one mole of SiO_2 as far as their contribution to the basicity of slag.[16]

4. 2. Slag Preparation

Required amounts of CaO, SiO_2, Al_2O_3, and MgO were mixed in an alumina agate mortar to obtain the desired compositions and transferred to a graphite crucible[17] to be premelted at 1600°C for 1 h under a N_2 flow. MgO was added as a slag component to minimize the consumption of the magnesia crucible used in this work for the reasons explained in Section 4.6. Thus, all the slags tested in this work were MgO-saturated. The premelted slag was crushed into fine powder in the alumina agate mortar. Premelting was confirmed by light polarizing microscope and XRD, shown in Figure 4-1, displaying gehlenite, akermanite, spinel, and monticilite, the presence of which proves the slag melting as expected from the phase diagram.[18]

The slag powder prepared in a graphite crucible was transferred to a 99.8% alumina boat to be decarburized[6] at 1200°C for 24 h under an air flow. Dry FeO, $Ca_2P_2O_7$, and FeS powders were added and mixed well. Each of the $Ca_2P_2O_7$ and FeS powders was added at 0.1 wt% of the total slag and the resulting synthetic slag was stored in a desiccator to be used in the experiments.

4. 3. Experimental Apparatus

The details of the experimental apparatus were presented in details in Chapter 2 (Section 2.4).

4. 4. Experimental Procedure

The initial slag composition other than FeO was chosen to be similar to that of the blast furnace slag. The FeO content in the slag was fixed by the equilibrium of molten

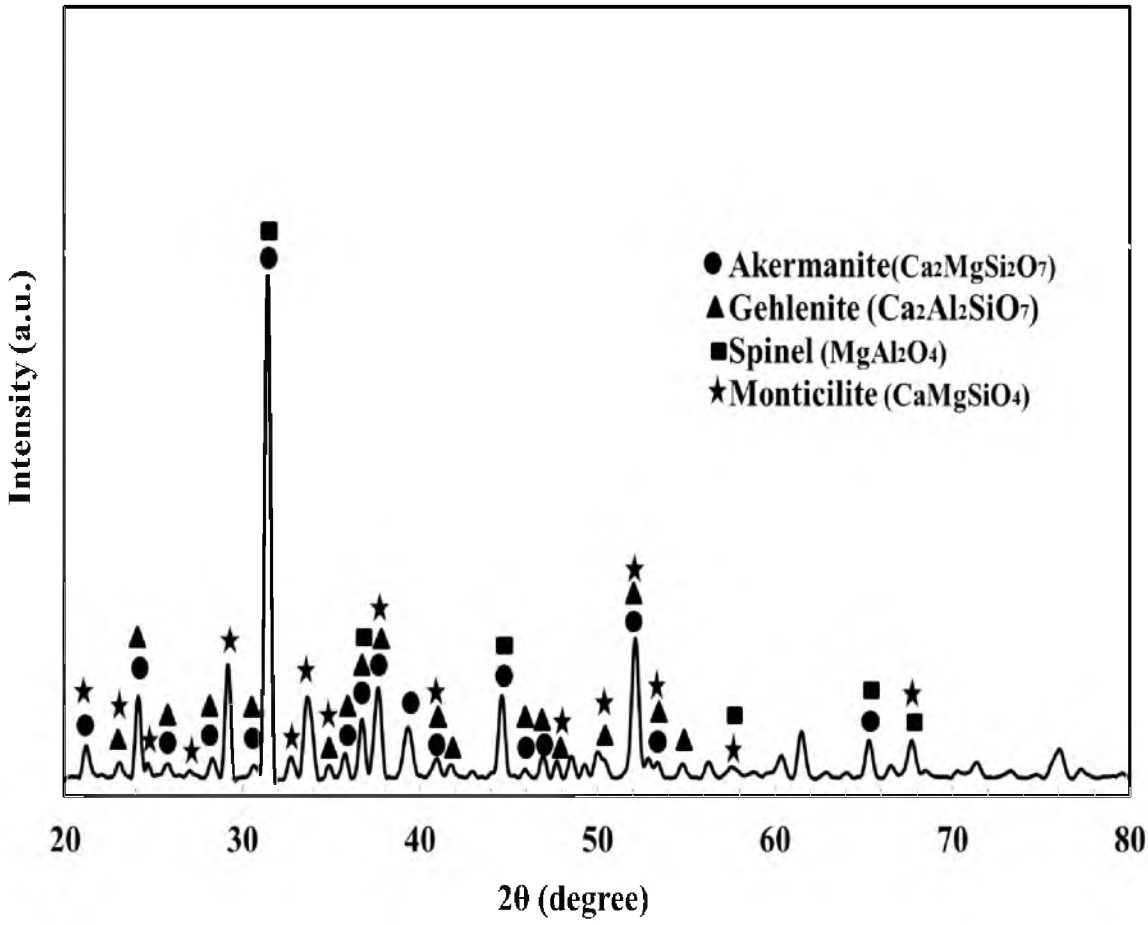

Figure 4-1. XRD pattern showing the peaks for gehlenite, akermanite, spinel, and monticilte, the presence of which verifies uniform slag melting.

iron with the gas phase affected by the contents of other slag constituents. The temperature range was chosen to be 1550-1650°C, which was wide enough to encompass the expected operating temperature of the novel ironmaking process. The ratio of H_2/H_2O was chosen in the range of 1.7-10 to include the expected operating conditions and determine its effect over a wide range.

The samples were prepared as 2.5 g of slag mixed with 2.5 g of iron powder. They were mixed well to reduce the time to reach equilibrium in magnesia crucibles (1.8 cm OD, 4 cm height, 0.25 cm wall thickness) supplied by Ozark Technical Ceramics, Inc. (Webb City, MO). Several materials, such as calcia (CaO), magnesia (MgO), platinum (Pt), and alumina (Al_2O_3), were carefully examined as the crucible material. Each of these materials was evaluated in terms of mechanical strength, high-temperature stability and resistance to thermal shock, inertness toward molten slag, corrosion or wettability by liquid iron, cost, and availability. After careful consideration of the different parameters and on the basis of the trials conducted with different materials, dense-sintered magnesia crucibles were selected.

The furnace was heated to the target temperature under a flow of N_2. At the target temperature, the furnace was opened to introduce the four-sample alumina holder to the even temperature zone within less than 5 min. Then, N_2 was switched to the experimental gas mixture. In previous research, 6 and 8 h were found to be sufficient for a similar sample size.[19, 20] To ensure the 3-phase (gas-slag-metal) equilibrium, 10 h was chosen in this work. After 10 h, the experimental gases were switched back to N_2 by stopping the water pump and gradually decreasing the H_2 and SO_2 flows while increasing the N_2 flow. After 5 min of purging, the furnace was opened, the holder was pulled out

within 5 min, and the samples were quenched in water. The crucible itself together with the sample was crushed, and iron was separated from the slag. Then, the iron was shredded and the slag finely ground.

The compositions of the iron and the slag phases were analyzed for their sulfur contents by ICP-OES. Prior to analysis, the samples were digested in closed Savillex® (Savillex, Eden Prairie, MN) microwavable vessels. The chemical analysis results are listed in Table 4-1.

Table 4-2 lists the oxygen and sulfur partial pressures for the H_2-H_2O-SO_2 gas mixture at the experimental temperatures calculated by HSC 5.11 (Outokumpu Oy, Riihitontuntie 7, Finland), in which 15 gaseous species were taken into consideration.

Comparing our gas rate/reactor volume to the previous work,[2-7,12] it was found that this ratio in our system is smaller. Thus, we could also assume that gaseous species were in equilibrium with each other, as well as with the condensed phases.

Reproducibility of the experiments was confirmed by the consistency of the results of repeated experiments under the same conditions.

4. 5. Results and Discussion

The effect of basicity, oxygen potential, and temperature on sulfur distribution ratio will be discussed. Also, the L_S values for the blast furnace operation will be compared with those under the conditions of the proposed process. From previous research, water has a significant solubility in slag, indicating that it could affect L_S. This made it difficult to obtain predictions using any of the available models since none of them included the effect of water solubility in slag.

Table 4-1. The chemical analysis of the samples

Sample	T (°C)	(S) (wt%)	FeO (wt%)	MgO (wt%)	CaO (wt%)	Al_2O_3 (wt%)	SiO_2 (wt%)	[S] (wt%)	Log(*Ls*)
S1	1550	1.55	25.3	17.3	20.7	6.26	29.8	11.9	-0.89
S2	1550	2.72	35.4	12.9	20.6	6.72	24.6	6.11	-0.35
S3	1550	2.88	33.1	11.7	26.3	7.81	28.5	7.16	-0.40
S4	1550	4.77	41.3	10.8	21.5	6.20	21.0	6.03	-0.10
S5	1550	0.93	21.6	19.2	20.9	8.74	28.3	7.15	-0.89
S6	1550	1.01	19.9	20.2	23.0	7.99	33.0	6.96	-0.84
S7	1550	1.85	22.3	15.2	29.8	9.48	26.4	7.79	-0.62
S8	1550	2.03	20.7	10.6	32.1	9.35	23.7	6.21	-0.10
S9	1550	1.08	11.5	22.4	24.9	8.18	32.3	11.2	-1.02
S10	1550	1.34	12.0	18.7	29.0	9.71	29.9	9.67	-0.86
S11	1550	1.56	12.4	17.0	30.9	10.7	29.0	9.32	-0.78
S12	1550	2.16	14.2	14.5	34.7	9.82	31.0	9.38	-0.64
S13	1550	0.81	12.2	22.5	25.1	9.41	32.6	8.43	-1.02
S14	1550	1.20	12.6	16.9	27.4	8.77	39.7	8.28	-0.84
S15	1550	2.27	18.7	15.4	34.7	10.2	16.4	8.42	-0.57
S16	1550	1.72	15.3	16.3	32.4	10.4	28.4	9.49	-0.74
S17	1600	4.17	41.1	15.1	15.8	6.15	19.5	6.85	-0.22
S18	1600	3.44	34.6	13.6	20.4	7.37	24.4	6.69	-0.29
S19	1600	4.81	42.8	11.3	18.1	6.25	17.0	5.59	-0.06

Table 4-1. Continued.

Sample	T (°C)	(S) (wt%)	FeO (wt%)	MgO (wt%)	CaO (wt%)	Al_2O_3 (wt%)	SiO_2 (wt%)	[S] (wt%)	Log(*Ls*)
S20	1600	5.26	52.8	12.4	14.9	4.90	12.2	4.99	0.02
S21	1600	1.31	20.4	22.6	20.7	7.55	27.7	10.2	-0.89
S21	1600	2.12	20.3	22.6	20.7	8.63	27.6	6.08	-0.46
S22	1600	2.52	27.1	15.7	22.7	8.24	23.5	9.42	-0.57
S22	1600	1.66	27.0	17.6	22.6	8.23	23.2	8.24	-0.69
S23	1600	3.55	29.7	14.2	26.2	8.77	22.0	9.20	-0.41
S23	1600	2.37	29.7	14.2	23.7	8.34	22.0	8.83	-0.57
S24	1600	4.46	31.1	14.7	24.9	7.93	21.7	10.1	-0.35
S25	1600	0.78	8.7	25.5	24.3	9.71	36.0	5.60	-0.85
S26	1600	1.17	9.3	21.2	27.1	9.83	31.5	5.30	-0.66
S27	1600	1.80	11.8	18.7	29.1	10.1	28.2	7.45	-0.62
S28	1600	2.48	13.2	19.4	31.0	9.89	23.9	6.26	-0.40
S29	1600	1.02	7.1	23.9	23.9	9.62	31.5	8.56	-0.92
S30	1600	1.77	14.7	20.9	25.5	9.55	28.9	9.71	-0.74
S31	1600	1.97	14.9	25.3	25.2	8.90	23.6	9.37	-0.68
S37	1650	1.34	32.6	20.5	17.8	7.62	23.5	4.85	-0.56
S38	1650	4.15	47.5	14.2	13.5	5.52	16.3	4.71	-0.06

Table 4-2. Oxygen and sulfur partial pressures calculated at the experimental temperatures and P_T = 0.85 atm using $H_2/H_2O/SO_2$ gas mixture (1 atm = 101.3 kPa and Sxx is sample designation.)

H_2/ H_2O (molar ratio)	p_{O_2} (atm)			p_{S_2} (atm)			Flow Rates* (mL/min)		
	1550°C	1600°C	1650°C	1550°C	1600°C	1650°C	H_2	H_2O	SO_2
1.7	2.2×10^{-09}	4.8×10^{-09}	-	1.4×10^{-03}	1.7×10^{-03}	-	125	0.047	5.7
	S1-S4	S17-S20	-	S1-S4	S17-S20	-			
3.0	7.0×10^{-10}	1.8×10^{-09}	4.2×10^{-09}	1.0×10^{-03}	1.3×10^{-03}	1.6×10^{-03}	149	0.032	5.7
	S5-S8	S21-S24	S37-S38	S5-S8	S21-S24	S37-S38			
6.0	2.4×10^{-10}	5.3×10^{-10}	-	8.3×10^{-04}	1.0×10^{-03}	-	170	0.018	5.7
	S13-S16	S29-S32	-	S13-S16	S29-S32	-			
10.0	1.1×10^{-10}	2.7×10^{-10}	-	7.3×10^{-04}	9.5×10^{-04}	-	181	0.011	5.7
	S9-S12	S25-S28	-	S9-S12	S25-S28	-			

*Flow rates are calculated at 0.85 atm (atmospheric pressure at Salt Lake City) and 25°C.

4. 5. 1. Effect of Basicity

The effect of basicity on the sulfur partition at various temperatures and pO_2 values is shown in Figure 4-2. As mentioned earlier, eq 4-9 was used to express basicity. It was found that the higher the basicity, the higher the L_S. This is the same trend as for other systems that used CO_2/CO equilibrium.[2-7] A larger amount of CaO or MgO leads to higher O^{2-}, which captures sulfur dissolved in the metal, as shown in reaction (1). For pO_2 of 10^{-10} in Figure 4-2(a) and 2×10^{-9} atm in Figure 4-2(b), the basicity range was narrow, and the variation in the results represents the effect of slag composition more than that of pO_2. Since both slag composition and pO_2 were different, it was difficult to directly compare the results to the previous work.

4. 5. 2. Effect of Oxygen Potential

Figure 4-3 shows the effect of oxygen potential on L_S at different basicity ranges and temperatures. The trend was similar to thermodynamics expectation according to reaction (1), which indicates that L_S increases with oxygen activity. Direct comparison of our results to the previous results was difficult mainly because the available theoretical models either use adjustable parameters[7, 17, 22, 23] or are limited to certain ranges of compositions or even different slag components.[2, 15, 24, 25] Further, there are no models that take H_2O solubility in slag into consideration.

4. 5. 3. Effect of Temperature

It is shown in Figure 4-4 that L_S increased with temperature at constant input gas composition and basicity, which is consistent with the previously reported results.[2-7]

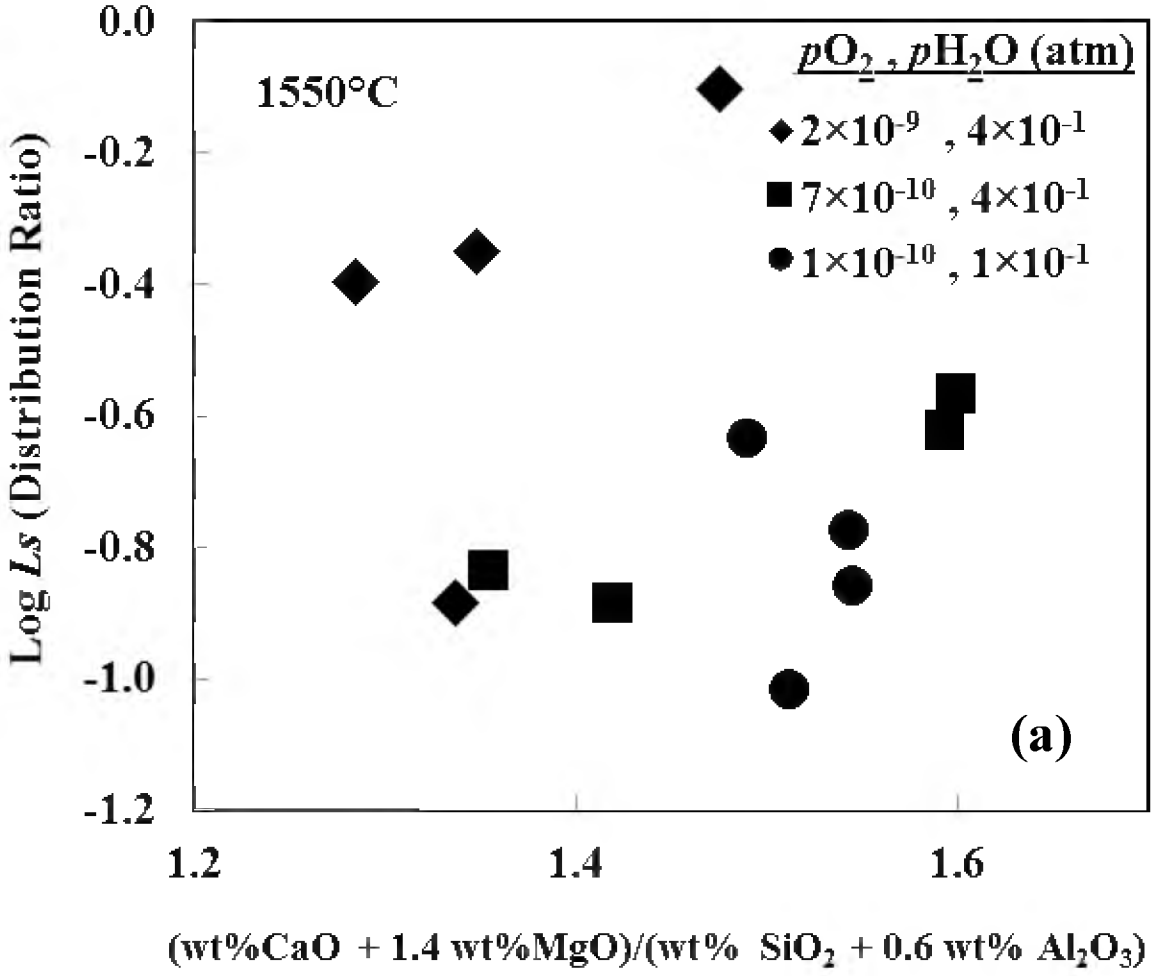

Figure 4-2. The effect of basicity [(wt%CaO + 1.4 wt%MgO)/(wt% SiO_2 + 0.6 wt% Al_2O_3)] on L_S at various temperatures and pO_2 values under H_2/H_2O atmosphere at different temperatures: (a)1550°C, (b)1600°C, and (c) 1650°C.

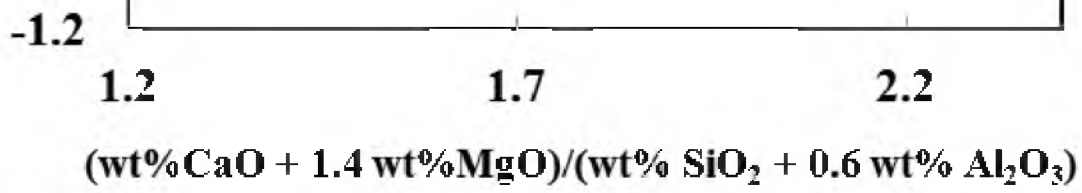

Figure 4-2. Continued.

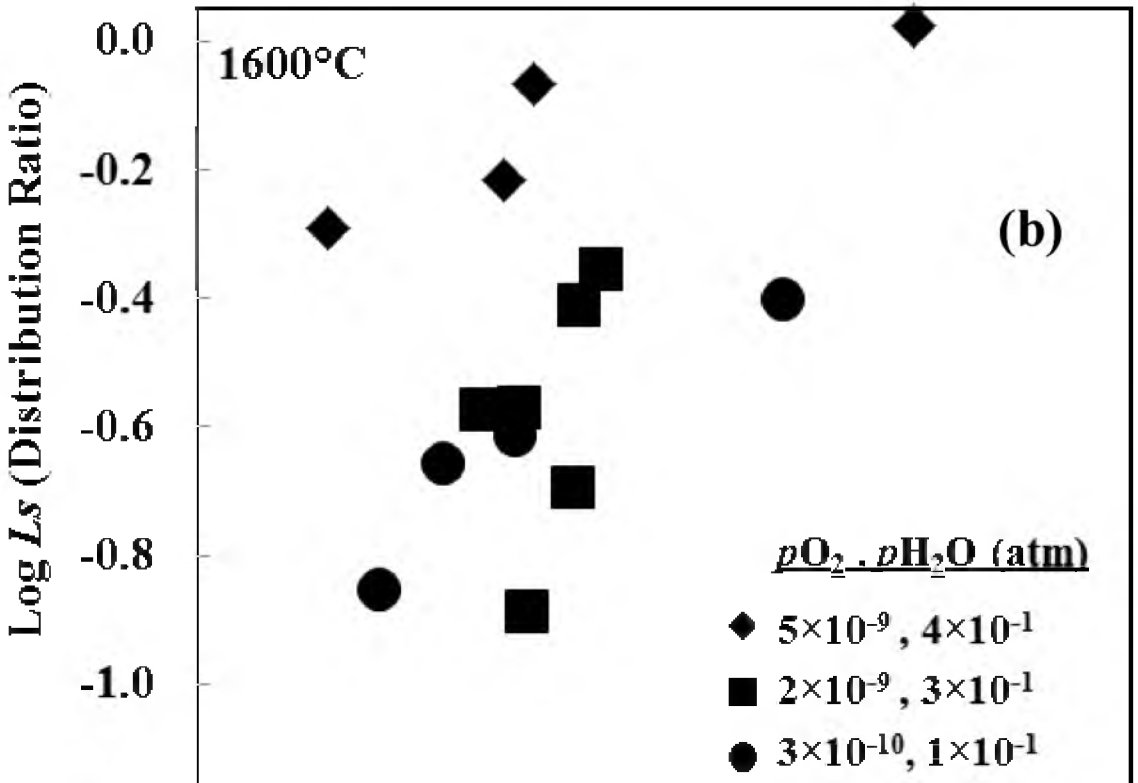
0.0
-0.2
-0.4
-0.6
-0.8
-1.0
Log Ls (Distribution Ratio)
1600°C
(b)
pO2 . pH2O (atm)
5×10-9 , 4×10-1
2×10-9 , 3×10-1
3×10-10, 1×10-1

$$(wt\%CaO + 1.4\,wt\%MgO)/(wt\%\ SiO_2 + 0.6\,wt\%\ Al_2O_3)$$

Figure 4-2. Continued.

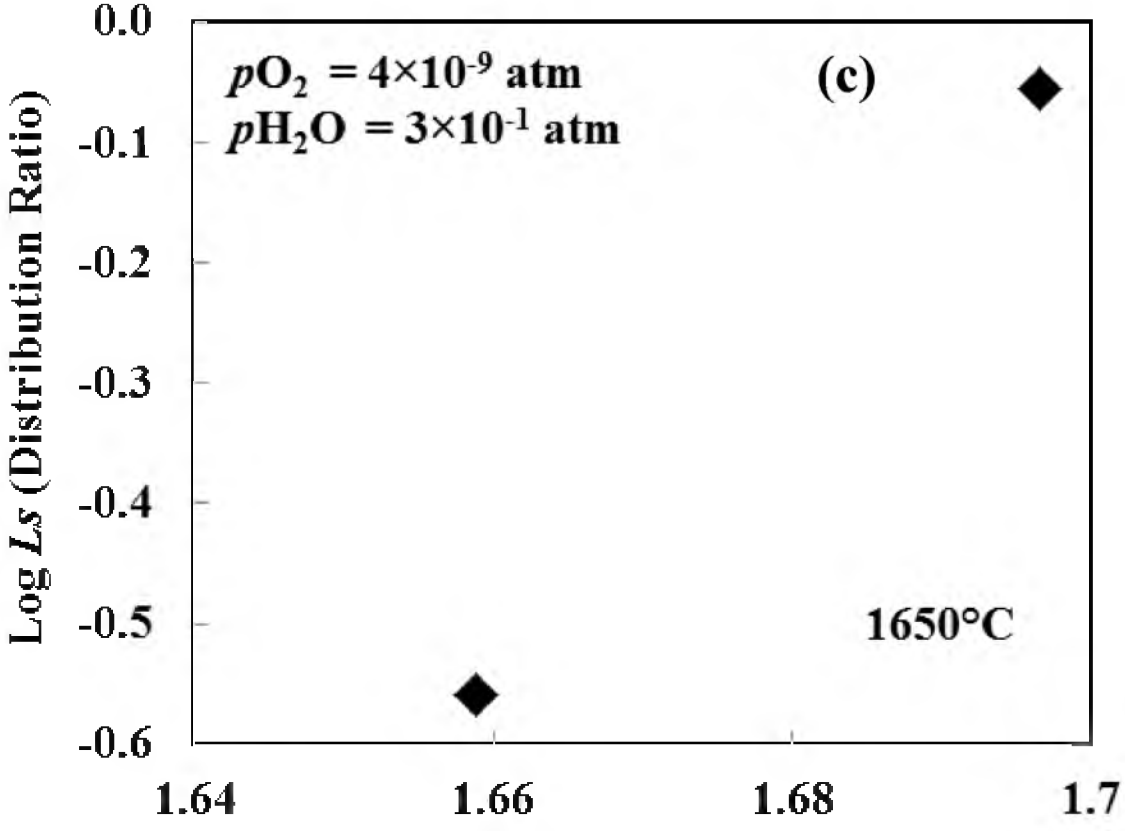
0.0
-0.1
-0.2
-0.3
-0.4
-0.5
-0.6
Log Ls (Distribution Ratio)
pO2 = 4×10-9 atm
pH2O = 3×10-1 atm
(c)
1650°C
1.64
1.66
1.68
1.7

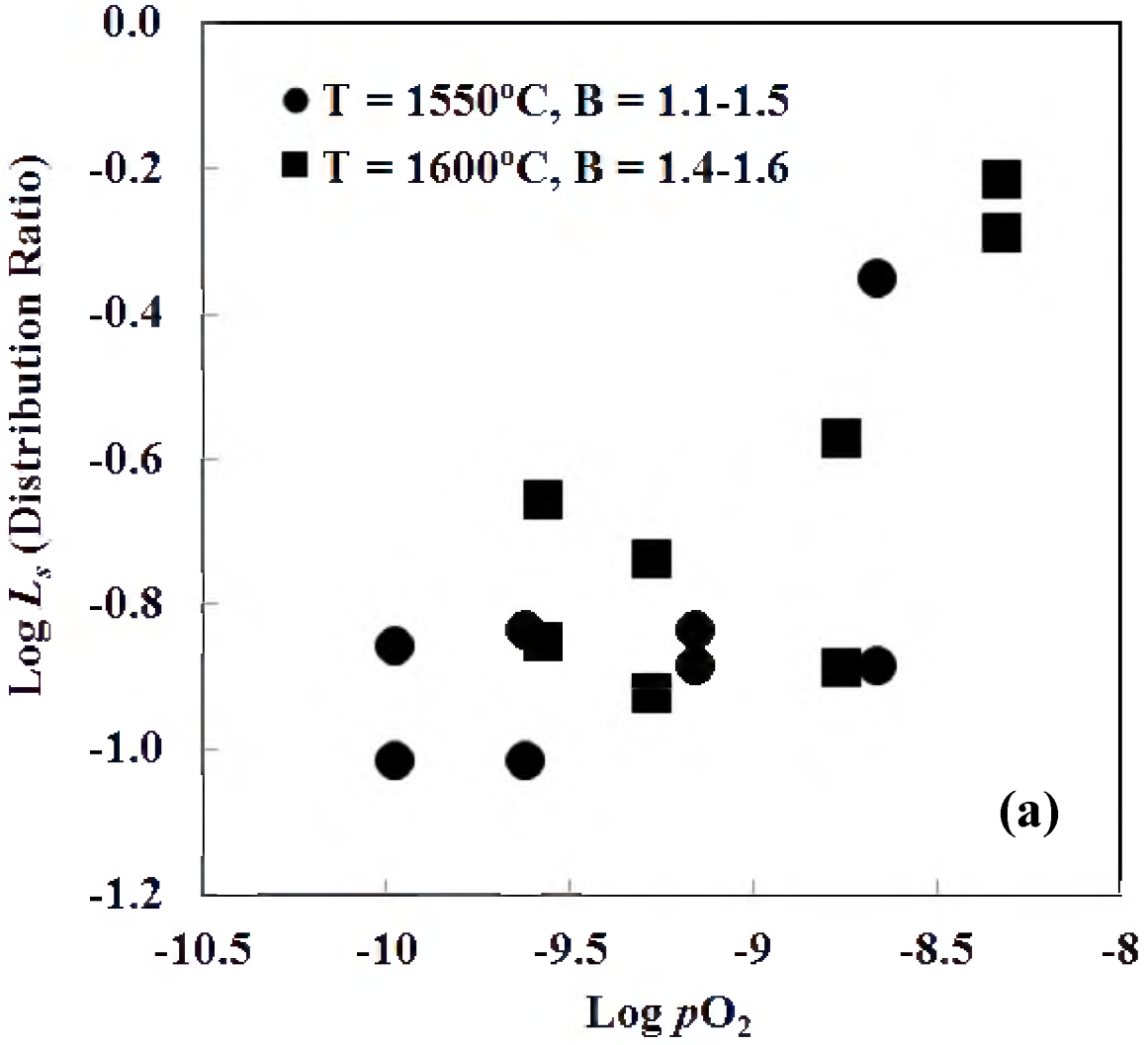

Figure 4-3. The effect of pO_2 on L_S at 1550-1600°C and pH_2O range of 0.1-0.4 atm under H_2/H_2O atmosphere in different basicity ranges: (a) 1.1-1.6 and (b) 1.3-2.5.

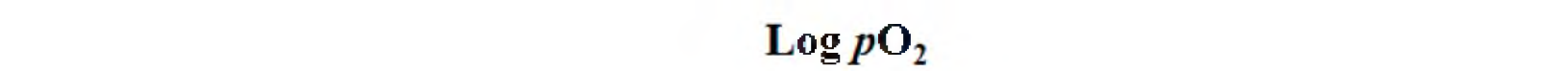

Figure 4-3. Continued.

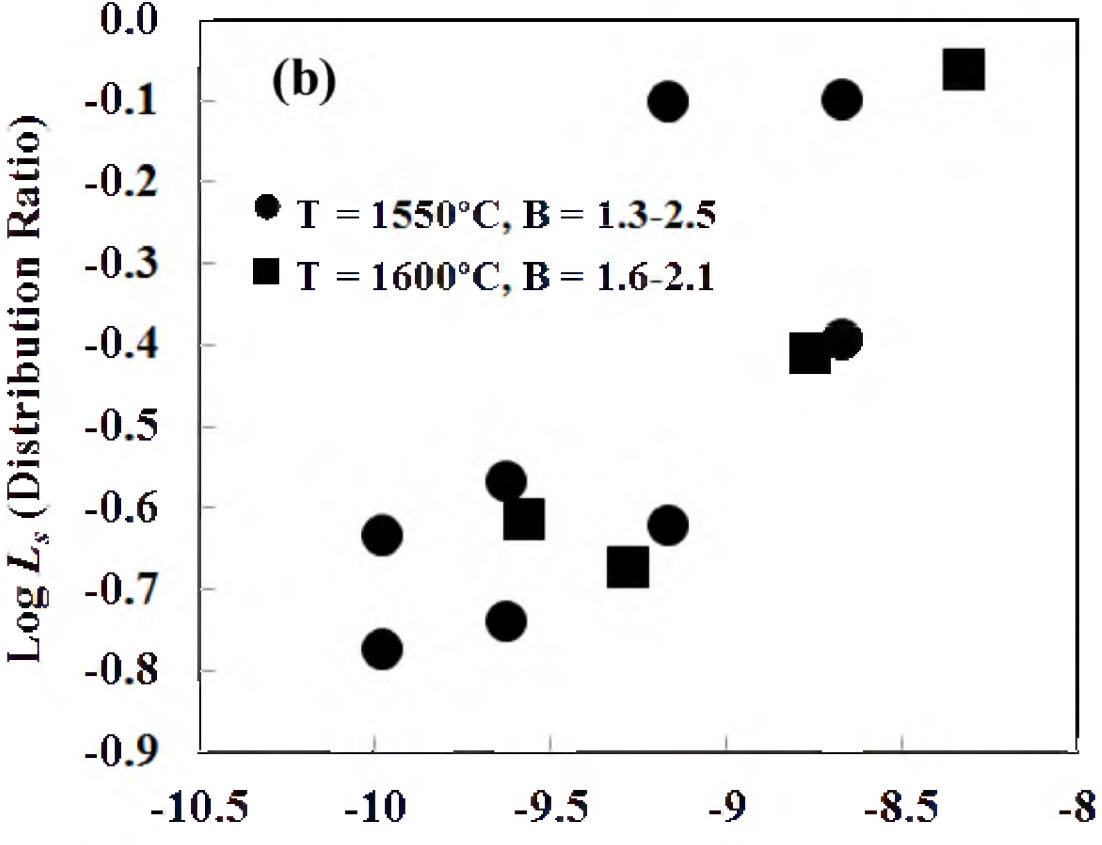
(b)
T = 1550°C, B = 1.3-2.5
T = 1600°C, B = 1.6-2.1
Log L_s (Distribution Ratio)
0.0
-0.1
-0.2
-0.3
-0.4
-0.5
-0.6
-0.7
-0.8
-0.9
-10.5
-10
-9.5
-9
-8.5
-8

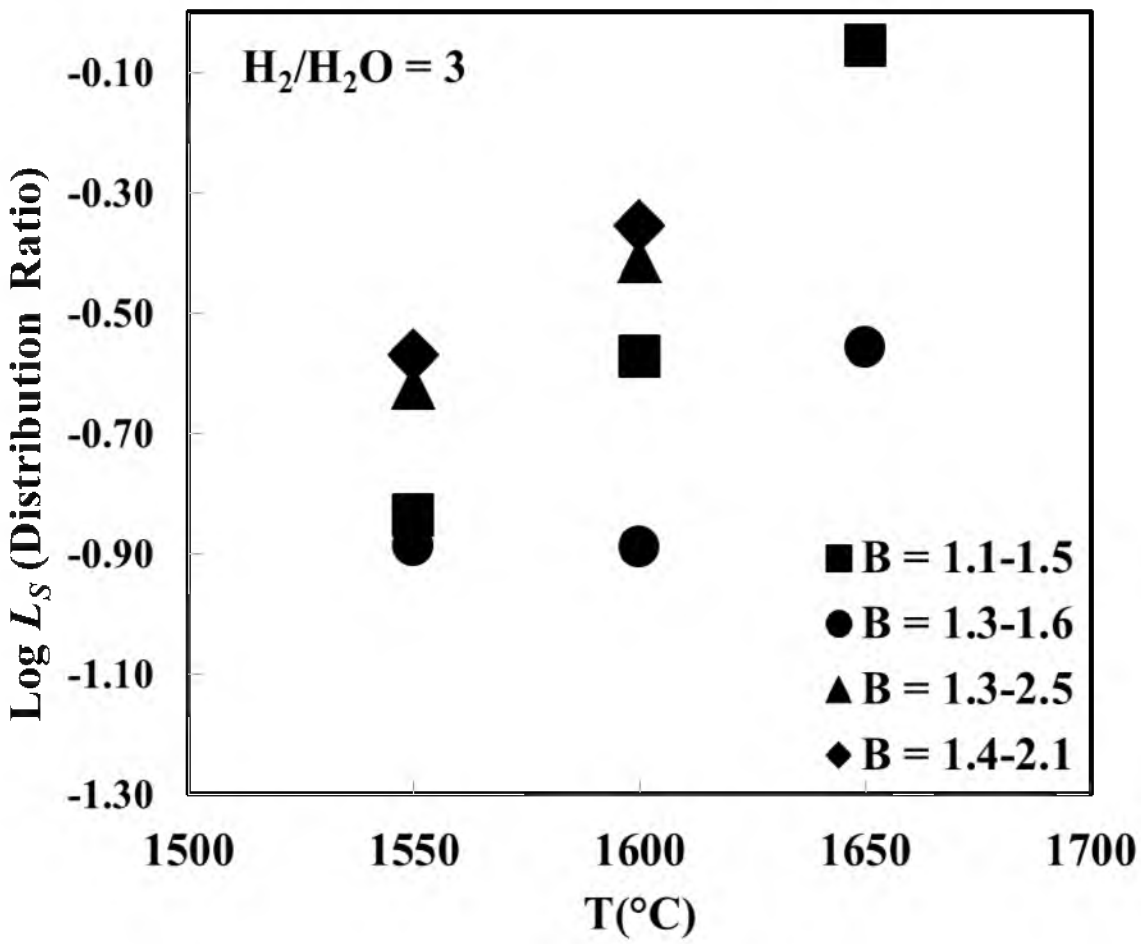

Figure 4-4. The effect of temperature on L_S at $H_2/H_2O = 3$ at different basicity ranges and $pH_2O = 0.3$ atm and pO_2 range of 7×10^{-10} - 4×10^{-9} atm.

4. 6. The Effect of Gas Composition on L_S

In the previous section, the comparison between the blast furnace (CO/CO_2) and the proposed ironmaking technology (H_2/H_2O) was based on literature for the blast furnace data and using mass balance; hence, the comparison had to be carried out through mass balance to account for the differences between slag compositions reported in literature and those used in this study, slag I. However, in this section, a slag with a closer composition the BF slag was used, slag II, and a set of experiments were carried out under the three different gas atmospheres to investigate the effect of gas composition on L_S.

Table 4-3 lists the analysis of the slag samples in addition to the oxygen partial pressures and basicity index. Figures 4-5 – 4-7 compare the effect of gas atmosphere on L_S with all the other variables fixed. It was found that L_S had the highest value of all under the H_2/H_2O atmosphere and the CO/CO_2 had the smallest L_S value, whereas the slag of $CO/CO_2/H_2/H_2O$ showed values in between the other two cases. It is noticed that this trend is similar for the three CaO/SiO_2 ratios studied: 0.8, 1.0, and 1.2.

Mysen[26] reported that the sulfide species in contact with silicate melts react with oxygen (BO) in the silicate structures as follows:

$$4Q^n + S_2 + 2M^{2+} = 4Q^{n+1} + O_2 + 2MS \qquad (4\text{-}10)$$

Therefore, the dissolution of sulfide in the slag implies the polymerization of the silicate melts. As discussed in Chapter 3, the presence of H_2O in the atmosphere of the studied

Table 4-3. The chemical analysis of the slags under the three atmospheres

Sample	Gas	T (°C)	pO_2	CaO/SiO_2	(S) (wt%)	FeO (wt%)	MgO (wt%)	CaO (wt%)	Al_2O_3 (wt%)	SiO_2 (wt%)	L_S
R10	$CO/CO_2/H_2/H_2O$	1550	1.9×10^{-9}	0.8	0.057	21.7	24.6	20.3	13.0	25.5	1.33
R19		1550	1.6×10^{-10}	0.8	0.039	10.1	24.4	26.2	16.3	34.8	1.60
R20		1550	1.6×10^{-10}	1	0.057	9.8	17.9	30.7	8.4	31.8	1.96
R21		1550	1.6×10^{-10}	1.2	0.044	10.8	16.8	33.5	18.8	29.8	2.54
R22		1600	3.6×10^{-10}	0.8	0.040	13.0	23.4	26.0	15.7	32.3	2.96
R23		1600	3.6×10^{-10}	1	0.043	12.7	19.2	30.0	17.0	30.9	2.74
R24		1600	3.6×10^{-10}	1.2	0.044	12.4	16.6	32.8	17.2	28.6	3.27
R27		1630	6.4×10^{-10}	1.2	0.044	11.2	19.2	30.1	17.0	30.5	2.04
R46	CO/CO_2	1550	1.6×10^{-10}	0.8	0.046	35.5	10.2	24.5	13.9	22.8	0.96
R48		1550	1.6×10^{-10}	1.2	0.051	16.9	26.2	26.3	15.0	23.6	0.56
R49		1600	3.6×10^{-10}	0.8	0.057	14.7	22.1	25.7	15.2	31.9	0.46
R50		1600	3.6×10^{-10}	1	0.068	16.9	16.9	28.5	15.2	29.4	1.42
R51		1600	3.6×10^{-10}	1.2	0.059	15.3	14.7	30.7	16.6	26.7	1.42
R52		1630	6.4×10^{-10}	0.8	0.064	13.7	15.7	24.7	23.4	32.9	1.86
R53		1630	6.4×10^{-10}	1	0.061	14.6	14.3	28.0	17.0	36.4	0.93
R54		1630	6.4×10^{-10}	1.2	0.047	26.4	14.8	25.2	14.3	27.4	0.62
R74	H_2/H_2O	1550	1.6×10^{-10}	1	0.052	9.9	20.7	34.9	5.1	27.8	3.84
R75		1550	1.6×10^{-10}	1.2	0.075	9.6	19.7	31.2	17.1	32.1	3.33
R78		1600	3.6×10^{-10}	1.2	0.041	10.5	16.1	33.7	17.7	29.5	7.78
R'78		1600	3.6×10^{-10}	1.2	0.046	9.5	16.9	33.8	18.1	29.6	4.88

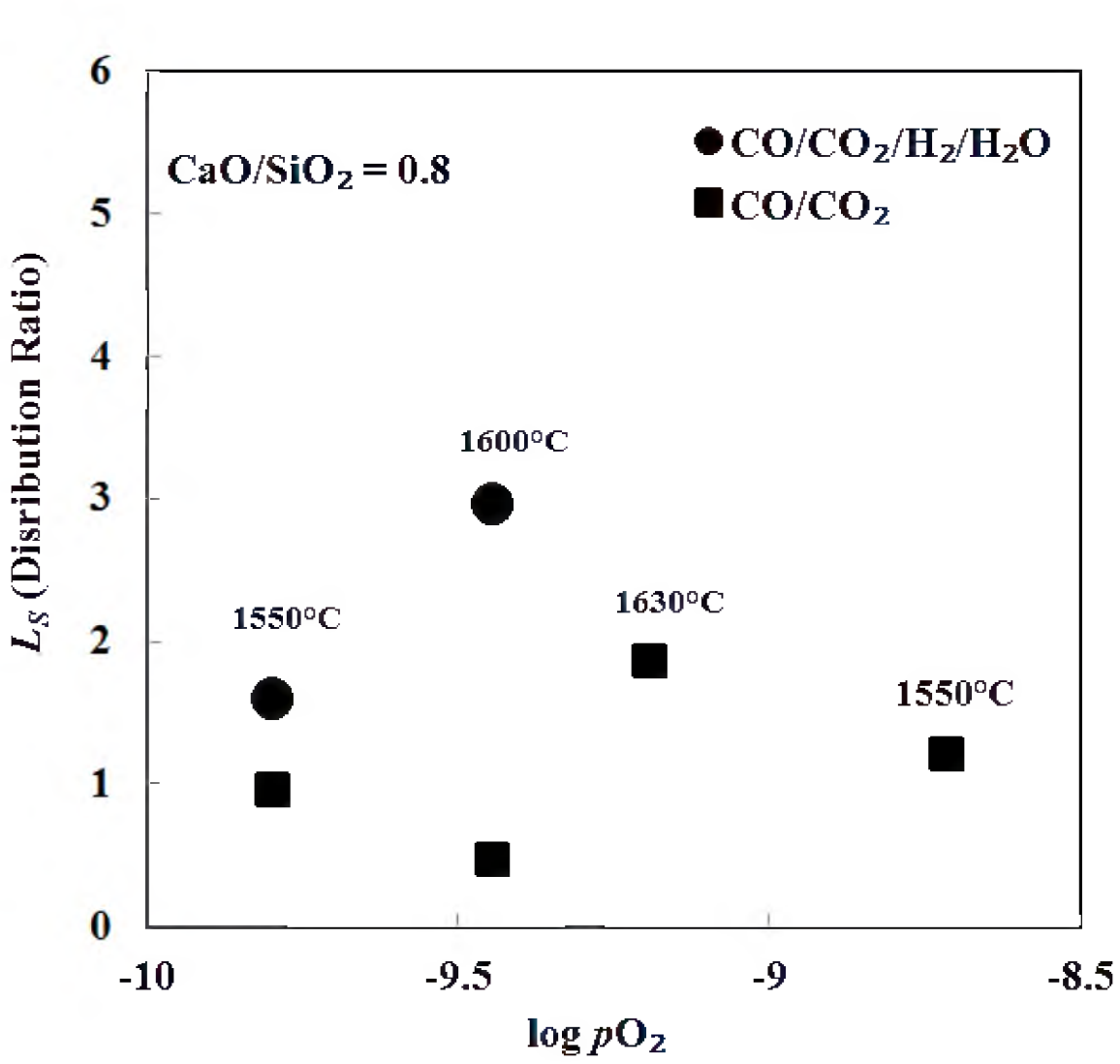

Figure 4-5. The effect of different gas atmospheres on L_S at different pO_2 and temperature values for slags with wt% CaO/ wt% SiO_2 of 0.8 and pH_2O of 0 and 0.1 atm in CO/CO_2 and $H_2/H_2O/CO/CO_2$, respectively.

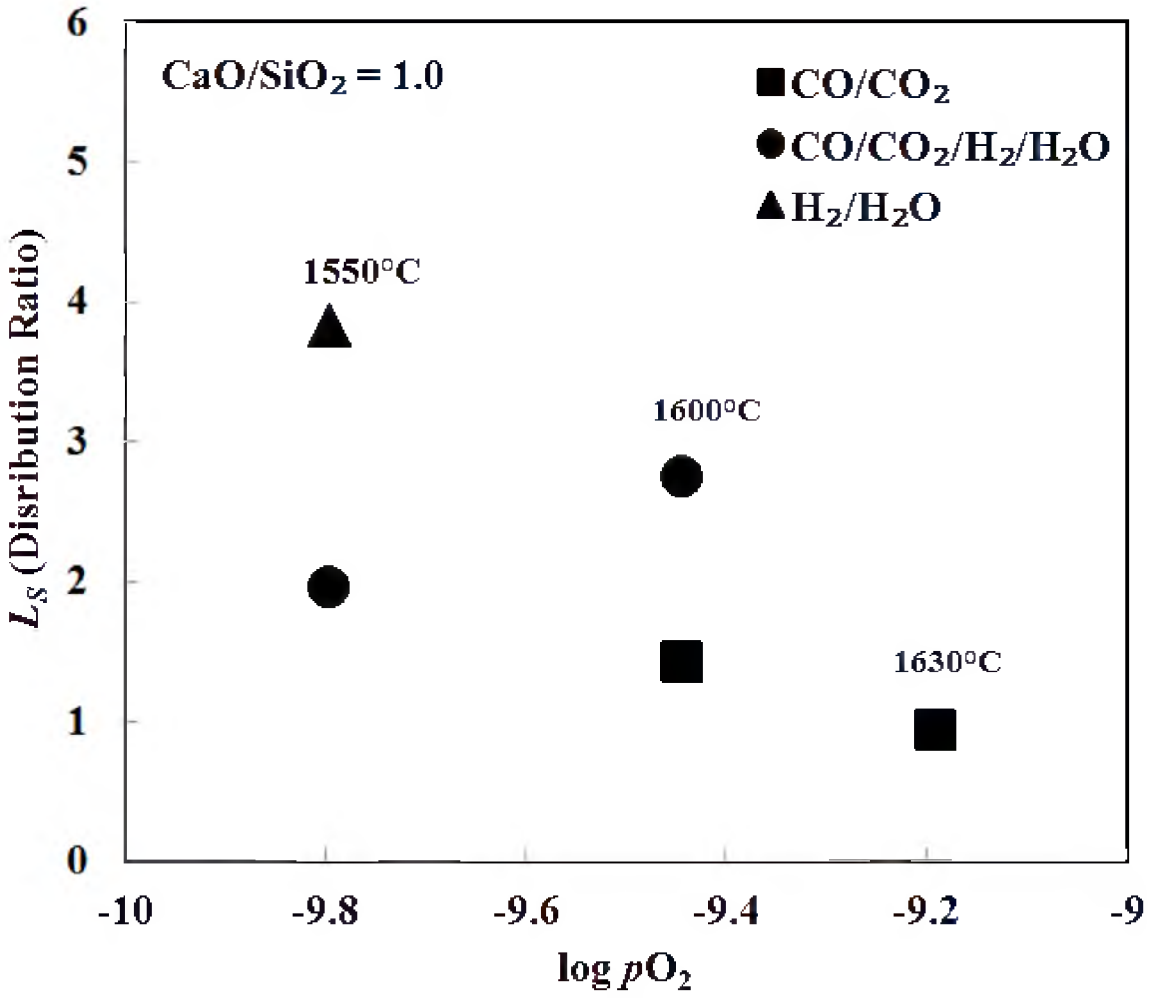

Figure 4-6. The effect of different gas atmospheres on L_S at different pO_2 and temperature values for slags with wt% CaO/ wt% SiO_2 of 1.0 and pH_2O of 0, 0.1, and 1.0 atm in CO/CO_2, $H_2/H_2O/CO/CO_2$, and $H_2/H_2O/CO$, respectively.

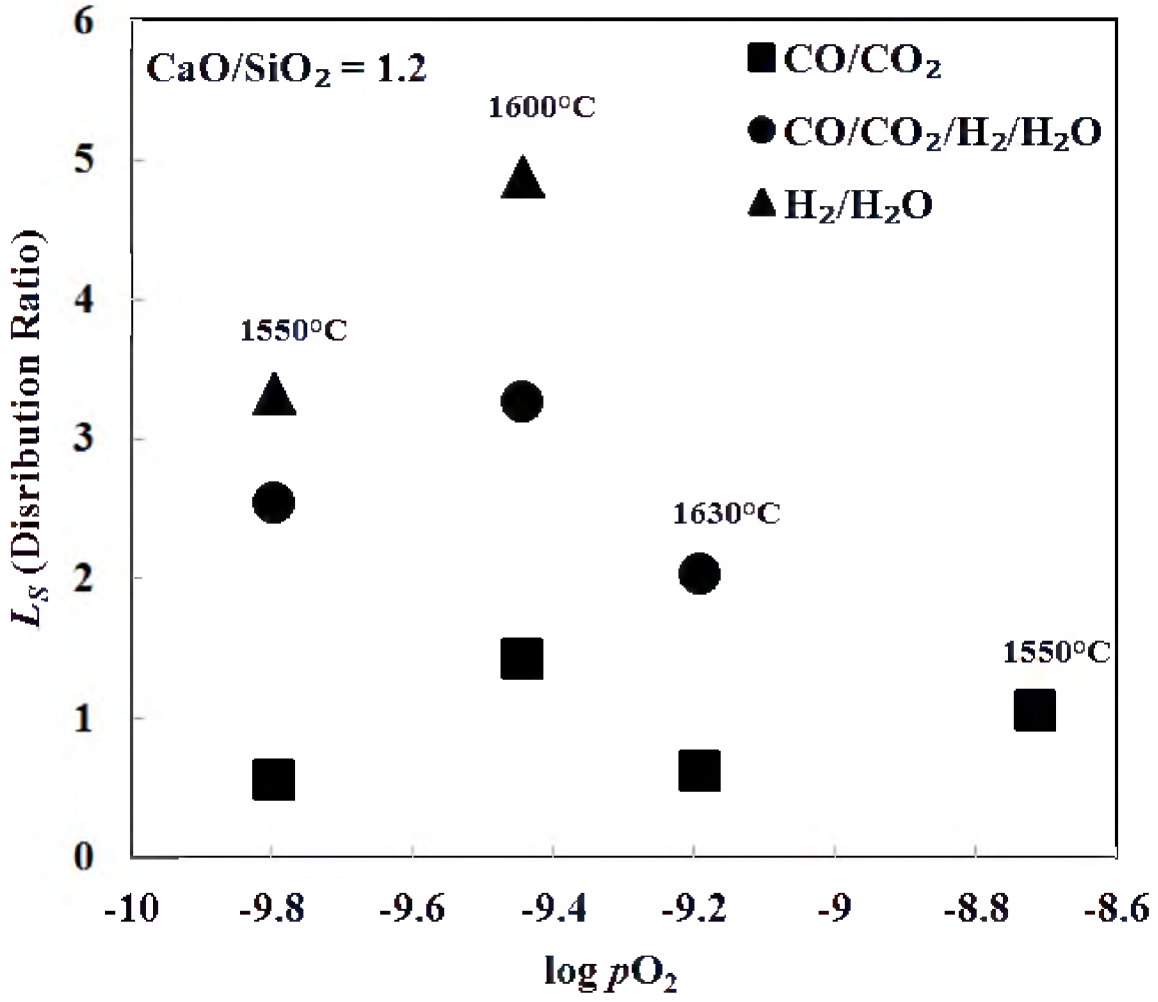

Figure 4-7. The effect of different gas atmospheres on L_S at different pO_2 and temperature values for slags with wt% CaO/ wt% SiO_2 of 1.2 and pH_2O of 0, 0.1, and 1.0 atm in CO/CO_2, $H_2/H_2O/CO/CO_2$, and $H_2/H_2O/CO$, respectively.

slags tends to polymerize the silicate structures in the slag. As a result, the sulfide species in the slag are expected to be more stable under H_2/H_2O. In other words, H_2O decreases the activity coefficient of S^{2-} ($f_{S^{2-}}$) in the studied slags, thus increasing the S wt% in the slag according to eqs 4-4 and 4-5. That explains the order of slag sulfide capacity where H_2/H_2O> $CO/CO_2/H_2/H_2O$> CO/CO_2. At constant pO_2, CaO/SiO2, and temperature, L_S increased with pH_2O, as Figures 4-8 – 4-9 show. That ensures the effect of H_2O on the sulfur distribution, which cannot be overlooked.

The representative L_S values under the three gas atmospheres were extracted from MgO-saturated CaO-FeO-Al_2O_3-SiO_2-MnO (0.2-0.8 wt%)-P_2O_5 (0.1-0.9 wt%), in the temperature range 1550-1600°C, with CaO/SiO_2 of 0.8 to 1.2, and under $pO_2 = 2\times10^{-10}$~2×10^{-9} atm. The average L_S was found to be 1.0 (0.46~1.42), 2.3 (1.33~3.27), and 5.0 (3.33~7.78) under CO/CO_2 (blast furnace, BF), $CO/CO_2/H_2/H_2O$ (natural/coal gas, NG/CG), and H_2/H_2O (hydrogen, H_2), respectively. These values were further used to compare the effects of the three reductant gases using material balance, as will be discussed in Section 4.7.

4. 7. Blast Furnace versus the Flash Ironmaking Technology

There was a previous attempt to compare L_S under H_2/H_2O atmosphere with that of the BF.[1] In that comparison, the latter L_S was extracted from literature. Due to the differences in the experimental conditions and slag composition, the comparison was approximate. In the following text, the current results under CO/CO_2 will be used to represent BF conditions, using the obtained average L_S of 1.0 (CO/CO_2) to represent the BF conditions.

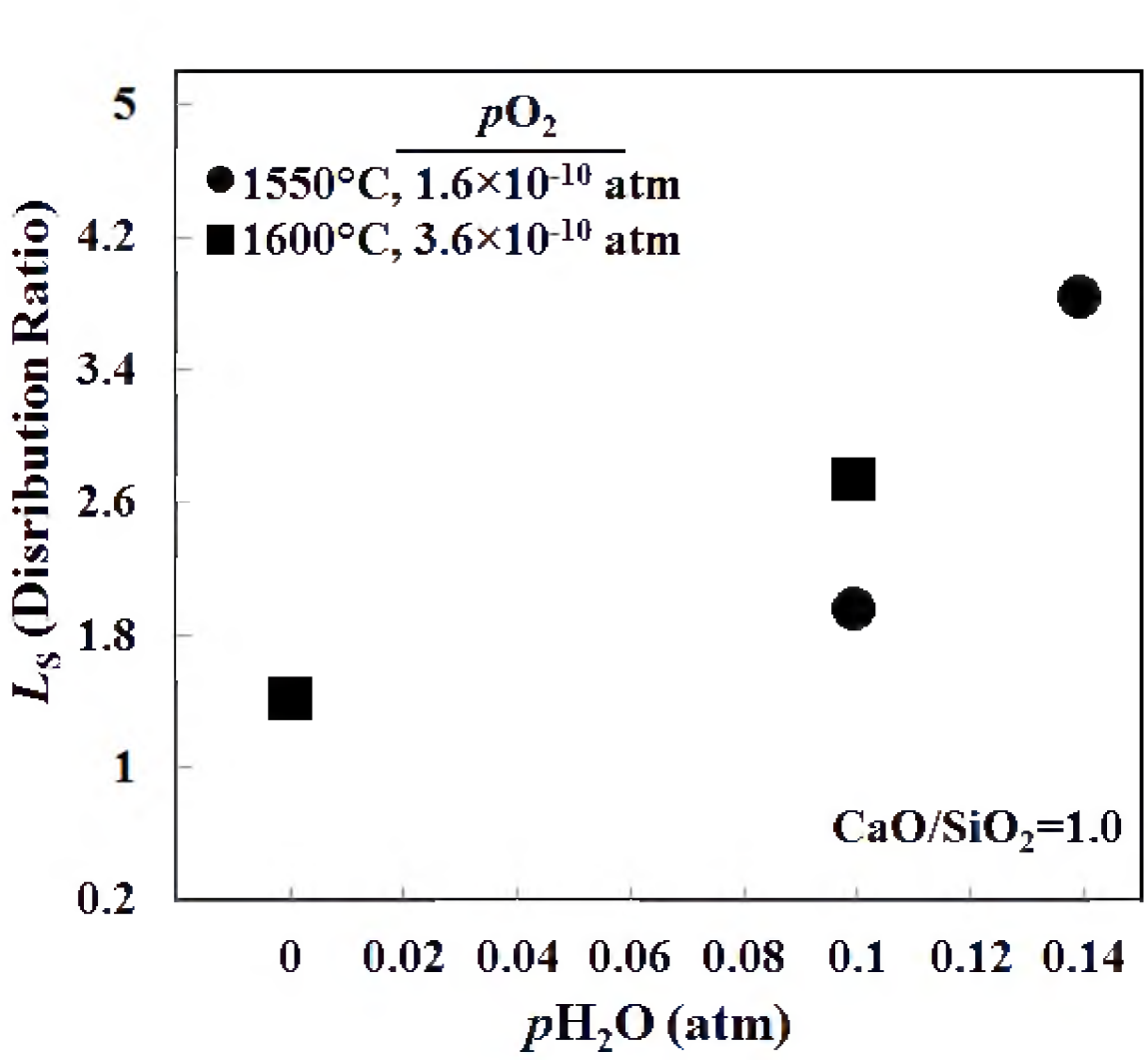

Figure 4-8. The influence of pH_2O on L_S at wt% CaO/ wt% SiO_2 of 1.0 at different temperatures and pO_2.

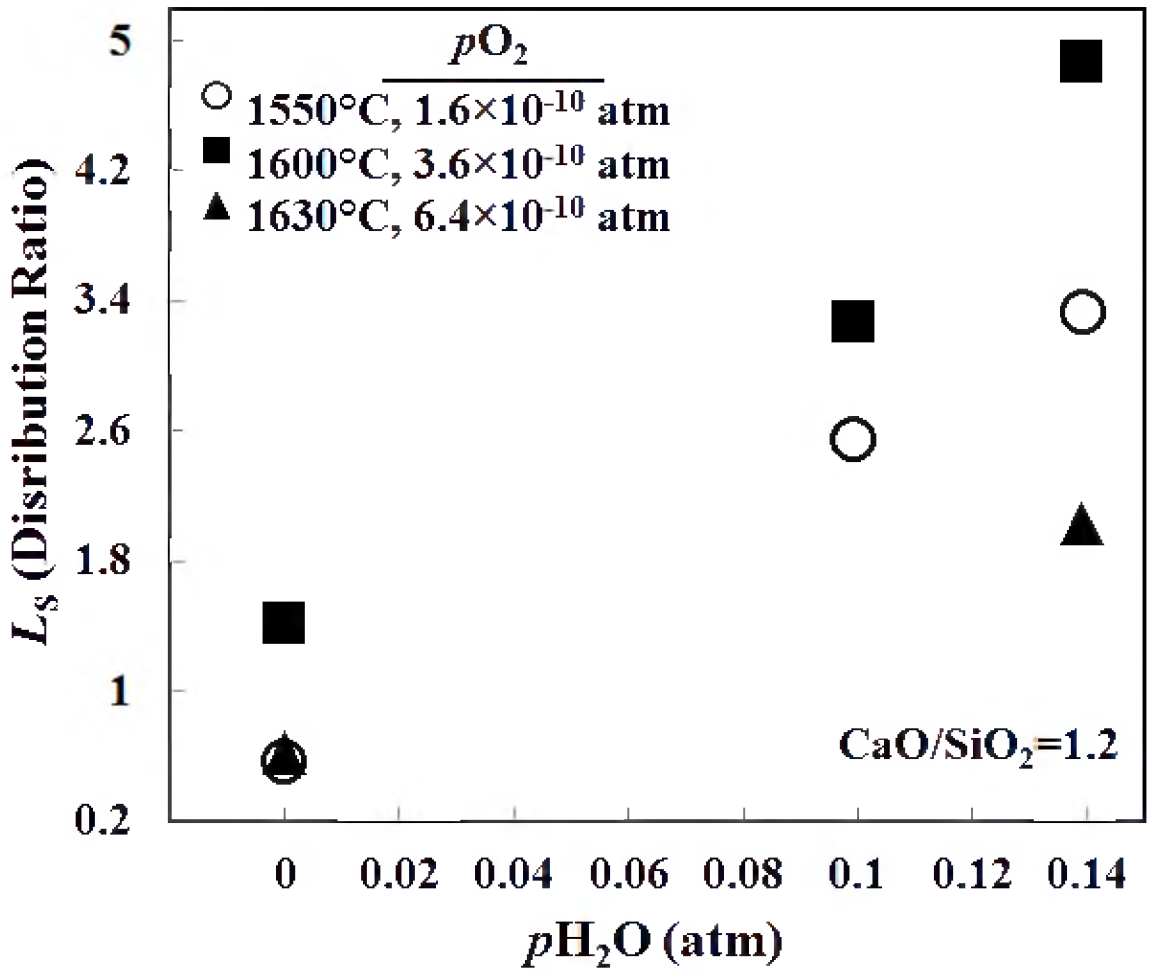

Figure 4-9. The influence of pH_2O on L_S at wt% CaO/ wt% SiO_2 of 1.2 at different temperatures and pO_2.

In the proposed process, sulfur comes only from the ore at approximately 0.02 wt% content,[28] whereas in the current blast furnace process, coke is another source of sulfur, with an average of 0.9 wt% content.[29] In addition to the low sulfur input from raw materials, a significant amount of sulfur will volatilize during the downward flight of the particles in the proposed flash reactor.[30] To obtain an approximate extent of volatilization, a representative sample was analyzed for sulfur before and after reduction in a simulated run for the proposed process. It was found that over 30 wt% of the sulfur in the ore was lost during particle flight.

The wt% of S in the reduced iron is related to L_S by the following relationship obtained from materials balance:

$$[wt\%S]=\frac{t}{(a\cdot L_S)+1}\times 100 \qquad (4\text{-}11)$$

where

$[wt\%S]$: sulfur weight percentage in produced iron,

t : total sulfur input per ton of iron, and

a : slag/metal mass ratio.

In the proposed process, L_S = 5.0 and 2.3 (H_2/H_2O and $CO/CO_2/H_2/H_2O$, respectively) versus 1.0 in BF (CO/CO_2), and t = 0.1 kg/ton iron (considering that 30 wt% sulfur in the ore will volatilize in the furnace shaft) versus 3.9 kg/ton iron in the blast furnace (using ore with 0.02 wt% sulfur content and coke with 0.9 wt%). Assuming the same slag/metal ratio of 0.3 as in the blast furnace, the wt% S in the metal from the

proposed process would be approximately 0.004 and 0.006 under H_2/H_2O and $CO/CO_2/H_2/H_2O$. In contrast, the *wt% S* in the blast furnace hot metal is calculated to be 0.3 %, using a typical coke-to-iron ratio of 0.4. This range of sulfur content is within the reported range for typical blast hot metal.[29] Figure 4-10 summarizes the L_S and the [wt% S] under the three gas environments, referring to CO/CO_2, H_2/H_2O, and $CO/CO_2/H_2/H_2O$ as BF, H_2, and natural/coal gas (NG/CG), respectively. The L_S and the S wt% values were normalized relative to those under BF conditions.

4. 8. Conclusions

For the slag compositions investigated, MgO-saturated CaO-FeO-Al_2O_3-SiO_2-MnO (0.2-0.8 wt%)-P_2O_5 (0.1-0.9 wt%), in the temperature range 1550-1600°C, with wt% CaO/wt% SiO_2 of 0.8 to 1.2, and under $pO_2 = 2\times10^{-10} \sim 2\times10^{-9}$ atm, the average L_S was found to be 1.0, 2.3, and 5.0 under CO/CO_2 (blast furnace, BF), $CO/CO_2/H_2/H_2O$ (natural/coal gas, NG/CG), and H_2/H_2O (hydrogen, H_2), respectively. These values were used as representative averages to compare the three reductants. In other words, H_2 causes the highest L_S of all the reducing agents. H_2 showed 400% enhancement in L_S, whereas NG/CG exhibited 130% improvement compared with the BF.

For a more meaningful comparison, if an iron ore was reduced by the three different routes, the hot metal produced by H_2 and NG/CG would have two orders of magnitude lower sulfur contents than in the BF conditions. This comparison was based on materials balance using iron ore with 0.02 wt% S in addition to coke, which comes with an average of 0.9 wt% S in the BF. In addition to the difference in S input between the Sohn process and the blast furnace, another important difference is the volatilization

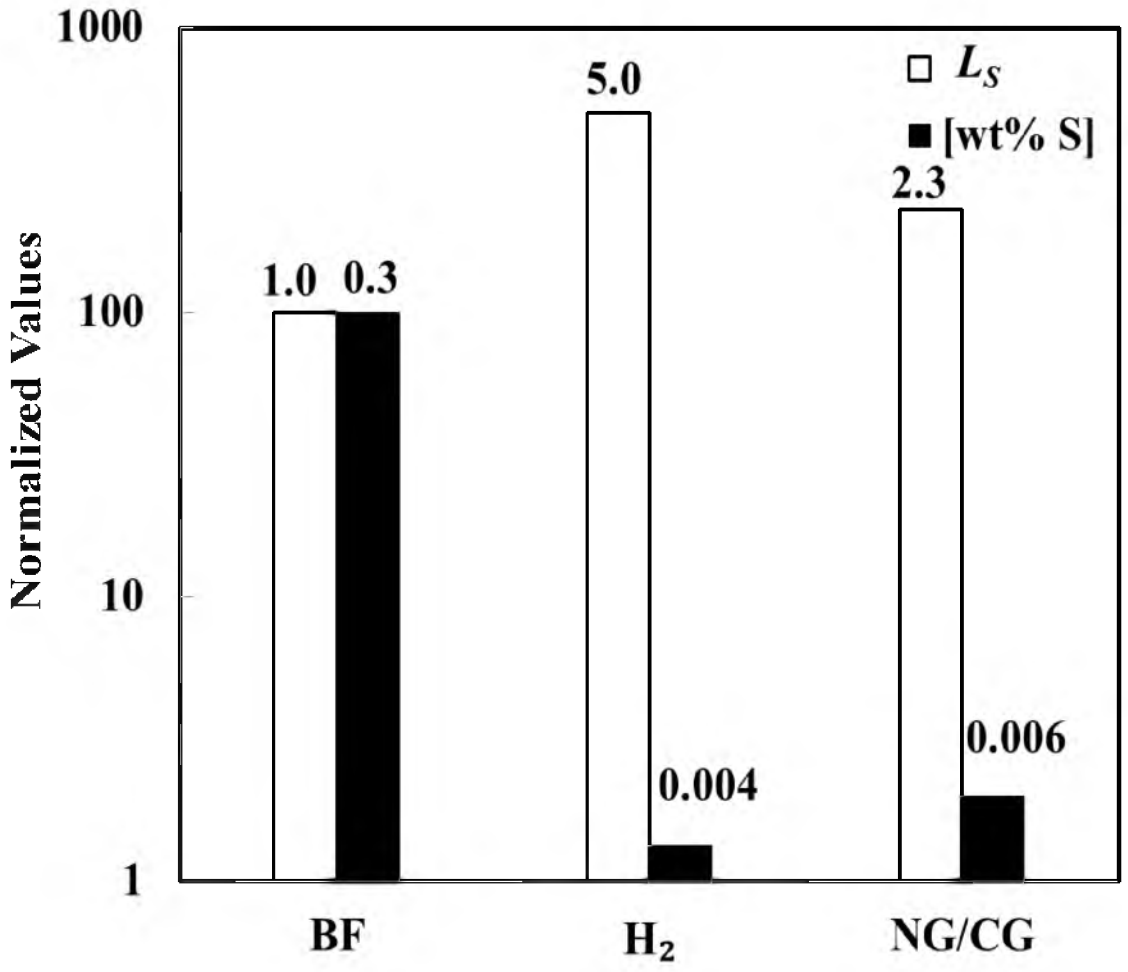

Figure 4-10. The effect of the type of reductant gas on L_S. The labels show the values of L_S and [wt% S]. (Note: ordinate in logarithmic scale)

of ~30 wt% S during the downward flight of the particles in the reactor shaft in the latter process, which was also considered in the calculations. The slag/metal ratio was kept at the same value of 0.3 in all the three routes.

4. 9. References

(1) Kang, Y.; Pelton, A. Thermodynamic Model and Database for Sulfides Dissolved in Molten Oxide Slags. *Metall. Mater. Trans. B* **2009**, *40*, 979-994.

(2) Taniguchi, Y. Sulphide Capacities of $CaO-Al_2O_3-SiO_2-MgO-MnO$ Slags in the Temperature Range 1 673 - 1 773K. *ISIJ Int.* **2009**, *49*, 156-163.

(3) Shankar, A.; Görnerup, M.; Seetharaman, S.; Lahiri, A. Sulfide capacity of high alumina blast furnace slags. *Metall. Mater. Trans. B* **2006**, *37*, 941-947.

(4) Hayakawa, H.; Hasegawa, M.; Oh-nuki, K.; Sawai, T.; Iwase, M. Sulphide capacities of $CaO-SiO_2-Al_2O_3-MgO$ slags. *Steel Res. Int.* **2006**, *77*, 14-20.

(5) Ban-Ya, S. Sulphide Capacity and Sulphur Solubility in $CaO-Al_2O_3$ and $CaO-Al_2O_3$ CaF_2 Slags. *ISIJ Int.* **2004**, *44*, 1810-1816.

(6) Seo, J. D.; Kim, S. H. The sulphide capacity of $CaO-SiO_2-Al_2O_3-MgO(-FeO)$ smelting reduction slags. *Steel Res. Int.* **1999**, *70*, 203-208.

(7) Nzotta, M.; Sichen, D.; Seetharaman, S. A study of the sulfide capacities of iron-oxide containing slags. *Metall. Mater. Trans. B* **1999**, *30*, 909-920.

(8) Ban-Ya, S.; Hino, M.; Sato, A.; Terayama, O. Oxygen, phosphorus, and sulfur distribution equilibria between liquid iron and calcium oxide-alumina-iron oxide slag saturated with calcia. *Tetsu to Hagane* **1991**, *77*, 361-368.

(9) Tsao, T. Sulphur distribution between liquid iron and $CaO-MgO-Al_2O_3-SiO_2$ slags used for ladle refining. *Trans. Iron Steel Inst. Jpn.* **1986**, *26*, 717-723.

(10) Kor, G.; Richardson, F. Sulfur in lime-alumina mixtures. *J. Iron Steel Inst.* **1968**, *206*, 700–704.

(11) Sohn, H. Y.; Choi, M. E.; Zhang, Y.; Ramos, J. E. Suspension reduction technology for ironmaking with low CO_2 emission and energy requirement. *Iron steel Tech.* **2009**, *6*, 158-165.

(12) Fincham, C.; Richardson, F. The behaviour of sulphur in silicate and aluminate melts. *Proc. Royal Soc. Lond. A* **1954**, 40-62.

(13) Richardson, F. D. *Physical chemistry of melts in metallurgy*, Academic Press UK: **1974**; Vol. 2.

(14) Karsrud, K. Alkali capacities of synthetic blast furnace slags at 1500 ^{0}C. *Scand. J. Metall.* **1984**, *13*, 98-106.

(15) Young, R.; Duffy, J.; Hassall, G.; Xu, Z. Use of optical basicity concept for determining phosphorus and sulphur slag-metal partitions. *Ironmaking Steelmaking* **1992**, *19*, 201-219.

(16) Fruehan, R. *The making, shaping and treating of. steel*, The AISE Steel Foundation, 11th edition: Pittsburgh, 1998.

(17) Nzotta, M. M.; Nilsson, R.; Sichen, D.; Seetharaman, S. Sulfide capacities in $MgO-SiO_2$ and $CaO-MgO-SiO_2$ slags. *Ironmaking Steelmaking* **1997**, *24*, 300-305.

(18) Osborn, E. F.; DeVries, R. C.; Gee, K. H.; Kraner, H. M. Optimum composition of blast-furnace slag as deduced from liquidus data for the quaternary system $CaO-MgO-Al_2O_3-SiO_2$. *J. Met.* **1954**, *6*, 33-45.

(19) Pak, J. J.; Fruehan, R. J. Soda slag system for hot metal dephosphorization. *Metall. Trans. B* **1986**, *17B*, 797-804.

(20) Basu, S.; Lahiri, A.; Seetharaman, S. Phosphorus Partition between Liquid Steel and $CaO-SiO_2-P_2O_5-MgO$ Slag Containing Low FeO. *Metall. Mater. Trans. B* **2007**, *38*, 357-366.

(21) Brandberg, J.; Yu, L.; and Sichen, D. Water capacity model of $Al_2O_3-CaO-MgO-SiO_2$ quaternary slag system. *Steel Res. Int.* **2007**, *78*, pp. 460-464.

(22) Nzotta, M.; Sichen, D.; Seetharaman, S. Sulphide capacities in some multi component slag systems. *ISIJ international* **1998**, *38*, 1170-1179.

(23) Nilsson, R.; Nzotta, M. M.; Sichen, D.; Seetharaman, S. Determination of the sulfide capacities of multicomponent slag systems by gas/slag equilibration method, *5th Int. Conf. on Molten Slags, Fluxes and Salts.* **1997**, 177-190.

(24) Sosinsky, D. J.; Sommerville, I. The composition and temperature dependence of the sulfide capacity of metallurgical slags. *Metall. Mater. Trans. B* **1986**, *17*, 331-337.

(25) Shankar, A. Sulphur partition between hot metal and high alumina blast furnace slag. *Ironmaking Steelmaking* **2006**, *33*, 413-418.

(26) Mysen, B. O.; Richet, P. *Silicate glasses and melts: Properties and structure*. Elsevier Science Limited, **2005**.

(27) Mohassab-Ahmed, M. Y.; Sohn, H. Y.; Kim, H. G., Sulfur distribution between liquid iron and magnesia-saturated slag in H_2/H_2O atmosphere relevant to a novel green ironmaking technology. *Ind. Eng. Chem. Res.* **2012,** *51*, 3639-3645.

(28) Zhang, Y. *Bench-scale flash reduction on iron ore concentrate.* M.S. Thesis, University of Utah, Salt Lake City, Utah, USA, **2008**.

(29) Habashi, F. *Handbook of Extractive Metallurgy.* Wiley-VCH: Weinheim, **1997**, Vol. *I*, p 53.

(30) Sohn, H. Y.; Choi, M. E.; Olivas-Martinez, M.; Kim, H. G. A Novel Flash Ironmaking Process. *Proceedings of Cleantech 2011*, Budapest, Hungary International Conference on Clean Technologies in the Steel Industry, Budapest, Hungary, September 26-28, **2011**.

CHAPTER 5

PHOSPHORUS DISTRIBUTION BETWEEN LIQUID IRON AND MAGNESIA-SATURATED SLAG IN $CO/CO_2/H_2/H_2O$ ATMOSPHERES RELEVANT TO A NOVEL FLASH IRONMAKING TECHNOLOGY

5.1. Introduction

Reducing the phosphorus content in steel is one of the critical factors to enhance the steel properties. Since the 1940s, researchers have worked on the distribution of phosphorus between hot metal or steel and slag.[1-3] These researchers used Ar,[3-5] Ar-CO mixture,[6-8] CO,[9] CO/CO_2,[10] or N_2/CO[11] for the gas phase. Others worked on theoretical thermodynamics and modeling approaches.[6,12-20]

This research was a part of an on-going research project that aims to develop a novel green ironmaking process based on the direct gaseous reduction of iron oxide concentrates in a suspension reduction process, with the ultimate goal of significantly reducing CO_2 emission, energy consumption, and environmental pollution in the steel industry.[21] This research was carried out because there is no previous research on phosphorus distribution under H_2O-conating atmosphere relevant to a Flash ironmaking process. For comparison, a set of experiments were conducted under CO/CO_2 resembling the blast furnace conditions and hence used as the reference system.

The distribution of phosphorus between liquid metal and slag is determined by the equilibrium of the following reaction[22]:

$$2[P]+5(FeO)+3(CaO)=(3CaO\cdot P_2O_5)+5[Fe] \qquad (5\text{-}1)$$

$$\log(K_P\times10^{-5})=\log\left\{\frac{(3CaO.P_2O_5)}{[P]^2(FeO)^5(CaO)^3}\times10^{-5}\right\}$$
$$=\left(\frac{1}{1.322}\right)\left\{\left(\frac{1}{1.8\times T}\times10^5\right)-28.52\right\} \qquad (5\text{-}2)$$

where K_P is the equilibrium constant; T is the temperature in Kelvin; [ ] and ( ) represent weight % in the metal and slag phases, respectively.

The phosphorus distribution ratio, L_P, between slag and metal is defined as:

$$L_P=\frac{(\%P)}{[\%P]}=\frac{0.4364\cdot(\%P_2O_5)}{[\%P]} \qquad (5\text{-}3)$$

where (%P) = wt% of phosphorus dissolved in slag and [%P] = wt% of phosphorus dissolved in metal.

To express the effect of slag composition on L_P, phosphorus pentoxide activity coefficient needs to be determined. Turkdogan and Pearson[23] estimated the equilibrium constant of reaction:

$$2[P] + 5[O] = (P_2O_5), \qquad \log K_P = 37160/T - 29.67 \qquad (5\text{-}4)$$

Combining reaction 5-4 with the following reaction[24]:

$$\frac{5}{2}O_2 = 5[O] \qquad \Delta G^\circ = 140000 - 3.45T \ cal/mol \tag{5-5}$$

$$2[P] + \frac{5}{2}O_2 = (P_2O_5) \qquad \Delta G^\circ = -209985.36 + 132.22T \quad cal/mol \tag{5-6}$$

The equilibrium constant for reaction 5-6 can be expressed as:

$$K_P = \frac{a_{P_2O_5}}{(pO_2)^{5/2} \times a_P^2} = \frac{\gamma_{P_2O_5} \times x_{P_2O_5}}{(pO_2)^{5/2} \times ([\%P] f_P)^2} \tag{5-7}$$

where

$a_{P_2O_5}$: P_2O_5 activity

a_P : Henrian activity of P

pO_2 : oxygen partial pressure

$\gamma_{P_2O_5}$: Raoultian activity coefficient of P_2O_5

$x_{P_2O_5}$: mole fraction of P_2O_5

f_P : Henrian activity coefficient of phosphorus

Therefore, after substituting $f_P = 1$, for low concentrations of P, the Raoultian activity coefficient of P_2O_5 can be obtained from

$$\gamma_{P_2O_5} = \frac{K_P \times (pO_2)^{5/2} \times [\%P]^2}{x_{P_2O_5}} \qquad (5\text{-}8)$$

In this study, the following ratio (B) was used to correlate the phosphorus distribution ratio:

$$\frac{wt\%CaO}{wt\%SiO_2} \qquad (5\text{-}9)$$

The following more general expression of slag basicity was also tried[25]:

$$\frac{wt\%CaO + 1.4 \times wt\%MgO}{wt\%SiO_2 + 0.6\, wt\%Al_2O_3} \qquad (5\text{-}10)$$

This definition uses the assumption that one mole of CaO is equivalent to one mole of MgO and one mole of Al_2O_3 is equivalent to one mole of SiO_2, as far as their contribution to the basicity of slag. Although eq 5-10 may better represent the overall 'basicity' than eq 5-9, plots of phosphorus distribution coefficient against eq 5-9 displayed a much better correlation than that against B'. This may be the reason why previous researchers[1-3, 5] also used eq 5-9 rather than eq 5-10 to represent their phosphorus distribution data. A possible interpretation of this phenomenon will be discussed in Section 5.5.

5.2. Experimental Details

5. 2. 1. Materials and Slag Preparation

A list of the chemicals used in the study with their purity and their suppliers is represented in Chapter 2. CaO was calcined in platinum crucibles at 1200°C for 12 h to decompose any hydroxide and carbonate present. It was then stored in a desiccator with dry powders of SiO_2, Al_2O_3, MgO, FeO, $Ca_2P_2O_7$, FeS, and Fe. Pure water was used to prevent any scale formation. A small amount of FeS was added to determine sulfur distribution from the same equilibration experiments. The distribution behavior of sulfur is the subject of a separate paper, most of which has been presented in Chapter 4.[26]

Required amounts of CaO, SiO_2, Al_2O_3, and MgO were mixed in an alumina agate mortar to obtain the desired compositions and transferred to a graphite crucible[27] to be premelted at 1600°C for 1 h under a N_2 flow. The premelted slag was crushed into fine powder in the alumina agate mortar. Premelting was confirmed by light polarizing microscope and XRD,[26] displaying gehlenite, akermanite, spinel, and monticilite as expected from the phase diagram.[28] The slag powder was transferred to a 99.8% alumina boat to be decarburized[26] at 1200°C for 24 h under an air flow. Dry FeO, $Ca_2P_2O_7$, and FeS powders were added and mixed well. Each of the $Ca_2P_2O_7$ and FeS powders was added at 0.1 wt% of the total slag and the resulting synthetic slag was stored in a desiccator to be used in the experiments.

5. 2. 2. Experimental Procedure

The samples were prepared as 2.5 or 1.0 g of slag mixed with 2.5 or 1.0 g of iron powder. They were mixed well to reduce the time to reach equilibrium in magnesia

crucibles (1.8 cm OD, 4 cm height, 0.25 cm wall thickness) supplied by Ozark Technical Ceramics, Inc. (Webb City, MO).

The furnace was heated to the target temperature under a flow of N_2. At the target temperature, the furnace was opened to introduce the four-sample alumina holder to the even temperature zone within less than 5 min. Then, N_2 was switched to the experimental gas mixture. In previous research, 6 h was found to be sufficient for a similar sample size.[7] From our preliminary experiments shown in Figure 5-1, it was found that 8 h was sufficient to reach equilibrium. To ensure the 3-phase (gas-slag-metal) equilibrium, 10 h was chosen in this work. After 10 h, the experimental gases were switched back to N_2 by stopping the water pump and gradually decreasing H_2 flow while increasing the N_2 flow. After 5 min of purging, the furnace was opened, the holder was pulled out within 5 min, and the samples were quenched in water. The crucible itself together with the sample was crushed, and iron was separated from the slag. Then, the iron was shredded and the slag finely ground.

The compositions of the iron and the slag phases were analyzed for their phosphorus contents by ICP-OES. Prior to analysis, the samples were digested in closed Savillex® (Savillex, Eden Prairie, MN) microwavable vessels. The chemical analysis results are listed in Table 5-1. Table 5-2 lists the oxygen partial pressures for the H_2-H_2O gas mixture at the experimental temperatures calculated by HSC 5.11 (Outokumpu Oy, Riihitontuntie 7, Finland). Reproducibility of the experiments was confirmed by the consistency of the results of repeated experiments under the same conditions, as will be shown in Section 5.5.

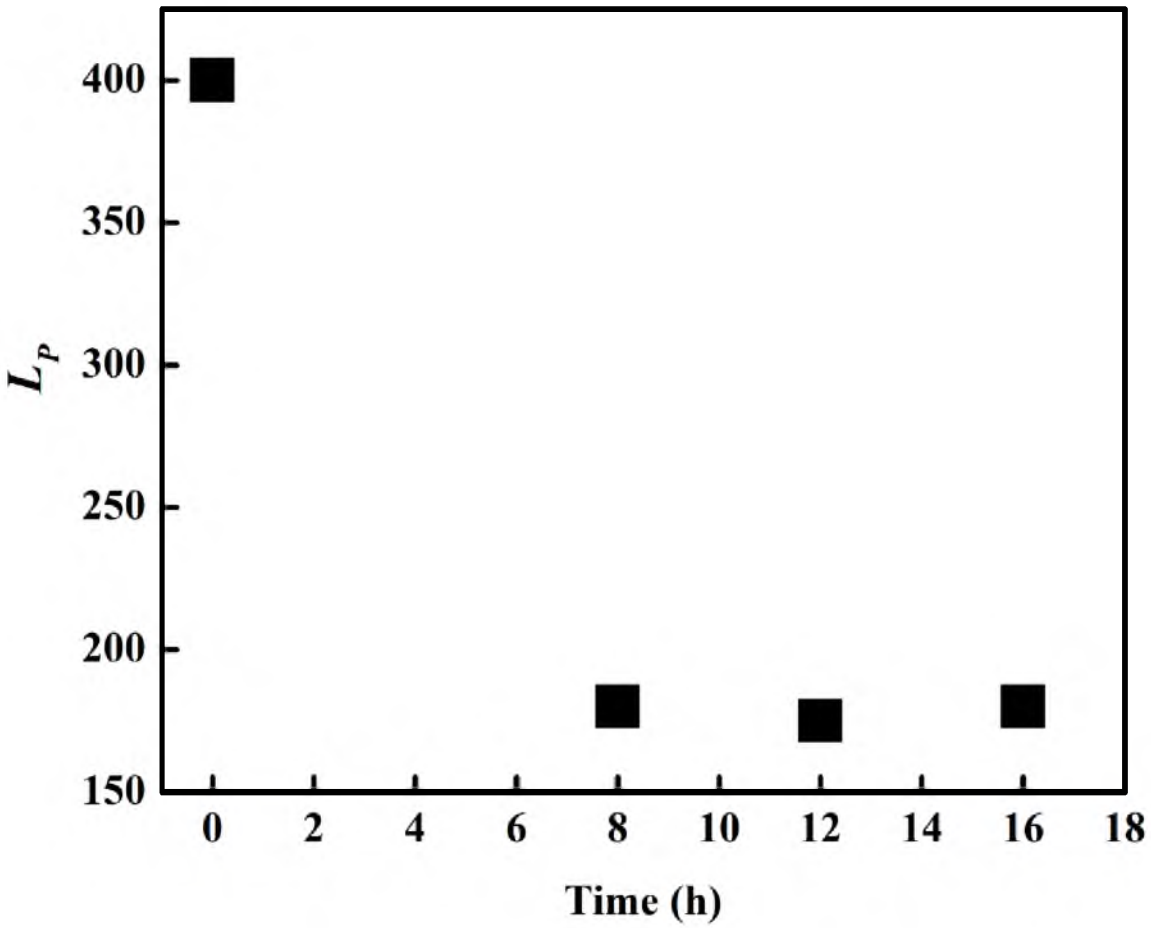

Figure 5-1. Variation of phosphorus distribution ratio with time under H_2/H_2O.

Table 5-1. Chemical analysis of the samples under H_2/H_2O atmosphere

Sample	T (°C)	P (wt%)	FeO (wt%)	MgO (wt%)	CaO (wt%)	Al_2O_3 (wt%)	SiO_2 (wt%)	[P] (wt%)	L_P
S1	1550	0.0602	25.3	17.3	20.7	6.26	29.8	0.00653	9.21
S2	1550	0.0953	35.4	12.9	20.6	6.72	24.6	0.00587	16.2
S3	1550	0.130	33.1	11.7	26.3	7.81	28.5	0.00682	19.1
S4	1550	0.112	41.3	10.8	21.5	6.20	21.0	0.00532	21.0
S5	1550	0.109	21.6	19.2	20.9	8.74	28.3	0.00645	17.0
S6	1550	0.107	19.9	20.2	23.0	7.99	33.0	0.00662	16.0
S7	1550	0.0965	22.3	15.2	29.8	9.48	26.4	0.00753	12.8
S8	1550	0.143	20.7	10.6	32.1	9.35	23.7	0.00640	22.3
S9	1550	0.119	11.5	22.4	24.9	8.18	32.3	0.0105	11.3
S10	1550	0.156	12.0	18.7	29.0	9.71	29.9	0.00880	17.6
S11	1550	0.0865	12.4	17.0	30.9	10.7	29.0	0.00779	11.1
S12	1550	0.129	14.2	14.5	34.7	9.82	31.0	0.00715	18.1
S13	1550	0.123	12.2	22.5	25.1	9.41	32.6	0.0106	11.6
S14	1550	0.137	12.6	16.9	27.4	8.77	39.7	0.00808	16.9
S15	1550	0.123	18.7	15.4	34.7	10.23	16.4	0.00628	19.6
S16	1550	0.132	15.3	16.3	32.4	10.4	28.4	0.00577	22.8
S17	1600	0.0238	41.1	15.1	15.8	6.15	19.5	0.00742	3.21
S18	1600	0.0627	34.6	13.6	20.4	7.37	24.4	0.00619	10.1
S19	1600	0.0802	42.8	11.3	18.1	6.25	17.0	0.00601	13.3

Table 5-1. Continued

Sample	*T* (°C)	P (wt%)	FeO (wt%)	MgO (wt%)	CaO (wt%)	Al_2O_3 (wt%)	SiO_2 (wt%)	[P] (wt%)	L_P
S20	1600	0.0577	52.8	12.4	14.9	4.90	12.3	0.00522	11.0
S21	1600	0.0526	20.4	22.6	20.7	7.55	27.7	0.00672	7.83
S21	1600	0.0438	20.3	22.6	20.7	8.63	27.6	0.00743	5.90
S22	1600	0.0790	27.1	15.7	22.7	8.24	23.5	0.00660	12.0
S22	1600	0.0876	27.0	17.6	22.6	8.23	23.2	0.00575	15.2
S23	1600	0.0828	29.7	14.2	26.2	8.77	22.0	0.00645	12.8
S23	1600	0.0826	29.7	14.2	23.7	8.34	22.0	0.00469	17.6
S24	1600	0.0251	31.1	14.7	24.9	7.93	21.7	0.00610	4.12
S25	1600	0.0752	8.70	25.5	24.3	9.71	36.0	0.0255	2.95
S26	1600	0.0527	9.31	21.2	27.1	9.83	31.5	0.0206	2.56
S27	1600	0.0815	11.8	18.7	29.1	10.1	28.2	0.0177	4.61
S28	1600	0.0903	13.2	19.4	31.0	9.89	23.9	0.0132	6.85
S29	1600	0.0765	7.12	23.9	23.9	9.62	31.5	0.0136	5.61
S30	1600	0.0740	14.7	20.9	25.5	9.55	28.2	0.0108	6.85
S31	1600	0.0853	14.9	25.3	25.2	8.90	23.6	0.00869	9.81
S37	1650	0.0652	32.6	20.6	17.8	7.62	23.5	0.0105	6.21
S38	1650	0.0715	47.5	14.2	13.5	5.52	16.3	0.00943	7.58

Table 5-2. Oxygen partial pressures calculated at the experimental temperatures and P_T = 0.85 atm using H_2/H_2O gas atmosphere (1 atm = 101.3 kPa and Sxx is sample designation)

H_2/H_2O (molar ratio)	$pO_2\,(atm)$			Flow Rates* (mL/min)	
	1550°C	1600°C	1650°C	H_2	H_2O (liq.)
1.7	2.2×10^{-09}	4.8×10^{-09}	-	125	0.047
	S1-S4	S17-S20	-		
3.0	7.0×10^{-10}	1.8×10^{-09}	4.2×10^{-09}	149	0.032
	S5-S8	S21-S24	S37-S38		
6.0	2.4×10^{-10}	5.3×10^{-10}	-	170	0.018
	S13-S16	S29-S32	-		
10.0	1.1×10^{-10}	2.7×10^{-10}	-	181	0.011
	S9-S12	S25-S28	-		

*Flow rates are calculated at 0.85 atm (atmospheric pressure at Salt Lake City) and 25°C.

5.3. Results and Discussion

The effect of CaO/SiO_2, pO_2, and temperature on phosphorus distribution ratio will be discussed. It was difficult to directly compare the results of the current work to those of earlier studies because of the differences in compositions and conditions.

Available correlations[13-15, 20, 29] were used to do that comparison. Large differences were observed from the measured values. The differences might be due to the high content of iron oxide in the slags in the current work. Secondly, it could be attributed to the fact that all these correlations did not consider H_2 and H_2O interaction with the slag. Previous research[30-36] has shown that water has a significant solubility in slag in the temperature range of 1500-1650°C. The overall reaction for both acidic and basic slags can be represented by[36]:

$$H_2O(g) + O^* = 2OH^* \qquad (5\text{-}11)$$

where O* represents double (BO) or single bonded oxygen (NBO), or O^{2-} (free O), and OH^* is single bonded to silicon or as a free ion.[34] As a result of water solubility, the slag chemistry is expected to change and thus affect the L_P, which will be deliberated in Section 5.8.

5. 3. 1. Effect of CaO Content and Basicity on L_P

Basicity was initially expressed using eq 5-10, (wt%CaO + 1.4 wt%MgO)/(wt% SiO_2 + 0.6 wt% Al_2O_3), to correlate its effect on L_P. The points were scatted to the extent that it was difficult to draw clear conclusions from them. On the other hand, when

(wt%CaO)/(wt% SiO_2) as in eq 5-9 was used, L_P showed a much closer dependence on that ratio. This may be attributed to the fact that Ca forms more thermodynamically stable phosphate compounds within the temperature range studied than Mg does. Thus, the ratio (wt%CaO)/(wt% SiO_2) was chosen to correlate the variation of L_P with slag composition, as shown in Figure 5-2. This indicates that the distribution of phosphorus depends on CaO content more strongly than on 'basicity' as a whole.

The effect of CaO/SiO_2 as a measure of CaO activity on the phosphorus partition is shown in Figure 5-2, which indicates that the higher that ratio, the higher the L_P, as expected from reaction 5-1. This is the same trend as determined by previous researchers[2, 3, 5, 8] in similar ranges of CaO/SiO_2. It is worth noting that Figure 5-2(b) shows the fair reproducibility of the experiment evidenced by L_p values of the repeated experiments at 1660°C and pO_2 of 2×10^{-9} atm.

5. 3. 2. Effect of pO_2 on L_P

Previous investigations[1-3,7- 8, 37-39] were performed under pO_2 lower than 10^{-9} atm and it was found that L_P increased with pO_2. In the current work, a wider range of pO_2 was studied. It was found that at 1600°C, the trend was similar to the previous investigations[7-8] when pO_2 was lower than 10^{-9} atm. At pO_2 higher than this value, there was a reversal in the trend: L_P started to decrease with increasing pO_2, as shown in Figure 5-3. Basu *et al.*[5] reported a similar trend at 1600 and 1650°C when FeO reached 15-20 wt%. L_P increased with FeO content until the latter reached 15-20 wt%, and a maximum in the distribution ratio was reached. Then, a reversal occurred where L_P decreased with increasing FeO content, as shown in Figure 5-4. This behavior can be attributed to the

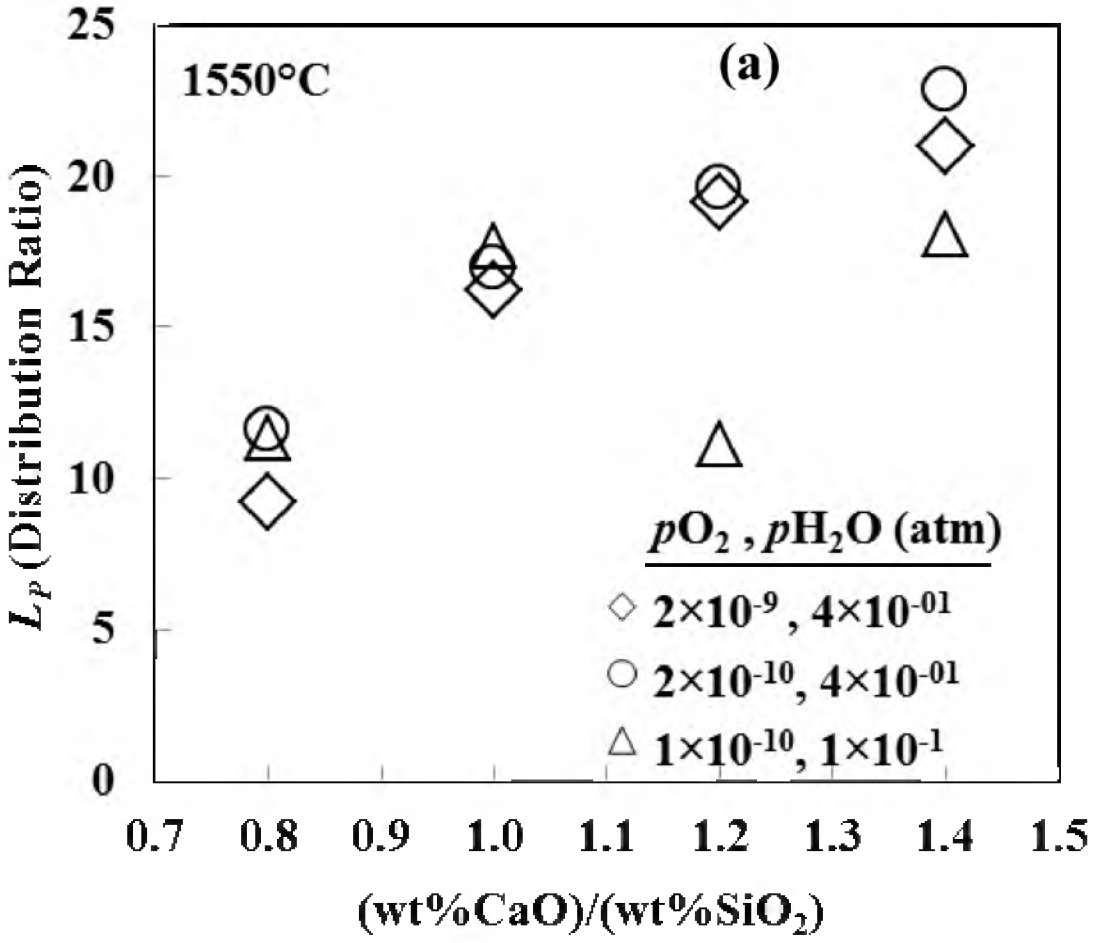

Figure 5-2. The effect of [(wt%CaO)/(wt% SiO_2)] on L_P at various pO_2 values under H_2/H_2O atmosphere at various temperatures: (a) 1550°C, (b) 1600°C, and (c) 1650°C.

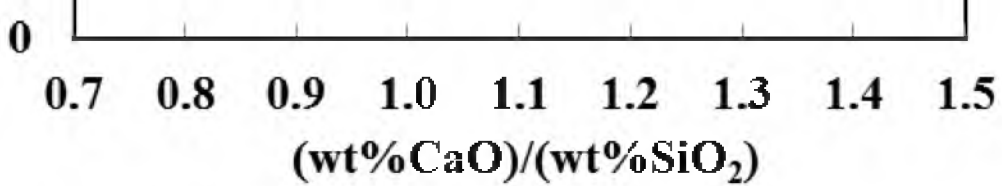

Figure 5-2. Continued.

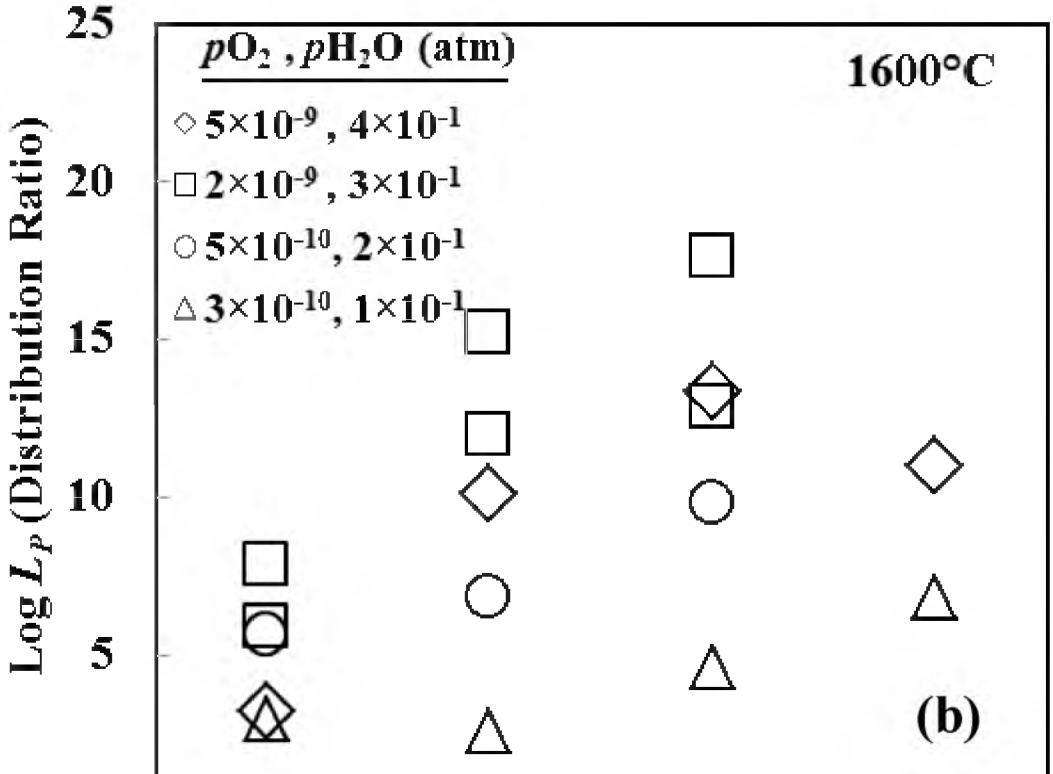
25
20
15
10
5
Log L_p (Distribution Ratio)
pO_2 , pH_2O (atm)
◇ 5×10^{-9} , 4×10^{-1}
□ 2×10^{-9} , 3×10^{-1}
○ 5×10^{-10}, 2×10^{-1}
△ 3×10^{-10}, 1×10^{-1}
1600°C
(b)

Figure 5-2. Continued.

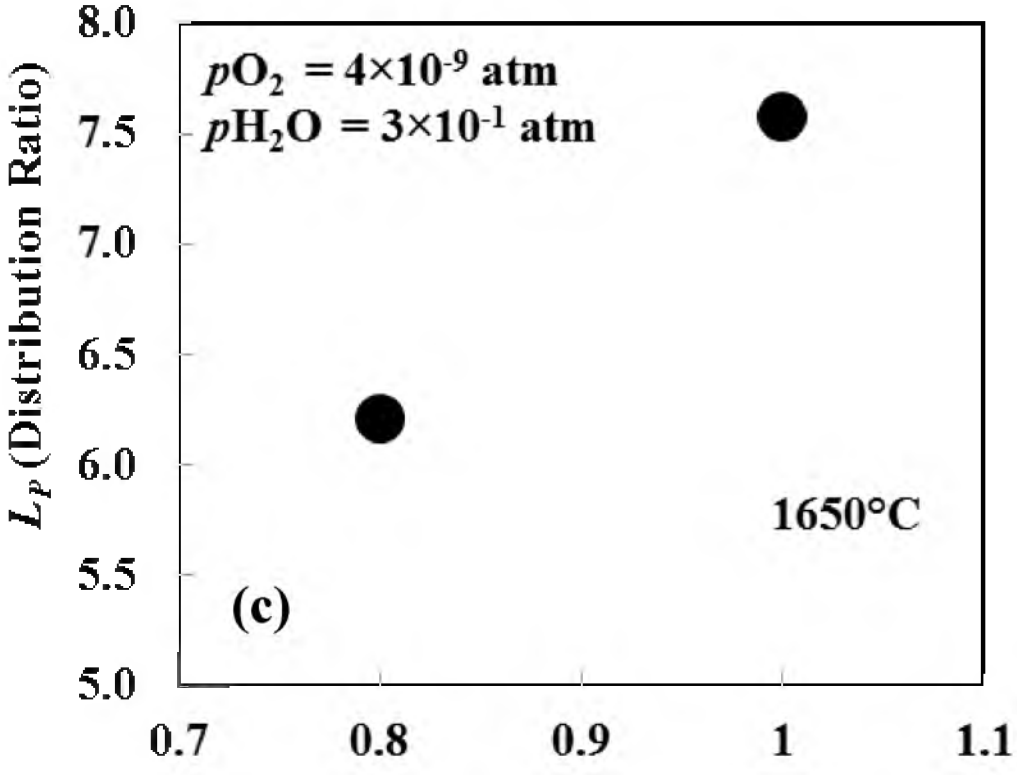
8.0
7.5
7.0
6.5
6.0
5.5
5.0
L_p (Distribution Ratio)
$pO_2 = 4\times10^{-9}$ atm
$pH_2O = 3\times10^{-1}$ atm
1650°C
(c)
0.7
0.8
0.9
1
1.1

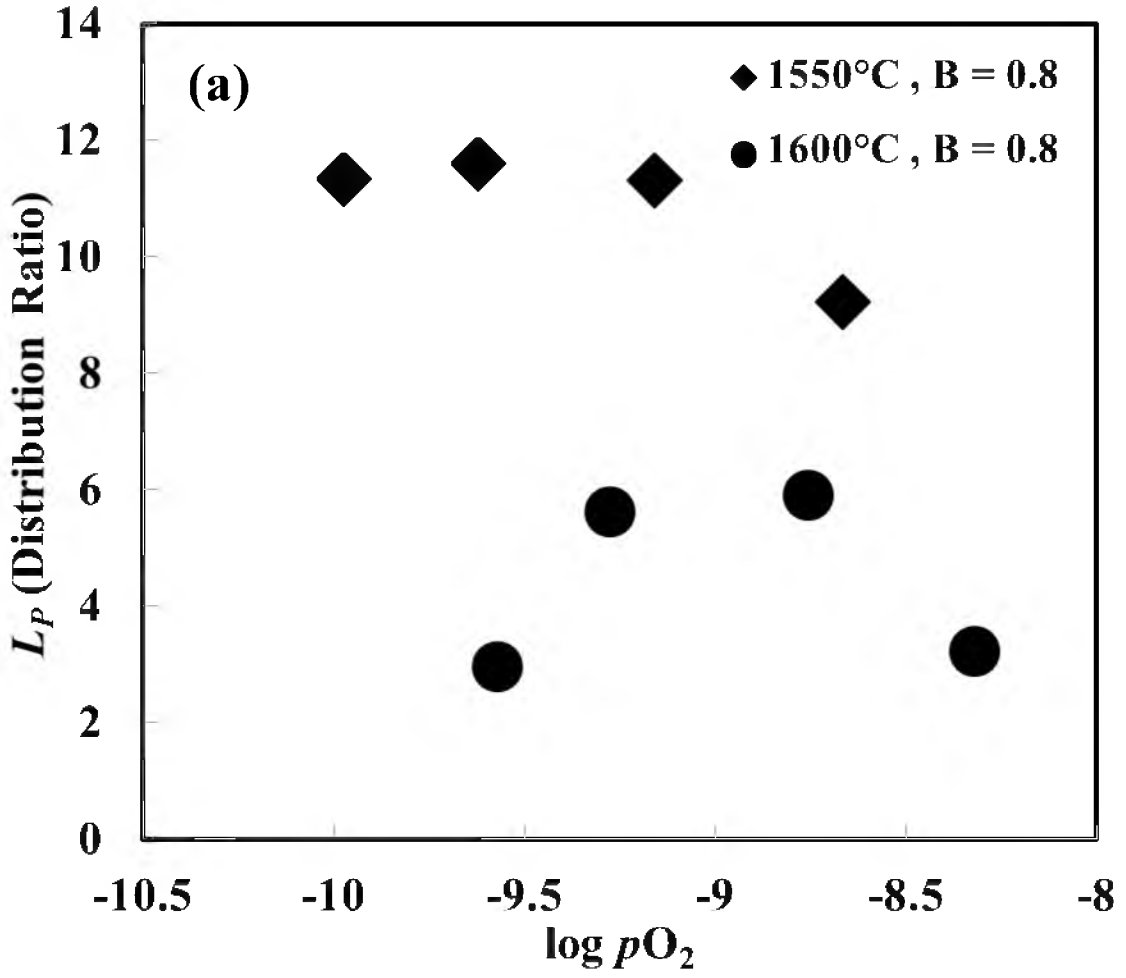

Figure 5-3. The effect of pO_2 on L_P at 1550-1600°C and pH_2O range of 0.1-0.4 atm under H_2/H_2O atmosphere at different [(wt%CaO)/(wt% SiO_2)]: (a) 0.8, (b) 1.0, (c) 1.2, and (d) 1.4.

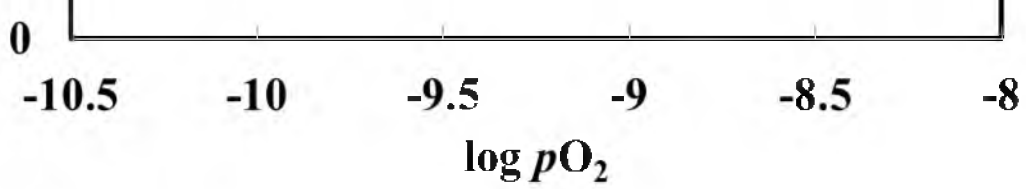

Figure 5-3. Continued.

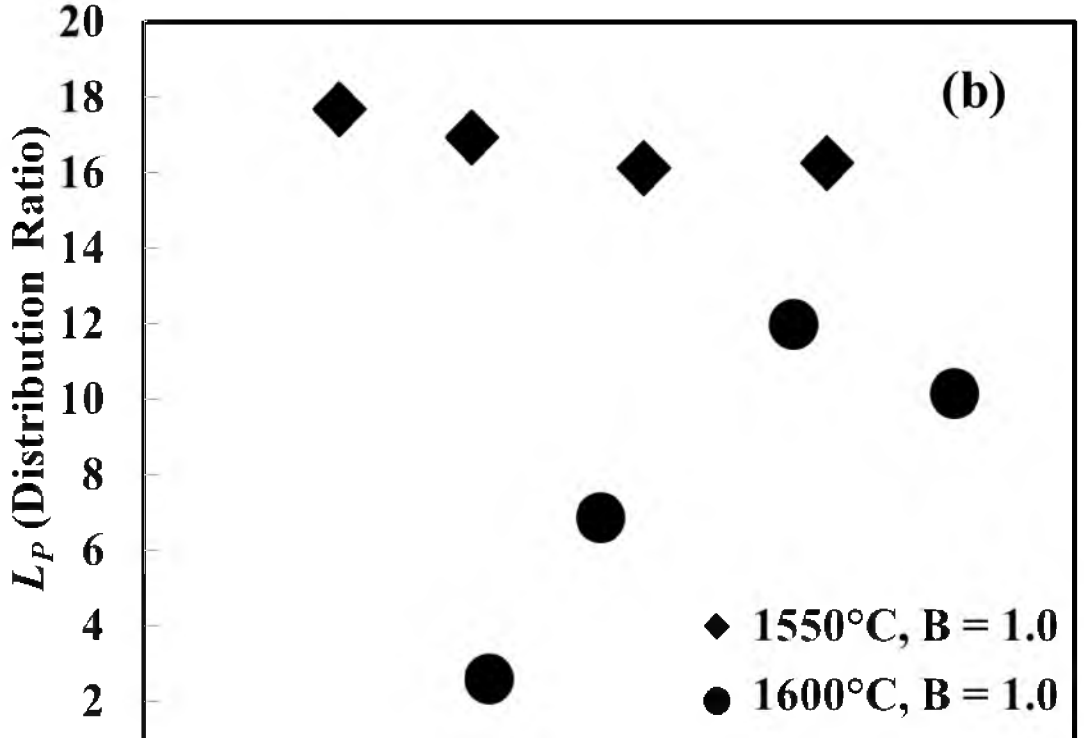
20
18
16
14
12
10
8
6
4
2
L_P (Distribution Ratio)
(b)
1550°C, B = 1.0
1600°C, B = 1.0

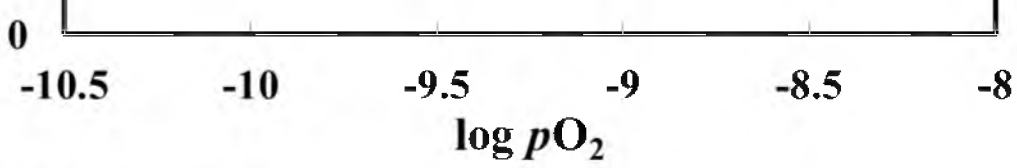

Figure 5-3. Continued.

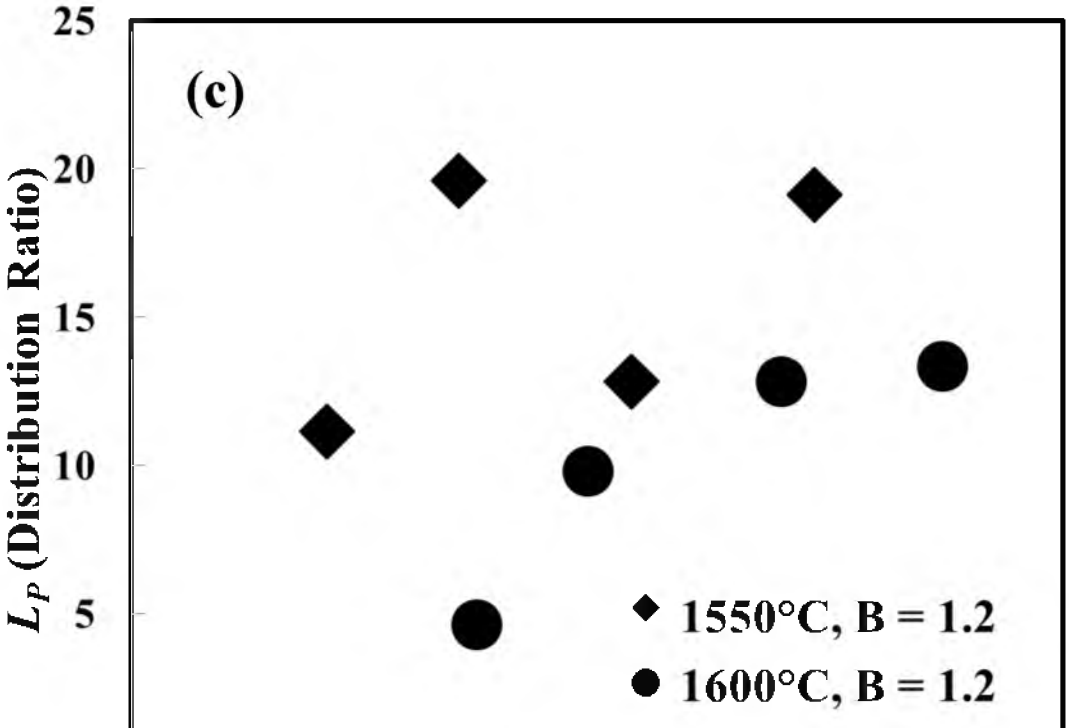
25
20
15
10
5
(c)
L_P (Distribution Ratio)
1550°C, B = 1.2
1600°C, B = 1.2

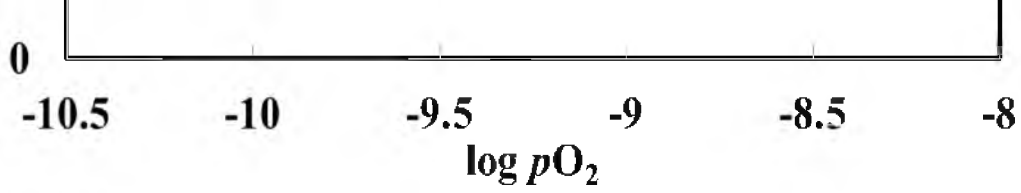

Figure 5-3. Continued.

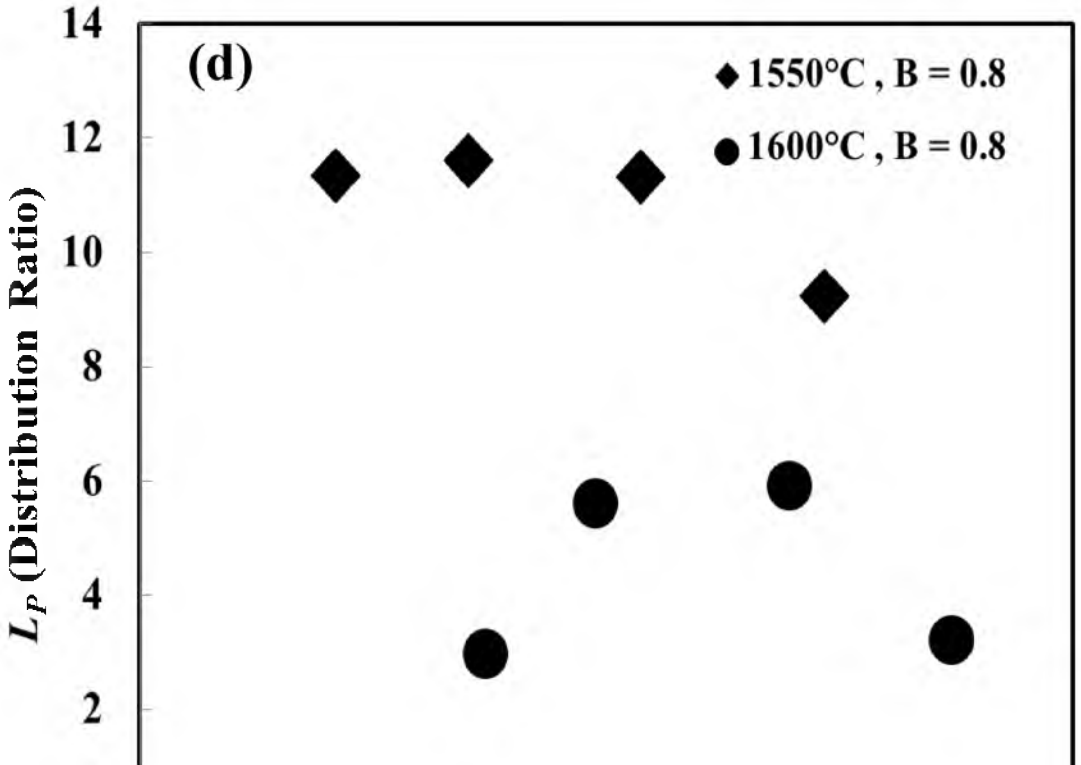
(d)
1550°C , B = 0.8
1600°C , B = 0.8
L_p (Distribution Ratio)
14
12
10
8
6
4
2

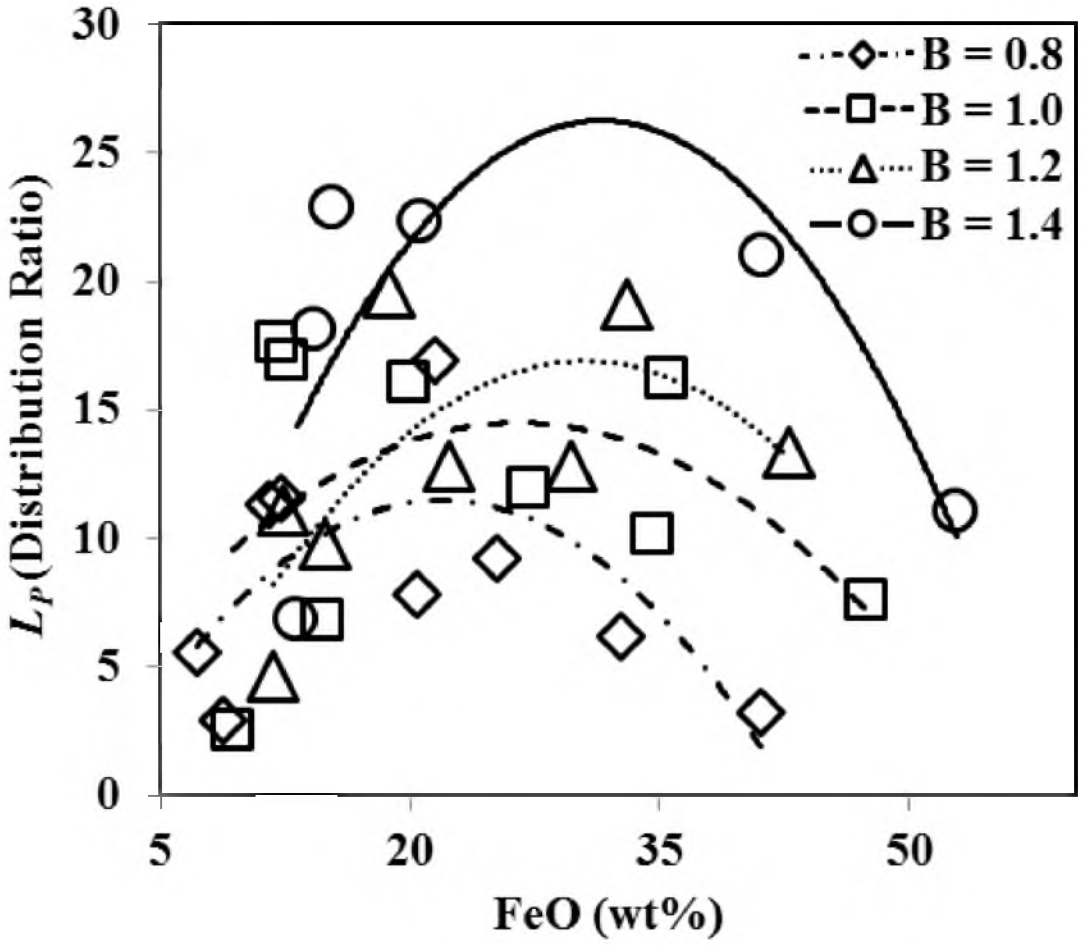

Figure 5-4. The effect of FeO content on L_P at different [(wt%CaO)/(wt% SiO_2)] values in the temperature range 1550 to 1650°C, pH_2O range of 0.1 to 0.4 atm and pO_2 10^{-10} to 10^{-9} atm under H_2/H_2O atmosphere. The continuous lines represent best-fit second-order polynomial functions.

variation of the activity coefficient of P_2O_5, $\gamma_{P_2O_5}$ with respect to FeO content. The same authors found that $\gamma_{P_2O_5}$ decreased with increasing FeO at FeO content less than 20-30 wt%. Beyond that value, $\gamma_{P_2O_5}$ started to increase. The $\gamma_{P_2O_5}$ values were calculated using eq 5-8. The relation between FeO content and $\gamma_{P_2O_5}$ is shown in Figure 5-5. The $\gamma_{P_2O_5}$ values decreased with increasing FeO concentration, at levels less than 20 wt%. This trend was reversed at higher FeO contents. The minima of $\gamma_{P_2O_5}$ correspond to the maxima in the partition ratio of liquid steel and slag shown in Figure 5-5.

5. 3. 3. Effect of Temperature on L_P

It is shown in Figure 5-6 that L_P decreased with increasing temperature at constant input gas composition and CaO/SiO_2, which is in agreement with the previously reported results.[2-3, 5, 9] This can be explained by the fact that P is transferred into slag through an exothermic (oxidation) process. Also, Herty[22] reported the same negative correlation between the equlibrium constant for the phosphate formation reaction and temperature, as seen in eqs 5-1 and 5-2.

5.4. The effect of Gas Composition on L_P

A major difference between the blast furnace slag and the slag of the proposed process is the iron oxide content in slag, which is < 4 wt% in the blast furnace slag, while in the present work, it was > 12 wt% due to the higher temperature on the experiment than the actual temperature in the BF process. According to eq 5-1, the large difference in L_P in the proposed process and the blast furnace can be attributed to the high iron oxide

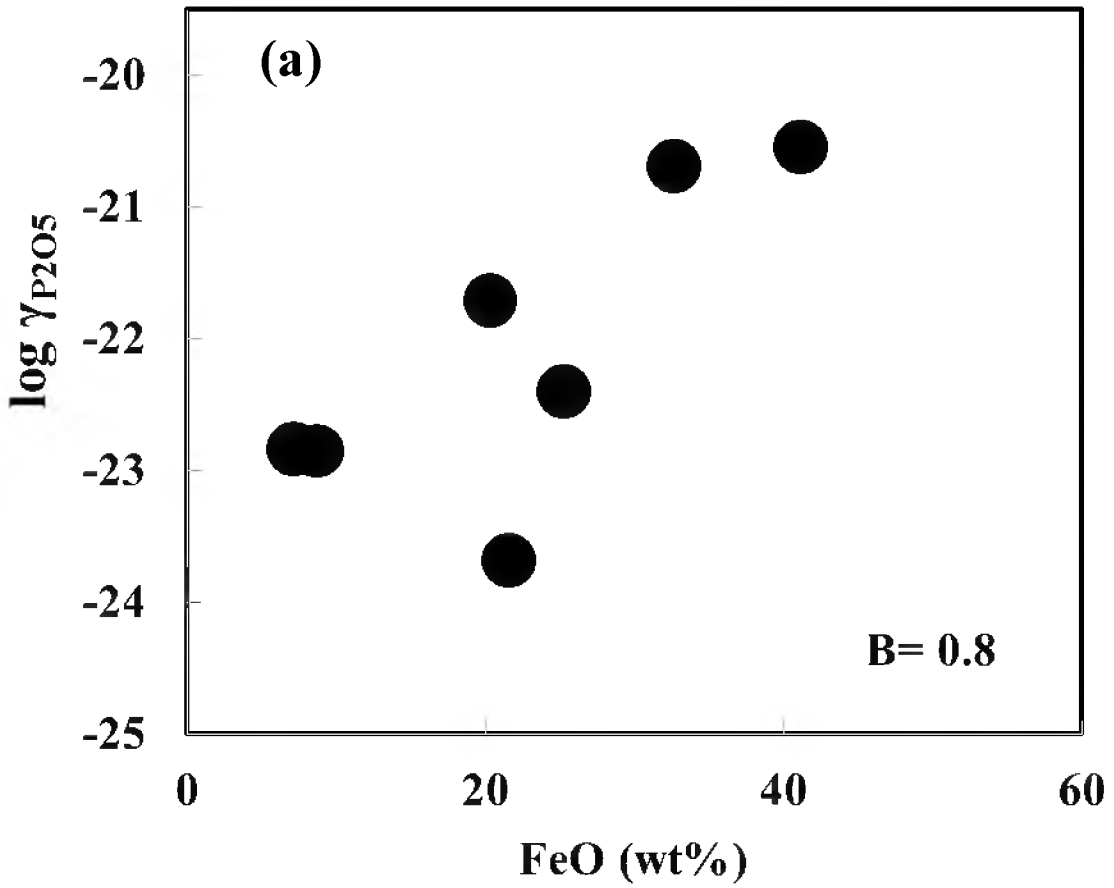

Figure 5-5. The effect of FeO content on $\gamma_{P_2O_5}$ in the temperature range 1550 to 1650°C, pH_2O range of 0.1 to 0.4 atm and pO_2 10^{-10} to 10^{-9} atm under H_2/H_2O atmosphere at different [(wt%CaO)/(wt% SiO_2)]: (a) 0.8, (b) 1.0, (c) 1.2, and (d) 1.4.

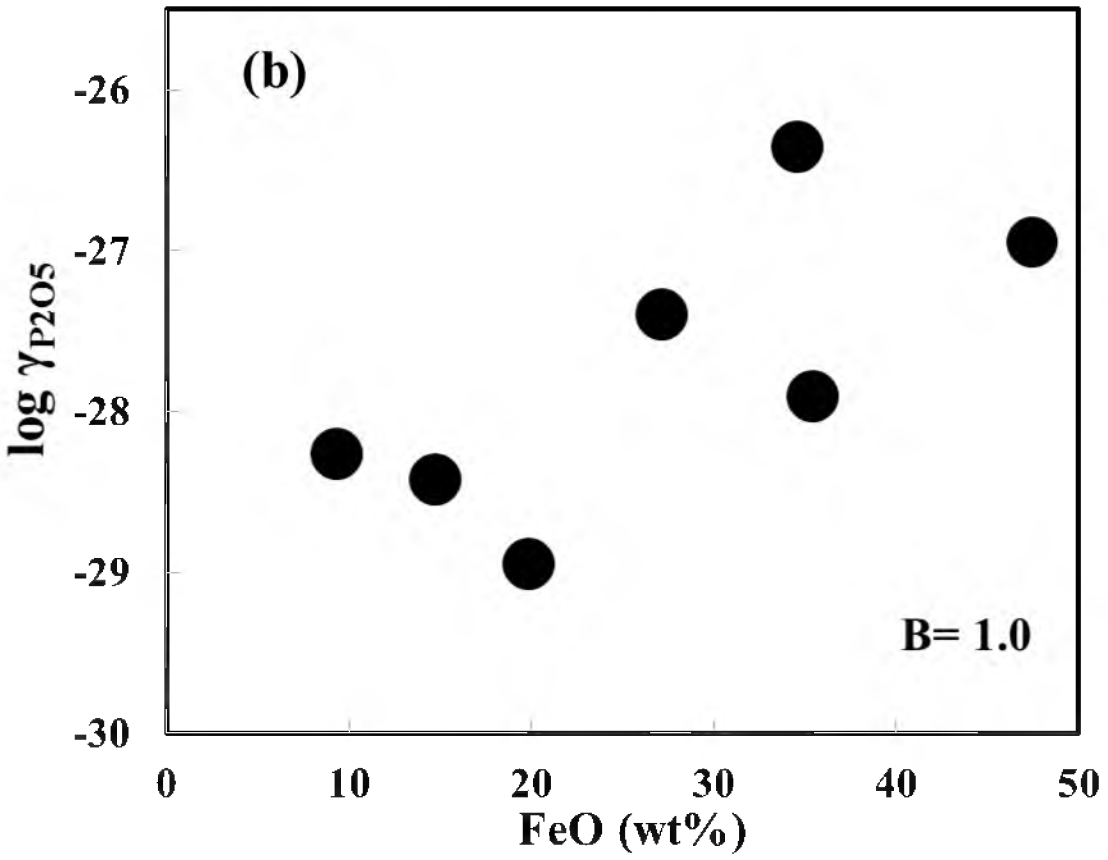

Figure 5-5. Continued.

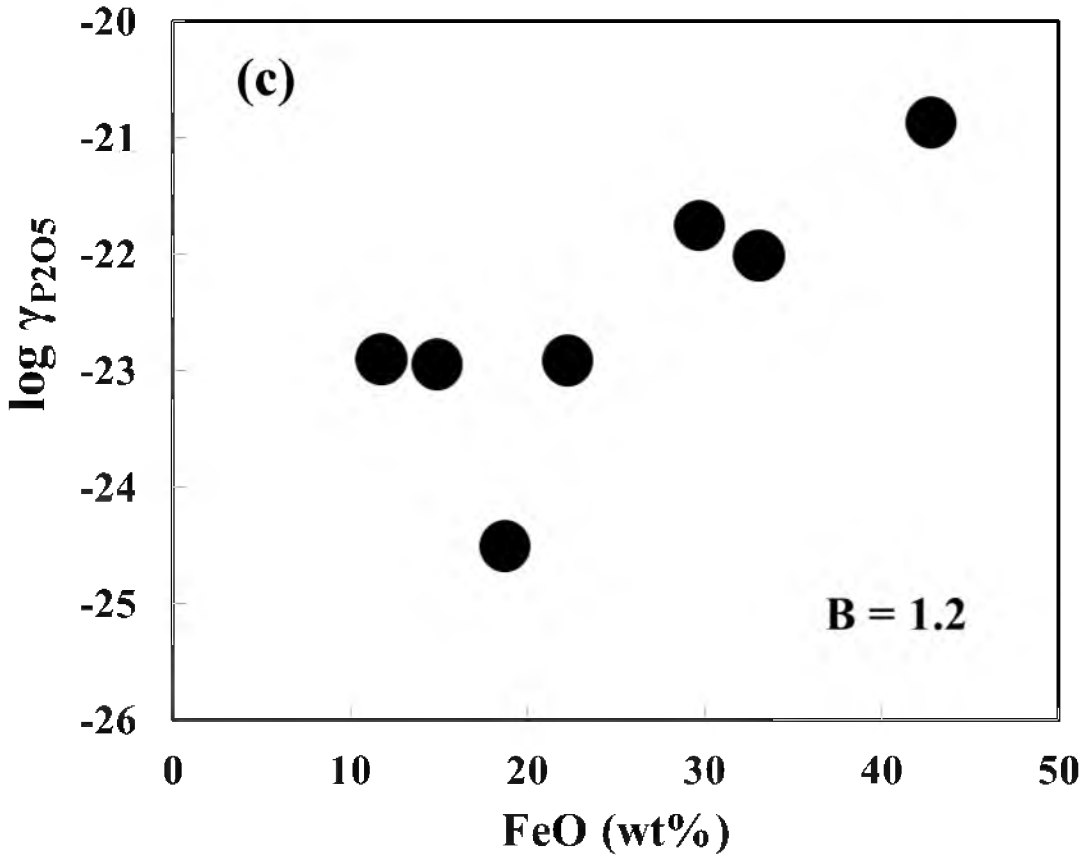

Figure 5-5. Continued.

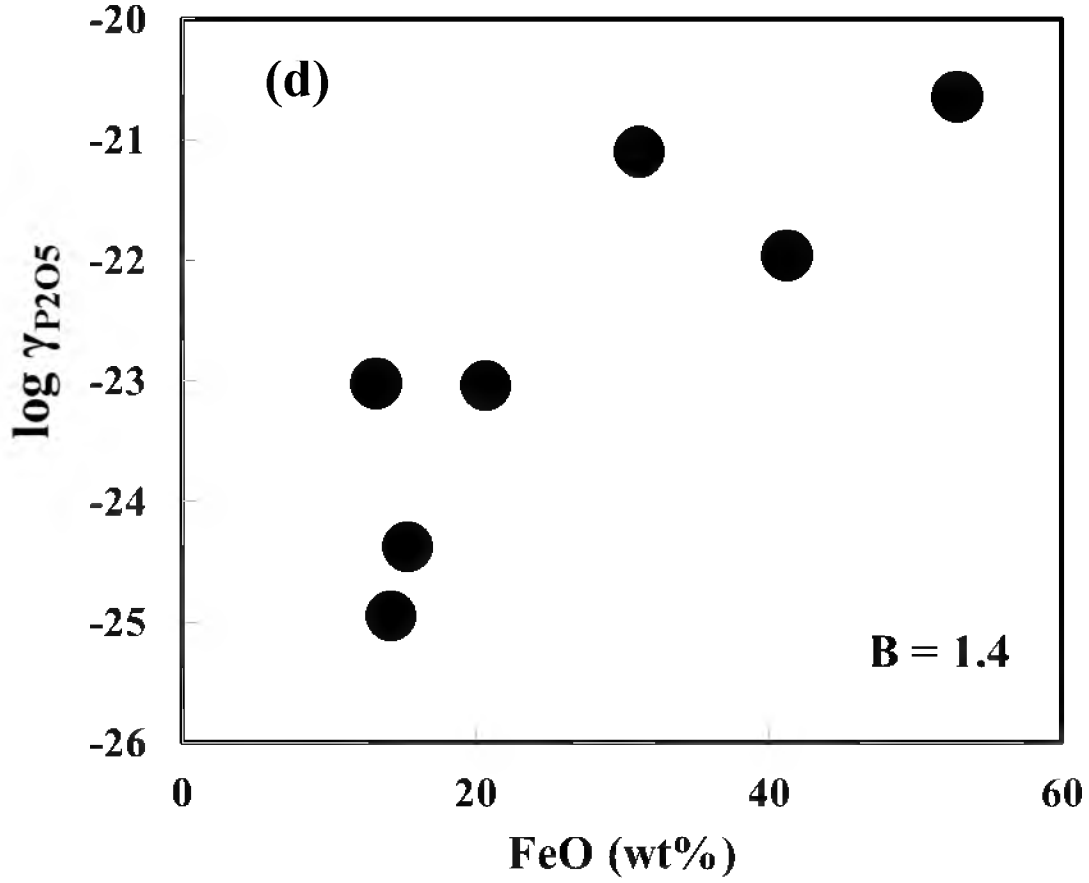

Figure 5-5. Continued.

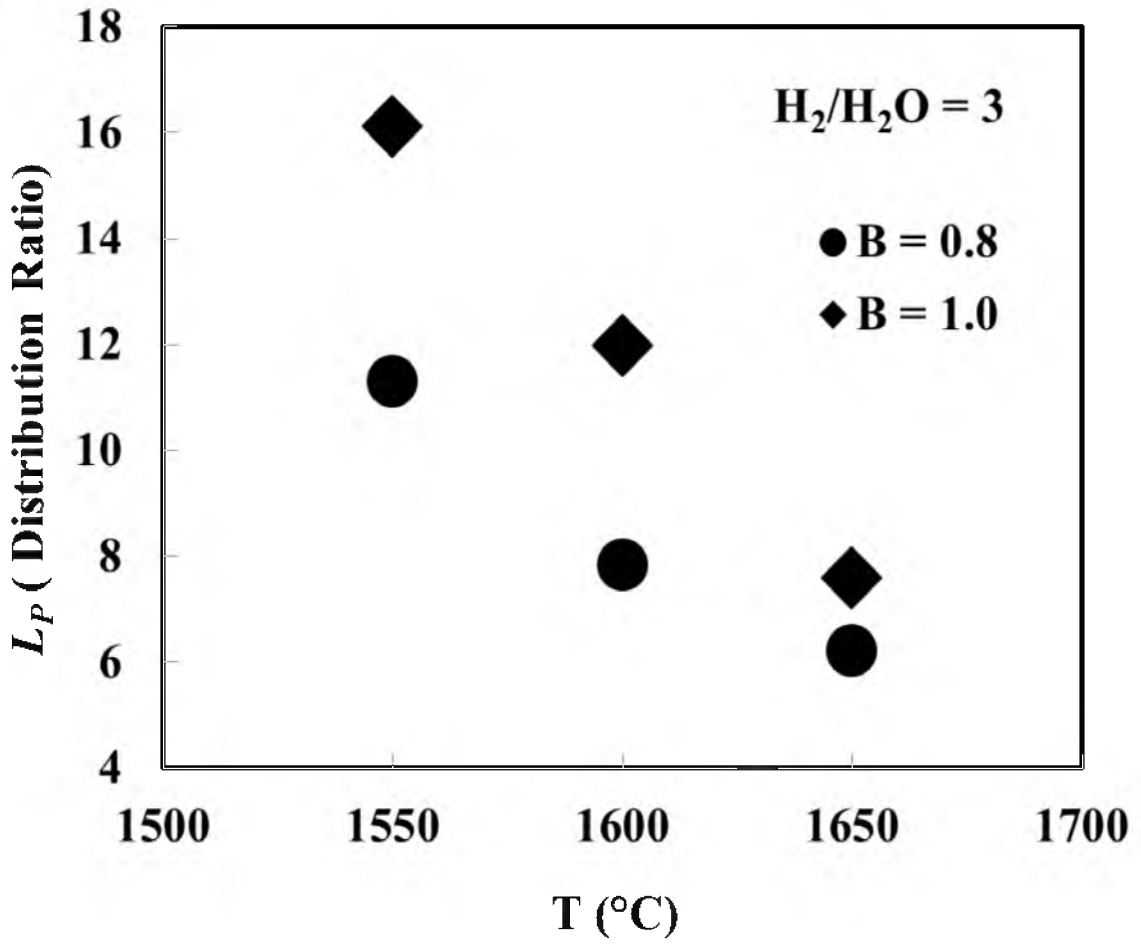

Figure 5-6. The effect of temperature on L_P at H_2/H_2O = 3 and different [(wt%CaO)/(wt% SiO_2)] values at pH_2O = 0.3 atm and pO_2 range of 7×10^{-10} - 4×10^{-9} atm.

content in the slag. Therefore, the direct comparison between the obtained L_P and that of the BF is difficult. Although an approximate comparison has been attempted earlier, the need for a better accuracy persisted, which drove us to conduct a comparison set of experiments under three different gas atmospheres, the details of which have been presented in Chapter 2.[40] The chemical analysis results of the slags of this set of experiments along with L_P in addition to some of the experimental conditions are listed in Table 5-3.

In the following text, the effect of only the type the gas mixture used to control pO_2 was attempted, whereas all the other variable that affect L_P were held constant, as shown in Figures 5-7 – 5-9.

It can be seen that L_P decreases when CO_2 is replaced by H_2O. In other words, the CO/CO_2 slag ranks first with the highest L_P, $CO/CO_2/H_2/H_2O$ comes next, and the H_2/H_2O has the lowest L_P.

The redox reaction that dominates the transfer of P from the molten iron to the slag phase, reaction 1-5, can be generally written as:

$$[P] + \frac{5}{2}[O] + \frac{3}{2}\left(O^{2-}\right) = \left(PO_4^{3-}\right) \qquad (5\text{-}12)$$

where [ ] and ( ) represent the concentration of species in metal and slag, respectively. The above equation suggests that the more the free oxygen in the slag, the more the phosphorus uptake in slag. Based on XPS analysis, the order of the slags base on free oxygen, O^{2-}, relative abundance is CO/CO_2 (44%) > $CO/CO_2/H_2/H_2O$ (41%) > H_2/H_2O

Table 5-3. The chemical analysis of the slag samples under the three gas atmospheres

Sample	Gas	T (°C)	pO_2	CaO/SiO_2	(P) (wt%)	FeO (wt%)	MgO (wt%)	CaO (wt%)	Al_2O_3 (wt%)	SiO_2 (wt%)	L_P
R10	$CO/CO_2/H_2/H_2O$	1550	1.9×10^{-9}	0.8	0.308	21.7	24.6	20.3	13.0	25.5	39.5
R19		1550	1.6×10^{-10}	0.8	0.283	10.1	24.4	26.2	16.3	34.8	8.9
R20		1550	1.6×10^{-10}	1	0.346	9.8	17.9	30.7	8.4	31.8	15.0
R21		1550	1.6×10^{-10}	1.2	0.318	10.8	16.8	33.5	18.8	29.8	25.6
R22		1600	3.6×10^{-10}	0.8	0.179	13.0	23.4	26.0	15.7	32.3	6.9
R23		1600	3.6×10^{-10}	1	0.183	12.7	19.2	30.0	17.0	30.9	7.7
R24		1600	3.6×10^{-10}	1.2	0.227	12.4	16.6	32.8	17.2	28.6	13.7
R27		1630	6.4×10^{-10}	1.2	0.206	11.2	19.2	30.1	17.0	30.5	5.4
R46	CO/CO_2	1550	1.6×10^{-10}	0.8	0.211	35.5	10.2	24.5	13.9	22.8	14.0
R48		1550	1.6×10^{-10}	1.2	0.299	16.9	26.2	26.3	15.0	23.6	25.4
R49		1600	3.6×10^{-10}	0.8	0.243	14.7	22.1	25.7	15.2	31.9	4.4
R50		1600	3.6×10^{-10}	1	0.263	16.9	16.9	28.5	15.2	29.4	17.7
R51		1600	3.6×10^{-10}	1.2	0.306	15.3	14.7	30.7	16.6	26.7	27.4
R52		1630	6.4×10^{-10}	0.8	0.275	13.7	15.7	24.7	23.4	32.9	15.9
R53		1630	6.4×10^{-10}	1	0.272	14.6	14.3	28.0	17.0	36.4	15. 5
R54		1630	6.4×10^{-10}	1.2	0.269	26.4	14.8	25.2	14.3	27.4	15.6
R74	H_2/H_2O	1550	1.6×10^{-10}	1	0.376	9.9	20.7	34.9	5.1	27.8	8.6
R75		1550	1.6×10^{-10}	1.2	0.388	9.6	19.7	31.2	17.1	32.1	7.9
R78		1600	3.6×10^{-10}	1.2	0.377	10.5	16.1	33.7	17.7	29.5	9.8
R'78		1600	3.6×10^{-10}	1.2	0.299	9.5	16.9	33.8	18.1	29.6	7.7

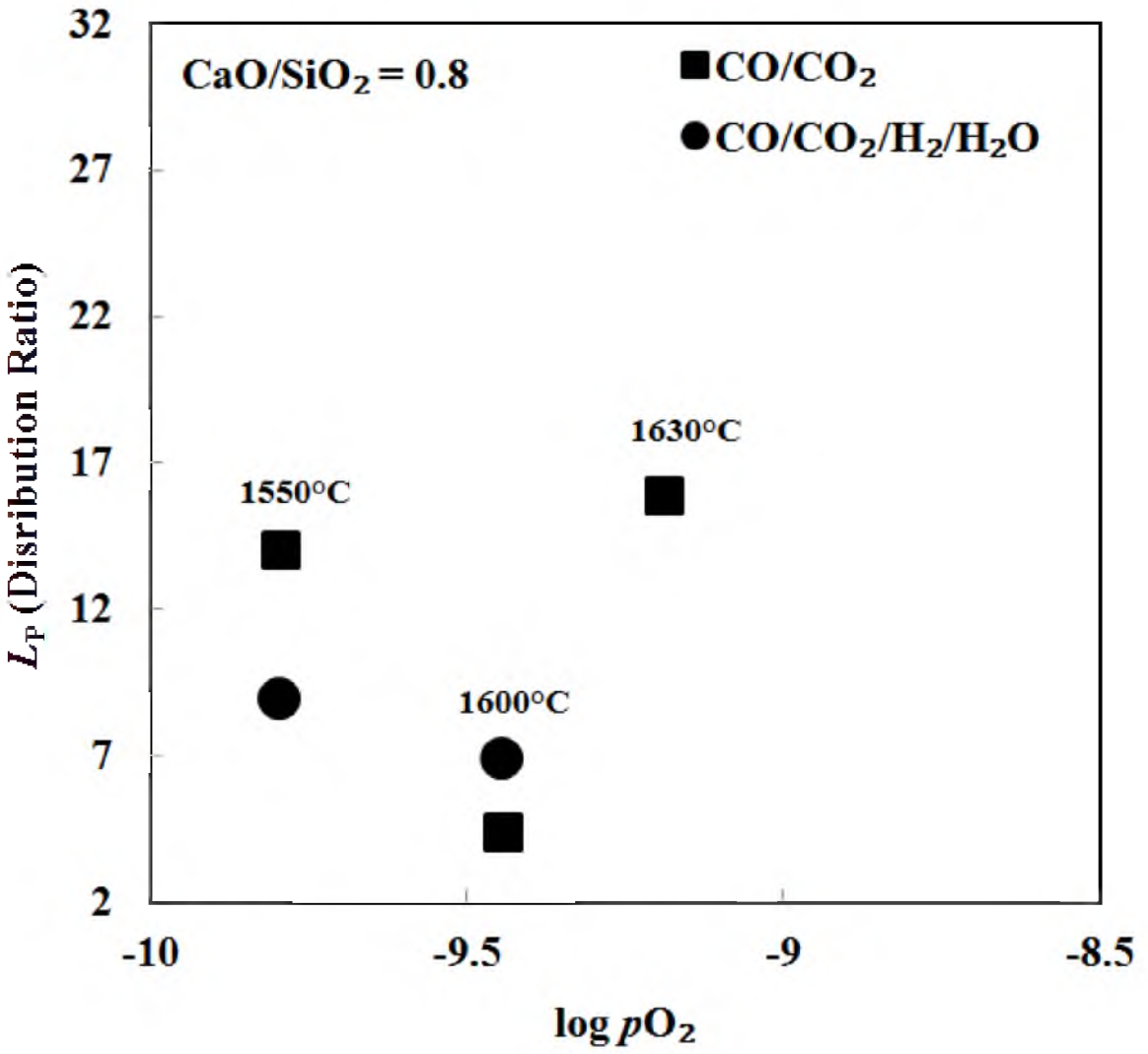

Figure 5-7. The effect of different gas atmospheres on L_P at various pO_2 and temperature values for slags with CaO/SiO_2 of 0.8 and pH_2O of 0 and 0.1 atm in CO/CO_2 and $H_2/H_2O/CO/CO_2$, respectively.

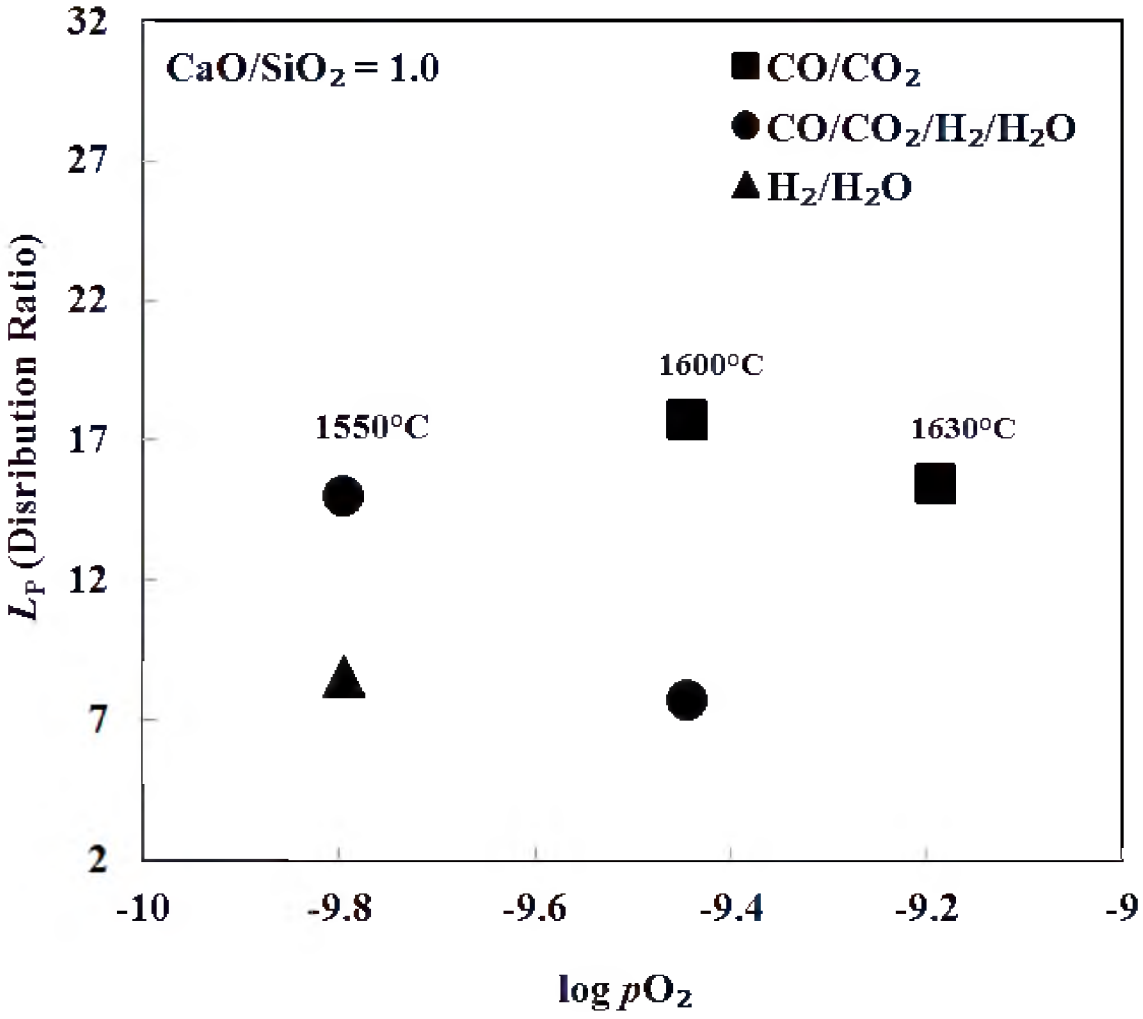

Figure 5-8. The effect of different gas atmospheres on L_P at various pO_2 and temperature values for slags with CaO/SiO_2 of 1.0 and pH_2O of 0, 0.1, and 1.0 atm in CO/CO_2, $H_2/H_2O/CO/CO_2$, and $H_2/H_2O/CO$, respectively.

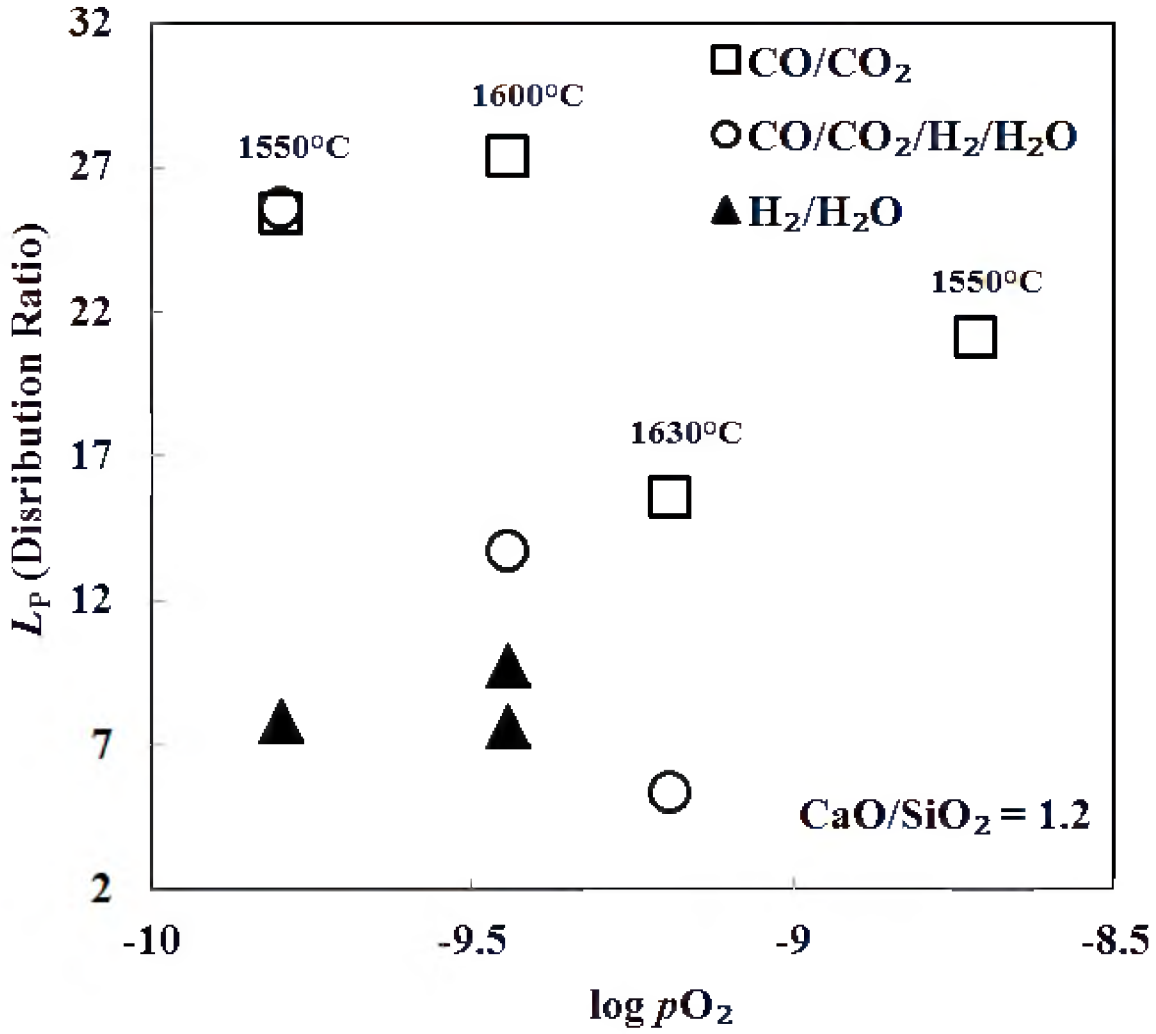

Figure 5-9. The effect of different gas atmospheres on L_P at various pO_2 and temperature values for slags with CaO/SiO_2 of 1.2 and pH_2O of 0, 0.1, and 1.0 atm in CO/CO_2, $H_2/H_2O/CO/CO_2$, and $H_2/H_2O/CO$, respectively.

(37%), which is in accordance with the L_P order. Moreover, there could be an interrelation between the FeO content in the slag and L_P, as Figure 5-4 suggests. That interdependence has been also reported for low P_2O_5 slags that are saturated with both magnesia and dicalcium silicates.[41] As shown in Table 5-3, L_P is proportional to FeO content of the slag. The effect of the gas atmospheres on the FeO activity will be discussed in Chapter 6. In an attempt to investigate the effect of pH_2O on L_P, Figures 5-10 – 5-11 were presented. It can be seen that at constant pO_2, L_P decreases with increasing pH_2O.

For the slag compositions investigated, MgO-saturated CaO-FeO-Al_2O_3-SiO_2-MnO (0.2-0.8 wt%)-P_2O_5 (0.1-0.9 wt%), in the temperature range 1550-1600°C, with CaO/SiO_2 rage 0.8 to 1.2, and under $pO_2 = 2\times10^{-10}$~2×10^{-9} atm, the average L_P was found to be 9 (7.7~9.8), 17 (6.9~39.5), and 18 (4.4~27.4) under H_2/H_2O, $CO/CO_2/H_2/H_2O$, and CO/CO_2, respectively. These values were used as representative values for comparing P contents in iron under different gas atmospheres, as shown in the next section.

5.5. Blast Furnace versus the Flash Ironmaking Technology

In the proposed process, phosphorus comes only from the ore that has an approximately 0.6 wt% phosphorus content.[42] In the current blast furnace process, coke is another source of phosphorus in addition to the ore, containing an average of 0.03 wt% phosphorus.[42] Also, more than 90 % of P input goes into the hot metal in the blast furnace conditions.[43] Our literature survey found only reports on L_P done under steelmaking conditions[3,5] and no consistent data for P distribution under BF conditions.

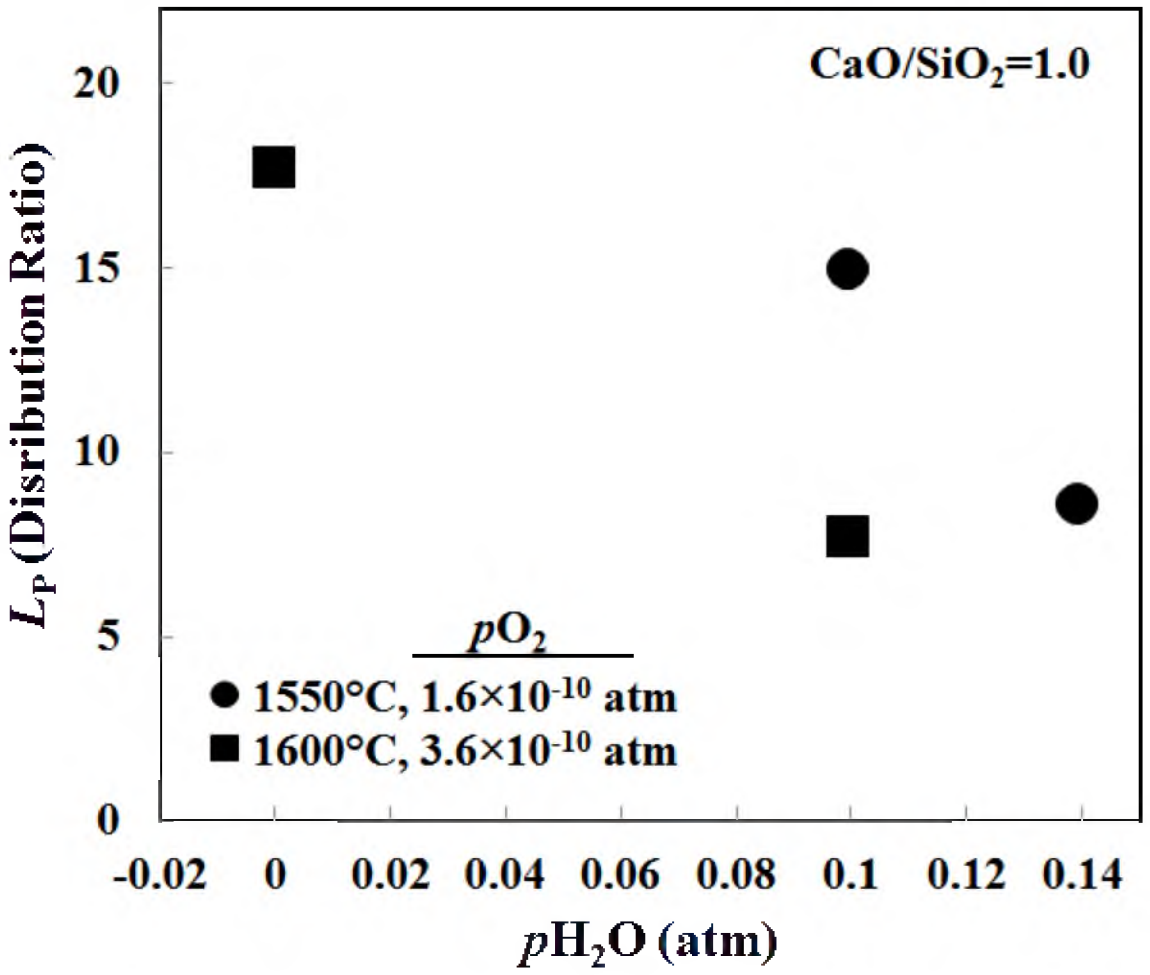

Figure 5-10. The effect of pH_2O on L_P for slag compositions with CaO/SiO_2 of 1.0 at various temperatures and pO_2.

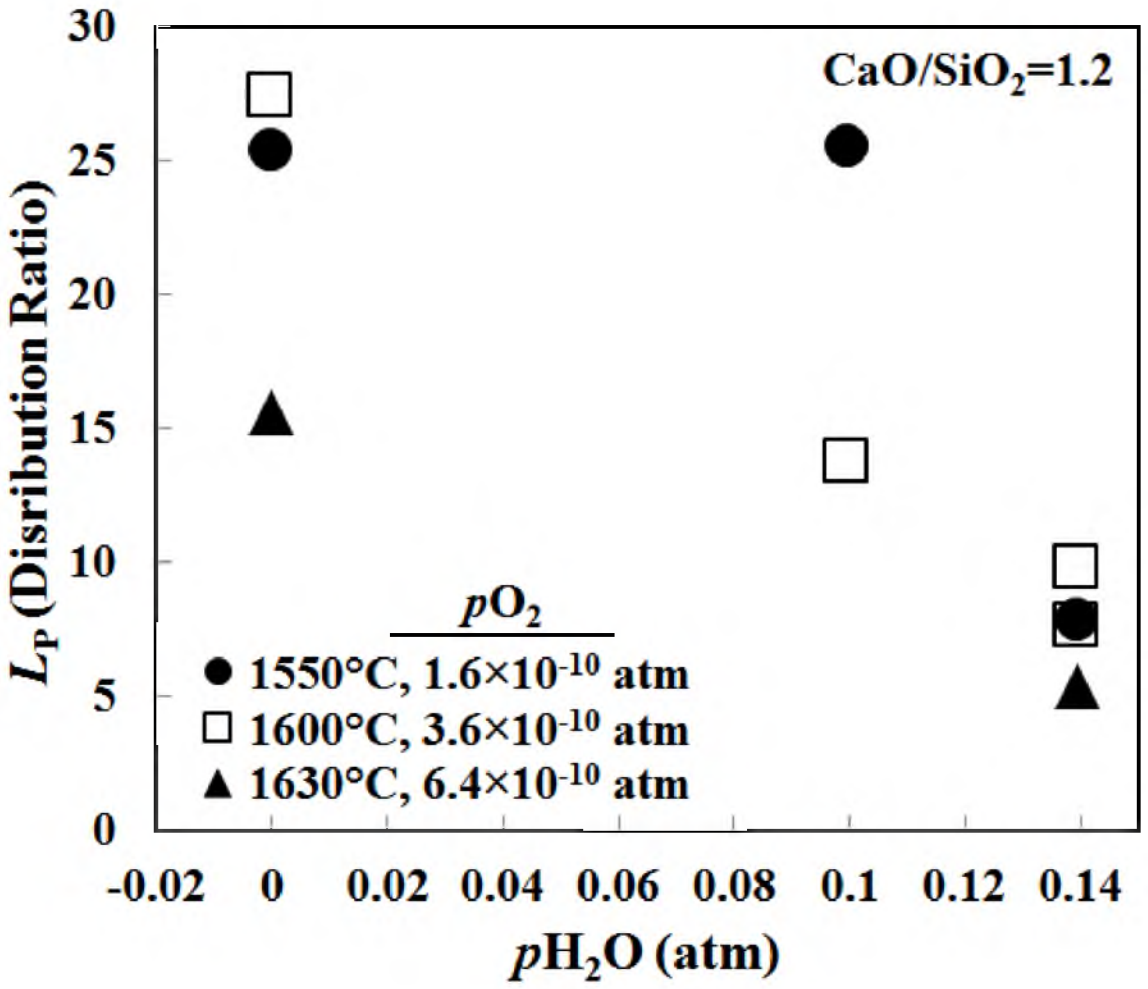

Figure 5-11. The effect of pH_2O on L_P for slag compositions with CaO/SiO_2 of 1.2 at various temperatures and pO_2.

In addition to the low phosphorus input from raw materials, a significant amount of phosphorus will volatilize during the downward flight of the particles in the proposed flash reactor.[44] To obtain an approximate extent of volatilization, a representative sample was analyzed for phosphorus before and after reduction in a simulated run for the proposed process. It was found that over 25 wt% of the phosphorus in the ore was lost during particle flight.

The wt% of P in iron is related to L_P by the following relationship obtained from materials balance:

$$[wt\%P]=\frac{t}{(a\cdot L_P)+1}\times 100 \qquad (5\text{-}13)$$

where

$[wt\%P]$: phosphorus weight percentage in produced iron

t : total phosphorus input per ton of iron

a : slag/metal mass ratio

In the proposed process, L_P = 9 and 17 (H_2/H_2O and $CO/CO_2/H_2/H_2O$, respectively) versus 18 in BF (CO/CO_2) and t = 4.5 kg/ton iron (considering that 25 wt% phosphorus in the ore will volatilize in the furnace shaft). Applying the same slag/metal ratio of 0.3 as in BF, the P content in the iron produced by the novel process would be ~ 0.12 and 0.07 wt% under H_2/H_2O (H_2 conditions) and $CO/CO_2/H_2/H_2O$ (natural/coal gas, NG/CG, conditions). In contrast, the P input to the blast furnace is 10.3 kg/ton iron, based on the same P content in the ore plus a typical coke-to-iron ratio of 0.4 and P content in

coke. Thus, the P content in hot metal produced under CO/CO_2 (BF conditions) would be about 0.16 %. The values of L_P and [wt% P] under the three gas atmospheres are normalized against the BF (CO/CO_2) and compared in Figure 5-12.

5.6. Conclusions

For the slag compositions investigated, MgO-saturated CaO-FeO-Al_2O_3-SiO_2-MnO (0.2-0.8 wt%)-P_2O_5 (0.1-0.9 wt%), in the temperature range 1550-1600°C, with wt% CaO/wt% SiO_2 of 0.8 to 1.2, and under $pO_2 = 2\times10^{-10}$~2×10^{-9} atm, the average L_P was found to be 9, 17, and 18 in the case of H_2, natural/coal gas (NG/CG), and blast furnace (BF), respectively. In other words, L_P is 50 and 6 % less under the H_2 and NG/CG conditions than in the BF conditions, respectively. The phosphorus content in the final product of the three routes was estimated using an ore with 0.6 wt% P in addition to coke containing 0.03 wt% P (for BF conditions) and considering that over 90% of the input phosphorus in the BF goes into the hot metal, whereas in the flash process over ~25 wt% P volatilize during ore concentrate downward flight in the reactor shaft in the flash ironmaking process. Based on materials balance calculations accounting for the aforementioned constraints in addition to using the slag/metal ratio of 0.3 in all the three routes, the hot metal produced by H_2 and NG/CG would have 25 and 56 % less P than in the BF conditions.

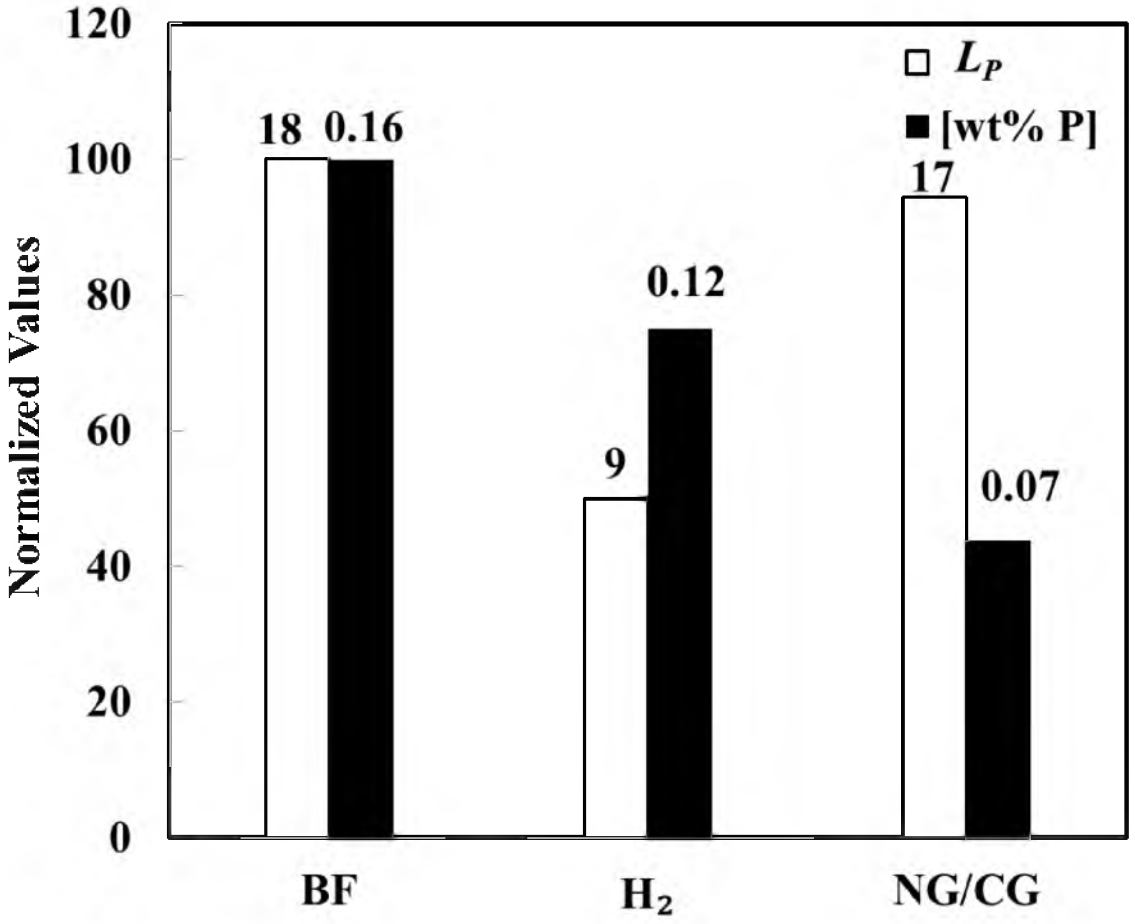

Figure 5-12. The effect of the type of reductant gas on L_P. The labels show the values of L_P and [wt% P].

5.7. References

(1) Cho, M. K.; Park, J. H.; Min, D. J. Phosphate capacity of CaO-SiO_2-MnO-FeO slag saturated with MgO. *ISIJ Int.*, **2010**, *50*, 324-326.

(2) Basu, S.; Lahiri, A. K.; Seetharaman, S. Distribution of phosphorus and oxygen between liquid steel and basic oxygen steelmaking slag. *Rev. Metall.*, **2009**, *106*, 21-26.

(3) Basu, S.; Lahiri, A. K.; Seetharaman, S. Phosphorus partition between liquid steel and CaO-SiO_2-FeO_x-P_2O_5-MgO slag containing 15 to 25 pct FeO. Metall. Mater. Trans. B, **2007**, *38B*, 623-630.

(4) Lee, C. M.; Fruehan, R. J. Phosphorus equilibrium between hot metal and slag. *Ironmaking Steelmaking,* **2005**, *32*, 503-508.

(5) Basu, S.; Lahiri, A.; Seetharaman, S. Phosphorus Partition between Liquid Steel and CaO-SiO_2-P_2O_5-MgO Slag Containing Low FeO. *Metall. Mater. Trans. B,* **2007**, *38*, 357-366.

(6) Chan, A. H.; Pak, J. J.; Fruehan, R. J. The thermodynamics of sulfur and phosphorus reacting between carbon-saturated iron and Na_2O-SiO_2 slags. *Proc. Process Technol. Conf.*, USA, **1986**, 467-473.

(7) Pak, J. J.; Fruehan, R. J. Soda slag system for hot metal dephosphorization. *Metall. Mater. Trans. B,* **1986**, *17B*, 797-804.

(8) Maramba, B.; Eric, R. Phosphide capacities of ferromanganese smelting slags. *Miner. Eng.*, **2008**, *21*, 132-137.

(9) Ahundov, N. F.; Tsukihashi, F.; Sano, N. Equilibrium partitions of manganese and phosphorus between BaO-BaF_2 melts and carbon saturated iron-manganese melts. *ISIJ Intl.*, **1991**, *31*, 685-688.

(10) Turkdogan, E.; Bills, P. A Thermodynamic Study of Fe-Ca-P-O, Fe-Ca-Si-P-O, and Some Complex Molten Silicophosphate Systems. *Iron and Steel Inst.*, London, **1958**, *188*, 143-153.

(11) Knuppel, H.; Oeters, F. The phosphorus-oxygen equilibrium between liquid iron and lime-saturated phosphate slags. *Stahl Eisen,* **1961**, *81*, 1437-1449.

(12) Bergman, A.; Gustafsson, A. The relation between optical basicity and phosphorus capacity of complex slags. *Steel Res.*, **1988**, *59*, 281-288.

(13) Deo, B.; Bose, P.; Mehrotra, K. Models for predicting phosphorus and sulphur distribution ratios in oxygen steel making. *Trans. Indian Inst. Met.*, **1988**, *41*, 475-479.

(14) Young, R.; Duffy,J.; Hassall, G.; Xu, Z. Use of optical basicity concept for determining phosphorus and sulphur slag-metal partitions. *Ironmaking steelmaking,* **1992**, *19*, 201-219.

(15) Novikov, V.; Nevidimov, V.; Toporishchev, G. Application of polymeric model for the calculation of phosphorus distribution between metal and slag. *Rasplavy(Russia)*, **1995**, *6*, 72-74.

(16) Yang, X.; Liu, T.; Guo, Z.; Wang, D. Study on the correlation between phosphate capacity index and slag basicity.In *Selected Papers of Engineering Chemistry and Metallurgy*, Science Press, China, **1996**, *8*, 8-21.

(17) Ide, K.; Fruehan, R. J. Evaluation of phosphorus reaction equilibrium in steelmaking. *Iron Steelmaker,* **2000**, *27*, 65-70.

(18) Hasegawa, M.; Iwase, M.; Wakimoto, K.; McLean, A. A thermochemical study of the $CaO + P_2O_5 + Fe_xO$ system-regions in equilibrium with solid $Ca_3P_2O_8$. *Scand. J. Metall.*, **2002**, *32*, 47-52.

(19) Li, G.; Hamano, T.; Tsukihashi, F. Thermodynamics of dephosphorization of molten steel by MgO saturated $CaO-Fe_tO-SiO_2-Na_2O$, Al_2O_3 fluxes. *Proc. of the Int. Congress on the Science and Technology of Steelmaking*, Association for Iron & Steel Technology, New York, **2005**, 125-130.

(20) Basu, S.; Lahiri, A.; Seetharaman, S. A model for activity coefficient of P_2O_5 in BOF slag and phosphorus distribution between liquid steel and slag. *ISIJ Intl.,* **2007**, *47*, 1236-1238.

(21) Sohn, H. Y.; Choi, M. E.; Zhang, Y.; Ramos, J. E. Suspension reduction technology for ironmaking with low CO_2 emission and energy requirement. *Iron Steel Tech. (AIST)*, **2009**, *6*, 158-165.

(22) Herty (Jr), C. H. Chemical equilibrium of manganese, carbon and phosphorus in the basic open hearth process. *Trans. AIME,* **1926**, *73*, 1107-1134.

(23) Turkdogan, E. T.; Pearson, J. Activities of constituents of iron and steelmaking slags. III. P_2O_5. *J. Iron Steel Inst., London,* **1953**, *175*, 393-401.

(24) Rosenqvist, T. *Principles of Extractive Metallurgy*, Tapir Forlag, **2004**, 305.

(25) Fruehan, R. J. *The making, shaping and treating of steel*, The AISE Steel Foundation, 11th edition: Pittsburgh, 1998.

(26) Mohassab-Ahmed, M. Y.; Sohn, H. Y.; Kim, H. G., Sulfur distribution between liquid iron and magnesia-saturated slag in H_2/H_2O atmosphere relevant to a novel green ironmaking technology. *Ind. Eng. Chem. Res.*, **2012**, *51*, 3639-3645.

(27) Nzotta, M. M.; Nilsson, R.; Sichen, D.; Seetharaman, S. Sulfide capacities in $MgO-SiO_2$ and $CaO-MgO-SiO_2$ slags. *Ironmaking Steelmaking,* **1997**, *24*, 300-305.

(28) Osborn, E. F.; DeVries, R. C.; Gee, K. H.; Kraner, H. M. Optimum composition of blast-furnace slag as deduced from liquidus data for the quaternary system $CaO-MgO-Al_2O_3-SiO_2$. *J. Met.,* **1954**, *6*, 33-45.

(29) Healy, G. W. New look at phosphorus distribution. *J. Iron Steel Inst.,* London, **1970**, *208*, 664-668.

(30) Brandberg, J.; Yu, L.; Sichen, D. Water capacity model of $Al_2O_3-CaO-MgO-SiO_2$ quaternary slag system. *Steel Res.,* **2007**, *78*, 460-464.

(31) Zuliani, D. J.; Iwase, M.; McLean, A.; Meadowcroft, T. R. An experimental study of the kinetics and thermodynamics of water vapor dissolution in a $CaO-SiO_2-MgO$ slag. *Can. Metall. Quart.*, **1981**, *20*, 181-187.

(32) Sosinsky, D. J.; Maeda, M.; McLean, A. Determination and prediction of water vapor solubilities in $CaO-MgO-SiO_2$ slags. *Metall. Trans. B,* **1985**, *16B*, 61-66.

(33) Yokokawa; T. Gas solubilities in molten salts and silicates. *Pure Appl. Chem,* **1986**, *58*, 1547-1552.

(34) Jo, S. K.; Kim, S. H. The solubility of water vapour in $CaO-SiO_2-Al_2O_3-MgO$ slag system. *Steel Res.,* **2000**, *71*, 15-21.

(35) Brandberg, J.; Sichen, D. Water vapor solubility in ladle-refining slags. *Metall. Trans. B,* **2006**, *37*, 389-393.

(36) Turkdogan, E.T. *Fundamentals of Steelmaking*, The Institute of Materials, London, **1996**.

(37) Selin, R.; Dong, Y.; Wu, Q. Uses of lime-based fluxes for simultaneous removal of phosphorus and sulphur in hot metal pretreatment. *Scand. J. Metall.,* **1990**, *19*, 98-109.

(38) Lu, Q.; Li, F. M.; Zhang, S. H.; Huang, J. M. Effect of temperature and gas pressure on phosphorus capacity of $CaO-SiO_2-Al_2O_3-MgO-Fe_tO$ system. *Chinese Journal of Nonferrous Metals*, **2007**, *17*, 1871-1875.

(39) Kawecka-Cebula, E. Determination of the phosphorus capacity and phosphor partition coefficient from the chemical composition of slag. *Metall. Foundry Eng.,* **1998**, *24*, 71-87.

(40) Mohassab-Ahmed, M. Y.; Sohn, H. Y.; Kim, H. G., Phosphorus distribution between liquid iron and magnesia-saturated slag in H_2/H_2O atmosphere relevant to a novel ironmaking technology. *Ind. Eng. Chem. Res.* **2012,** *51*, 7028-7034.

(41) Turkdogan, E. T., Physicochemical aspects of reactions in ironmaking and steelmaking processes. *Trans. Iron Steel Inst. Jpn.* **1984,** *24*, 591-611.

(42) Habashi, F. *Handbook of Extractive Metallurgy*, Vol. I, Wiley-VCH, Weinheim, **1997**, 53.

(43) Biswas, A. K. *Principles of Blast Furnace Ironmaking: theory and practice*, Cootha Pub. House, **1981**.

(44) Sohn, H. Y.; Choi, M. E.; Olivas-Martinez, M.; Kim, H. G. A novel flash ironmaking process. *Proceedings of Cleantech 2011*, Budapest, Hungary International Conference on Clean Technologies in the Steel Industry, Budapest, Hungary, September 26-28, **2011**.

CHAPTER 6

EFFECT OF GAS ATMOSPHERE ON ACTIVITY OF IRON OXIDE IN SLAGSRELEVANT TO A FLASH IRONMAKING TECHNOLOGY

6. 1. Introduction

Iron oxide plays an important role in metal-slag reactions, including those involved in sulfur and phosphorus distribution. In addition, FeO in the slag is considered as a loss in ironmaking and steelmaking processes. Moreover, FeO content in the slag affects its viscosity.[1] Thus, FeO activity (a_{FeO}) in slag and its thermodynamics attracted the attention of many researchers.[2-6] The present work is an integral part of a research project that aims to develop a novel green ironmaking process based on the direct gaseous reduction of iron oxide fine concentrate in a flash-type process. The ultimate goal of this new process is to significantly reduce CO_2 emissions, energy consumption, and environmental pollution in the steel industry.[7] Hydrogen, natural gas, and coal gas are the proposed reducing agents in that new process. To date, only a few studies have been performed to measure FeO activities under gas atmospheres containing H_2O and H_2.[8-10] Thus, as part of the development of this new green ironmaking project, there was a needto thoroughly investigate the behavior of FeO in the H_2/H_2O and $CO/CO_2/H_2/H_2O$ atmospheres, corresponding to an oxygen partial pressure (pO_2) range of 10^{-10} - 10^{-9} atm.

In addition, the activity of FeO under CO/CO_2 was investigated to enable a comparison with the blast furnace (BF) conditions. The major slag components were CaO, MgO, SiO_2, Al_2O_3, and FeO representing the blast furnace slag. The FeO activity coefficient was studied in the temperature range 1550-1650°C encompassing the expected operating temperatures in the proposed process.

There are two main methods to determine FeO activity. The first method is the thermodynamic relationships and EMF measurements. In this method, FeO activity can be measured using an oxygen sensor and thermodynamic relationship between $Fe_{(l)}$-$FeO_{(slag)}$ expressed as follows[11]:

$$Fe_{(l)} + \frac{1}{2}O_{2(g)} = FeO_{(l)},\ \Delta G^{\circ}_{FeO} = -225{,}460 + 41.26T \quad (J/mol) \qquad (6\text{-}1)$$

Using the EMF reading from an oxygen sensor, the equilibrium pO_2 can be calculated by the Nernest equation.[12] This technique was adopted by Liu *et al.*,[12, 13] Ogura *et al.*,[14] Iwase *et al.*,[15] and Hamm *et al.* [16]

The second method is the thermodynamic equilibrium technique with chemical analysis. This technique is the most common one used to measure a_{FeO} in which the slag sample is equilibrated with liquid iron or solid iron at a fixed temperature and under a stable atmosphere. In this technique, different principles could be employed to calculate the FeO or Fe_tO activity in the slags. These principles are listed as follows:

(1) Slag-Metal Equilibrium Technique:

This technique is based on the following reactions:

$$Fe_{(l)} + \underline{O} = FeO_{(slag)} \qquad (6\text{-}2)$$

$$Fe_{(l)} + \underline{O} = FeO_{(l)} \qquad (6\text{-}3)$$

$$a_{FeO} = \frac{(wt\%O)}{(wt\%O)^{\circ}} \qquad (6\text{-}4)$$

where a_{FeO} : FeO activity in the slag sample

$(wt\%O)$: analyzed oxygen content in liquid iron in equilibrium with molten slag under consideration, equilibrium 6-2

$(wt\%O)^{\circ}$: analyzed oxygen content in liquid iron in equilibrium with pure liquid FeO, equilibrium 6-3

This technique was adopted by Chipman.[17, 18] The technique was further modified to become more accurate by replacing the weight percent oxygen in eq 6-4 with the activity (by multiplying both the numerator and denominator by the corresponding Henrian activity coefficients). Furthermore, the interaction between other impurities and alloying elements was considered.[12]

Alternatively, molten slags contained in an iron crucible would be brought into equilibrium under a CO/CO_2 or H_2/H_2O atmosphere. The FeO activity can be obtained from the expression:

$$a_{FeO} = \left(\frac{pO_2}{pO_2^{\circ}} \right)^{1/2} \qquad (6\text{-}5)$$

where pO_2: the equilibrium oxygen partial pressure for a mixture of solid Fe + FeO in liquid slag

pO_2°: the equilibrium oxygen partial pressure for a mixture of solid Fe + pure liquid FeO.

This technique was used by Schumann and Ensio.[19] This technique requires a relatively complex experimental setup and long duration.[15]

(2) Gas-Slag-Metal Equilibrium Technique:

A different method to calculate the FeO activity considering the gas-slag-metal equilibria uses reaction 6-1, for which the equilibrium constant is given by:

$$K_{FeO} = e^{\frac{-\Delta G^\circ_{FeO}}{RT}} = \frac{a_{FeO}}{a_{Fe} \cdot pO_2^{1/2}} = \frac{x_{FeO} . \gamma_{FeO}}{a_{Fe} \cdot pO_2^{1/2}} \qquad (6\text{-}6)$$

where x_{FeO} and γ_{FeO} are FeO mole fraction and Raultian activity coefficient in the slag. This technique was employed in this study. ΔG°_{FeO} was calculated using HSC 5.11 (Outokumpu Oyj, Riihitontuntie 7, Finland).

(3) Minor Elements Distribution Techniques:

Alternatively, FeO activity can be obtained from sulfide capacity or phosphate capacity.[12] Using the following equation from Bell's work[20]:

$$L_S = \frac{f_S \cdot C_S \cdot a_{Fe} \cdot K_{FeO}}{a_{FeO} \cdot K_S} \qquad (6\text{-}7)$$

Also, using a relation obtained by Lee and Fruehan,[21] FeO activity can be obtained from the phosphorus distribution and phosphate capacity data.

FeO activity has been studied under different atmospheres. Basu *et al.*,[3] Hamm *et al.*,[16] Liu *et al.*, [12, 13] Morales *et al.*,[22] and Park and Lee[23] used argon atmosphere. More commonly, a larger number of researchers[4, 24-26] determined FeO activity by controlling pO_2 through the CO/CO_2 equilibrium. Few studies have been performed to determine free energy of formation of FeO using H_2/H_2O mixtures such as Chipman,[8] who used the equilibrium between liquid electrolytic iron and H_2/H_2O gas mixtures. Also, Chipman and Marshall[27] studied the equilibrium between solid iron and both liquid and solid wustite (separately) under H_2/H_2O gas mixtures. To the best of the authors' knowledge, there were no available data on the FeO activity coefficient under H_2/H_2O gas mixtures in ironmaking slags.

In this study, the following mass concentration ratio was used as slag basicity index:

$$\frac{wt\%CaO}{wt\%SiO_2} \qquad (6\text{-}8)$$

The nonstoichiometry of ferrous oxide observed by Darken[28] was found to be of negligible significance by Deo and Boom.[29] They suggested that the free energy of formation of ''FeO'' and that of Fe_xO may be considered as the same. Thus, this convention has been adopted in the present work.

6. 2. Experimental Details

The experimental procedure was discussed in details elsewhere.[30-32] The dry powders of SiO_2, Al_2O_3, and MgO were premelted at 1600°C for homogeneity. The premelted slag was ground to less than 40 μm particle size and mixed for 36 h in a tumbler mixer (Bioengineering Inc., Cambridge, MA). Then, the synthetic slag was stored in a desiccator to be used in the experiments. A horizontal electrical resistant furnace heated by $MoSi_2$ heating elements with an alumina reaction tube (8 cm OD, 7cm ID, 120 cm length) was used in the experimental set-up, which was equipped with a water vapor generator system. Temperature was controlled and monitored inside the tube by two B-type thermocouples (Pt6%Rh/Pt30%Rh). One connected to a 708P temperature controller (MTI Corporation, Richmond, CA) with an advanced PID adjustment to control the power supplied to the heating elements in the furnace with an accuracy of ±1°C. The other thermocouple monitored the experimental temperature near the samples, indicating a deviation of 0.2 - 0.5°C. The gases flow rates were controlled by Aalborg mass flow controllers (MFC) (AALBORG, Orangeburg, NY) with an accuracy of ±0.1, ±2, ±1.5, ±1.5 mL/min for SO_2, H_2, CO, and CO_2 gases, respectively. Water was injected as a liquid using a MASTERFLEX digital peristaltic pump drive (Cole-Parmer Instrument, Vernon Hills, Illinois), which provided flow rates from 0.001 mL/min to 3400 mL/min using the same brand pump head with an accuracy of ± 0.1% of the flow rate.

The initial slag composition other than FeO was chosen to be close to that in the blast furnace. The temperature and oxygen partial pressure ranges were chosen to be 1550-1650°C and 10^{-10} - 10^{-9} atm, respectively, which were wide enough to encompass

the expected operating temperature of the new process based on the hydrogen or natural gas reduction of iron ore concentrate.

The samples were prepared as 2.5 and 1.0 g of slag mixed with 2.5 and 1.0 g of iron powder, respectively, for experiments under H_2/H_2O and the comparison set of experiments under the three gas atmospheres (see Chapter 2 for details). They were mixed well to reduce the time to reach equilibrium in magnesia crucibles (1.8 cm OD, 4 cm height, 0.25 cm wall thickness) supplied by Ozark Technical Ceramics, Inc. (Webb City, MO). The furnace was heated to the target temperature under a flow of N_2. At the target temperature, the furnace was opened to introduce the four-sample alumina holder to the even temperature zone. Then, N_2 was switched to the experimental gas mixture. From preliminary experiments,[30, 31] it was confirmed that no perceptible change in FeO content in the slag occurred after 4 h. To assure 3-phase (gas-slag-metal) equilibrium, 10 and 15 h were chosen in this work. After equilibrium, the system was purged with ultra-high purity N_2 for 5 min. The furnace was then opened, the holder was pulled out quickly, and the samples were quenched in ice bath or cold water. The crucible itself together with the sample was crushed, and iron was separated from the slag. Then, the slag was finely ground.

The composition of the slag phase was analyzed by ICP-OES. Prior to analysis, the samples were digested in closed Savillex® microwavable vessels. The chemical analysis results are listed in Tables 6-1 and 6-2, respectively. Reproducibility of the experiments was confirmed by the consistency of the results of repeated experiments under the same conditions, as well as the reproducibility of the analysis method. [30, 31] The experimental accuracy was better than ±10 %.

Table 6-1. Chemical analysis of the samples under H_2/H_2O atmosphere

Sample	T (°C)	pO_2	CaO/ SiO_2	FeO (wt%)	MgO (wt%)	CaO (wt%)	Al_2O_3 (wt%)	SiO_2 (wt%)	X_{FeO}	γ_{FeO}	a_{FeO}
S5	1550	7.0×10^{-10}	0.8	21.6	19.2	20.9	8.7	28.3	0.21	2.17	0.45
S6	1550	7.0×10^{-10}	1	19.9	20.2	23.0	8.0	33.0	0.18	2.54	0.45
S7	1550	7.0×10^{-10}	1.2	22.3	15.2	29.8	9.5	26.4	0.21	2.16	0.45
S8	1550	7.0×10^{-10}	1.4	20.7	10.6	32.1	9.4	23.7	0.21	2.15	0.45
S9	1550	1.0×10^{-10}	0.8	11.5	22.4	24.9	8.2	32.3	0.10	1.75	0.17
S10	1550	1.0×10^{-10}	1	12.0	18.7	29.0	9.7	29.9	0.10	1.64	0.17
S11	1550	1.0×10^{-10}	1.2	12.4	17.0	30.9	10.7	29.0	0.11	1.58	0.17
S12	1550	1.0×10^{-10}	1.4	14.2	14.5	34.7	9.8	31.0	0.12	1.41	0.17
S13	1550	2.0×10^{-10}	0.8	12.2	22.5	25.1	9.4	32.6	0.10	2.34	0.24
S14	1550	2.0×10^{-10}	1	12.6	16.9	27.4	8.8	39.7	0.10	2.31	0.24
S15	1550	2.0×10^{-10}	1.2	18.7	15.4	34.7	10.2	16.4	0.18	1.33	0.24
S16	1550	2.0×10^{-10}	1.4	15.3	16.3	32.4	10.4	28.4	0.13	1.80	0.24
S17	1600	5.0×10^{-9}	0.8	41.1	15.1	15.8	6.2	19.5	0.49	1.57	0.77
S18	1600	5.0×10^{-9}	1	34.6	13.6	20.4	7.4	24.4	0.37	2.06	0.77
S19	1600	5.0×10^{-9}	1.2	42.8	11.3	18.1	6.3	17.0	0.54	1.41	0.77

Table 6-1. Continued

Sample	T (°C)	pO_2	CaO/ SiO_2	FeO (wt%)	MgO (wt%)	CaO (wt%)	Al_2O_3 (wt%)	SiO_2 (wt%)	X_{FeO}	γ_{FeO}	a_{FeO}
S20	1600	5.0×10^{-9}	1.4	52.8	12.4	14.9	4.9	12.2	0.74	1.03	0.77
S21	1600	2.0×10^{-9}	0.8	20.4	22.6	20.7	7.6	27.7	0.19	2.60	0.49
S21	1600	2.0×10^{-9}	0.8	20.3	22.6	20.7	8.6	27.6	0.18	2.62	0.49
S22	1600	2.0×10^{-9}	1	27.1	15.7	22.7	8.2	23.5	0.28	1.73	0.49
S22	1600	2.0×10^{-9}	1	27.0	17.6	22.6	8.2	23.2	0.28	1.76	0.49
S23	1600	2.0×10^{-9}	1.2	29.7	14.2	26.2	8.8	22.0	0.30	1.62	0.49
S23	1600	2.0×10^{-9}	1.2	29.7	14.2	23.7	8.3	22.0	0.32	1.52	0.49
S24	1600	2.0×10^{-9}	1.4	31.1	14.7	24.9	7.9	21.7	0.31	1.55	0.49
S25	1600	3.0×10^{-10}	0.8	8.7	25.5	24.3	9.7	36.0	0.07	2.77	0.19
S26	1600	3.0×10^{-10}	1	9.3	21.2	27.1	9.8	31.5	0.08	2.42	0.19
S27	1600	3.0×10^{-10}	1.2	11.8	18.7	29.1	10.1	28.2	0.10	1.84	0.19
S28	1600	3.0×10^{-10}	1.4	13.2	19.4	31.0	9.9	23.9	0.11	1.64	0.19
S29	1600	5.0×10^{-10}	0.8	7.1	23.9	23.9	9.6	31.5	0.06	4.09	0.24
S30	1600	5.0×10^{-10}	1	14.7	20.9	25.5	9.6	28.9	0.13	1.88	0.24
S31	1600	5.0×10^{-10}	1.2	14.9	25.3	25.2	8.9	23.6	0.13	1.90	0.24
S37	1650	4.0×10^{-9}	0.8	32.6	20.5	17.8	7.6	23.5	0.34	1.33	0.45
S38	1650	4.0×10^{-9}	1	47.5	14.2	13.5	5.5	16.3	0.63	0.72	0.45

Table 6-2. Chemical analysis of the samples under three different atmospheres

Sample	Gas Mixture	T (°C)	pO_2	CaO/SiO_2	FeO (wt%)	MgO (wt%)	CaO (wt%)	Al_2O_3 (wt%)	SiO_2 (wt%)	X_{FeO}	γ_{FeO}	a_{FeO}
R10	$CO/CO_2/H_2/H_2O$	1550	1.9×10^{-9}	0.8	21.7	24.6	20.3	13.0	25.5	0.16	4.5	0.74
R19		1550	1.6×10^{-10}	0.8	10.1	24.4	26.2	16.3	34.8	0.07	3.0	0.21
R20		1550	1.6×10^{-10}	1	9.8	17.9	30.7	8.4	31.8	0.08	2.8	0.21
R21		1550	1.6×10^{-10}	1.2	10.8	16.8	33.5	18.8	29.8	0.08	2.7	0.21
R22		1600	3.6×10^{-10}	0.8	13.0	23.4	26.0	15.7	32.3	0.09	2.2	0.21
R23		1600	3.6×10^{-10}	1	12.7	19.2	30.0	17.0	30.9	0.09	2.2	0.21
R24		1600	3.6×10^{-10}	1.2	12.4	16.6	32.8	17.2	28.6	0.09	2.2	0.21
R27		1630	6.4×10^{-10}	1.2	11.2	19.2	30.1	17.0	30.5	0.08	2.5	0.21
R46	CO/CO_2	1550	1.6×10^{-10}	0.8	35.5	10.2	24.5	13.9	22.8	0.29	0.7	0.20
R48		1550	1.6×10^{-10}	1.2	16.9	26.2	26.3	15.0	23.6	0.12	1.6	0.20
R49		1600	3.6×10^{-10}	0.8	14.7	22.1	25.7	15.2	31.9	0.11	1.9	0.21
R50		1600	3.6×10^{-10}	1	16.9	16.9	28.5	15.2	29.4	0.13	1.6	0.21
R51		1600	3.6×10^{-10}	1.2	15.3	14.7	30.7	16.6	26.7	0.12	1.7	0.21
R52		1630	6.4×10^{-10}	0.8	13.7	15.7	24.7	23.4	32.9	0.11	2.0	0.21
R53		1630	6.4×10^{-10}	1	14.6	14.3	28.0	17.0	36.4	0.11	1.9	0.21
R54		1630	6.4×10^{-10}	1.2	26.4	14.8	25.2	14.3	27.4	0.20	1.0	0.21
R74	H_2/H_2O	1550	1.6×10^{-10}	1	9.9	20.7	34.9	5.1	27.8	0.08	2.6	0.20
R75		1550	1.6×10^{-10}	1.2	9.6	19.7	31.2	17.1	32.1	0.07	2.8	0.20
R78		1600	3.6×10^{-10}	1.2	10.5	16.1	33.7	17.7	29.5	0.08	2.5	0.20
R'78		1600	3.6×10^{-10}	1.2	9.5	16.9	33.8	18.1	29.6	0.07	2.8	0.20

6. 3. Results and Discussion

Due to the lack of thorough studies on the activity of FeO under H_2/H_2O, the first part of this paper will be devoted to the discussion of the effect of different parameters such as basicity, FeO concentration, and MgO on γ_{FeO}, which was calculated using eq 6-6, under H_2/H_2O. Also, various models to estimate γ_{FeO} were evaluated to predict γ_{FeO} under H_2/H_2O (Section 6.4). An empirical formula was developed to correlate γ_{FeO} under experimental conditions adopted in this work. The second part of this paper compared the effect of gas composition on γ_{FeO}. In that part, a separate set of experiments were carefully carried out under the same conditions but different gas atmospheres ($CO/CO_2/H_2/H_2O$, CO/CO_2, and H_2/H_2).

6. 3. 1. Effect of X_{FeO} on Its Activity, a_{FeO}

Figure 6-1 presents the variation of a_{FeO} with X_{FeO} obtained in this work. It is apparent that FeO exhibits positive deviation from ideality for all slag compositions investigated. Similar behavior was reported by several authors, [13, 33, 34] including Basu *et al.*,[3] who reported the same trend with the transition from the positive deviation to ideality when X_{FeO} exceeded 0.4 under Ar atmosphere, as presented in Figure 6-2.

The results of the present work have been presented in Figure 6-2 along with the earlier work[3, 13, 33, 34] for comparison. Positive deviation of the activity of FeO was observed by these workers. Turkdogan and Pearson[34] had reported positive deviation of a_{FeO} in CaO-MgO-MnO-FeO-SiO_2 slags at all FeO concentrations with the exception of negative deviation only when X_{SiO2} was less than 0.008. Ichise and Iwase[35] observed negative

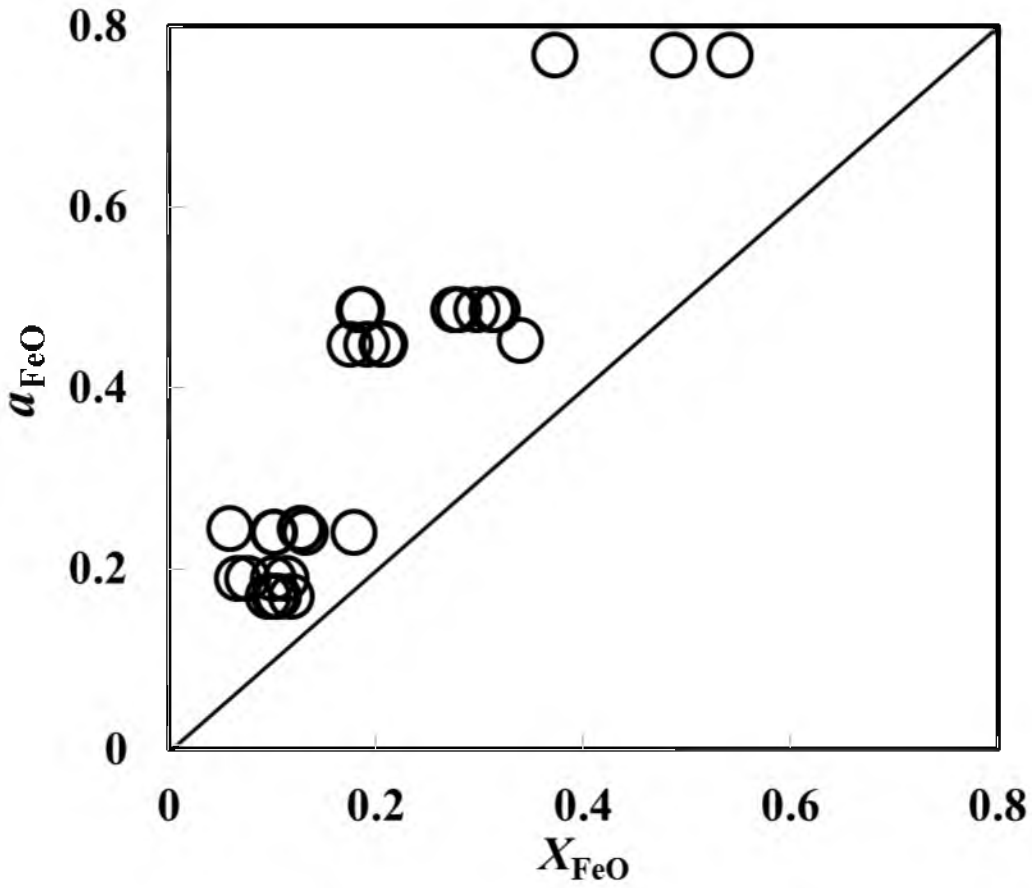

Figure 6-1. Variation of the activity of FeO with FeO mole fraction under H_2/H_2O atmosphere in the temperature range 1550 to 1650°C for slags with CaO/SiO_2 of 0.8 to 1.4.

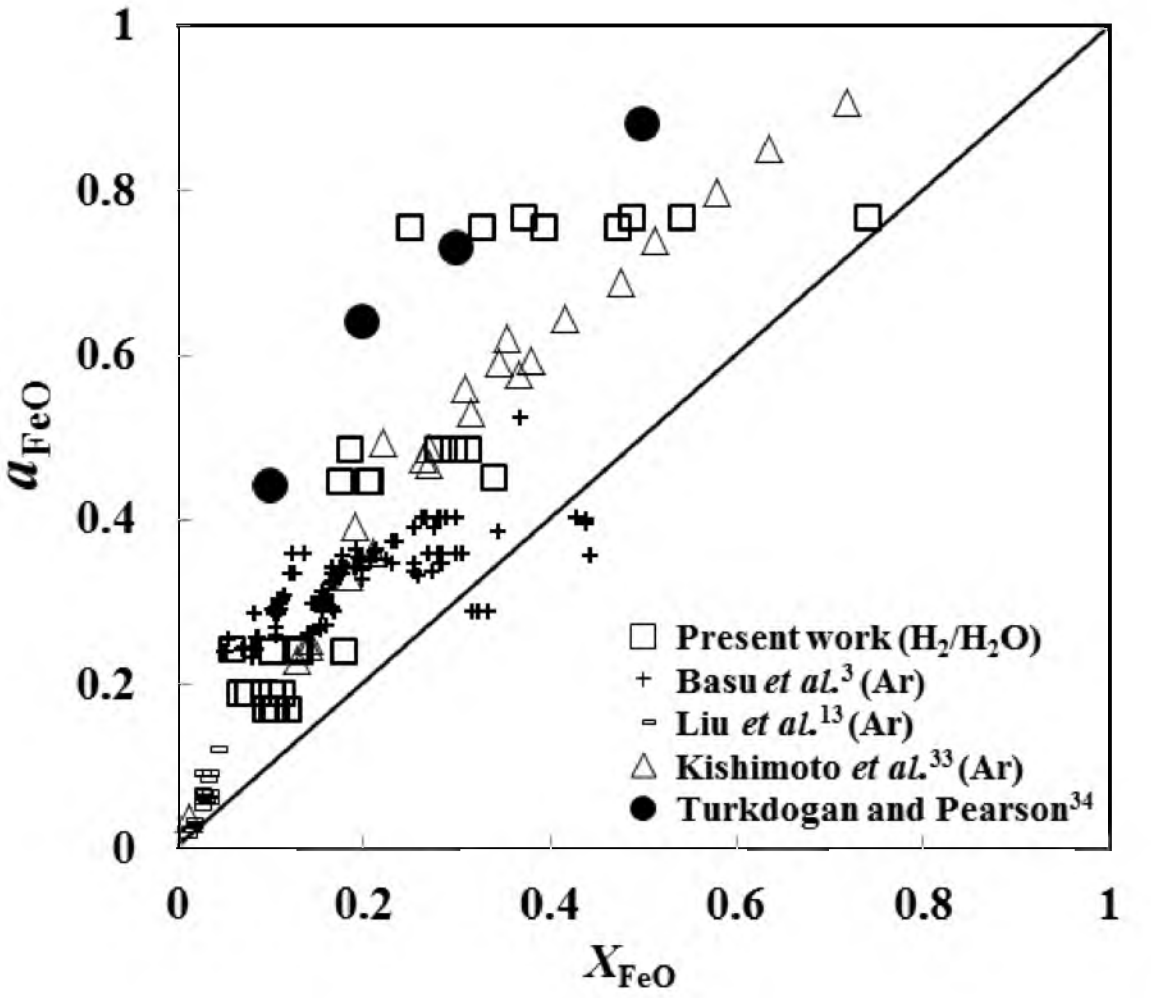

Figure 6-2. Variation of the activity of FeO with its mole fraction in complex slags, reported by others.[3, 13, 33, 34]

deviation in a few cases at low iron oxide concentrations ($X_{FeO} < 0.1$), whereas Wrampelmeyer *et al.*[36] observed some incidences of negative deviation of FeO at intermediate concentrations (X_{FeO} = 0.25 to 0.4). In contrast, Chipman[8] reported no positive deviation at all, but a small negative deviation of a_{FeO} at X_{FeO} exceeding 0.4.

6. 3. 2. Effect of Basicity on γ_{FeO}

Figures 6-3 – 6-6 show the variation of γ_{FeO} with basicity, defined as (wt% CaO/ wt% SiO_2), eq 6-8, for different pO_2, corresponding to different FeO concentration, and temperatures. It is noted that other more comprehensive basicity indices were attempted, but the results were too scattered to draw a conclusion. The current work used slag composition resembling ironmaking conditions so the basicity was in the range of 0.8-1.4. It is notable that γ_{FeO} shows a small decrease with an increase in basicity over the studied range at 1550°C, as shown in Figure 6-3, whereas at 1600°C and 1650°C γ_{FeO} decreases significantly with an increase in basicity, as shown in Figures 6-4 and 6-5.

Basu *et al.*,[3] in their experiment under Ar atmosphere in the temperature range 1600 to 1650°C, reported that the change in basicity as well as temperature has only a negligible effect on the activity coefficient of FeO, for any given range of FeO concentration. In their work, basicity was varied in the range of 1.2 to 3.5, resembling the conditions in a basic oxygen furnace (BOF). Over this wider range of basicity, only a moderate decrease in γ_{FeO} with increasing basicity was observed. In the present study, smaller increments in basicity were used, 0.2, over a narrower range where a noticeable decrease in γ_{FeO} with increasing basicity was observed, especially at 1600°C and 1650°C,

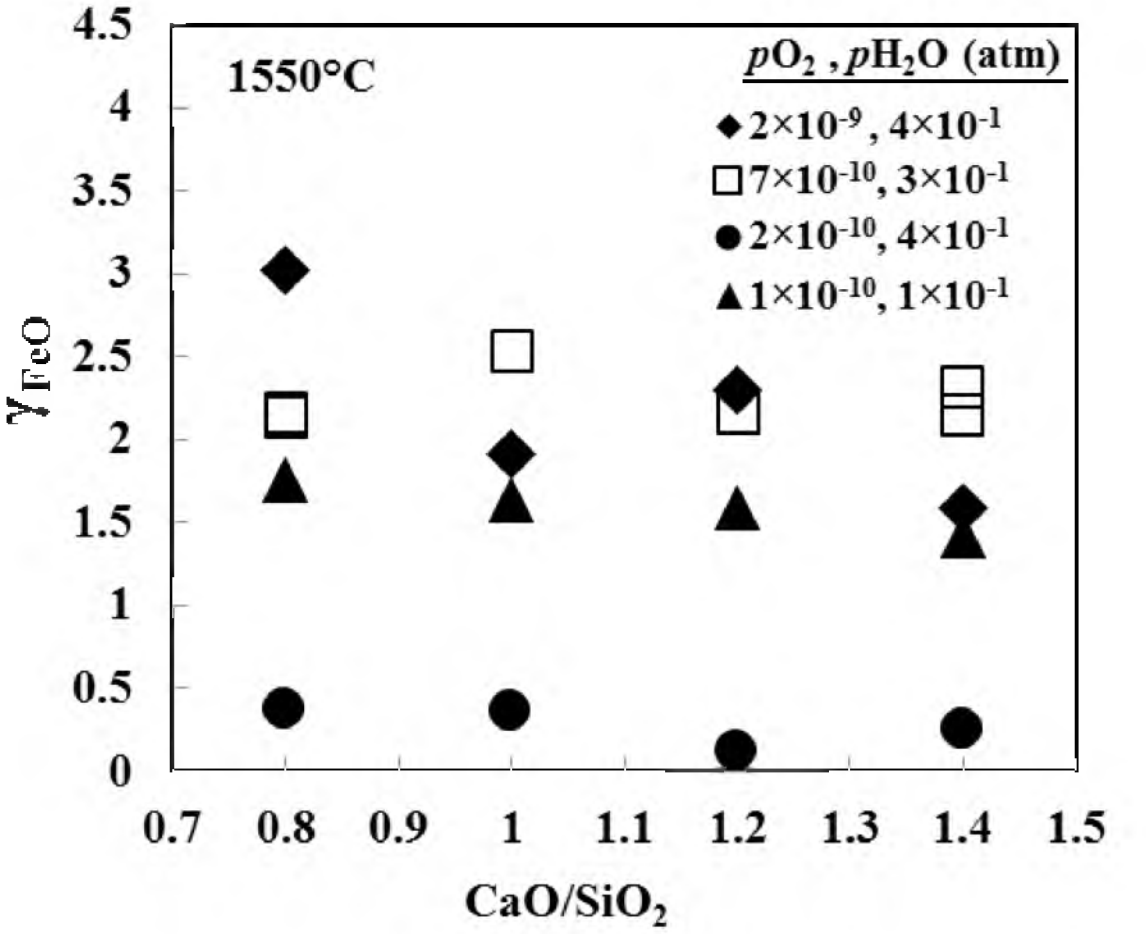

Figure 6-3. The effect of basicity on γ_{FeO} at 1550°C and different gas compositions under H_2/H_2O.

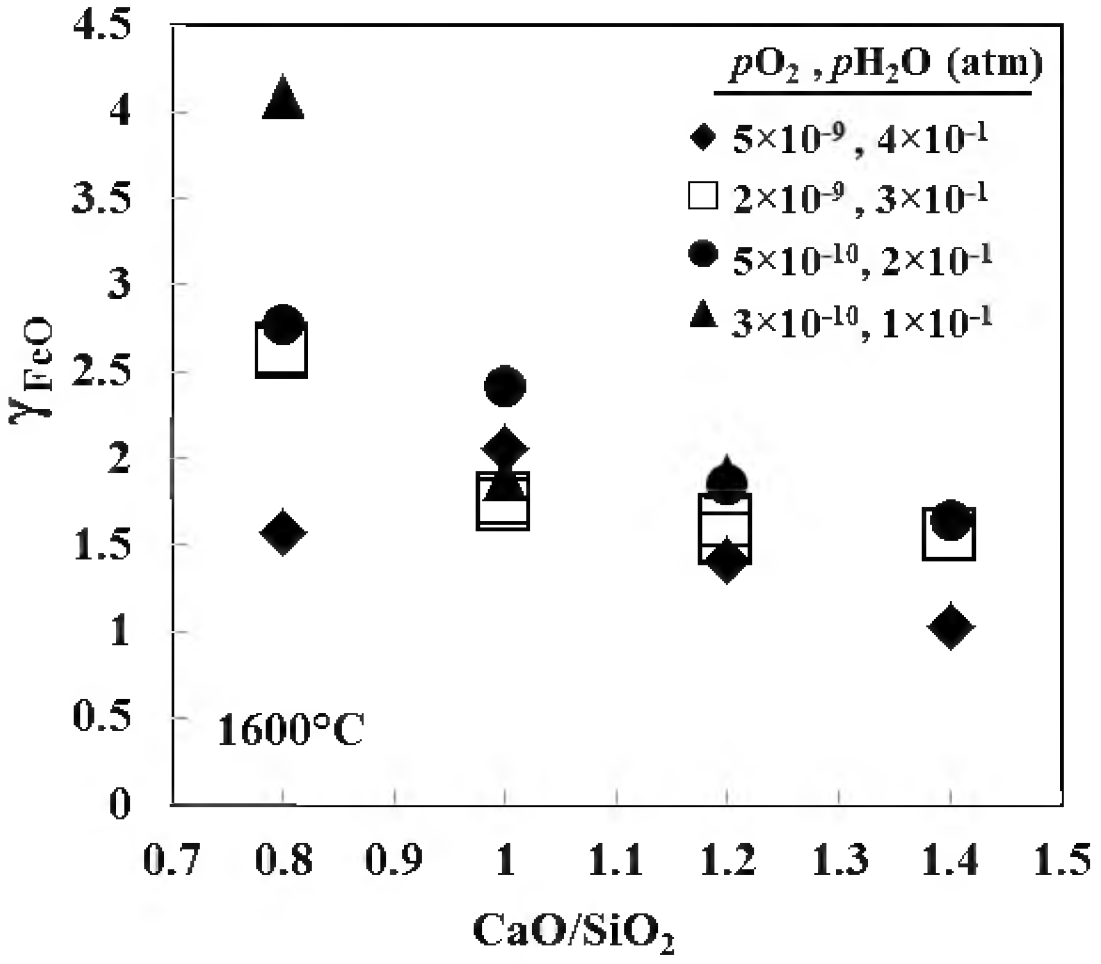

Figure 6-4. The effect of basicity on γ_{FeO} at 1600°C and different gas compositions under H_2/H_2O.

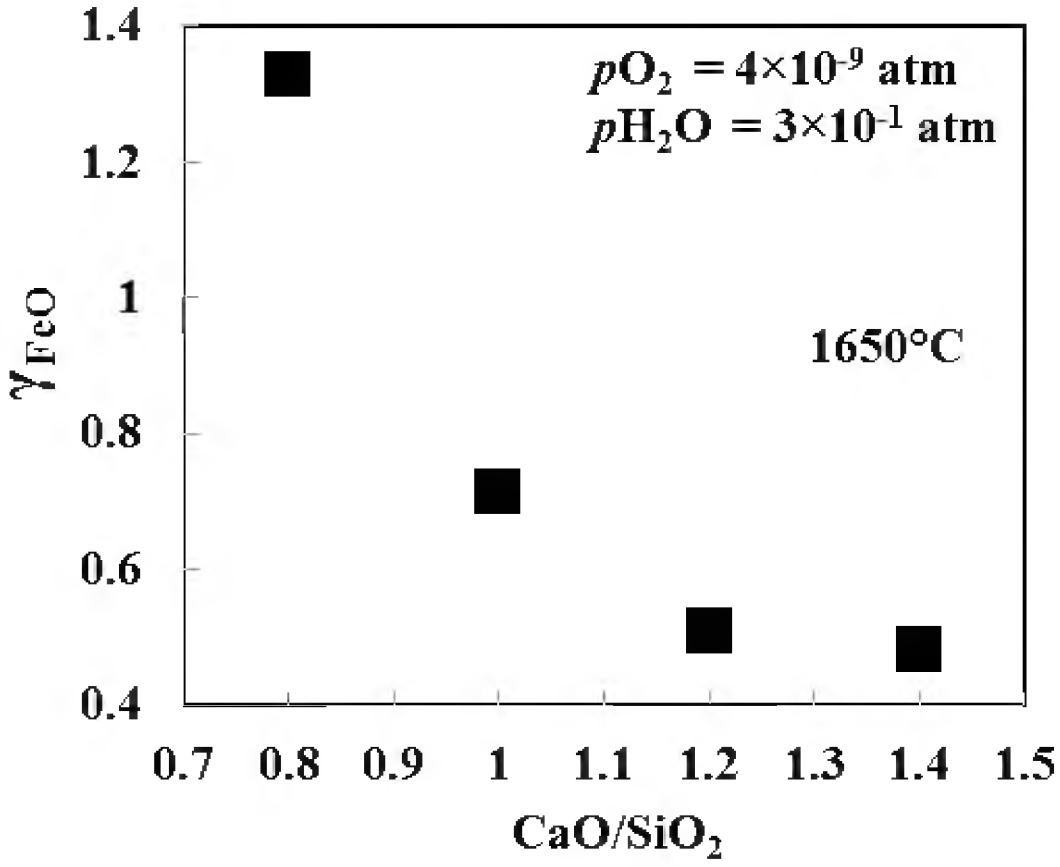

Figure 6-5. The effect of basicity on γ_{FeO} at 1650°C and pO_2= 4×10^{-9} atm under H_2/H_2O.

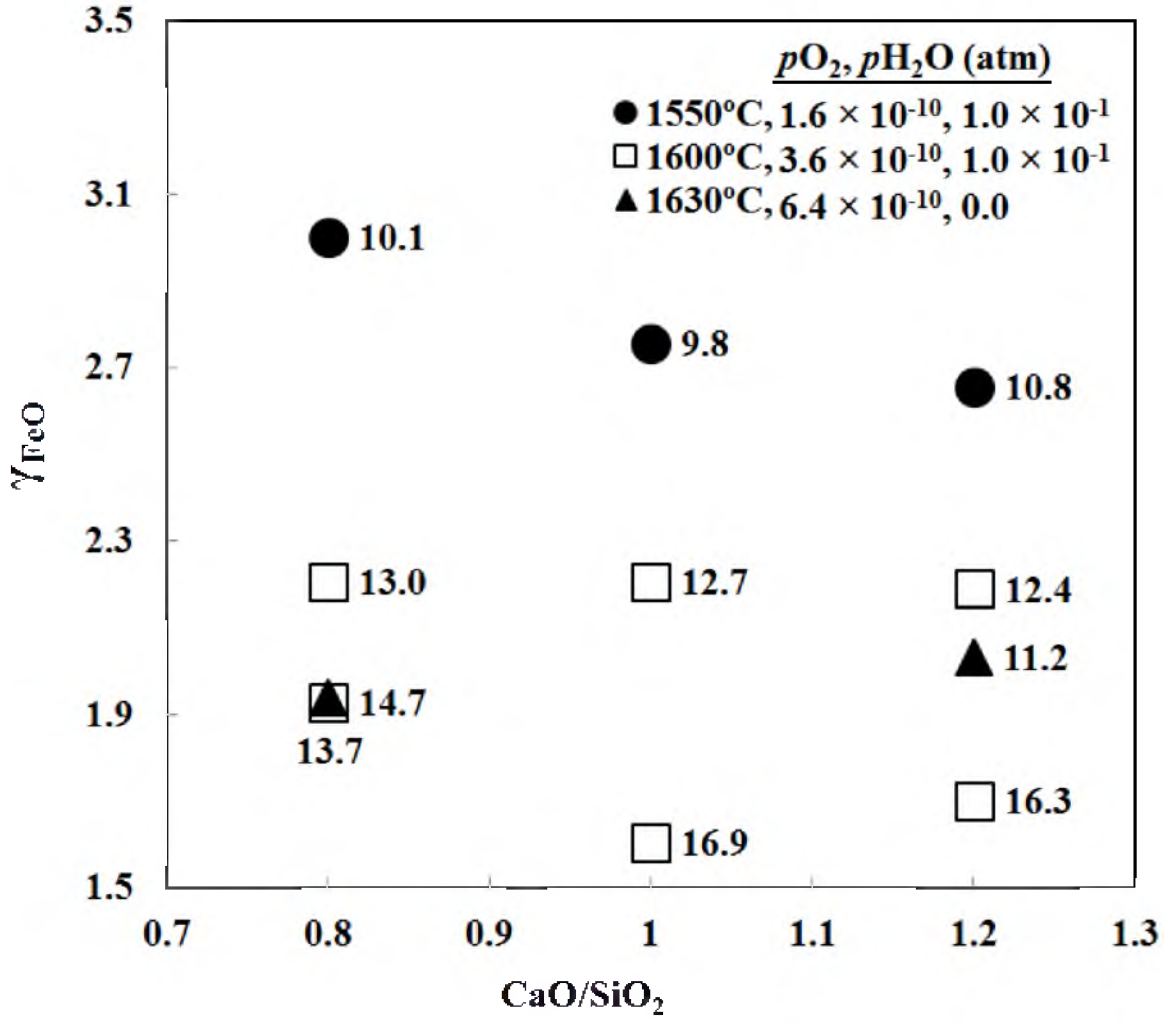

Figure 6-6. The effect of basicity on γ_{FeO} at 1550-1600°C and 1630°C under $CO/CO_2/H_2/H_2O$ and CO/CO_2, respectively.

as shown in Figures 6-4 and 6-5.

Kishimoto *et al.*[33] also reported a similar trend to that of Basu *et al.*[3] under Ar atmosphere. They concluded that the increase in basicity over the range X_{CaO}/X_{SiO2} = 2.0 to 6.0, at any level of FeO concentration, caused only a marginal decrease in the activity coefficient of FeO. Bishop *et al.*[18] reported a small decrease in a_{FeO} when the basicity, defined as the mole % ratio $(CaO+MgO+MnO)/(SiO_2+PO_{2.5}+Al_2O_3)$, increased beyond 2, for Fe_tO concentration within the range of 10 to 60 mole %. It is seen that all the above-mentioned authors reported smaller effects of basicity on γ_{FeO} than that in the current work over a wider basicity range.

6. 3. 3. Effect of FeO Concentration on γ_{FeO}

The main factor affecting γ_{FeO} is FeO concentration, besides basicity and temperature, over the investigated composition range. Figure 6-7 shows the variation of log γ_{FeO} with respect to log X_{FeO} at 1550°C, 1600°C, and 1650°C obtained in this work. As seen in this figure, no clear relation between log γ_{FeO} and log X_{FeO} could be obtained, other than an overall decrease in γ_{FeO} with X_{FeO}. A similar trend was reported by Basu *et al.*,[3] Kishimoto *et al.*,[20] Liu *et al.*[13] and by Henao and Itagaki,[4] whose findings are shown in Figure 6-8. On the other hand, Basu *et al.*[3] reported a systematic decrease of γ_{FeO} with increasing FeO concentration. Also, Figures 6-7 and 6-8 illustrate that the activity of FeO shows positive deviation at lower FeO concentrations and moves closer to ideality with FeO concentration increase. The activity coefficient of FeO appears to be very weakly dependent on temperature over the interval investigated.

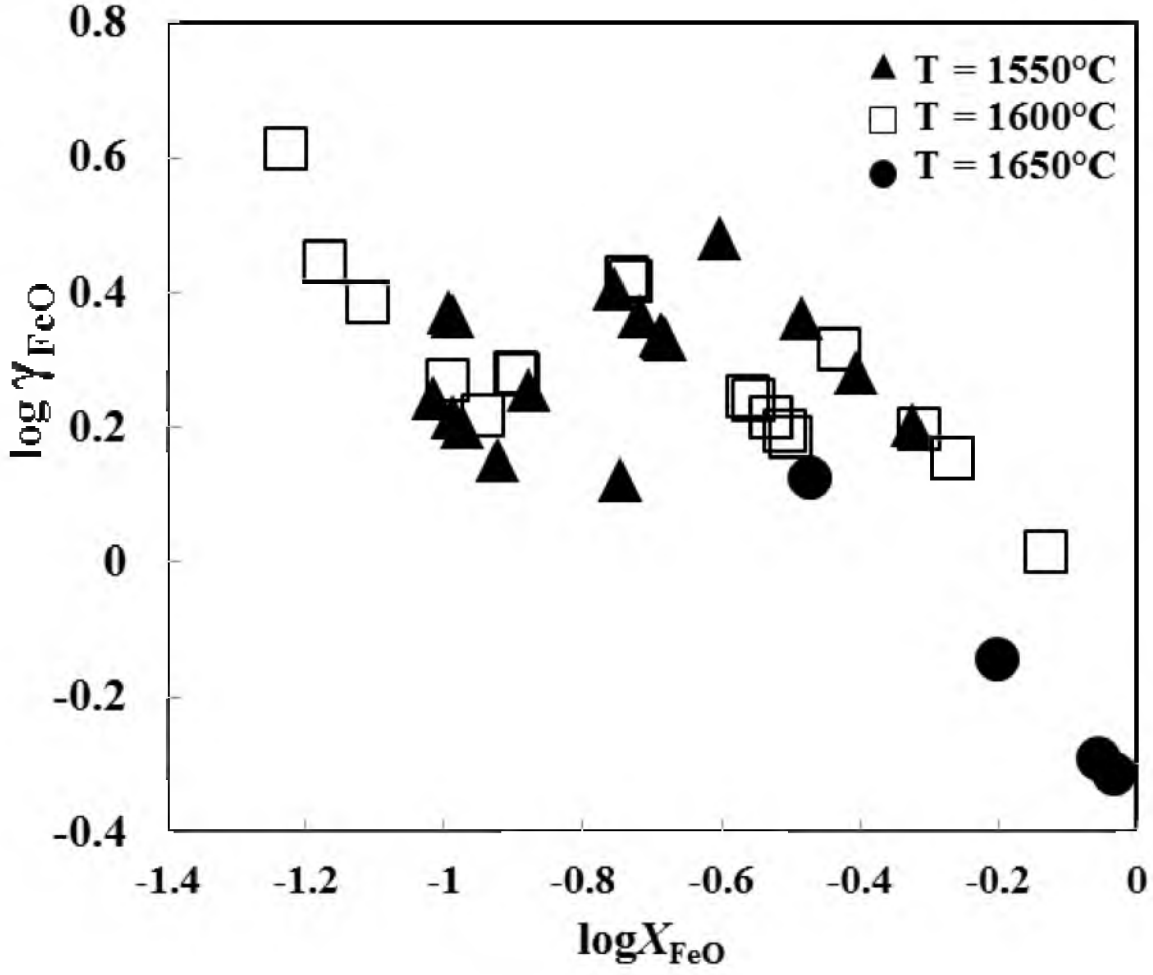

Figure 6-7. Effect of X_{FeO} on γ_{FeO} at different temperatures atm under H_2/H_2O.

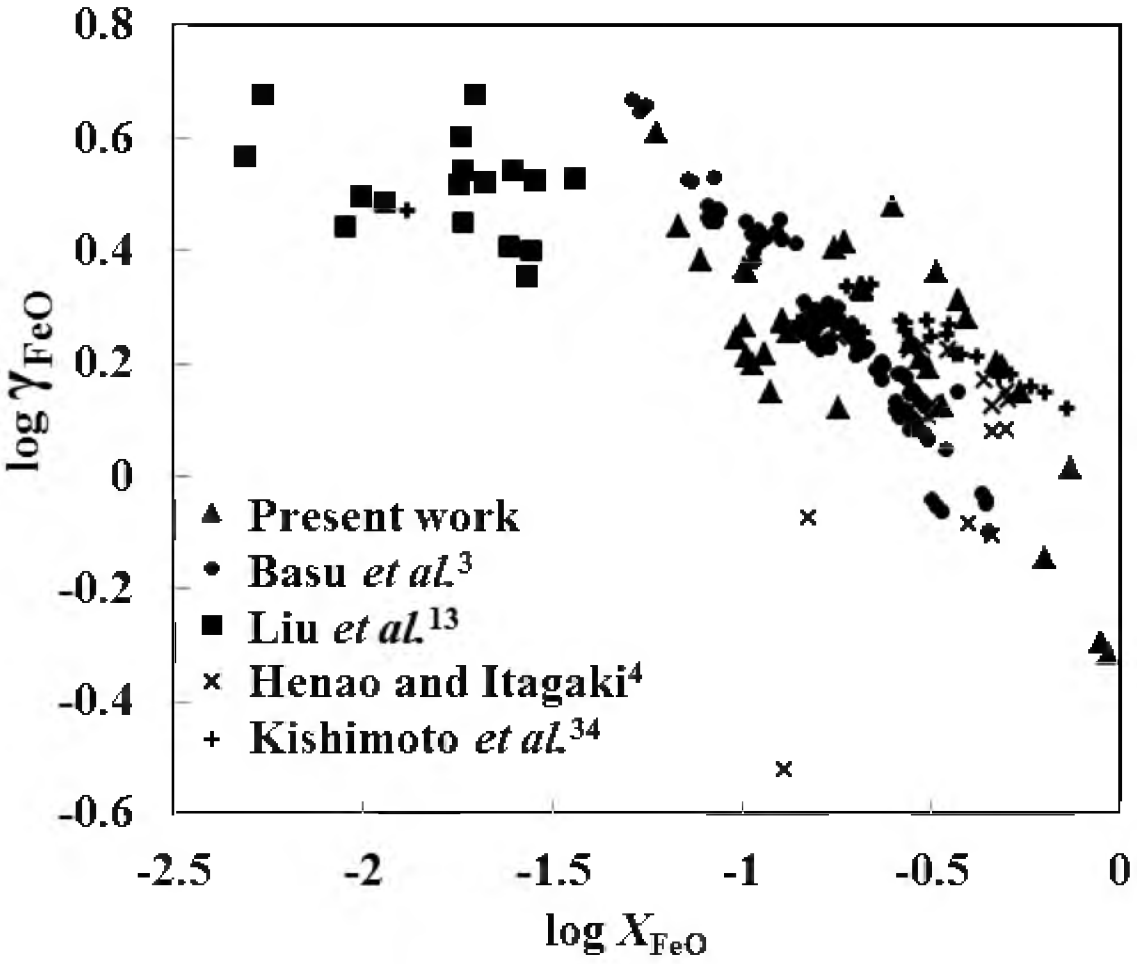

Figure 6-8. Effect of X_{FeO} on γ_{FeO} in complex slags reported by others.[3, 4, 13, 33]

6. 3. 4. Effect of MgO Concentrations on γ_{FeO}

Figure 6-9 shows the sffeect of X_{MgO} on $\log \gamma_{FeO}$ over different ranges of FeO concentration and at different temperatures under H_2/H_2O. It can be seen that γ_{FeO} increases with X_{MgO} in the invistigated slag compositions, regardless of the temperature, for slag with small X_{FeO} ($\leq$0.1), whereas MgO has negligible effect on γ_{FeO} in slag with higher X_{FeO}. Park and Lee[23] concluded that MgO has neglegible influence on γ_{FeO} for X_{FeO} >0.04, whereas increase of MgO decreases γ_{FeO} for slags with lower X_{FeO} in the $CaO\text{-}Al_2O_3\text{-}MgO_{sat.}\text{-}SiO_2\text{-}Fe_tO\text{-}MnO\text{-}P_2O_5$ system. Basu *et al.*[3] showed that γ_{FeO} was irresponsive to the change on MgO content regardless of X_{FeO} in the $CaO\text{-}MgO_{sat.}\text{-}SiO_2\text{-}FeO\text{-}MnO\text{-}P_2O_5$ slag.

6. 4. Thermodynamic and Mathematical Models of γ_{FeO}

In this section, an assessment of five models, available in the literature, for predicting γ_{FeO} in multicomponent slags was made with the experimentally obtained γ_{FeO}. These models will be referred to as Ohta and Suito's model,[37] Tao's model,[38] Yan's model,[39] Park and Lee's model,[40] and Zhang's model.[6]

Ohta and Suito's model[37] is an empirical model developed based on experimental data at 1600°C under deoxidized Ar atmosphere. They used MgO, Al_2O_3, SiO_2, and CaO as the only variables that affect γ_{FeO}. Ohta and Suito[37] used multiple regression analysis to obtain this empirical model without using any thermodynamic basis. Thus, the validity of this model is confined to slag compositions and conditions used in their work. The model predicts values that are quite different from the measured values in this work.

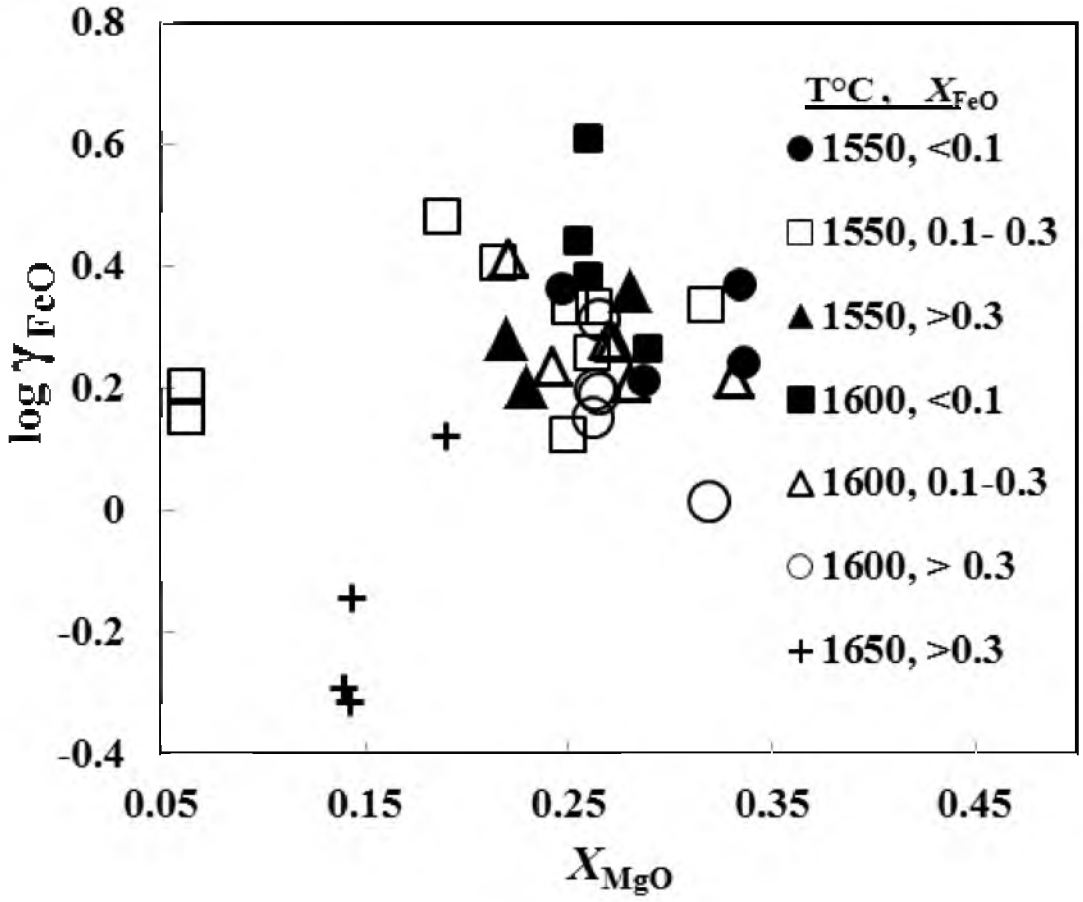

Figure 6-9. Effect of X_{MgO} on log γ_{FeO} over different ranges of FeO concentration and at different temperature atm under H_2/H_2O.

Thus, it was excluded from the evaluation of the experimental data. Tao's model [38] is only applicable to a CaO-SiO_2-FeO ternary slag system, which is quite different from the slag of the current study. Moreover, Tao's model is too complicated, many parameters of which need to be measured from binary slag systems. As a result, Tao's model was not further evaluated either.

Yan's model[39] was derived by quadratic formalism based on the regular solution moldel which was expressed as follows:

$$\begin{aligned}\ln\gamma_{FeO} = \frac{1}{RT}\{&-18660x^2_{FeO1.5} + 7110x^2_{MnO} - 41840x^2_{SiO_2} + 33470x^2_{MgO} - 31380x^2_{CaO}\\ &+ 44930x_{FeO1.5}x_{MnO} - 93140x_{FeO1.5}x_{SiO_2} + 17740x_{FeO1.5}x_{MgO} + 45770x_{FeO1.5}x_{CaO}\\ &+ 40580\,x_{MnO}.x_{SiO2} - 21340\,x_{MnO}.x_{MgO} + 67780\,x_{MnO}.x_{CaO} + 58570\,.x_{SiO2}x_{MgO}\\ &+ 60670\,.x_{SiO2}x_{CaO} + 102510x_{MgO}.x_{CaO}\}(J/mol)\end{aligned} \qquad (6-9)$$

Park and Lee's model[40] is also based on the regular solution model, as follows:

$$\begin{aligned}\ln\gamma_{FeO} = \frac{1}{RT}\{&-18670x^2_{FeO1.5} + 7120x^2_{MnO} - 41860x^2_{SiO_2} + 33490x^2_{MgO} - 31400x^2_{CaO}\\ &- 31400x^2_{PO_{2.5}} - 41020x^2_{AlO_{1.5}} + 44960x_{FeO1.5}x_{MnO} - 93180x_{FeO1.5}x_{SiO_2} - 21350x_{MnO}x_{MgO}\\ &+ 45790x_{FeO1.5}x_{CaO} + 40600\,x_{MnO}.x_{SiO2} + 67810\,x_{MnO}.x_{CaO} + 82460\,.x_{CaO}x_{AlO_{1.5}}\\ &+ 60700\,.x_{SiO2}x_{CaO} + 102560x_{MgO}.x_{CaO} + 39770.x_{MgO}x_{PO_{2.5}} + 58600x_{MgO}x_{SiO2}\\ &+ 188370x_{CaO}x_{PO2.5} + 17750x_{MgO}x_{FeO1.5} + 63630\,x_{MgO}x_{AlO_{1.5}} + 49810x_{AlO_{1.5}}x_{MnO}\\ &+ 44790x_{AlO_{1.5}}x_{SiO2} + 189210x_{AlO_{1.5}}x_{PO_{2.5}} + 101470x_{AlO_{1.5}}x_{FeO1.5} + 60700x_{MnO}x_{PO_{2.5}}\\ &- 156980x_{SiO_2}x_{PO_{2.5}} - 64720x_{PO_{2.5}}x_{FeO1.5}\}(J/mol)\end{aligned} \qquad (6-10)$$

In eqs 6-9 and 6-10, x_i is mole fraction of slag component *i*, T is absolute temperature,

and R is the universal gas constant (J/mol. K).

Zhang[6] developed his model based on the ion and molecule coexistence theory (IMCT) to quantify γ_{FeO}. This model is composed of a set of nonlinear equations to be solved using adequate thermodynamic correlations to predict the equilibrium X_{FeO} and a_{FeO} accordingly. The predicted γ_{FeO} using these three models was compared to the observed γ_{FeO} from this work; it was found that the coefficient of determination (r^2) < 0.5, which implies a poor ability of these models in calculating γ_{FeO} for the studied slags under H_2/H_2O. This is attributed to the fact that none of the aforementioned models considered the effect of gas atmosphere on γ_{FeO}. It is worth noting that the range of the obtained γ_{FeO} values under H_2O/H_2O were comparable to those ranges reported in the literature under Ar or CO/CO_2 atmospheres,[3, 4, 13, 33, 41, 42] as summarized in Table 6-3.
An empirical correlation was formulated using linear regression to adequately predict γ_{FeO} under H_2/H_2O in the studied slags. As mentioned earlier, the temperature was found to have a negligible effect on γ_{FeO} under the investigated conditions. Thus, it was excluded from the empirical correlation:

$$\log \gamma_{FeO} = -3.0623 X_{FeO} - 3.1421 X_{CaO} - 2.5068 X_{MgO} + 2.1957 \ (r^2 = 0.72) \quad (6\text{-}11)$$

Figure 6-10 used eq 6-11 to compare the measured values of γ_{FeO} to the predicted results. It is concluded that γ_{FeO} can be adequately estimated using this correlation. Incorporating additional compositional variables did not yield any significant improvement.

Table 6-3. Comparison of measured values of FeO activity coefficients in complex slags under different gas atmospheres

Reference	X_{FeO}	γ_{FeO}	T (°C)	Atmosphere
Nassaralla *et al.*[41]	0.006 - 0.014	4.2 - 9.3	1500 - 1550	Ar
Park and Lee[42]	0.009 - 0.052	1.8 - 2.5	1600	Ar
Liu *et al.*[13]	0.005 - 0.037	2.2 - 4.7	1550	Ar
Basu *et al.*[3]	0.051 - 0.444	0.803 - 4.698	1600 - 1650	Ar
Kishimoto *et al.*[33]	0.013 - 0.719	1.318 - 2.967	1450	Ar
Henao and Itagaki[4]	0.13 - 0.51	0.3 - 1.92	1400	CO/CO_2
Current study	0.056 - 0.483	0.483 - 4.086	1550 - 1650	H_2/H_2O

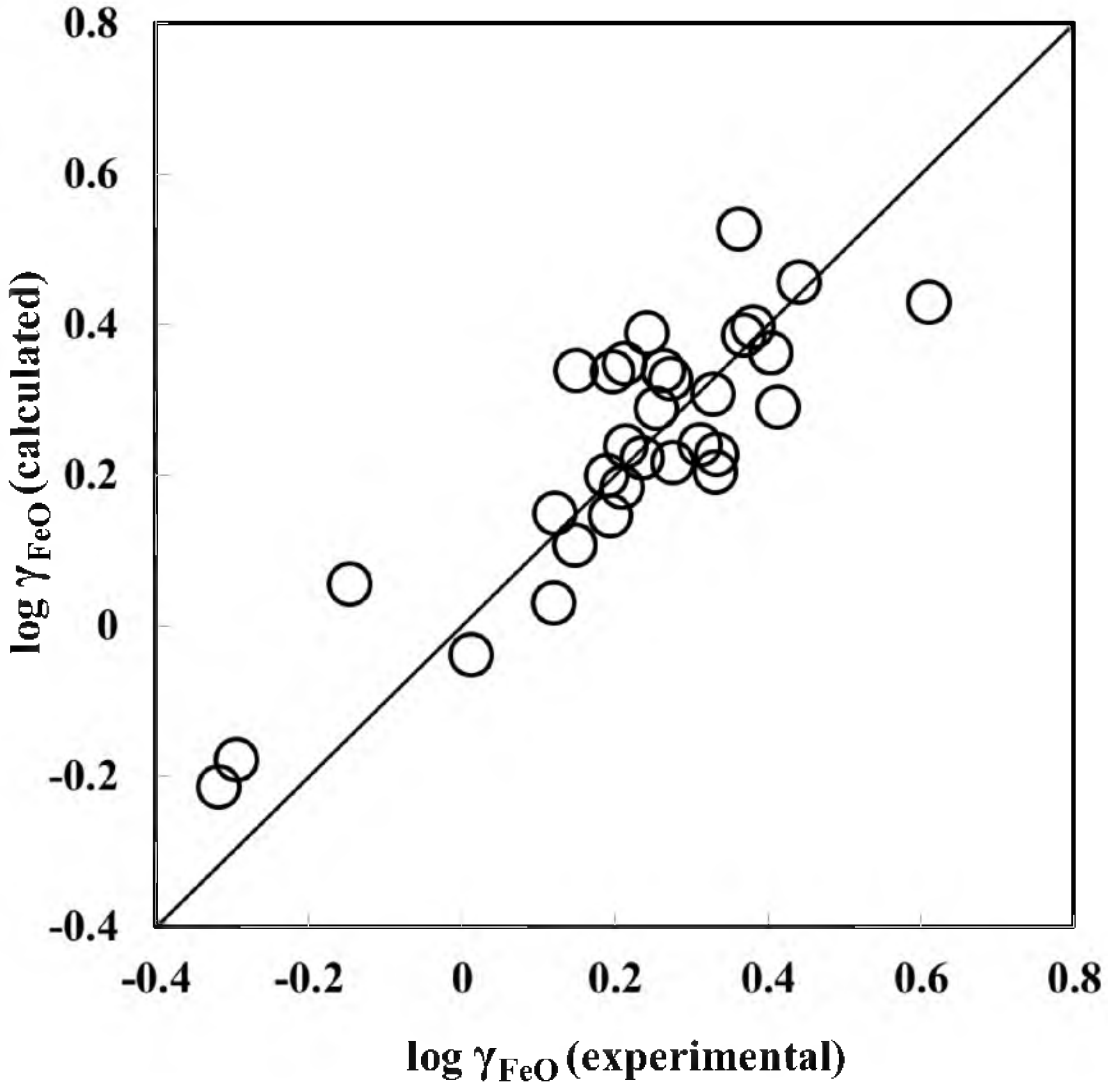

Figure 6-10. Comparison of $\log \gamma_{FeO}$ measured versus calculated using eq 6-11 under H_2/H_2O atmosphere in the temperature range 1550 to 1650°C and wt% CaO/ wt% SiO_2 range of 0.8 to 1.4 under pO_2 range of 10^{-10} to 10^{-9} atm.

6. 5. The Effect of Gas Atmosphere on γ_{FeO}

The major reactions involving FeO in the investigated slags under the experimental conditions are as follows, according to ion and molecule coexistence theory (IMCT)[6]:

$$2Fe^{2+} + SiO_4^{-4} = Fe_2SiO_4 \qquad (6\text{-}12)$$

$$Fe^{2+} + Al_2O_4^{2-} = FeAl_2O_4 \qquad (6\text{-}13)$$

It is worth noting that according to ion and molecule coexistence theory (IMCT), SiO_2 and Al_2O_3 exist as simple oxides, SiO_2 and Al_2O_3, equilibrated with complex molecules such as Fe_2SiO_4 and $FeAl_2O_4$. Iron oxide exists in the form ion couples, Fe^{2+} and O^{2-}, equilibrated with complex compounds such as Fe_2SiO_4 and $FeAl_2O_4$. We will focus on reaction 6-10 for the following reasons: 1) no previous research reported the interaction of H_2O with aluminate, 2) the higher silica content, at least 2-4 times higher, compared with alumina, and 3) no change was observed in spectroscopic analyses that could be related to alumina species as a result of changing the gas composition, as discussed in Chapter 3. Therefore, FeO would be stabilized in the slag mostly in the form of Fe_2SiO_4, i.e., Fe^{2+} forms stable silicates with the least polymerized silicate anion, SiO_4^{-4}.

Previous research [43-49] has shown that water has a significant solubility in slag in the temperature range of 1500-1650°C. In weakly to moderately basic slags, water analyses in the studied slags, Chapter 3)[49]:

$$H_2O + Si—O^{-}\cdots\cdots Fe^{2+}\cdots\cdots O^{-}—Si = 2Si—O—Si + Fe^{2+} + 2OH^{-} \qquad (6\text{-}14)$$

where the dotted and the solid lines represent coordination and covalent (stronger than coordination bond) bonds, respectively. It is noted that reaction 6-14 competes with reaction 6-12. Most FeO in the slag is combined with silicate ions according to reaction 6-12 and, therefore, any reaction that might perturb equilibrium 6-10 will affect γ_{FeO}. As discussed in Chapter 3, FeO is a network modifier, which breaks the BO bonds; hence, its dissolution implies the depolymerization of the silicate anions. Based on the spectroscopic results, the H_2O-containing atmospheres tend to stabilize the polymerized silicate anions, i.e., the higher Q^n. Therefore, it is expected that H_2O increases γ_{FeO}, whereas CO_2 decreases it. Based on the abovementioned equilibria, H_2O-containg atmospheres should have higher γ_{FeO}, i.e., less FeO wt%. Figures 6-11 – 6-13 show the variation of X_{FeO} with pO_2 and temperature for various CaO/SiO_2 ratios. It is seen that the slags under CO/CO_2 have higher FeO contents following this order: CO/CO_2 > $CO/CO_2/H_2/H_2O$ > H_2/H_2O. In support of that observation, Figures 6-14 – 6-16 show a reverse order of the atmospheres with respect to γ_{FeO}. Moreover, Figure 6-17 indicates that H_2O-containg atmospheres have higher γ_{FeO} than CO/CO_2 atmospheres based on the average of all experimental points. Based on these observations, the unprecedented role H_2O plays that affects γ_{FeO} in the slag compared with the other gases was evidenced. That has also been substantiated by the effect of pH_2O on γ_{FeO} at constant pO_2 and CaO/SiO_2, as shown in Figures 6-18 – 6-19. It is notable that γ_{FeO} is a linear function of pH_2O when the other parameters are held constant, which can be expressed in terms of the interaction

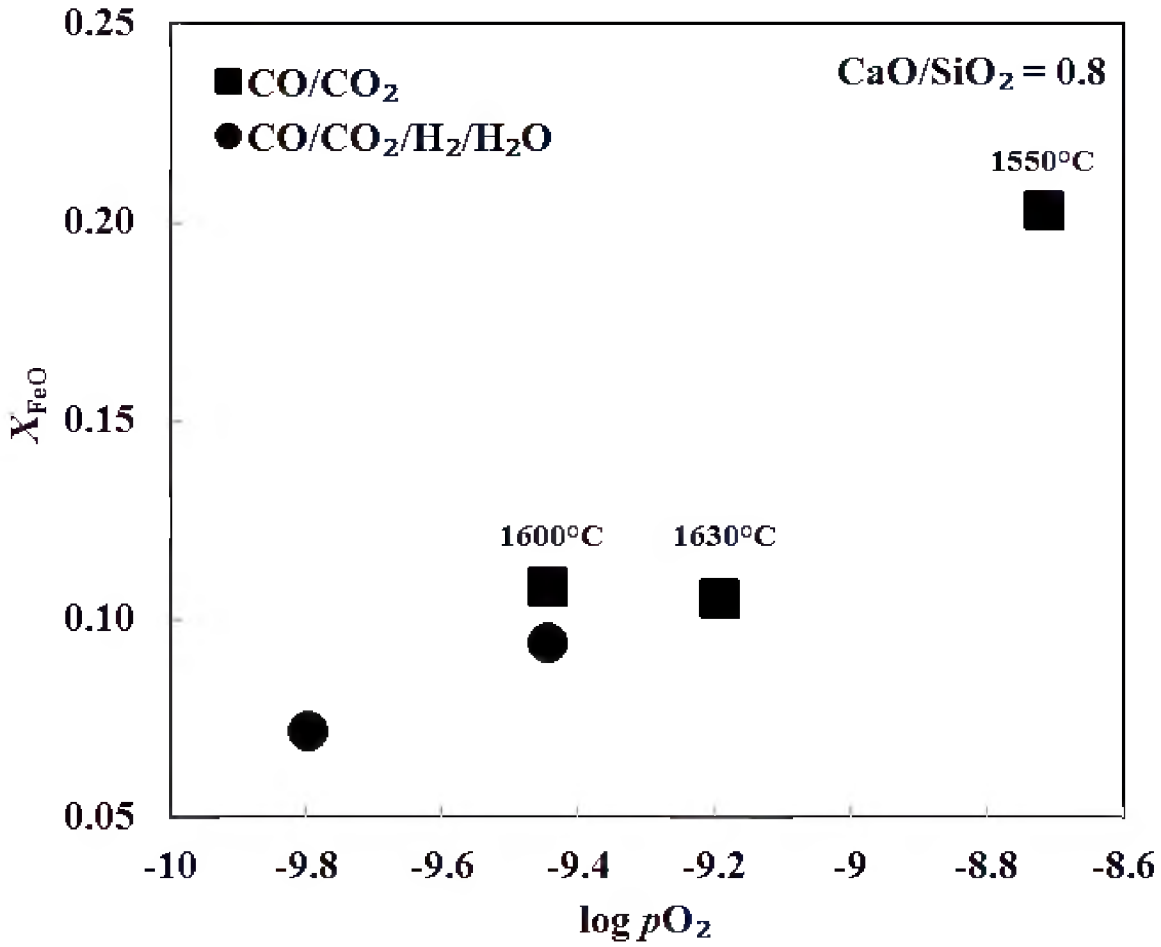

Figure 6-11. The effect of gas atmosphere on X_{FeO} at various pO_2 and temperature values for slags with wt% CaO/ wt% SiO_2 of 0.8 and pH_2O of 0 and 0.1 atm in CO/CO_2 and $H_2/H_2O/CO/CO_2$, respectively.

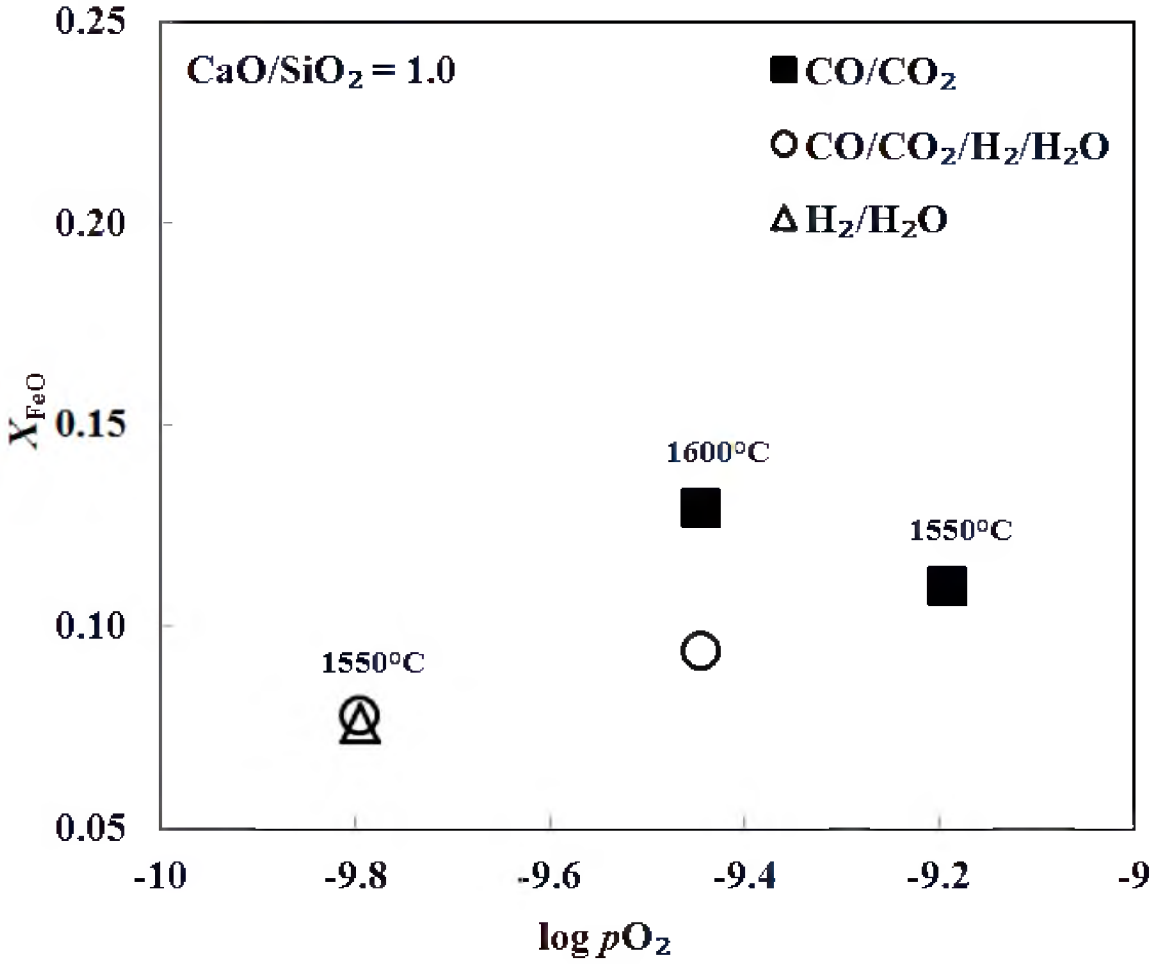

Figure 6-12. The effect of gas atmosphere on X_{FeO} at various pO_2 and temperature values for slags with wt% CaO/ wt% SiO_2 of 1.0 and pH_2O of 0, 0.1, and 1.0 atm in CO/CO_2, $H_2/H_2O/CO/CO_2$, and $H_2/H_2O/CO$, respectively.

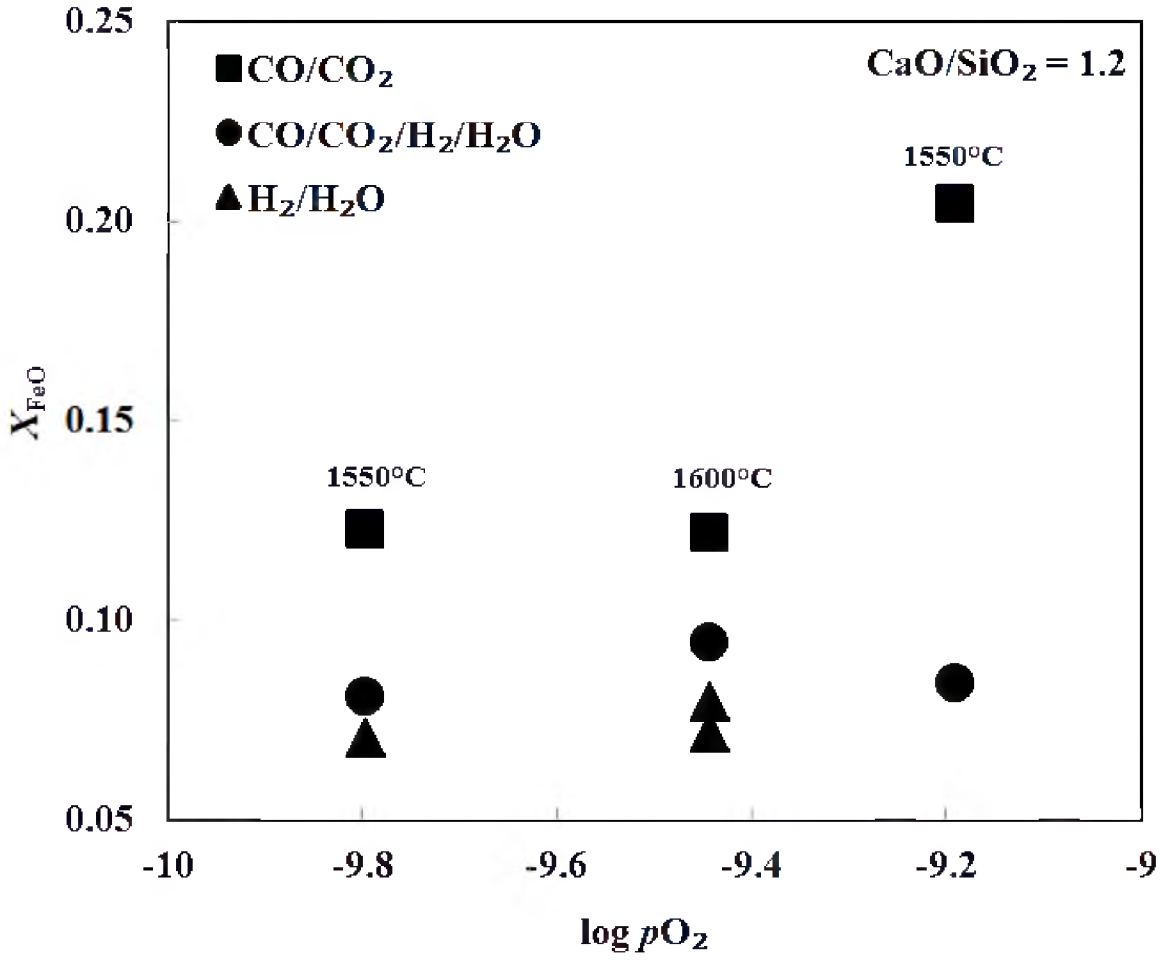

Figure 6-13. The effect of gas atmosphere on X_{FeO} at various pO_2 and temperature values for slags with wt% CaO/ wt% SiO_2 of 1.2 and pH_2O of 0, 0.1, and 1.0 atm in CO/CO_2, $H_2/H_2O/CO/CO_2$, and $H_2/H_2O/CO$, respectively.

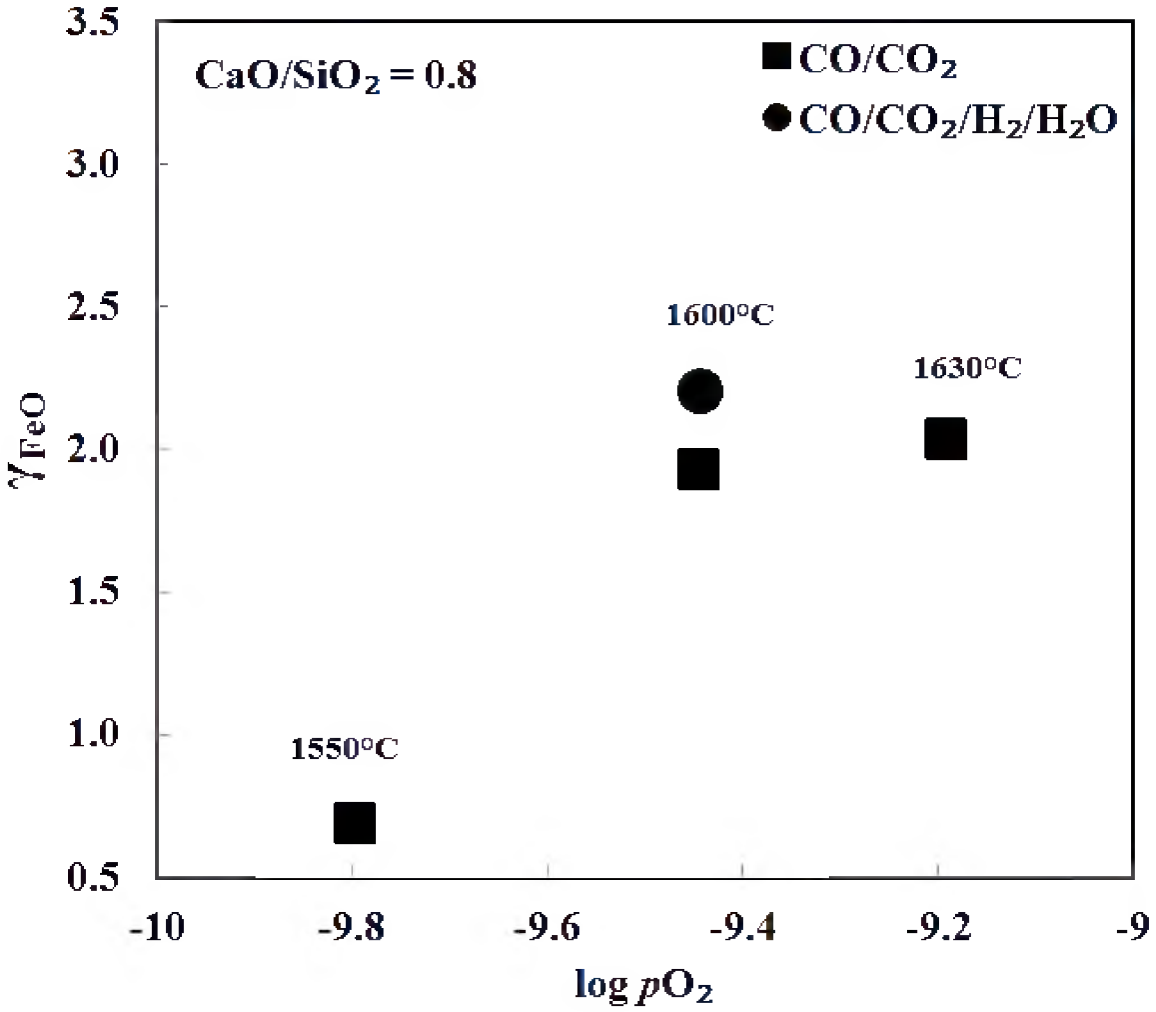

Figure 6-14. The effect of gas atmosphere on γ_{FeO} at various pO_2 and temperature values for slags with wt% CaO/ wt% SiO_2 of 0.8 and pH_2O of 0 and 0.1 atm in CO/CO_2 and $H_2/H_2O/CO/CO_2$, respectively.

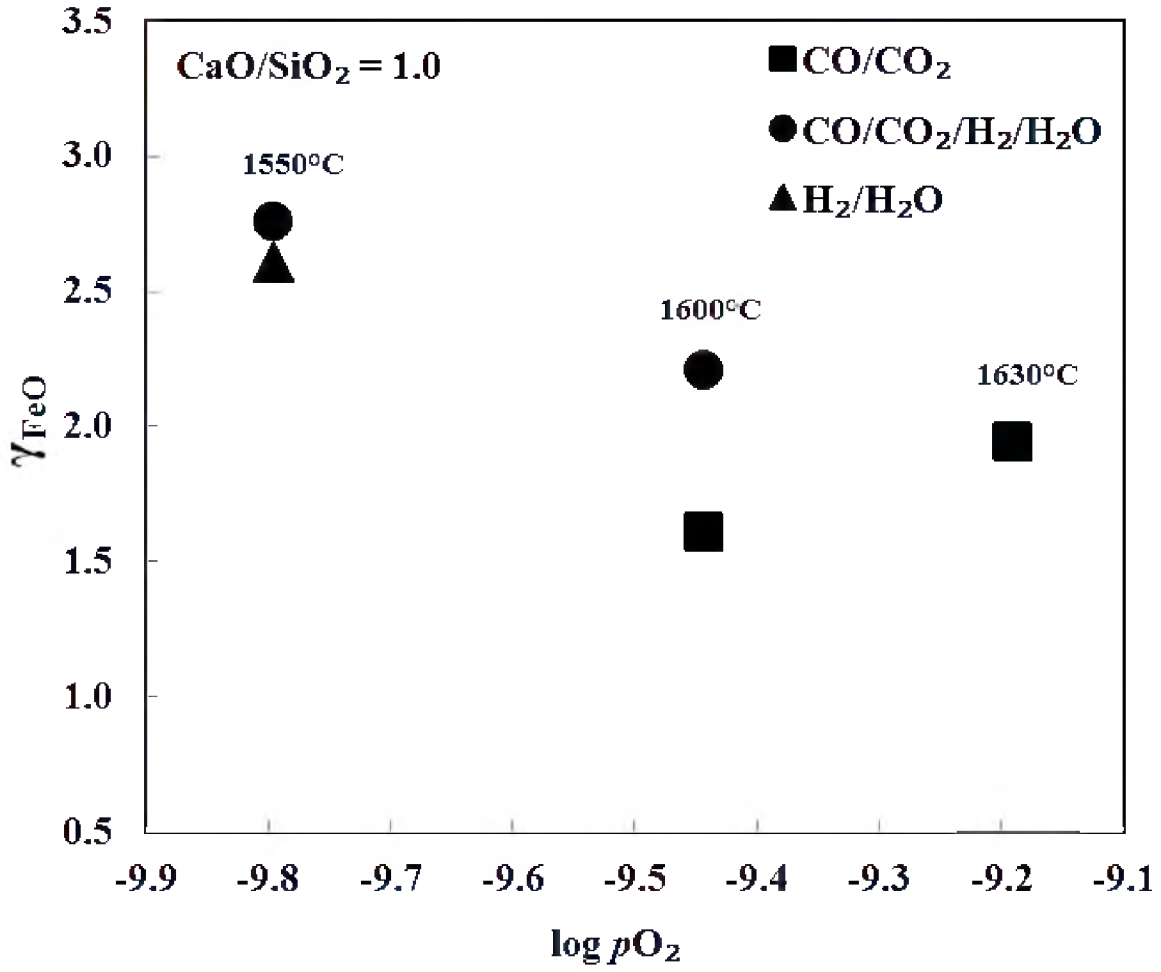

Figure 6-15. The effect of gas atmosphere on γ_{FeO} at various pO_2 and temperature values for slags with wt% CaO/ wt% SiO_2 of 1.0 and pH_2O of 0, 0.1, and 1.0 atm in CO/CO_2, $H_2/H_2O/CO/CO_2$, and $H_2/H_2O/CO$, respectively.

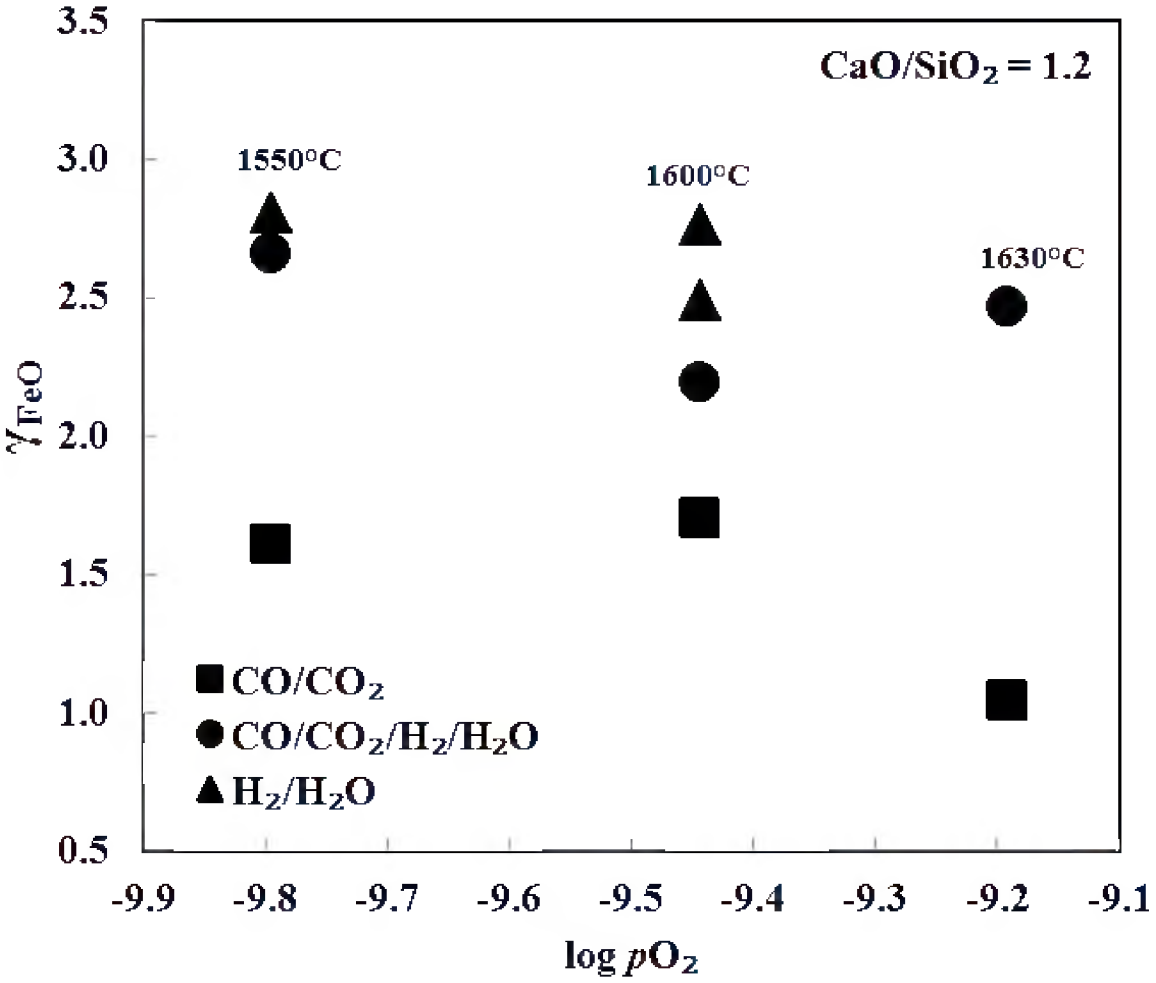

Figure 6-16. The effect of gas atmosphere on γ_{FeO} at various pO_2 and temperature values for slags with wt% CaO/ wt% SiO_2 of 1.2 and pH_2O of 0, 0.1, and 1.0 atm in CO/CO_2, $H_2/H_2O/CO/CO_2$, and $H_2/H_2O/CO$, respectively.

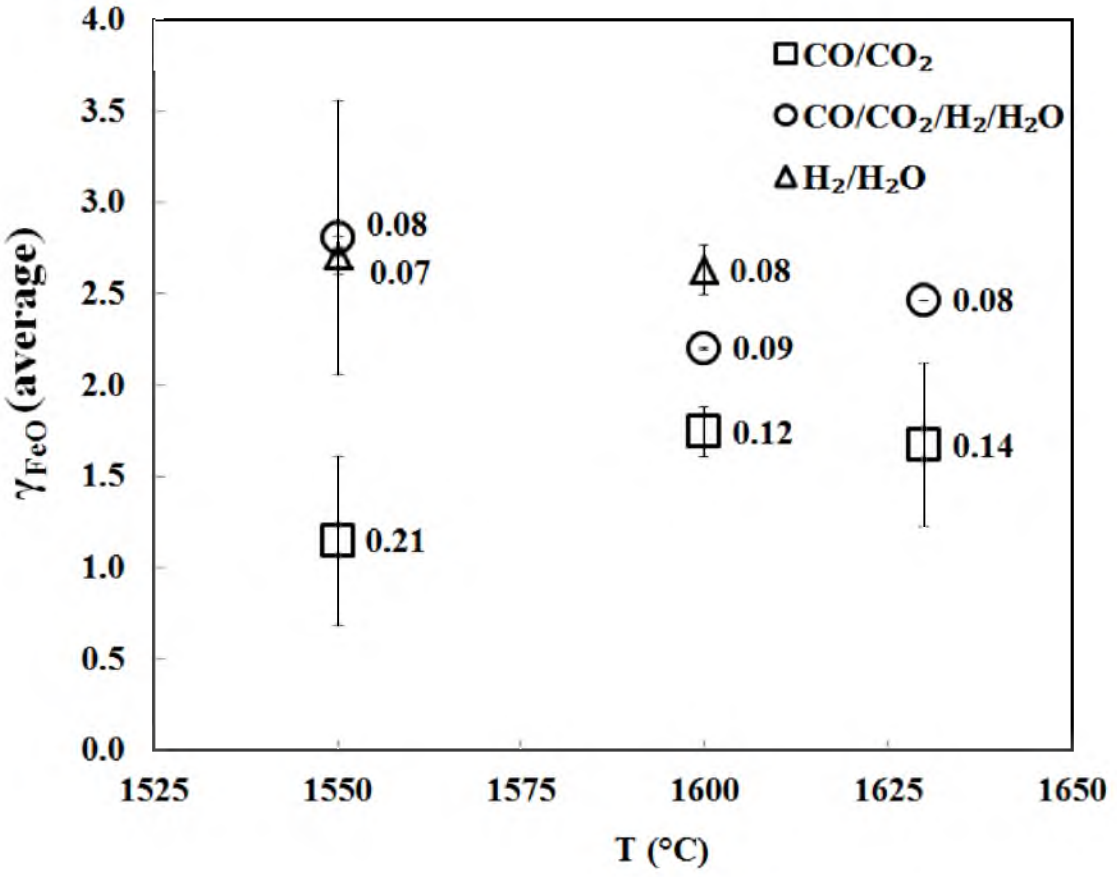

Figure 6-17. Comparison of the average values of γ_{FeO} of the three gas atmospheres at the experimental temperatures for slags with wt% CaO/ wt% SiO_2 of 1.2 and pH_2O of 0, 0.1, and 1.0 atm in CO/CO_2, $H_2/H_2O/CO/CO_2$, and $H_2/H_2O/CO$, respectively, and pO_2 range of 10^{-10} to 10^{-9} atm. The error bars are the experimental standard deviation and the labels are the average X_{FeO}.

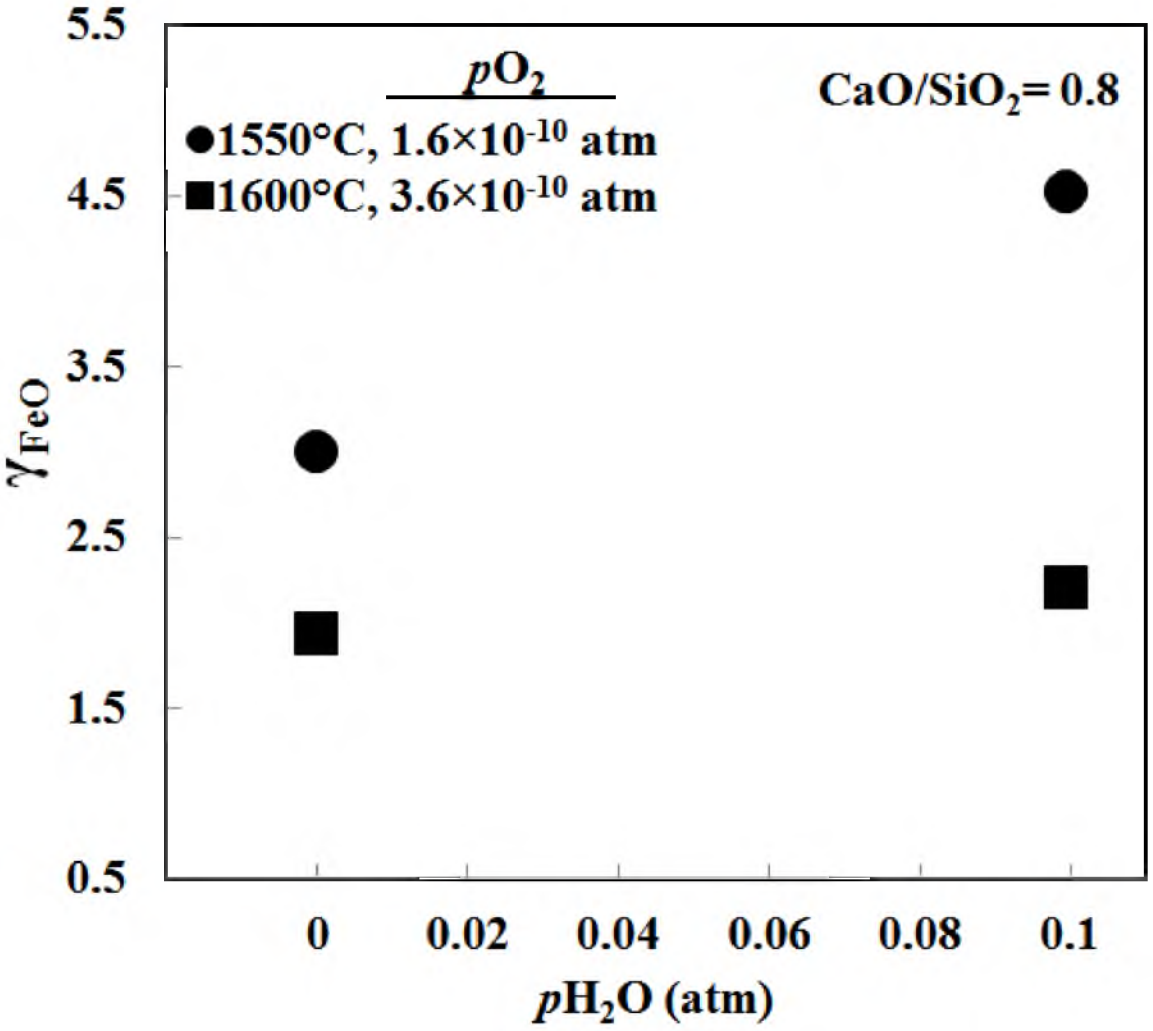

Figure 6-18. The effect of pH_2O on γ_{FeO} wt% CaO/ wt% SiO_2 of 0.8 at different temperatures and pO_2.

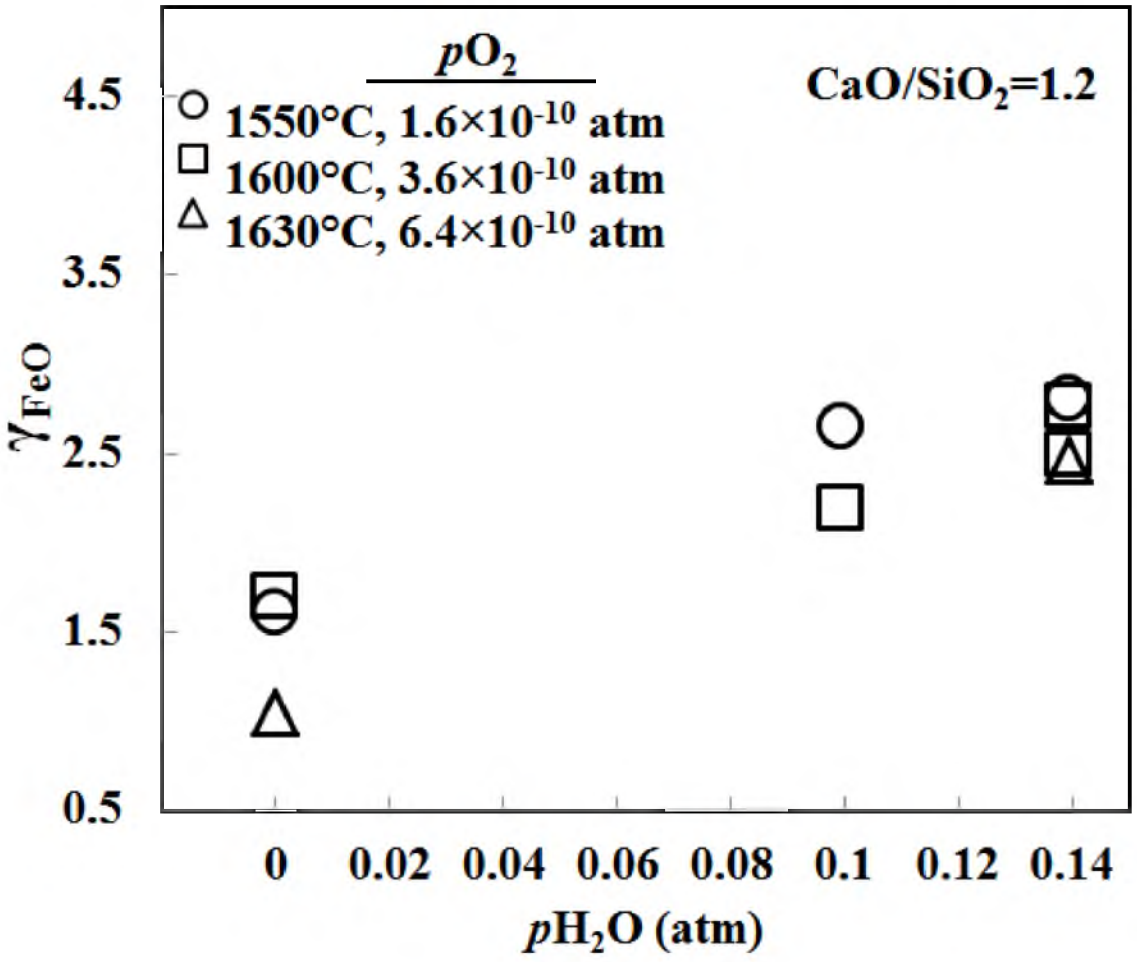

Figure 6-19. The effect of pH_2O on γ_{FeO} wt% CaO/ wt% SiO_2 of 1.2 at different temperatures and pO_2.

of H_2O with γ_{FeO}, as follows:

$$\left(\frac{\partial \gamma_{FeO}}{\partial pH_2O}\right)_{T,\ Comp.} = \varepsilon_{FeO}^{H_2O} \qquad (6\text{-}15)$$

where $\varepsilon_{FeO}^{H_2O}$ is the interaction coefficient, which was found to be positive at constant temperature and slag composition in the current study.

It is worth mentioning that the positive deviation of a_{FeO} from ideality is exhibited by all the slags under the three gas atmospheres, as Figure 6-20 presents.

For the slag compositions investigated, MgO-saturated CaO-FeO-Al_2O_3-SiO_2-MnO (0.2-0.8 wt%)-P_2O_5 (0.1-0.9 wt%), in the temperature range 1550-1600°C, with CaO/SiO_2 rage 0.8 to 1.2, and under pO_2 = 2×10^{-10}~2×10^{-9} atm, the average FeO wt% was found to be 10 (9.5~10.5), 11 (9.8~13), and 16 (14.7~16.9) under H_2/H_2O, $CO/CO_2/H_2/H_2O$, and CO/CO_2, respectively. These gas mixtures resemble H_2 reductant, natural or coal gas (NG/CG), and blast furnace (BF) conditions, respectively. The activity of FeO remained at a constant value of 0.2 under all the conditions tested. The average content of FeO under H_2 and NG/CG was presented relative to that under BF conditions in Figure 6-21.

6. 6. Conclusions

Water was found to have an advantageous effect on the content of FeO in the slags investigated, MgO-saturated CaO-FeO-Al_2O_3-SiO_2-MnO (0.2-0.8 wt%)-P_2O_5 (0.1-0.9 wt%), in the temperature range 1550-1600°C, with wt% CaO/wt% SiO_2 of 0.8 to 1.2,

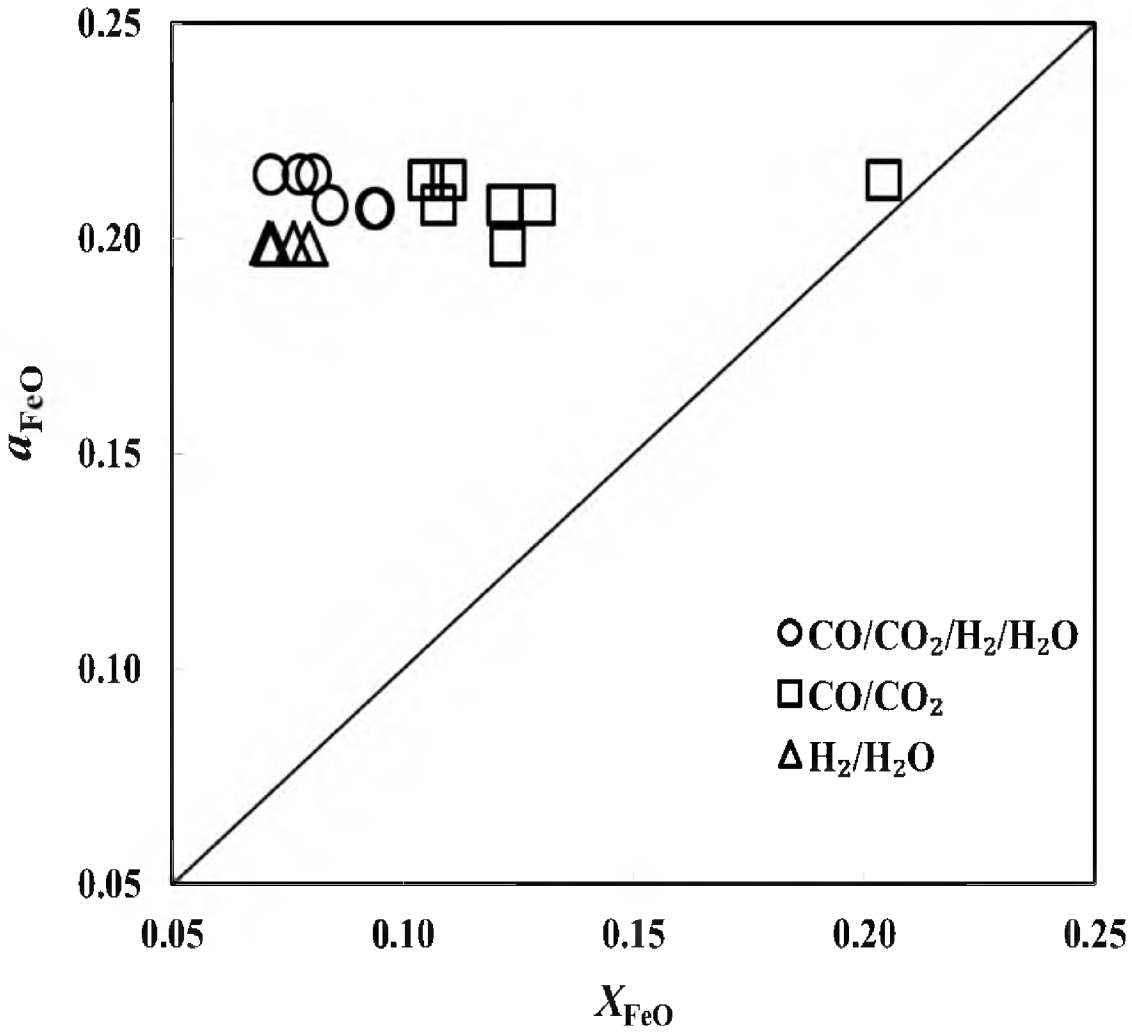

Figure 6-20. Variation of the activity of FeO with FeO mole fraction under different gas mixtures in the temperature range 1550 to 1630°C, wt% CaO/ wt% SiO_2 range of 0.8 to 1.2, and pH_2O ranges of 0, 0.1 - 0.2, and 0.1 - 0.2 atm in CO/CO_2, $H_2/H_2O/CO/CO_2$, and $H_2/H_2O/CO$, respectively, and pO_2 range 10^{-10} to 10^{-9} atm.

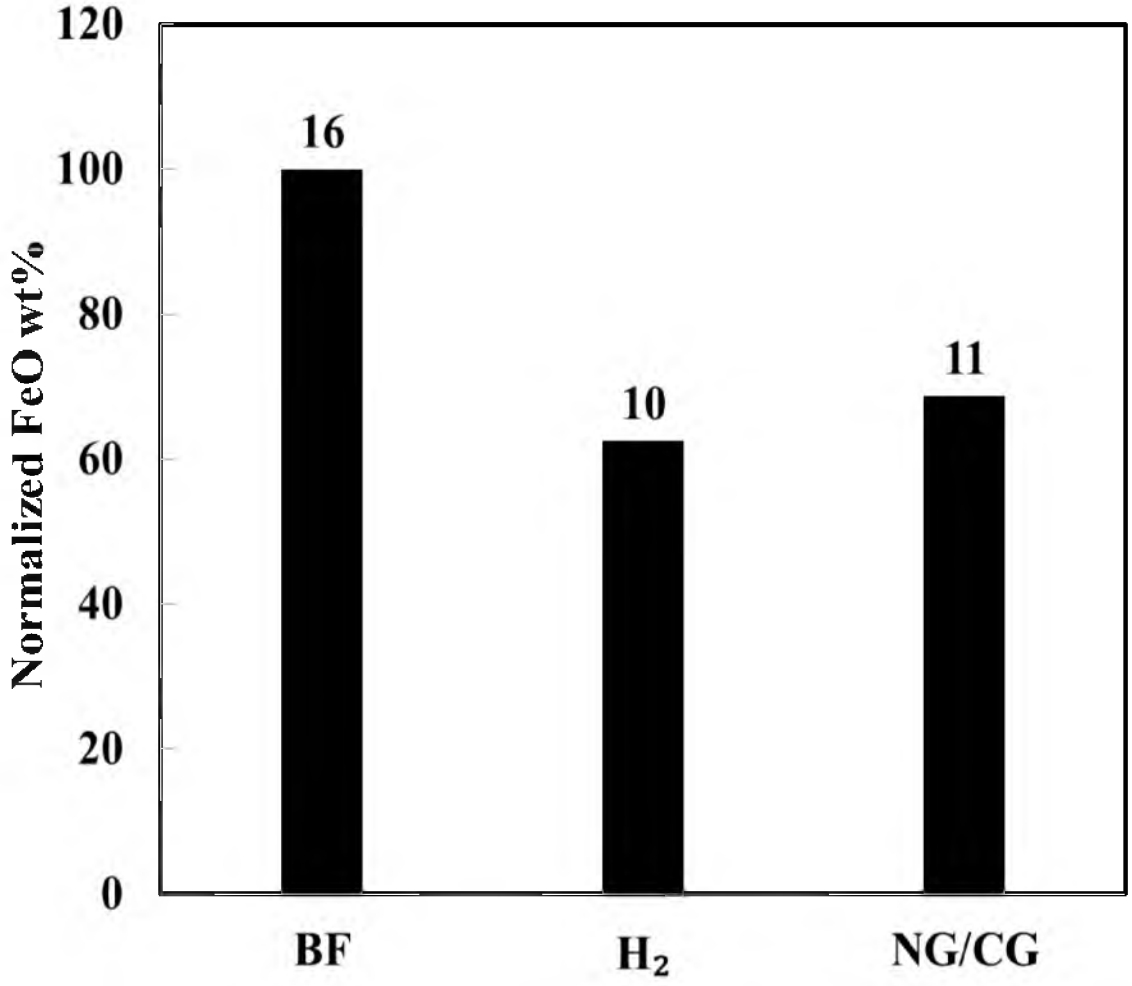

Figure 6-21. The influence of the type of reductant gas on FeO content in the slag. The labels show average FeO wt%.

and under pO_2 = 2×10^{-10}~2×10^{-9} atm. It was found that water increases the activity coefficient of FeO in the slag and accordingly lowers the FeO content. The average FeO content was found to be 10, 11, and 16 wt% under H_2/H_2O (H_2), $CO/CO_2/H_2/H_2O$ (natural/ coal gas), and CO/CO_2 (blast furnace), respectively. In other words, the slags under H_2 and natural/coal gas will contain 37 and 31% less FeO wt% than in the BF conditions, respectively.

An empirical correlation was formulated using linear regression to adequately predict γ_{FeO} under H_2/H_2O in slags:

$$\log\gamma_{FeO} = -3.0623X_{FeO} - 3.1421X_{CaO} - 2.5068X_{MgO} + 2.1957 \ (r^2 = 0.72)$$

That correlation should fairly well predict the γ_{FeO} in slags similar to those studied.

6. 7. References

(1) Lee, Y. S.; Min, D. J.; Jung, S. M.; Yi, S. H. Influence of basicity and FeO content on viscosity of blast furnace type slags containing FeO. *ISIJ Int.* **2004,** *44*, 1283-1290.

(2) Nikolic, S.; Henao, H.; Hayes, P. C.; Jak, E. Phase equilibria in ferrous calcium silicate slags: Part ii. Evaluation of experimental data and computer thermodynamic models. *Metall.Trans. B* **2008,** *39*, 189-199.

(3) Basu, S.; Lahiri, A. K.; Seetharaman, S. Activity of iron oxide in steelmaking slag. *Metall.Trans. B* **2008,** *39*, 447-456.

(4) Henao, H. M.; Itagaki, K. Activity and activity coefficient of iron oxides in the liquid FeO-Fe_2O_3-CaO-SiO_2 slag systems at intermediate oxygen partial pressures. *Metall.Trans. B* **2007,** *38*, 769-780.

(5) Henao, H.; Itagaki, K. Phase relations and activity of iron oxide in the FeO_X-CaO-SiO_2 system at 1300-1400 °C under various partial pressures of oxygen. Sohn International Symposium; Advanced Processing of Metals and Materials Volume 1: Thermo and Physicochemical Principles: Non-Ferrous High-Temperature Processing **2006**, 755-766.

(6) Yang, X. M.; Shi, C. B.; Zhang, M.; Zhang, J. A thermodynamic model for prediction of iron oxide activity in some FeO-containing slag systems. *Steel Res. Int.* **2012,** *83*, 244-258.

(7) Sohn, H. Y.; Choi, M. E.; Zhang, Y.; Ramos, J. E. Suspension reduction technology for ironmaking with low CO_2 emission and energy requirement. *Iron Steel Technol. (AIST Trans.)* **2009,** *6*, 158-165.

(8) Chipman, J. Equilibrium in the oxidation of liquid iron by steam and the free energy of ferrous oxide in liquid steel. *J. Am. Chem. Soc.* **1933,** *55*, 3131-3139.

(9) Chipman, J.; Fetters, K. L. The solubility of iron oxide in liquid iron. *Trans. Am. Soc. Met.* **1941,** *29*, 953-966.

(10) Bodsworth, C. The activity of ferrous oxide in silicate melts. *J. Iron Steel Inst.*, **1959,** *193*, 13-24.

(11) Suito, H.; Inoue, R. Thermodynamic considerations on manganese equilibria between molten iron and Fe_tO-MnO-MO_X slags (MO_X = $PO_{2.5}$, SiO_2, $AlO_{1.5}$, MgO, CaO). *Trans. Iron Steel Inst. Jpn.* **1984,** *24*, 301-307.

(12) Liu, S. H. Measurement of feo activity in bath smelting slags. Ph.D. Dissertaion, Carnegie Mellon University, Pennsylvania, USA, **1996**.

(13) Liu, S. H.; Fruehan, R.; Morales, A.; Ozturk, B. Measurement of FeO activity and solubility of MgO in smelting slags. *Metall.Trans. B* **2001**, *32*, 31-36.

(14) Ogura, T.; Fujiwara, R.; Mochizuki, R.; Kawamoto, Y.; Oishi, T.; Iwase, M. Activity determinator for the automatic measurements of the chemical potentials of ferrous oxide in metallurgical slags. *Metall. Trans. B* **1992,** *23B*, 459-466.

(15) Iwase, M.; Uchida, Y.; Tomii, Y.; McLean, A.; Katogi, K. Measurements of the ferrous oxide activities in slags to reduce steelmaking slag volume. *High Temp. Mater. P.* **2001,** *20*, 269-277.

(16) Hamm, A.; Cundiff, B.; McCauley, W.; Frigm, G. In The use of slag iron oxide activity measurements for steel making process control. *Steelmaking Conf. Proc.* **1994**, *77*, 153-156.

(17) Winkler, T. B.; Chipman, J. An equilibrium study of the distribution of phosphorus between liquid iron and basic slags. *Trans. AIME* **1946,** *167*, 111-133.

(18) Bishop, H. L., Jr.; Grant, N. J.; Chipman, J. Equilibria of molten iron and liquid slags of the system $CaO\text{-}SiO_2\text{-}(FeO)_t$. *Trans. Metall. Soc. AIME* **1958,** *212*, 890-892.

(19) Schuhmann, R., Jr.; Ensio, P. J. Thermodynamics of iron silicate slags:Slags saturated with γ-iron. *J. Met.* **1951,** *3*, 401-411.

(20) Venkatradi, A. S.; Bell, H. B., Sulfur partitioning between slag and metal in the iron blast furnace. *J. Iron Steel Inst.* **1969,** *207*, 1110-1113.

(21) Lee, C. M.; Fruehan, R. J. Phosphorus equilibrium between hot metal and slag. *Ironmaking Steelmaking* **2005,** *32*, 503-508.

(22) Morales, A. T.; Fruehan, R. J. Thermodynamics of MnO, FeO, and phosphorus in steelmaking slags with high MnO contents. *Metall. Trans. B* **1997,** *28B*, 1111-1118.

(23) Park, J. M.; Lee, K. K. Reaction equilibria between liquid iron and $CaO\text{-}Al_2O_3\text{-}MgO_{sat.}\text{-}SiO_2\text{-}Fe_tO\text{-}MnO\text{-}P_2O_5$ slag. *Steelmaking Conf. Proc.* **1996,** *79*, 165-171.

(24) Fujiwara, H.; Ichise, E.; Kitou, M.; Matsui, T. Thermodynamics of iron oxide in Fe_xO-dilute $CaO + Al_2O_3 + MgO + Fe_xO$ slags at 1873 K. *Metall. Trans. B* **1999,** *30B*, 419-427.

(25) Yang, L.; Belton, G., Iron redox equilibria in $CaO\text{-}Al_2O_3\text{-}SiO_2$ and $MgO\text{-}CaO\text{-}Al_2O_3\text{-}SiO_2$ slags. *Metall. Trans. B* **1998,** *29*, 837-845.

(26) Fujiwara, H.; Ichise, E.; Kitou, M.; Matsui, T. Thermodynamics of iron oxide in Fe_xO-dilute $CaO+Al_2O_3+ Fe_xO$ fluxes at 1873 K. *Metall. Trans. B* **1997,** *28*, 243.

(27) Chipman, J.; Marshall, S., The equilibrium $FeO + H_2 = Fe + H_2O$ at temperatures up to the melting point of iron. *J. Am. Chem. Soc.* **1940,** *62*, 243-250.

(28) Darken, L. S.; Gurry, R. W. The System iron-oxygen. I. The wüstite field and related equilibria. *J. Am. Chem. Soc.* **1945,** *67*, 1398-1412.

(29) Deo, B.; Boom, R., *Fundamentals of steelmaking metallurgy*; Prentice Hall International: New York, USA, **1993**.

(30) Mohassab-Ahmed, M. Y.; Sohn, H. Y.; Kim, H. G., Phosphorus distribution between liquid iron and magnesia-saturated slag in H_2/H_2O atmosphere relevant to a novel ironmaking technology. *Ind. Eng. Chem. Res.* **2012,** *51*, 7028-7034.

(31) Mohassab-Ahmed, M. Y.; Sohn, H. Y.; Kim, H. G., Sulfur distribution between liquid iron and magnesia-saturated slag in H_2/H_2O atmosphere relevant to a novel ironmaking technology. *Ind. Eng. Chem. Res.* **2012,** *51*, 3639-3645.

(32) Mohassab Ahmed, M. Y. Sulfur and phosphorus distribution between liquid iron and magnesia-saturated slag in H_2/H_2O atmosphere relevant to a novel green ironmaking technology. M.S. Thesis, University of Utah, Utah, USA, **2011**.

(33) Kishimoto, T.; Hasegawa, M.; Ohnuki, K.; Sawai, T.; Iwase, M., The activities of Fe_xO in $\{CaO\text{-}SiO_2\text{-}Al_2O_3\text{-}MgO\text{-}Fe_xO\}$ slags at 1723 K. *Steel Res. Int.* **2005,** *76*, 341-347.

(34) Turkdogan, E. T.; Pearson, J., Activities of constituents of iron and steelmaking slags. I. Iron oxide. *J. Iron Steel Inst.* **1953,** *173*, 217-223.

(35) Ichise, E.; Iwase, M. Activities of iron oxide (Fe_xO) in CaO-based metallurgical fluxes used for the external dephosphorization of hot metal. *Metall. Soc. AIME*, **1984**, 517-531.

(36) Wrampelmeyer, J. C.; Dimitrov, S.; Janke, D. Dephosphorization equilibria between pure molten iron and CaO-saturated $FeO\text{-}CaO\text{-}SiO_2$ and $FeO\text{-}CaO\text{-}Al_2O_3$ slags. *Steel Res.* **1989**, *60*, 539-549.

(37) Ohta, H.; Suito, H. Activities of SiO_2 and Al_2O_3 and activity coefficients of Fe_tO and MnO in $CaO\text{-}SiO_2\text{-}Al_2O_3\text{-}MgO$ slags. *Metall. Trans. B* **1995,** *26*, 119-129.

(38) Ping Tao, D., Prediction of activities of three components in the ternary molten slag $CaO\text{-}FeO\text{-}SiO_2$ by the molecular interaction volume model. *Metall. Trans. B* **2006,** *37*, 1091-1097.

(39) Ban-Ya, S. Mathematical expression of slag-metal reactions in steelmaking process by quadratic formalism based on the regular solution model. *ISIJ. Int.* **1993,** *33*, 2-11.

(40) Park, J. M.; Lee, K. K. Reaction equilibria between liquid iron and CaO-Al_2O_3-$MgO_{sat.}$-SiO_2-Fe_tO-MnO-P_2O_5 slag. *Steelmaking Conf. Proc.* **1996,** *79*, 165-171.

(41) Nassaralla, C.L.; Sarma, B.; Morales, A.T.; Myers, J.C. *Proc. E.T. Turkdogan Symp.*, Pittsburgh, Pennsylvania, USA, **1994**, 61-71.

(42) Park, J. M.; Lee, K. K. *79th Steelmaking Conf. Proc.*, ISS, Pennsylvania, USA,1996; pp 1745–1754.

(43) Brandberg, J.; Sichen, D. Water vapor solubility in ladle-refining slags. *Metall. Trans. B,* **2006**, *37*, 389-393.

(44) Rosenqvist, T. *Principles of.Extractive Metallurgy*, Tapir Forlag, **2004**, 305.

(45) Orrling, C.; Cramb, A., The effect of water vapor on mold slag crystallization. *Metall. Trans. B* **2000,** *31*, 403-406.

(46) Jo, S. K.; Kim, S. H. The solubility of water vapour in CaO-SiO_2-Al_2O_3-MgO slag system. *Steel Res.*, **2000**, *71*, 15-21.

(47) Leekes, G.; Nowack, N.; Schlegelmilch, F., Dissolution of water vapor in ESR-slags of the systems CaO-Al_2O_3 and CaF_2-CaO-Al_2O_3 by application of Fourier-transform-infrared-spectroscopy. *Steel Res.* **1988,** *59*, 406-416.

(48) Sosinsky, D. J.; Maeda, M.; McLean, A. Determination and prediction of water vapor solubilities in CaO-MgO-SiO_2 slags. *Metall. Trans. B,* **1985**, *16B*, 61-66.

(49) Iguchi, Y.; Ban-Ya, S.; Fuwa, T. Solubility of water in liquid CaO-SiO_2 with Al_2O_3, TiO_2, and FeO at 15500. *Trans. Iron Steel Inst. Jap.* **1969**, *9*, 189-195.

CHAPTER 7

SOLUBILITY OF MgO IN THE SLAG RELEVANT TO A NOVEL FLASH IRONMAKING TECHNOLOGY

7. 1. Introduction

Magnesia-based refractory linings are widely used to contain molten metals and slags in iron and steelmaking.[1] In BOF, MgO is usually charged in the form of dolomite to minimize the lining wear.[2] Also, MgO has an impact on the slag's refining ability as it plays a critical rule in the minor elements distribution between slag and molten metal. Since the work of Trömel *et al.*[3] in the late 1960s, a lot of investigations have been carried out to determine the solubility limit of MgO in slags and mathematically/ thermodynamically model its solubility. Trömel *et al.*[3] constructed the $CaO\text{-}FeO_n\text{-}SiO_2\text{-}MgO$ phase diagram and determined the saturation phase to be mainly (Fe, Mg)O phase at the slag/MgO crucible interface. The type of this saturation phase is dependent upon the oxygen partial pressure (pO_2) of the system. This saturation phase is MgO.FeO (magnesiowustite) at low pO_2 ($< 10^{-9}$ atm), whereas it is predominated by $MgO.Fe_2O_3$ (magnesioferrite) at higher oxygen partial pressure.[3, 4] Leonard and Herron[5] studied the solubility of MgO in BOF-type slags to determine the required amount of dolomite additions to saturate the BOF slag with MgO. They found that MgO solubility decreases

with CaO/SiO_2 ratio while it increases with FeO content. Their findings were consistent with those of Trömel *et al.*[3] and Fetters and Chipman.[6] Later, Kim *et al.*[7] determined the mechanism of slag attack on magnesite brick by Al_2O_3-containg slag with a CaO/SiO_2 ratio of 1.5 and found that it was matrix dissolution, where alumina diffuses through the brick, rather than dissolution of MgO grains in the slag at steelmaking temperatures. According to their observation, the higher the Al_2O_3 content in the slag, the deeper the penetration and the greater the refractory disruption. This work was followed by the work of Shim and Ban-ya[8] on SiO_2-CaO-MgO- Fe_tO slags in the temperature range of 1550-1650°C under the flow of Ar. They reported that MgO solubility decreases with Fe_tO content and slag basicity (CaO/SiO_2), whereas it stays constant at basicity higher than 2.0. In the meantime, Suito and Inoue[9, 10] determined the Mn and P distributions in MgO-saturated CaO-Fe_tO-SiO_2-P_2O_5-MnO slags over 1550-1650°C temperature range and also, they reported on MgO solubility. Schuermann and Kolm[11] used the previous research results reported by others to formulate a numerical description to determine the MgO content in a magnesiowustite saturation surface in multicomponent slag systems. They also developed a temperature correction factor to extrapolate MgO solubility values to any temperature knowing MgO solubility at 1600°C. Bergman[2] defined MgO capacity ($C_{Mg^{2+}}$) and correlated it to optical basicity. He found that MgO solubility in a complex slag, which is equilibrated with magnesiowustite, could be derived from the activity of MgO (a_{MgO}) in the magnesiowustite phase. This work was followed by Selin's[12, 13] work to asses MgO solubility at 1600°C relevant to steelmaking slags. Park and Lee[14] analyzed MgO solubility data of multicomponent slags saturated with MgO and equilibrated with molten iron at 1600°C relevant to the secondary refining process of Al-killed steel. They

found that MgO solubility increased with Fe_tO and temperature while it decreased with slag basicity. Liu *et al.*[15] determined MgO solubility in the $CaO-SiO_2-Al_2O_3-FeO$ slag at 1550°C. Their values were higher than Trömel *et al.*'s[3] results and they attributed that to the absence of Al_2O_3 in the latters' slags. Park[4] evaluated the effect of slag composition on MgO solubility in $CaO-MgO-Fe_tO-SiO_2-MnO-Al_2O_3$ slag under ambient atmosphere at 1600°C in his effort to control slag coating in BOF practice where an appropriate amount of slag from a previous heat is reused to coat the BOF linings after adjusting its physicochemical properties by dolomitic additions. His study revealed that MgO solubility decreases with basicity, which is consistent with the previous studies. On the other hand, Al_2O_3, SiO_2, and P_2O_5 were found to increase MgO solubility as a result of their dilution effect of the basic oxides. Moreover, Park[4] reported the basicity-dependent effect of Fe_tO content in which he found that Fe_tO increases MgO solubility in basic slags and decreases the solubility in acidic slags. Moreover, Jung *et al.*[16, 17, 18] investigated the effect of temperature and slag composition on MgO solubility in $CaO-SiO_2-Al_2O_3-Fe_tO-MnO$ slags over the temperature range of 1350-1500°C under a CO/CO_2 atmosphere. They concluded that Fe_tO activity plays a critical role in the solubility of MgO into the slag. Also, Demidov *et al.*[19] have recently evaluated MgO solubility in slag formed during the iron oxygen lancing in high-load BOFs. Their results indicated that MgO solubility increases with Fe_tO content at CaO/SiO_2 of 3.0 at 1650°C.

The purpose of this work was to investigate the behavior of MgO solubility in BF-type slags under atmospheres containing H_2O and eventually to answer the question of whether the type of gas atmosphere affects the solubility at the same pO_2, composition, and temperature. Therefore, the dissolution of MgO in the $CaO-FeO-Al_2O_3-SiO_2-MnO$

(0.0-0.8 wt%)-P_2O_5 (0.1-0.9 wt%) slags has been studied in the temperature rage 1550 to 1650°C under CO/CO_2, H_2/H_2O, and $CO/CO_2/H_2/H_2O$ atmospheres using the experimental method described elsewhere.[20, 21, 22]

7. 2. Thermodynamic Considerations

The solubility of MgO in slag is controlled by the saturation phase, which could be magnesiowustite (MgO.FeO), magnesioferrite ($MgO.Fe_2O_3$), or another spinel ($MgO.Al_2O_3$).[1, 3, 4] In the current work, the iron/wustite boundary is maintained in all the experiments by controlling pO_2 within the range of 10^{-9}-10^{-10} atm. Therefore, magnesiowustite is expected to dominate the saturation phase, which has been verified by SEM-EDS analyses. Figure 7-1 displays a representative slag sample showing the existence of magnesiowustite layer at the interface between the crucible and the slag as well as the islands the magnesiowustite dispersed in the silicate matrix. Consequently, the dissolution of magnesia should be limited by the saturation of the slag with magnesiowustite phase.[2] Therefore, the dissolution of MgO into slag can be expressed as:

$$MgO\ (\text{as magnesiowustite}) = (Mg^{2+}) + (O^{2-}) \qquad (7\text{-}1)$$

with an equilibrium constant:

$$K_{Mg^{2+}} = \frac{a_{Mg^{2+}} . a_{O^{2-}}}{a_{MgO}} \qquad (7\text{-}2)$$

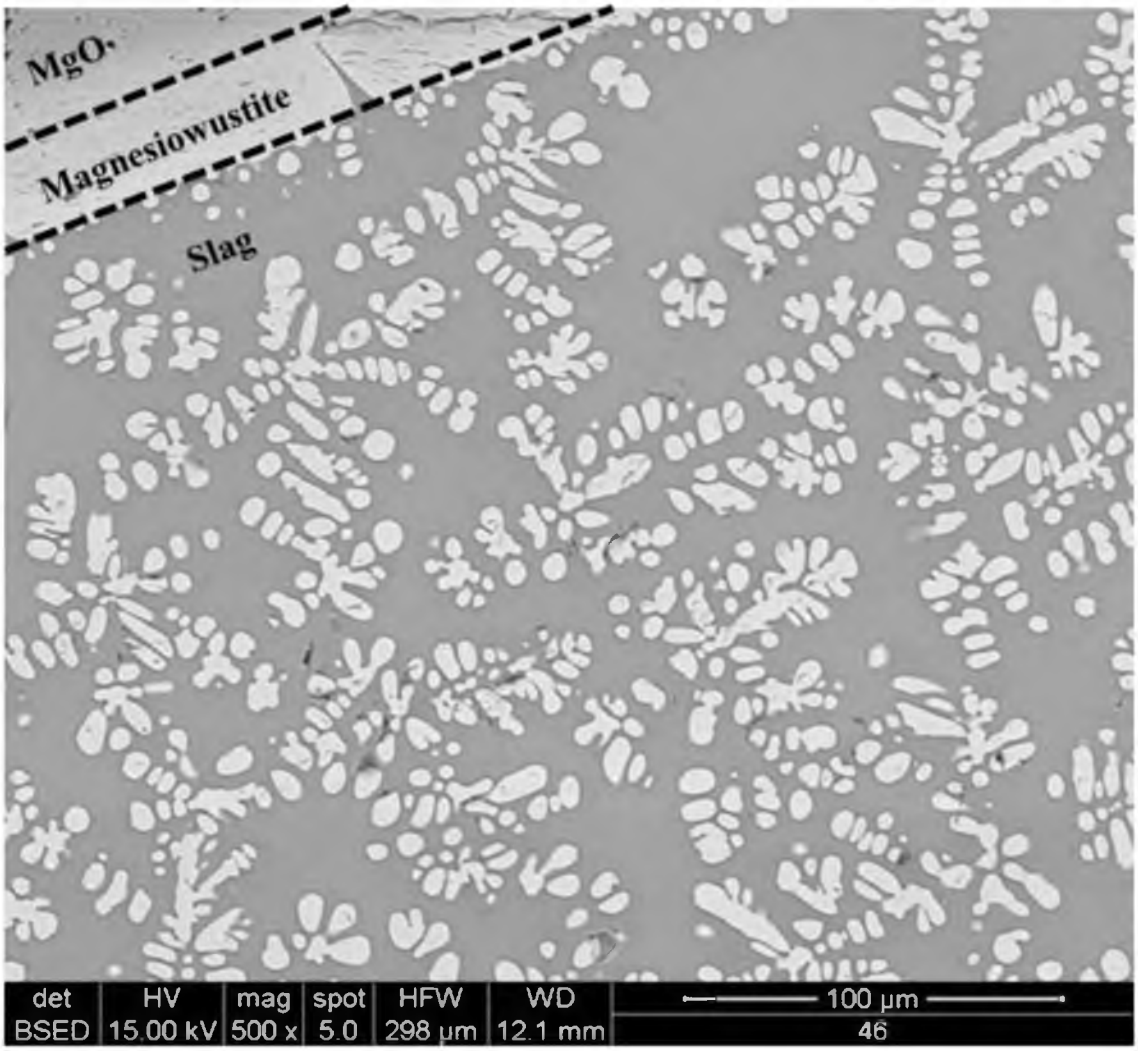

Figure 7-1. A micrograph of a slag sample along with the MgO-crucible wall at 1550°C and $pO_2 = 1.6\times10^{-10}$ atm under CO/CO_2 atmosphere. (In the slag the bright islands are mostly magnesiowustite and the gray matrix is the silicate melt.)

where the activity of MgO is with respect to pure MgO. Then, the saturation mole fraction of MgO can be calculated as follows:

$$X_{Mg^{2+}} = a_{MgO} \cdot \frac{K_{Mg^{2+}}}{\gamma_{Mg^{2+}} \cdot a_{O^{2-}}} = X_{(MgO),\ in\ slag} \qquad (7\text{-}3)$$

Equation 7-3 shows that MgO content in the slag is a function of the MgO activity (a_{MgO}) in the magnesiowustite and slag basicity ($a_{O^{2-}}$), assuming that $K_{Mg^{2+}}$, Mg^{2+} Raultian activity coefficient ($\gamma_{Mg^{2+}}$) are constant in the studied slags.[18]

In magnesiowustite, FeO coexists along with MgO, which in turn affects a_{MgO}. As a result, it is indispensable to calculate iron oxide activity (a_{MgO}) in the magnesiowustite layer, which equals a_{FeO} in the slag at equilibrium. In slag, FeO reaction at gas-slag-metal equilibrium could be expressed as:

$$Fe_{(l)} + \frac{1}{2}O_{2(g)} = FeO_{(l)},\ \Delta G^{\circ}_{FeO} = -225460 + 41.26T\ \ (J/mol)^{23} \qquad (7\text{-}4)$$

hence, a_{FeO} can be obtained as:

$$a_{FeO} = K_{FeO} \cdot pO_2^{\frac{1}{2}} = e^{\frac{\Delta G^{\circ}_{FeO}}{RT}} \cdot pO_2^{\frac{1}{2}} \qquad (7\text{-}5)$$

7. 3. Experimental Details

The MgO solubility data were collected from the experiment described in Chapter 3. A set of the experiments was aimed at studying the MgO solubility under the H_2/H_2O atmosphere and the other set was designed to compare the solubility under the $CO/CO_2/H_2/H_2O$, CO/CO_2, and H_2/H_2O atmospheres holding all the other variables constant as will be discussed in the following sections. Tables 7-1 and 7-2 show the conditions of the two experiments.

7. 4. Results and Discussions

7. 4. 1. The Effect of Basicity on MgO Solubility

As one of the strong basic oxides, MgO dissolves into slag by adding O^{2-}, as shown in reaction 7-1. In other words, the more the acidity of the slag, the more the solubility of MgO. That has been supported by the work of Fetters and Chipman[6], Trömmel,[3] in addition to others[5, 8, 12] in which the MgO solubility was found to decrease with increasing CaO/SiO_2 ratio, especially in the lower basicity region ($CaO/SiO_2 < 2.0$).[8, 17] Also, the same tendency was found in the works of Suito and Inoue[9], Liu *et al.*[15], and Shim and Ban-ya[8] within CaO/SiO_2 ranges of 0.5-1.6, 0.8-1.2, and 0.4-1.3, respectively.

Figures 7-2 – 7-4 compare the current work to the work done by Suito and Inoue[9] at the corresponding temperatures using a pseudo ternary system. It can be observed that the trend of MgO iso-solubility lines shows an agreement between the slags of the current work and that of Suito and Inoue[9] considering the experimental error and the difference in the composition. It can be seen that MgO solubility at a given slag composition

Table 7-1. Chemical analysis of the samples under H_2/H_2O

Sample	T (°C)	pO_2	CaO/ SiO_2	FeO (wt%)	MgO (wt%)	CaO (wt%)	Al_2O_3 (wt%)	SiO_2 (wt%)	a_{FeO}
5	1550	7.0×10^{-10}	0.8	21.5	19.2	20.9	8.7	28.3	0.121
6	1550	7.0×10^{-10}	1	19.9	20.2	23.0	8.0	33.0	0.108
7	1550	7.0×10^{-10}	1.2	22.3	15.2	29.8	9.5	26.4	0.109
8	1550	7.0×10^{-10}	1.4	20.7	10.6	32.1	9.4	23.7	0.092
8	1550	7.0×10^{-10}	1.4	21.4	16.3	32.1	9.4	23.7	0.108
9	1550	1.0×10^{-10}	0.8	11.5	22.4	24.9	8.2	32.3	0.067
10	1550	1.0×10^{-10}	1	12.0	18.7	29.0	9.7	29.9	0.065
11	1550	1.0×10^{-10}	1.2	12.4	17.0	30.9	10.7	29.0	0.065
12	1550	1.0×10^{-10}	1.4	14.2	14.5	34.7	9.8	30.9	0.066
13	1550	2.0×10^{-10}	0.8	12.2	22.5	25.1	9.4	32.6	0.070
14	1550	1.0×10^{-10}	1	12.6	16.8	27.4	8.8	39.7	0.062
15	1550	1.0×10^{-10}	1.2	18.7	15.4	34.7	10.2	16.4	0.098
16	1550	1.0×10^{-10}	1.4	15.3	16.3	32.4	10.4	28.4	0.077
17	1600	5.0×10^{-9}	0.8	41.1	15.1	15.8	6.2	19.5	0.217
18	1600	5.0×10^{-9}	1	34.6	13.6	20.4	7.4	24.4	0.168
19	1600	5.0×10^{-9}	1.2	42.8	11.3	18.1	6.3	17.0	0.204
20	1600	5.0×10^{-9}	1.4	52.8	12.4	14.9	4.9	12.3	0.261
21	1600	2.0×10^{-9}	0.8	20.3	22.6	20.7	8.6	27.6	0.121
21	1600	2.0×10^{-9}	0.8	20.4	22.6	20.7	7.5	27.7	0.121
22	1600	2.0×10^{-9}	1	27.1	15.6	22.7	8.2	23.5	0.143
22	1600	2.0×10^{-9}	1	27.0	17.6	22.6	8.2	23.2	0.148
23	1600	2.0×10^{-9}	1.2	29.7	14.2	26.2	8.8	22.0	0.146
23	1600	2.0×10^{-9}	1.2	29.7	14.2	23.7	8.3	22.0	0.150
24	1600	2.0×10^{-9}	1.4	31.1	14.7	24.8	7.9	21.7	0.156
25	1600	3.0×10^{-10}	0.8	8.7	25.5	24.3	9.7	36.0	0.051
26	1600	3.0×10^{-10}	1	9.3	21.2	27.1	9.8	31.5	0.053
27	1600	3.0×10^{-10}	1.2	11.8	18.7	29.1	10.1	28.2	0.065
28	1600	3.0×10^{-10}	1.4	13.2	19.4	31.0	9.9	23.8	0.075
29	1600	5.0×10^{-10}	0.8	7.1	23.9	23.9	9.6	31.5	0.044
30	1600	5.0×10^{-10}	1	14.7	20.9	25.5	9.5	28.2	0.085
31	1600	5.0×10^{-10}	1.2	14.9	25.3	25.2	8.9	23.6	0.093
37	1650	4.0×10^{-9}	0.8	32.6	20.6	17.8	7.6	23.5	0.186
38	1650	4.0×10^{-9}	1	47.5	14.2	13.5	5.5	16.3	0.248

Table 7-2. Chemical analysis of the samples of the comparison experiments

Sample	Gas	T (°C)	pO_2	CaO / SiO_2	FeO (wt%)	MgO (wt%)	CaO (wt%)	Al_2O_3 (wt%)	SiO_2 (wt%)	a_{FeO}
R10	$CO/CO_2/H_2/H_2O$	1550	1.9×10^{-9}	0.8	21.7	24.6	20.3	13.0	25.5	4.5
R19		1550	1.6×10^{-10}	0.8	10.1	24.4	26.2	16.3	34.8	3.0
R20		1550	1.6×10^{-10}	1	9.8	17.9	30.7	8.4	31.8	2.8
R21		1550	1.6×10^{-10}	1.2	10.8	16.8	33.5	18.8	29.8	2.7
R22		1600	3.6×10^{-10}	0.8	13.0	23.4	26.0	15.7	32.3	2.2
R23		1600	3.6×10^{-10}	1	12.7	19.2	30.0	17.0	30.9	2.2
R24		1600	3.6×10^{-10}	1.2	12.4	16.6	32.8	17.2	28.6	2.2
R27		1630	6.4×10^{-10}	1.2	11.2	19.2	30.1	17.0	30.5	2.5
R46	CO/CO_2	1550	1.6×10^{-10}	0.8	35.5	10.2	24.5	13.9	22.8	0.7
R48		1550	1.6×10^{-10}	1.2	16.9	26.2	26.3	15.0	23.6	1.6
R49		1600	3.6×10^{-10}	0.8	14.7	22.1	25.7	15.2	31.9	1.9
R50		1600	3.6×10^{-10}	1	16.9	16.9	28.5	15.2	29.4	1.6
R51		1600	3.6×10^{-10}	1.2	15.3	14.7	30.7	16.6	26.7	1.7
R52		1630	6.4×10^{-10}	0.8	13.7	15.7	24.7	23.4	32.9	2.0
R53		1630	6.4×10^{-10}	1	14.6	14.3	28.0	17.0	36.4	1.9
R54		1630	6.4×10^{-10}	1.2	26.4	14.8	25.2	14.3	27.4	1.0
R74	H_2/H_2O	1550	1.6×10^{-10}	1	9.9	20.7	34.9	5.1	27.8	2.6
R75		1550	1.6×10^{-10}	1.2	9.6	19.7	31.2	17.1	32.1	2.8
R78		1600	3.6×10^{-10}	1.2	10.5	16.1	33.7	17.7	29.5	2.5
R'78		1600	3.6×10^{-10}	1.2	9.5	16.9	33.8	18.1	29.6	2.8

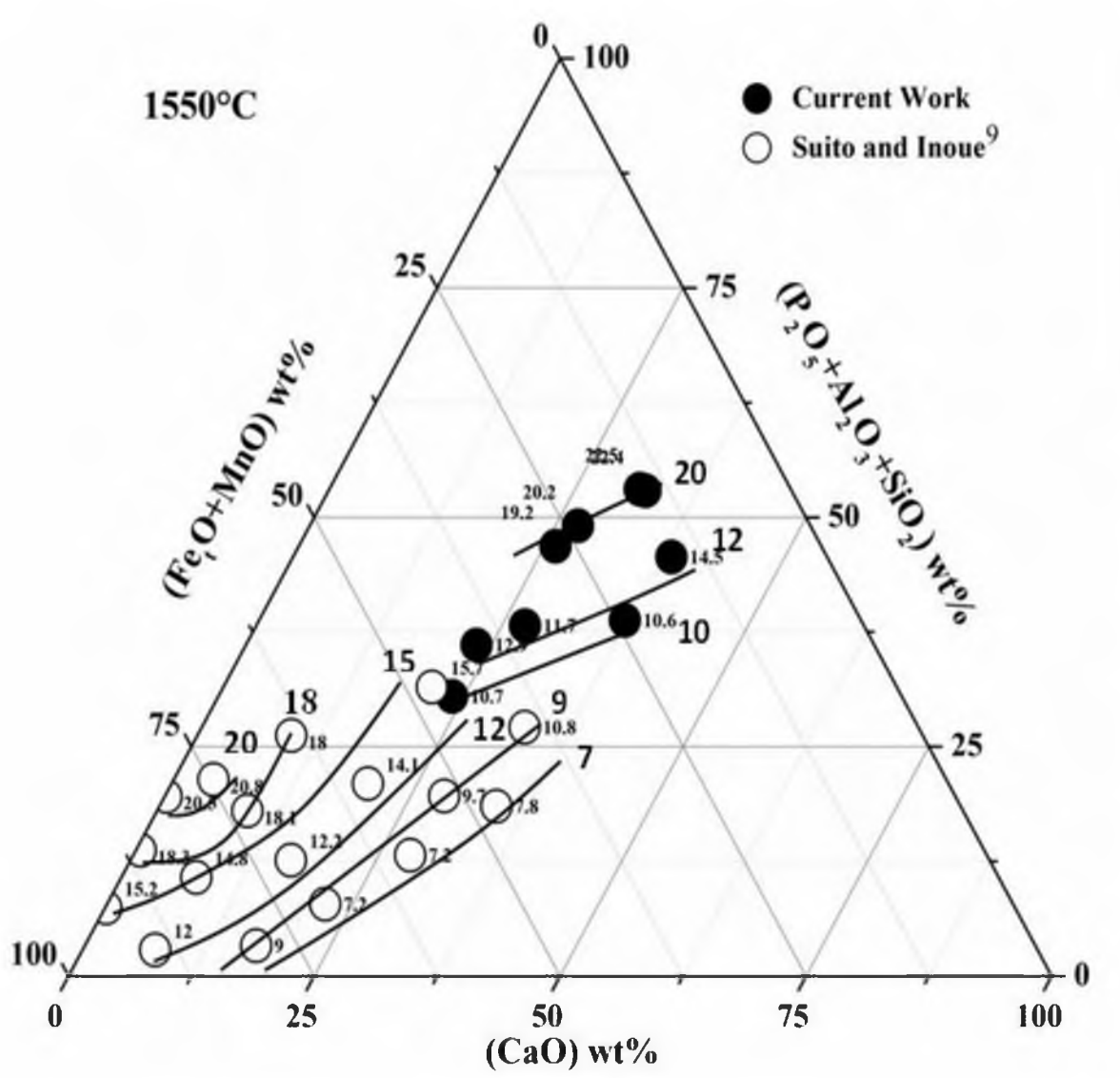

Figure 7-2. The iso-solubility lines of the CaO-Fe_tO-MnO-Al_2O_3-SiO_2-P_2O_5 system of the current work under H_2/H_2O and the work of Suito and Inoue[9] at 1550°C under Ar atmosphere. The labels denote MgO wt%.

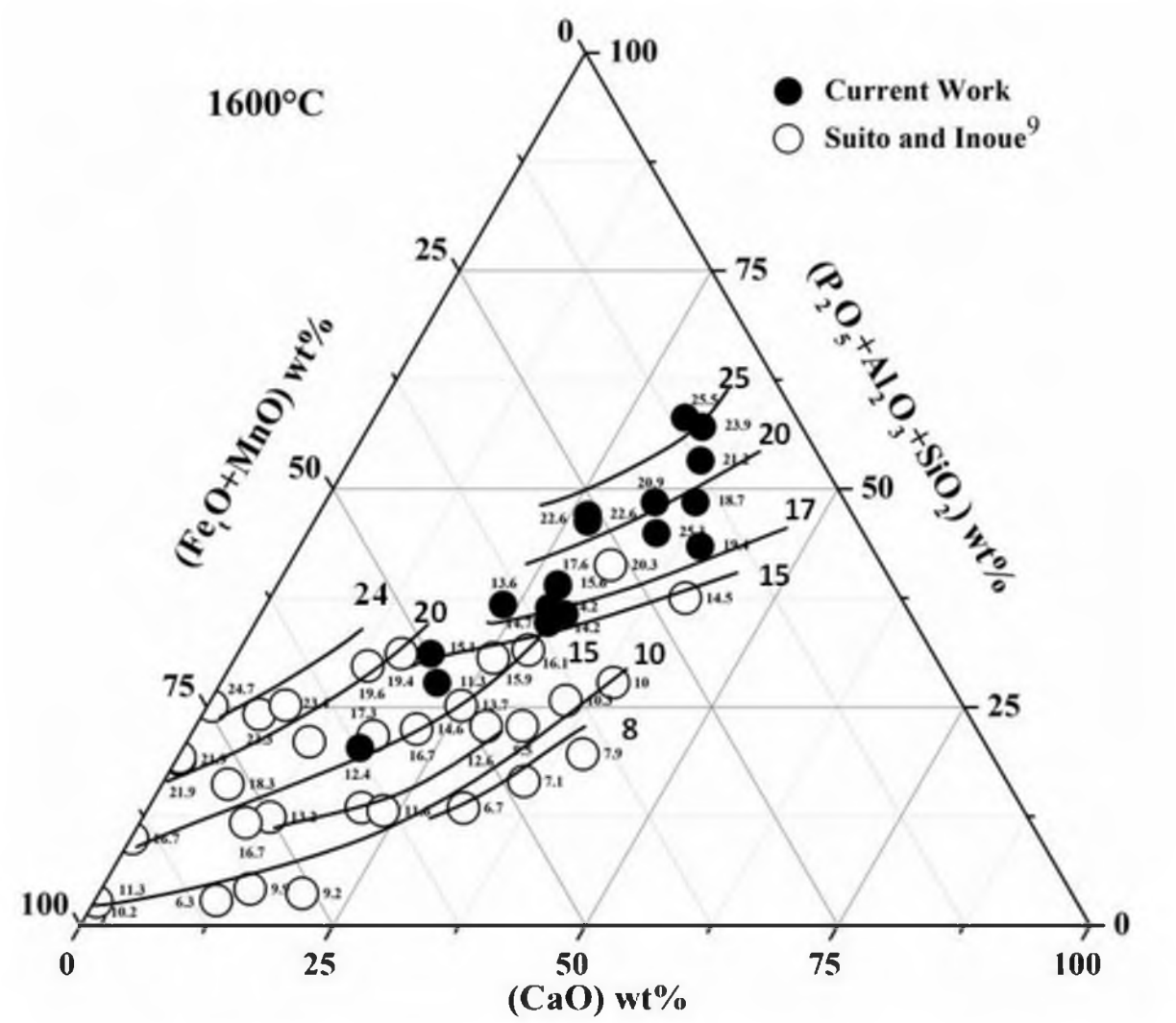

Figure 7-3. The iso-solubility lines of the CaO-Fe_tO-MnO-Al_2O_3-SiO_2-P_2O_5 system of the current work under H_2/H_2O and the work of Suito and Inoue[9] at 1600°C under Ar atmosphere. The labels denote MgO wt%.

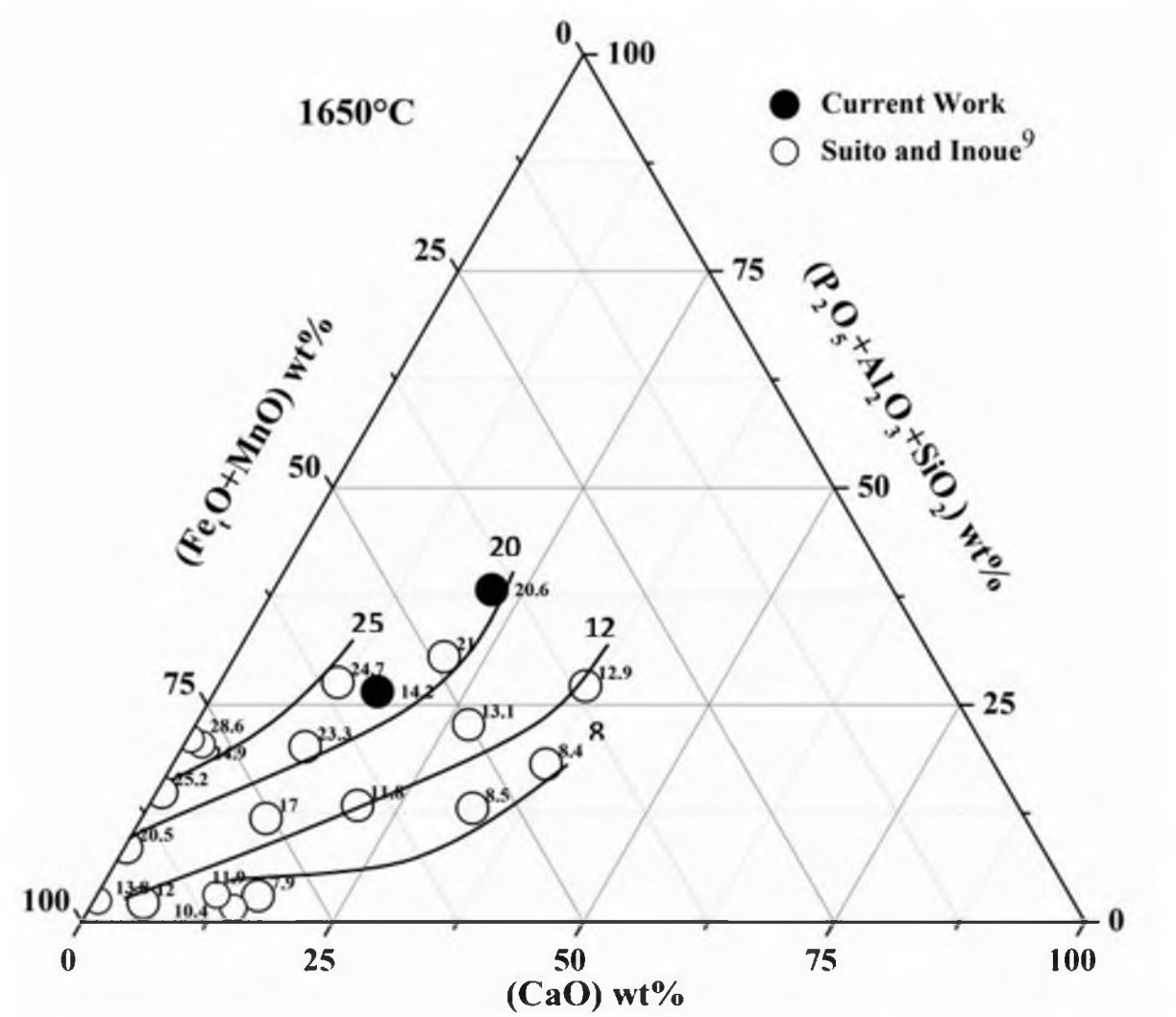

Figure 7-4. The iso-solubility lines of the CaO-Fe$_t$O-MnO-Al_2O_3-SiO_2-P_2O_5 system of the current work under H_2/H_2O and the work of Suito and Inoue[9] at 1650°C under Ar atmosphere. The labels denote MgO wt%.

increases with temperature. Also, it is noted that MgO solubility increases approaching the P_2O_5-Al_2O_3-SiO_2 side while it decreases approaching the (CaO)-(Fe_tO-MnO) pseudo-binary system. In their experiment, Suito and Inoue[9] used slags with no alumina, 2-5 wt% MnO, 0.1-3 wt% P_2O_5, in addition to the higher Fe_tO wt%. The MgO iso-solubility lines accordingly are condensed towards the Fe_tO+MnO corner in the pseudo ternary system. In order to compare the current work to the previous work, a correction factor was applied considering the contribution of the oxides in the slag to MgO solubility. The values of 1.0, 0.70, 0.59, 0.50, and 0.60 were assigned to CaO, FeO, MnO, SiO_2, and Al_2O_3, respectively, to represent their relative contributions to MgO solubility. These values gave the better correlation amongst all the tried values based on linear regression. It is worth noting that these factors are close to optical basicity of each oxide. This is consistent with Bergman's[2] finding that magnesia capacity, which is directly proportional to MgO wt% in the slag, is strongly correlated to slag optical basicity. Therefore, the following expression was used to express slag basicity index:

$$B' = (\text{wt\% CaO}+0.7\times\text{wt\% } Fe_tO+0.59\times\text{wt\% MnO}) - (0.5\times\text{wt\% } SiO_2+0.6\times\text{wt\% } Al_2O_3) \quad (7\text{-}6)$$

which should account for the differences in slag composition in the previous and the present work. Various basicity indices from the literature were tested, but eq 7-6 was found to best correlate MgO solubility to slag basicity. Figures 7-5 – 7-7 show the dependence of MgO solubility on the basicity index, as expressed by eq 7-6 in the present work. It is noted that MgO solubility decreases with the increase of basicity following an

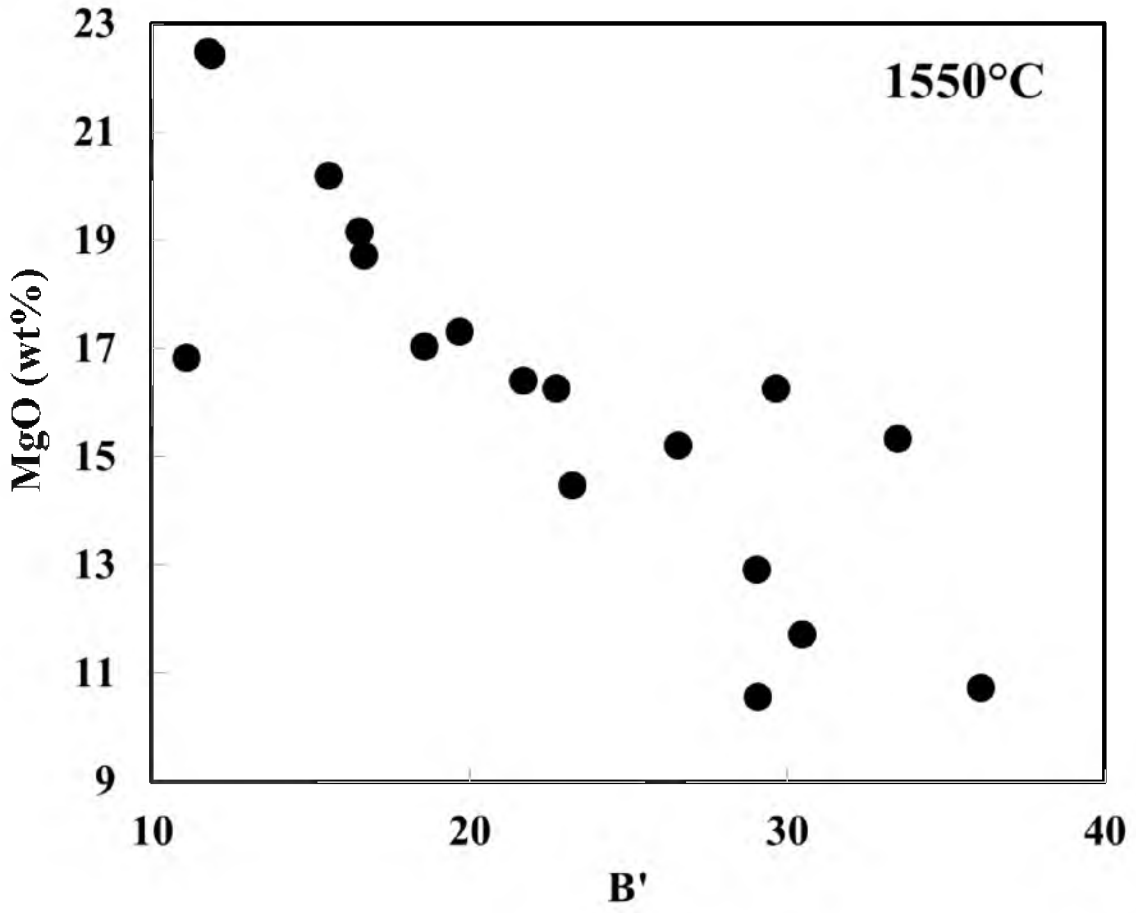

Figure 7-5. The effect of slag composition, basicity, on the MgO solubility under H_2/H_2O at 1550°C and pO_2 and pH_2O ranges of 1×10^{-10}-5×10^{-9} atm and 0.1-0.4 atm, respectively.

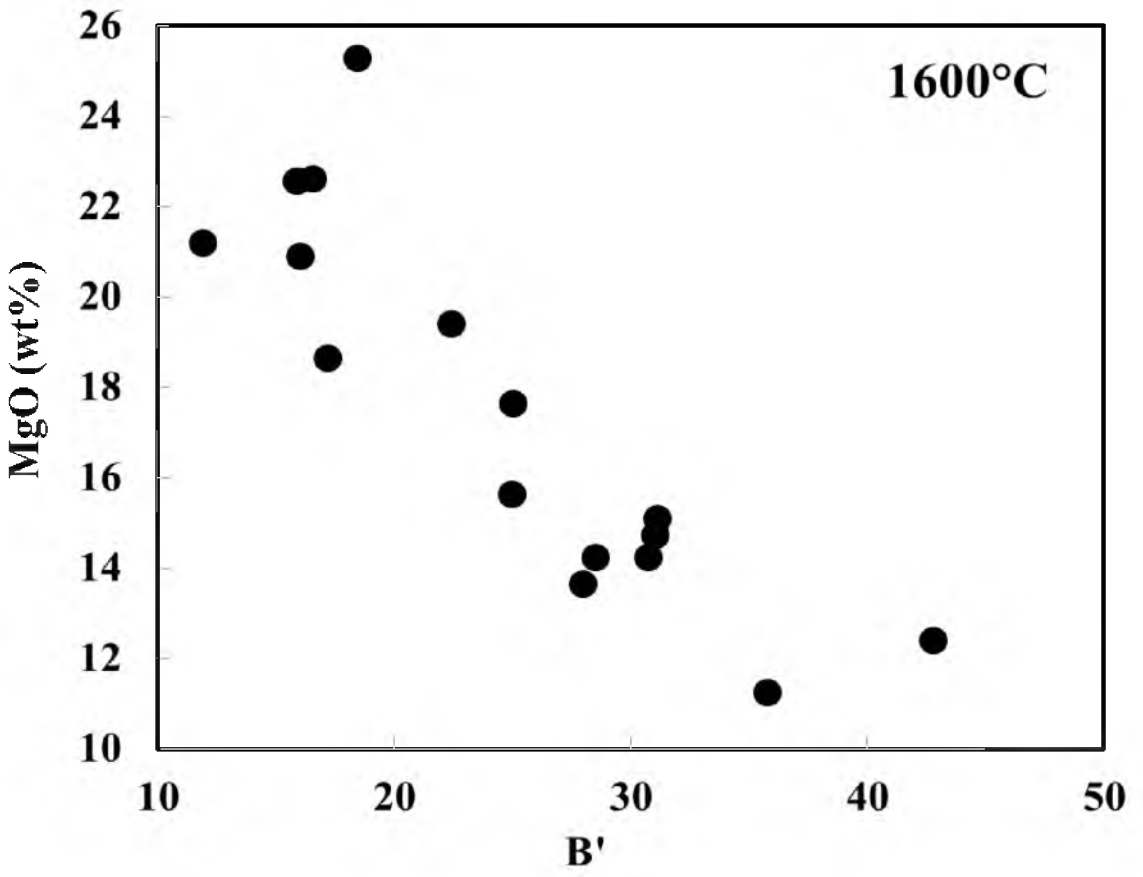

Figure 7-6. The effect of slag composition, basicity, on the MgO solubility under H_2/H_2O at 1600°C and pO_2 and pH_2O ranges of 5×10^{-10}-5×10^{-9} atm and 0.1-0.4 atm, respectively.

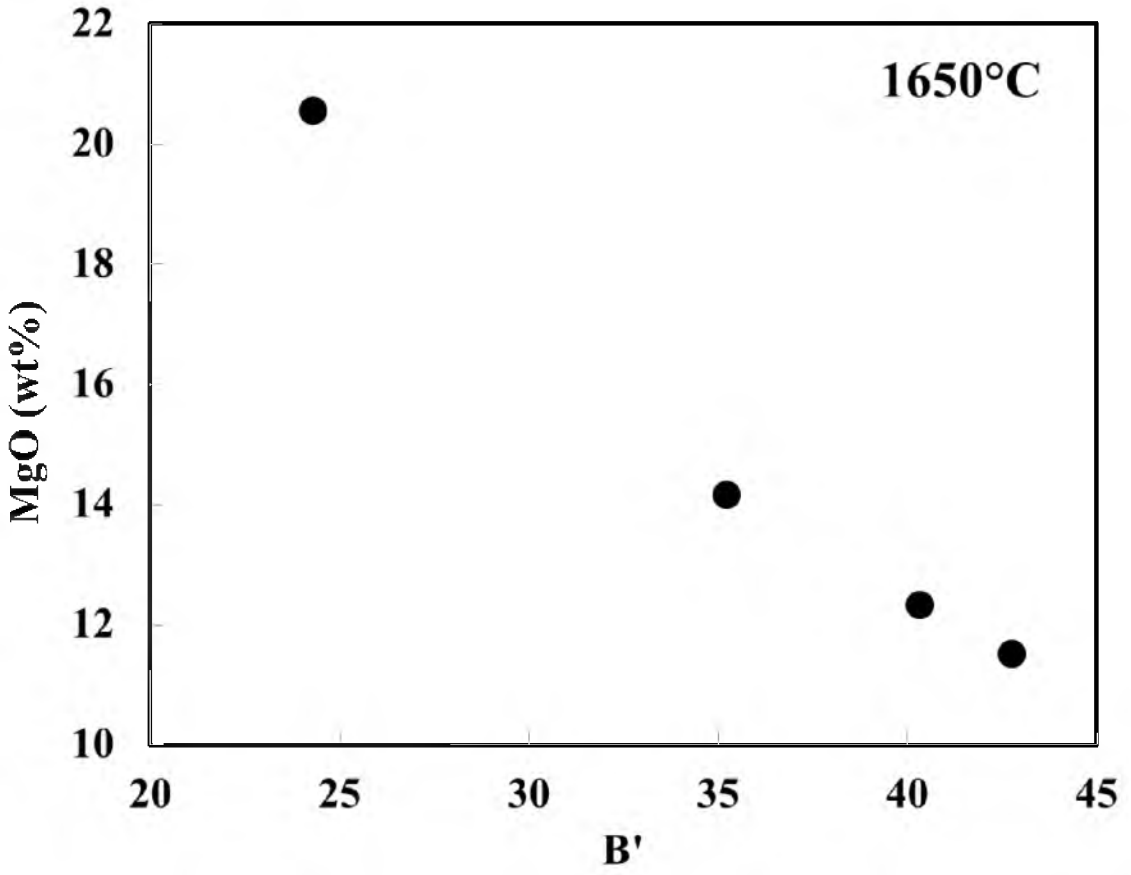

Figure 7-7. The effect of slag composition, basicity, on the MgO solubility under H_2/H_2O at 1650°C and pO_2 and pH_2O of 4×10^{-9} and 0.3 atm, respectively.

almost linear relationship. The developed basicity index, eq 7-6, was used to compare, as Figure 7-8 reveals, the results of the current work under H_2/H_2O and those of Suito and Inoue[9] and Liu *et al.*[15] That comparison implies consistently the negative dependence of MgO solubility on basicity observed in the current work. Figure 7-9 presents the variation of MgO solubility with basicity under the three gas mixtures: $CO/CO_2/H_2/H_2O$, CO/CO_2, and H_2/H_2O. It was found that MgO solubility obeyed the same trend, the negative dependence on B′ regardless of the type of gas atmosphere, although the data are rather scattered.

7. 4. 2. Effect of Temperature on MgO Solubility

In order to evaluate the influence of temperature on MgO solubility, MgO content was plotted as a function of temperature at constant CaO/SiO_2 over narrow ranges of FeO content, as shown in Figures 7-10 – 7-13. They reveal the positive linear relationship for each FeO content range, which has also been shown by previous researchers.[11, 14, 16] Figure 7-14 demonstrates a comparison of the current work to the Suito and Inoue[9] employing the B′ expression to account for the differences in slag composition. It is seen that the solubility increase with increasing temperature for the same slag composition in the investigated temperature range 1550 to 1650°C under the H_2/H_2O atmosphere, which is consistent with Suito and Inoue's[9] results in the same temperature range.

Schürmann and Kolm[11] formulated a mathematical relationship for the effect of temperature on MgO solubility based on their analysis of various steelmaking slag data. Their relation uses MgO solubility at 1600°C, which is multiplied by a function of

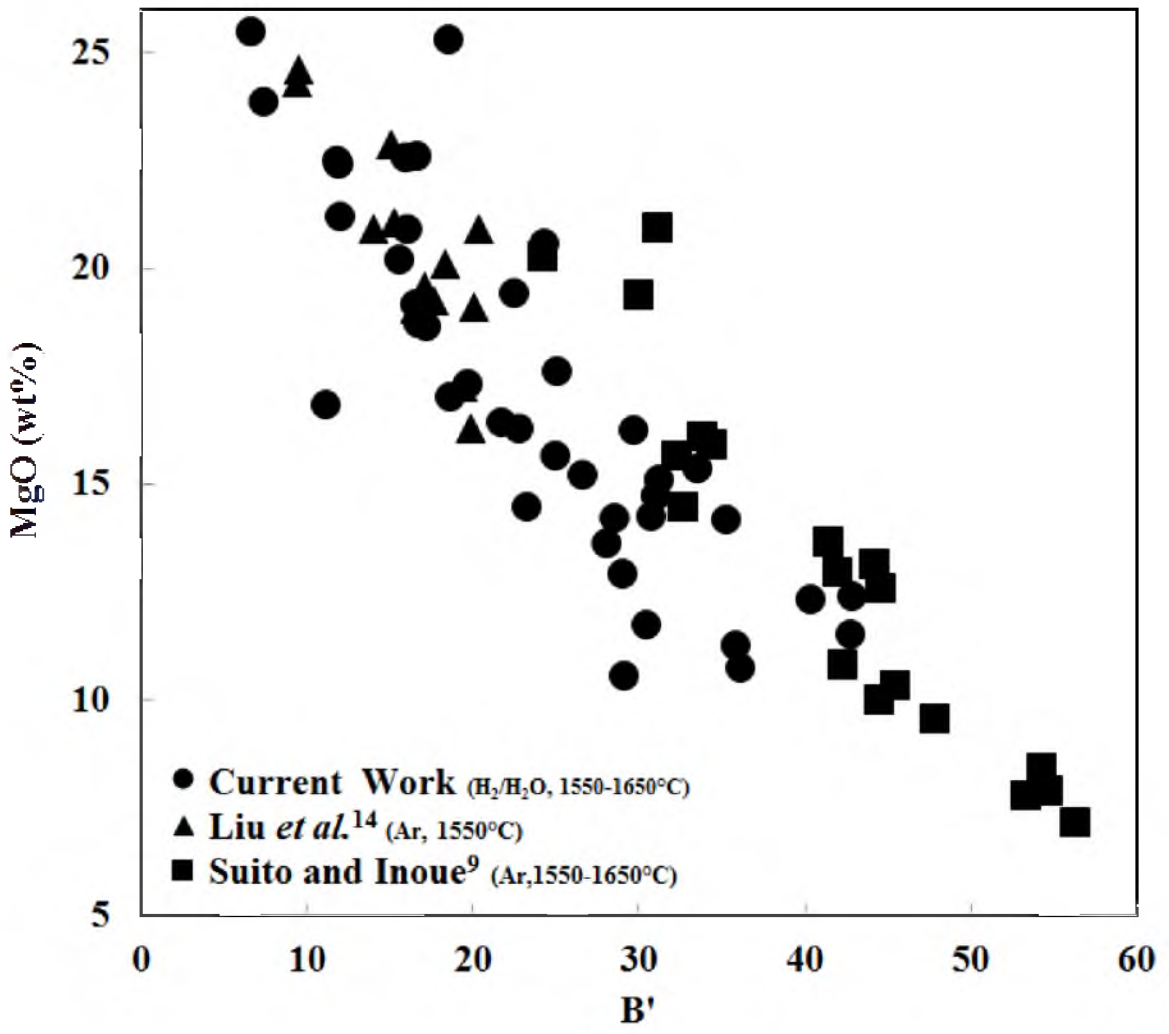

Figure 7-8. The dependence of MgO on slag basicity from the current (under H_2/H_2O atmosphere) and previous work (under Ar atmosphere).

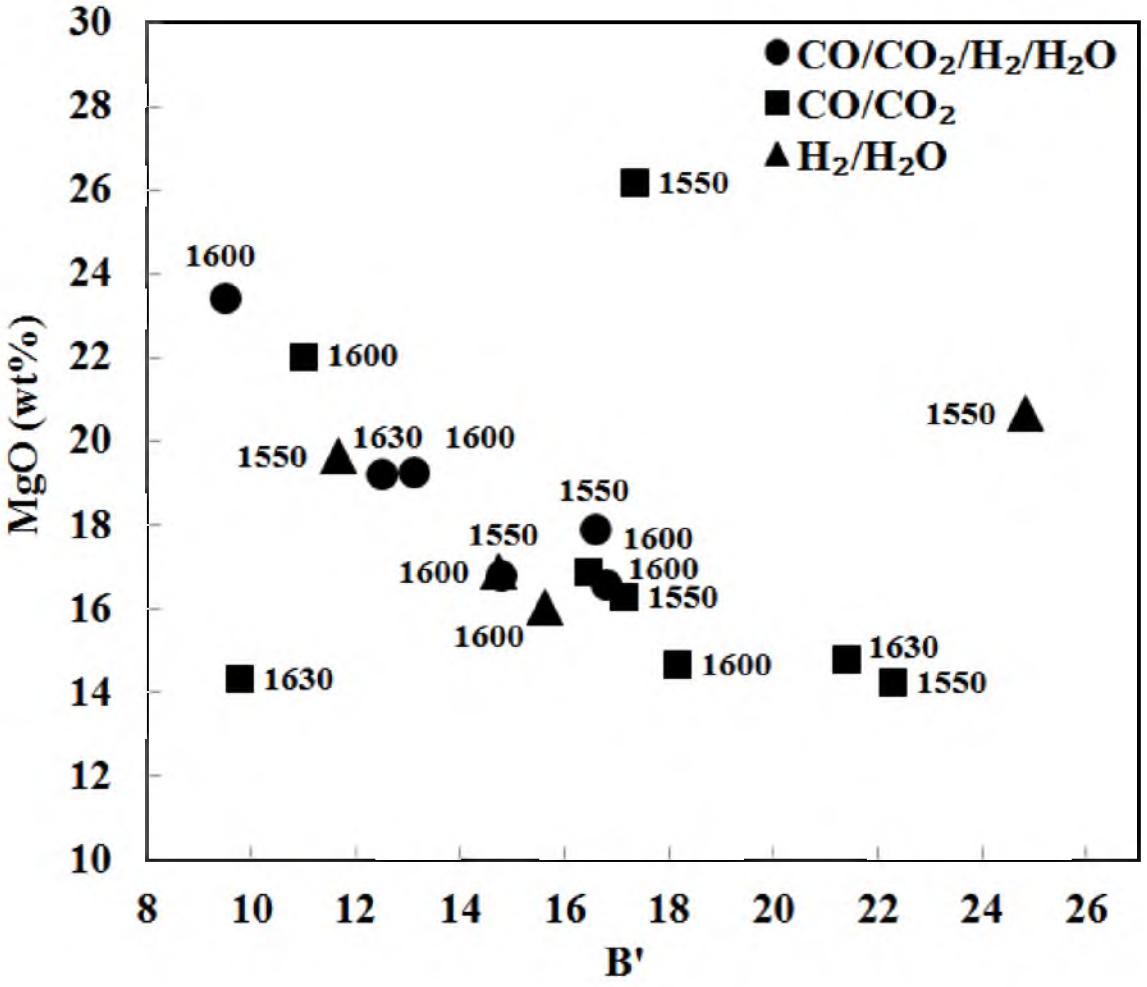

Figure 7-9. The dependence of MgO on slag basicity under the three different gas atmospheres in the temperature range 1550 to 1630°C and pO_2 of 10^{-9} to 10^{-10} atm for slags with CaO/SiO_2 of 0.8 to 1.2. The labels indicate the temperature in °C.

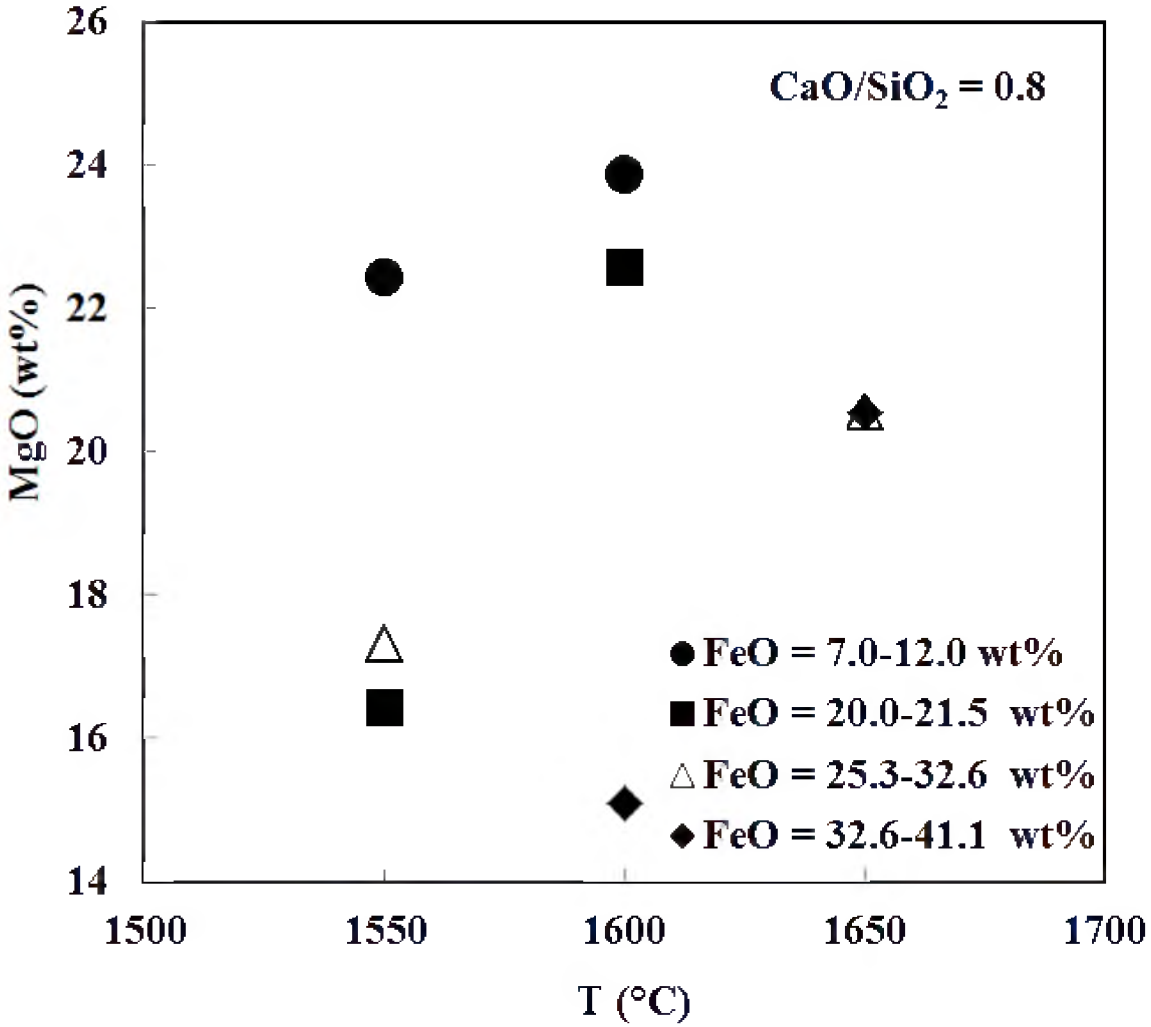

Figure 7-10. The influence of temperature on MgO solubility at $CaO/SiO_2 = 0.8$ under H_2/H_2O atmosphere.

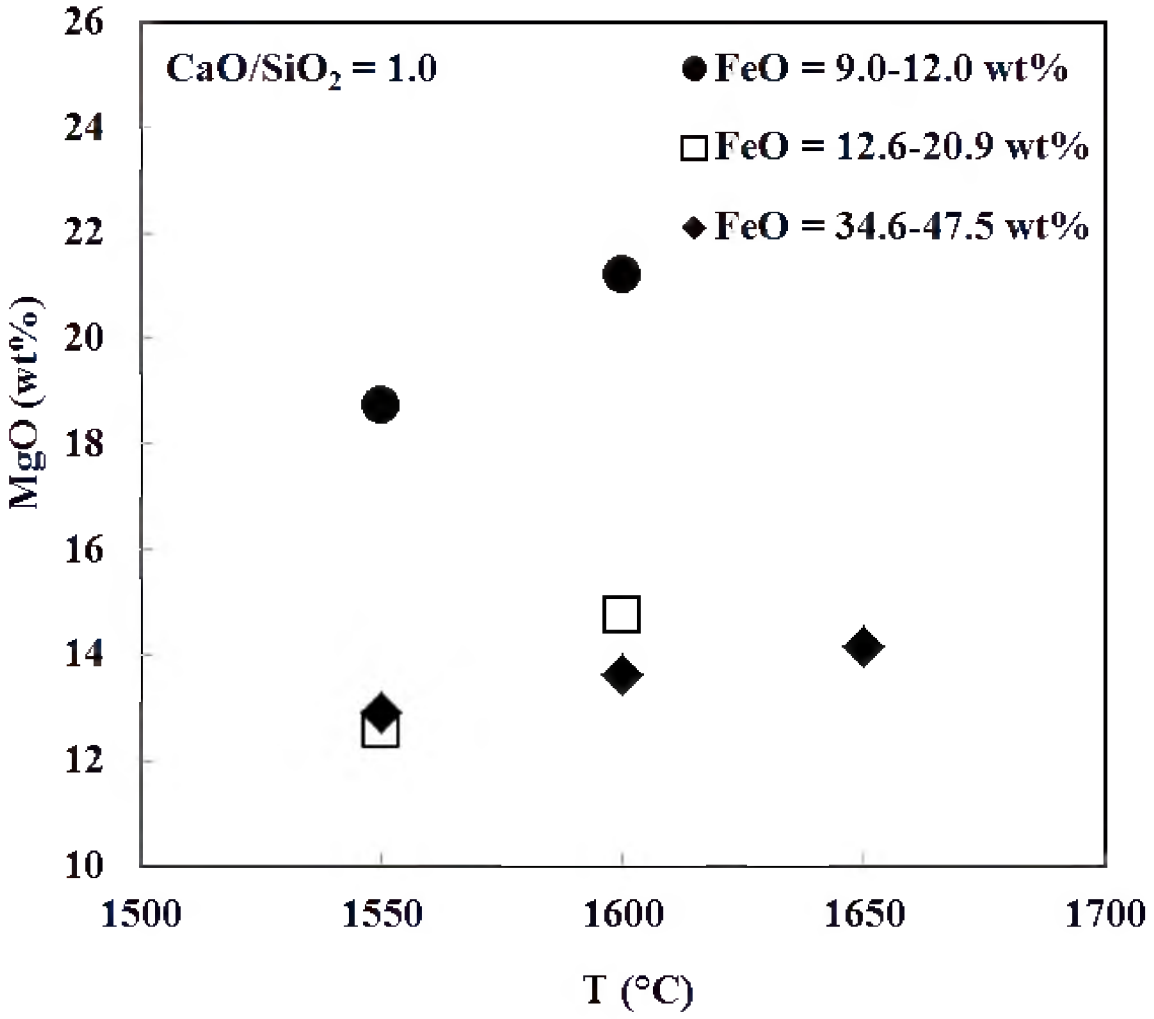

Figure 7-11. The influence of temperature on MgO solubility at CaO/SiO_2 = 1.0 under H_2/H_2O atmosphere.

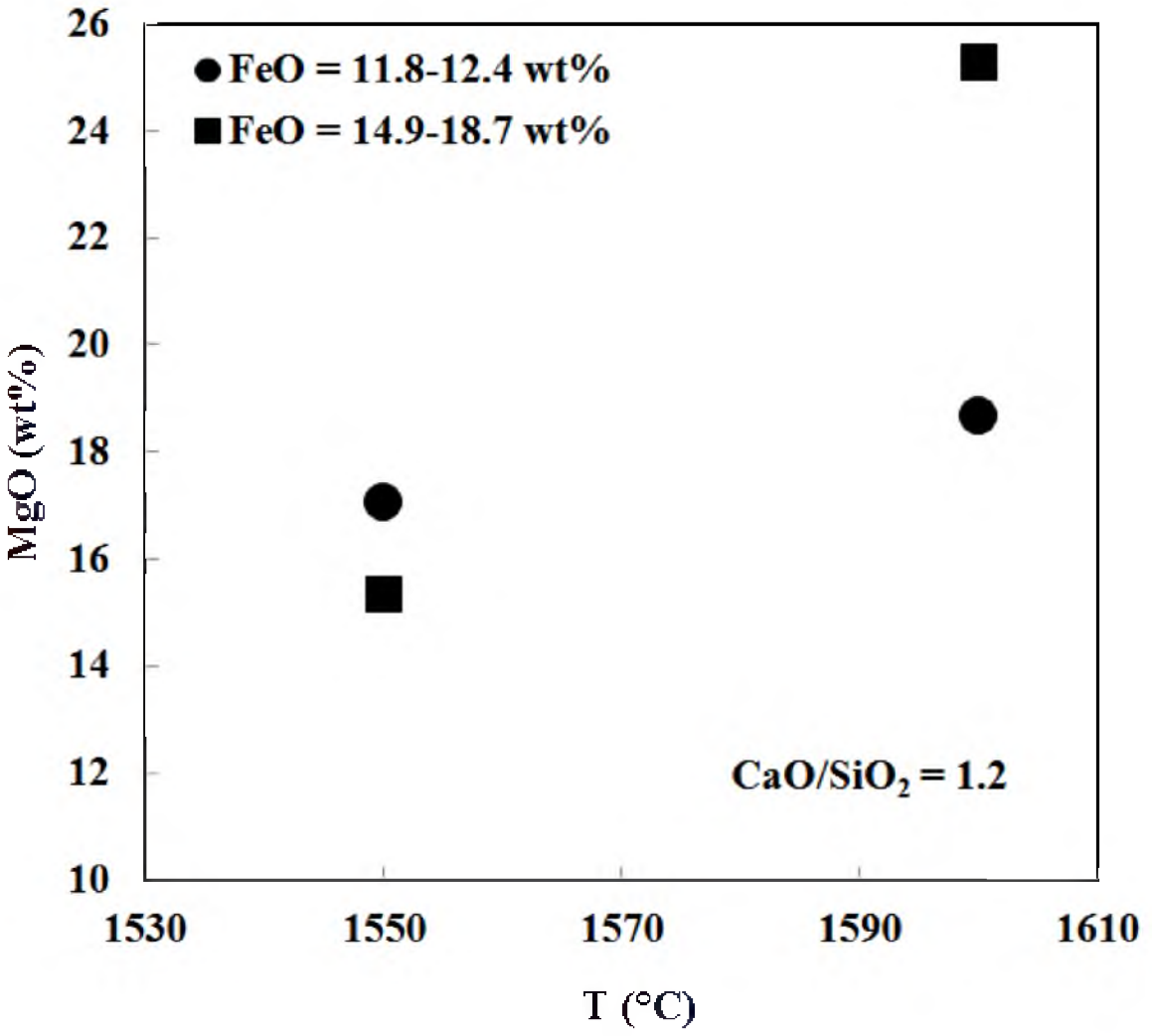

Figure 7-12. The influence of temperature on MgO solubility at CaO/SiO_2 = 1.2 under H_2/H_2O atmosphere.

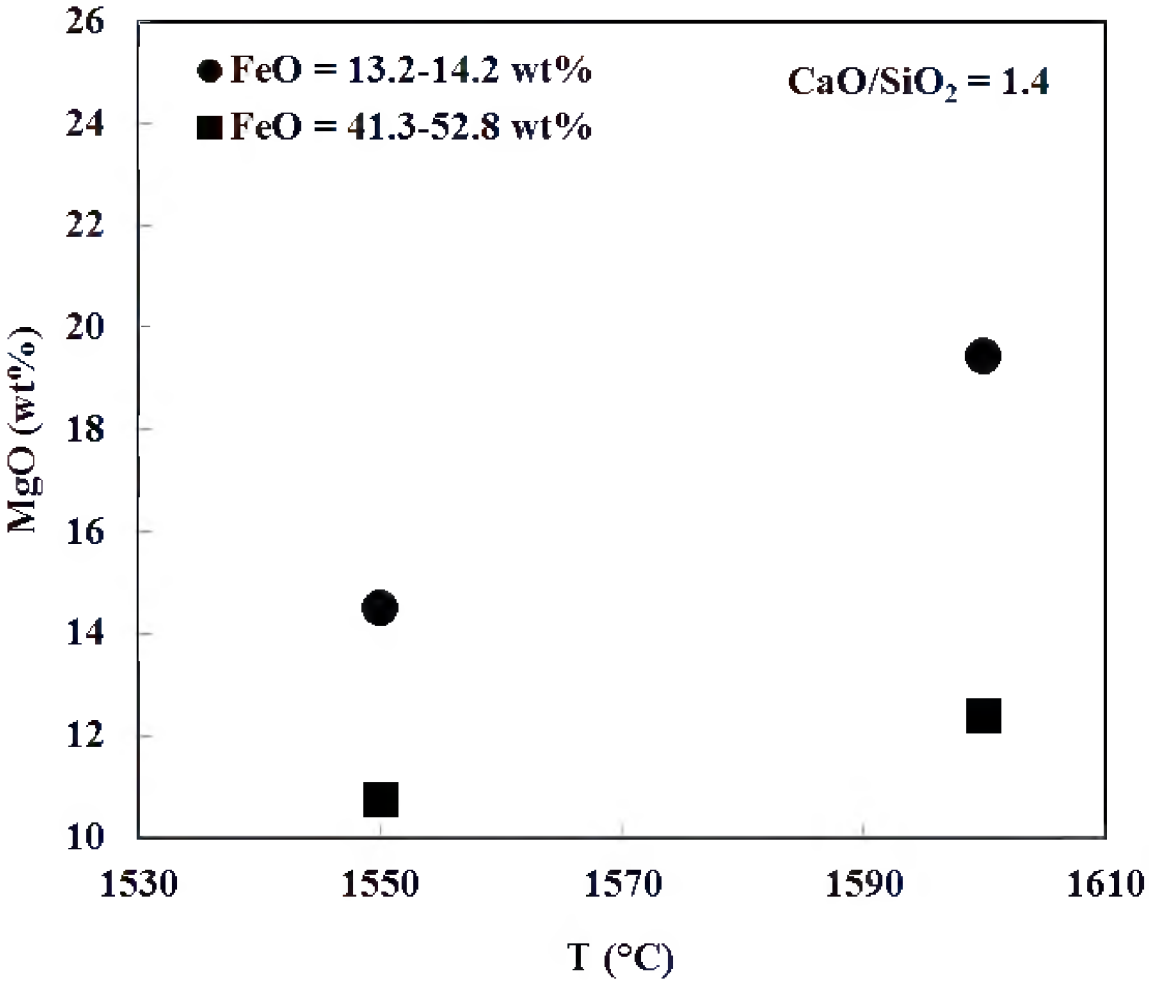

Figure 7-13. The influence of temperature on MgO solubility at $CaO/SiO_2 = 1.4$ under H_2/H_2O atmosphere.

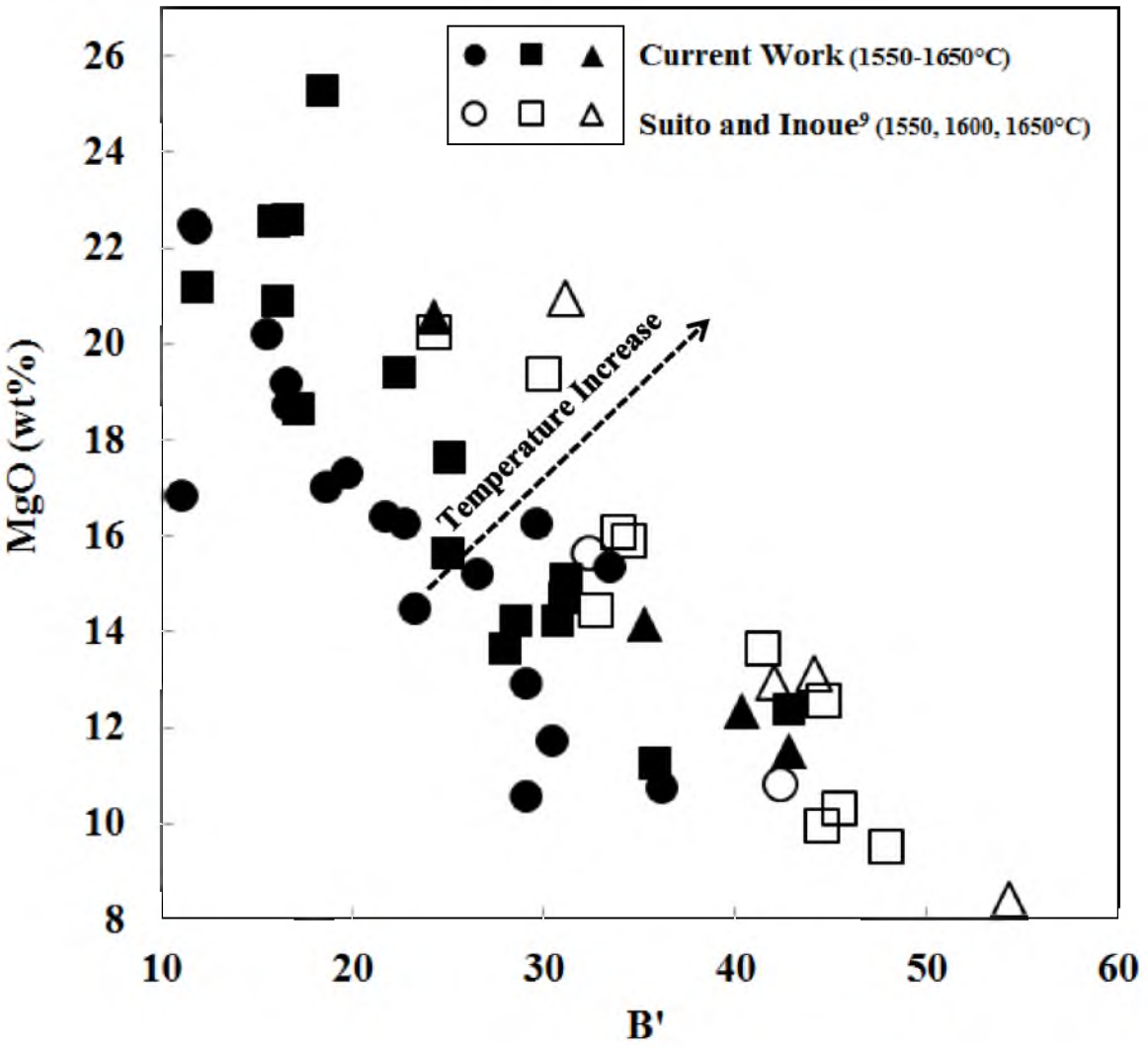

Figure 7-14. The effect of temperature on MgO solubility in the current work under H_2/H_2O atmosphere along with that of Suito and Inoue[9] under Ar atmosphere.

temperature to obtain MgO solubility at the desired temperature for the same slag composition. They developed the following empirical relation:

$$\frac{wt\%\ MgO_{sat,T}}{wt\%\ MgO_{sat,1873}} = k_T = e^{\left(5.5478 - \frac{10391}{T}\right)} \qquad (7\text{-}7)$$

where T and $wt\%\ MgO_{sat,T}$ are the temperature in Kelvin and the MgO content in wt% in the slag at magnesiowustite saturation at the target temperature, respectively. This relation was evaluated using the results under H_2/H_2O where MgO solubility at 1550°C was calculated using the experimentally obtained data at 1600°C. Both the calculated and observed values are plotted versus B′, as illustrated in Figure 7-15. The calculated values offer good agreement with the observed values. Hence, eq 7-7 fairly well predict the influence of temperature on MgO solubility in the studied slags under H_2/H_2O atmospheres.

7. 4. 3. Effect of FeO Content on MgO Solubility

FeO plays a dramatic role affecting MgO solubility depending on the basicity of the slag. In highly basic slags, FeO was found to increase MgO solubility as Demidov *et al.*[19] reported for slags with CaO/SiO_2 of 3.0 at 1600°C where FeO behaved as an acidic oxide. On the other hand, FeO tends to decrease MgO solubility in low to moderate basicity slags where it acts as a basic oxide. This trend has been supported by the investigations of Suito and Inoue,[9] Liu *et al.*,[15] Shim and Ban-ya,[8] and Jung *et al.*[17] within CaO/SiO_2 ranges of 0.5-1.6, 0.8-1.2, 0.4-1.3, and 1-1.2, respectively, and under Ar

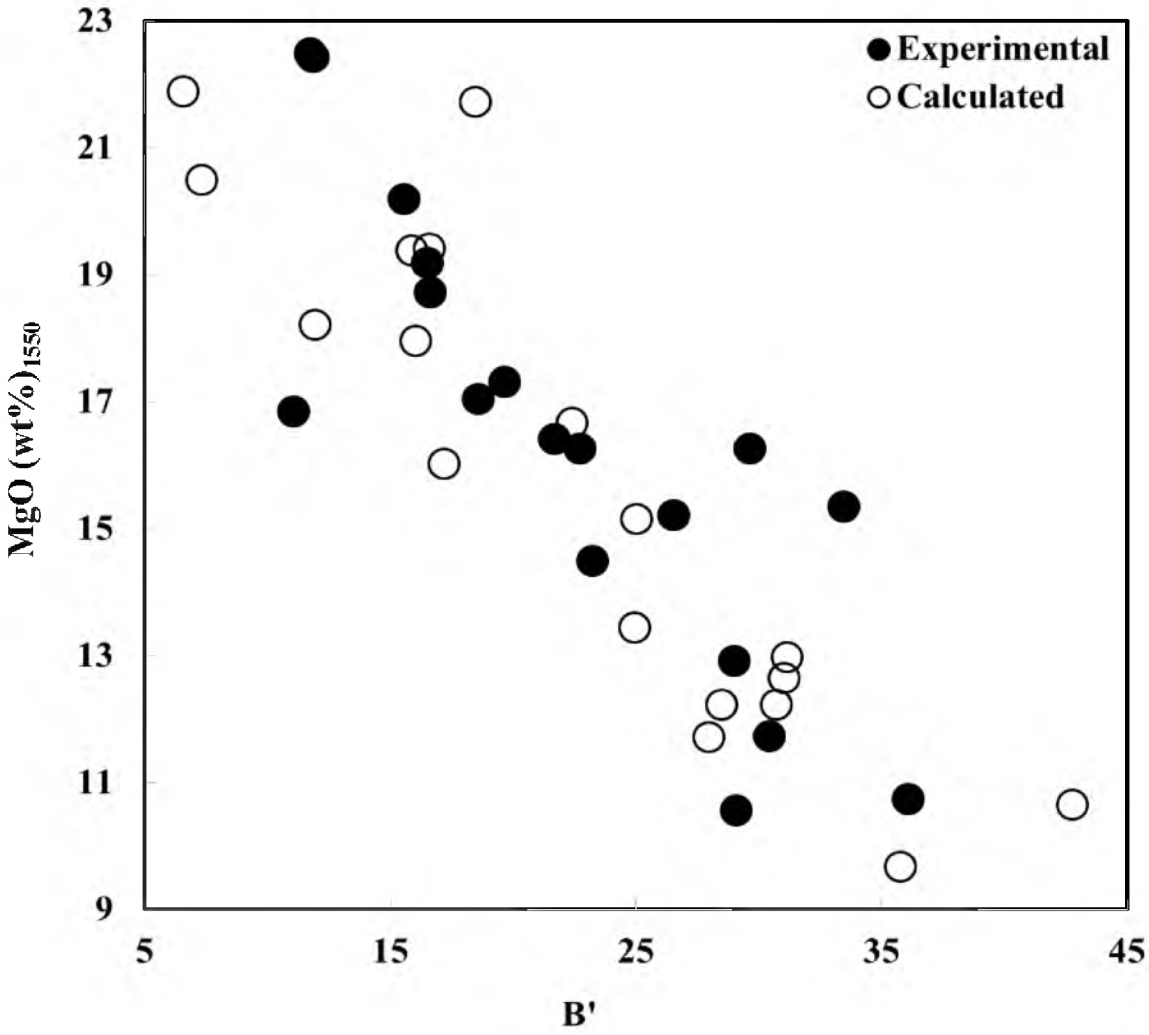

Figure 7-15. MgO solubility as calculated with eqs 7-7 and 7-8 along with experimental results at 1550°C under H_2/H_2O atmosphere.

atmosphere in the first three experiments and CO/CO_2 atmosphere in the latter. The same trend was found to apply to the current work, under H_2/H_2O, and within $\%CaO/\%SiO_2$ in the range of 0.8-1.4, as Figures 7-16 – 7-19 present. Because of this dependency, γ_{FeO} is expected to play an important role in MgO solubility. Since γ_{FeO} is affected by pH_2O in the gas atmosphere in contact with the slag as found in Chapter 6, the gas atmosphere impacts MgO solubility in the slag; *vide infra*.

7. 4. 4. The Effect of Gas Atmosphere on MgO Solubility

In the temperature range of 1550-1630°C and with slags of CaO/SiO_2 of 0.8-1.2, the order of MgO solubility follows H_2/H_2O > $CO/CO_2/H_2O/H_2O$ > CO/CO_2 regardless of the temperature and slag composition, as the results in Figures 7-20 – 7-22 indicate. That observation implies that the higher pH_2O in the gas atmosphere, the higher MgO dissolution is. That trend is seen in Figures 7-23 – 7-25 where it can be seen that MgO solubility increases with pH_2O. For instance, the effect of H_2O was pronounced at 1600 and CaO/SiO_2 of 1.0 where MgO wt% increased 12% with a pH_2O change from 0 to 0.1 atm, as shown in Figure 7-24. That observation is consistent with the previously discussed effect of FeO on MgO solubility. In other words, the interaction coefficient of H_2O on γ_{FeO}, $\varepsilon_{FeO}^{H_2O}$, as mentioned in Chapter 6, was found to be positive. In turn, the FeO content should decrease with the increase of pH_2O under constant pO_2. Since MgO, in the investigated slags, decreases with FeO increase, it is expected that MgO will increase with pH_2O, as Figures 7-23 – 7-25 prove.

For the slag compositions investigated, MgO-saturated CaO-FeO-Al_2O_3-SiO_2-MnO (0.2-0.8 wt%)-P_2O_5 (0.1-0.9 wt%), in the temperature range 1550-1600°C, with

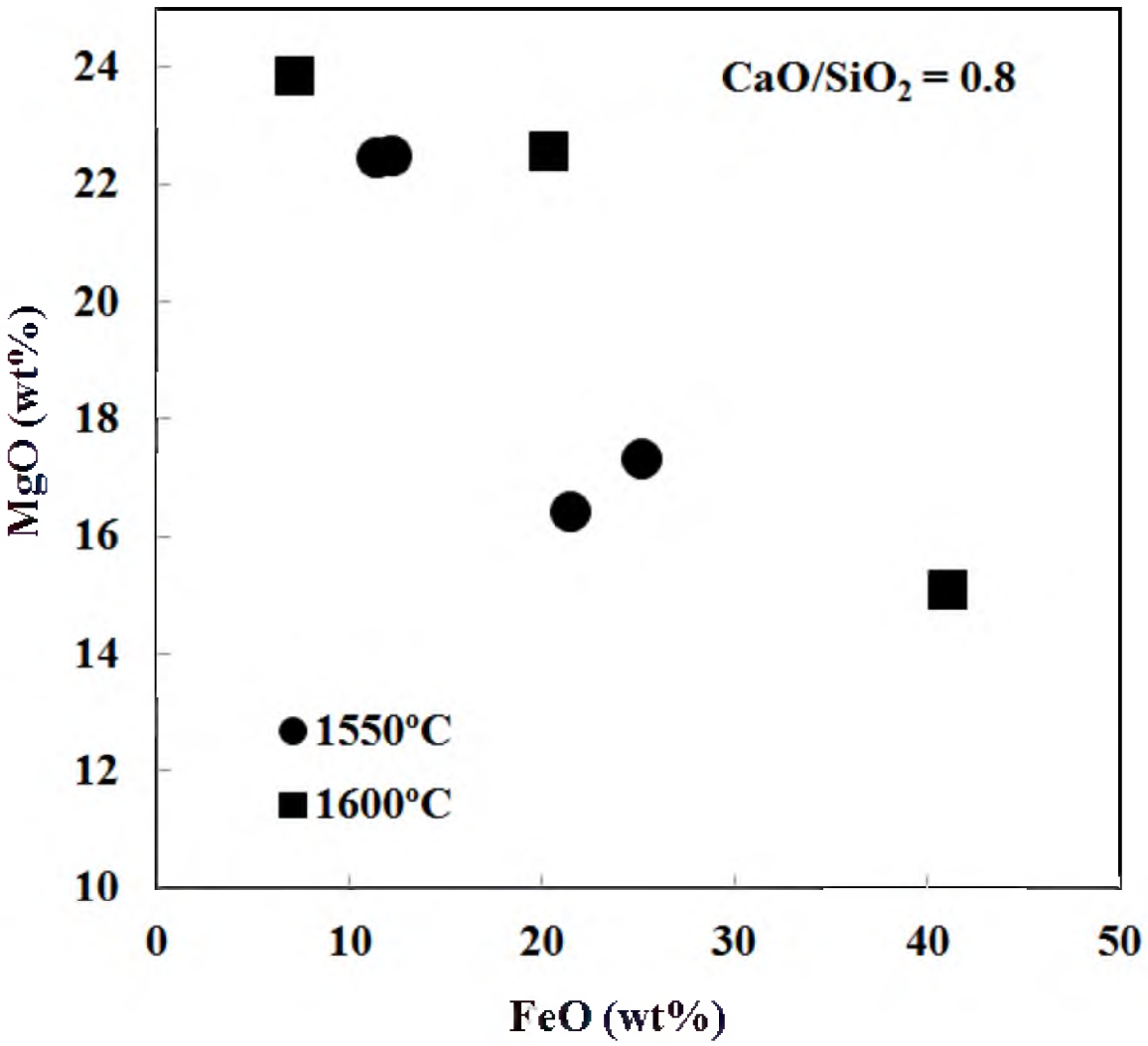

Figure 7-16. The change of MgO solubility as a function of FeO content in the slag at $CaO/SiO_2 = 0.8$ and temperatures of 1550°C and 1600°C under H_2/H_2O atmosphere.

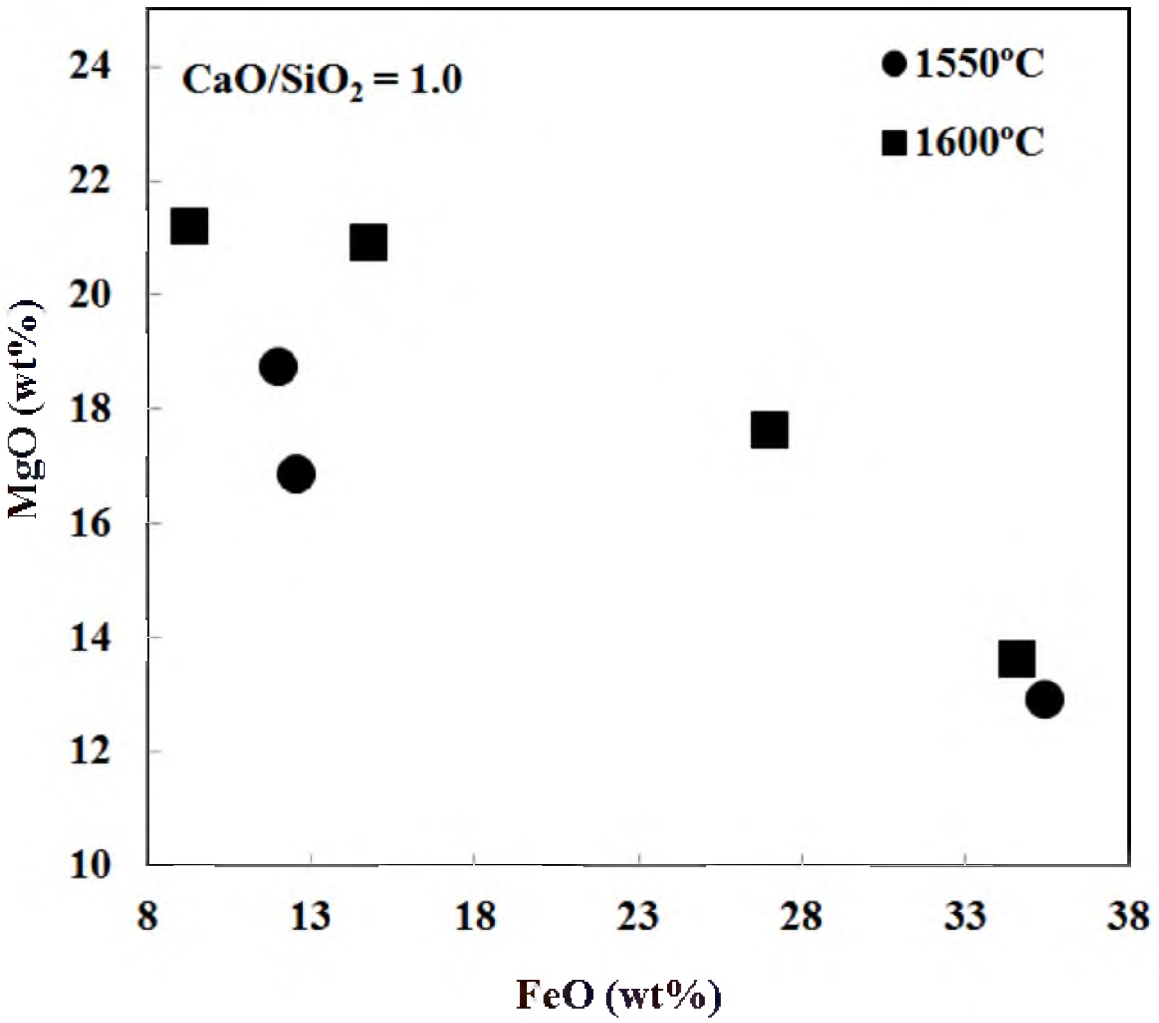

Figure 7-17. The change of MgO solubility as a function of FeO content in the slag at CaO/SiO_2 = 1.0 and temperatures of 1550°C and 1600°C under H_2/H_2O atmosphere.

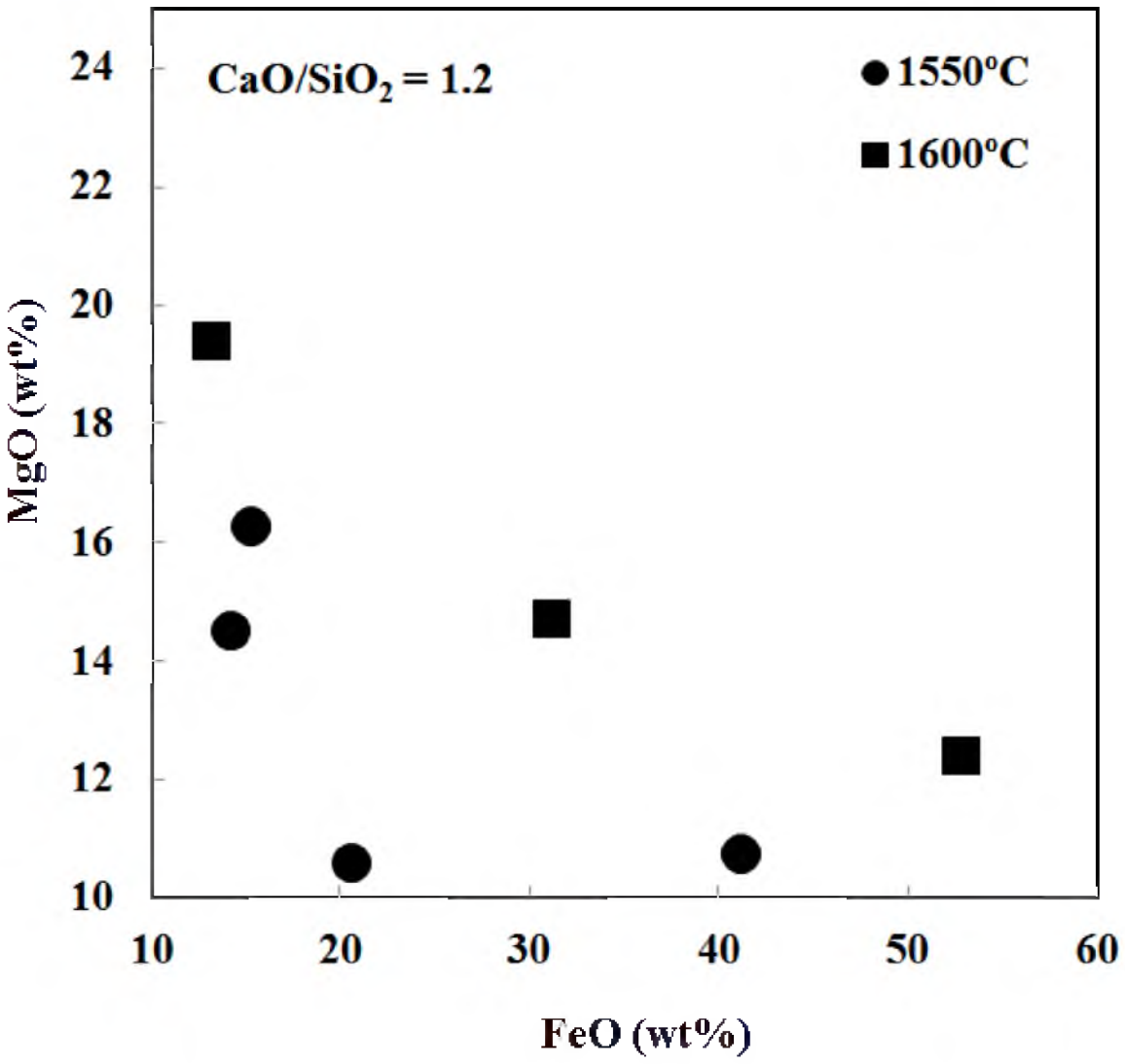

Figure 7-18. The change of MgO solubility as a function of FeO content in the slag at CaO/SiO_2 = 1.2 and temperatures of 1550°C and 1600°C under H_2/H_2O atmosphere.

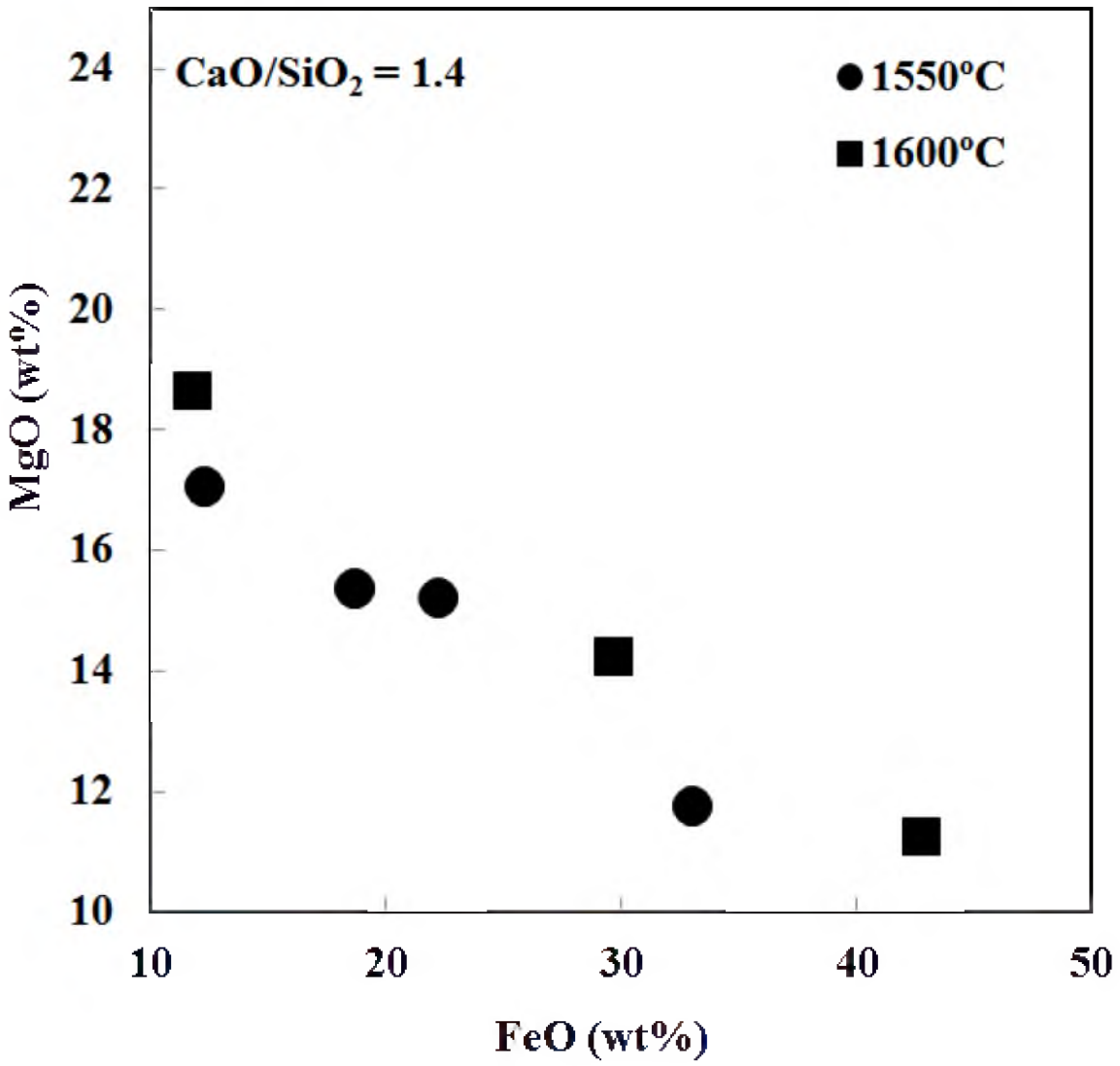

Figure 7-19. The change of MgO solubility as a function of FeO content in the slag at CaO/SiO_2 = 1.4 and temperatures of 1550°C and 1600°C under H_2/H_2O atmosphere.

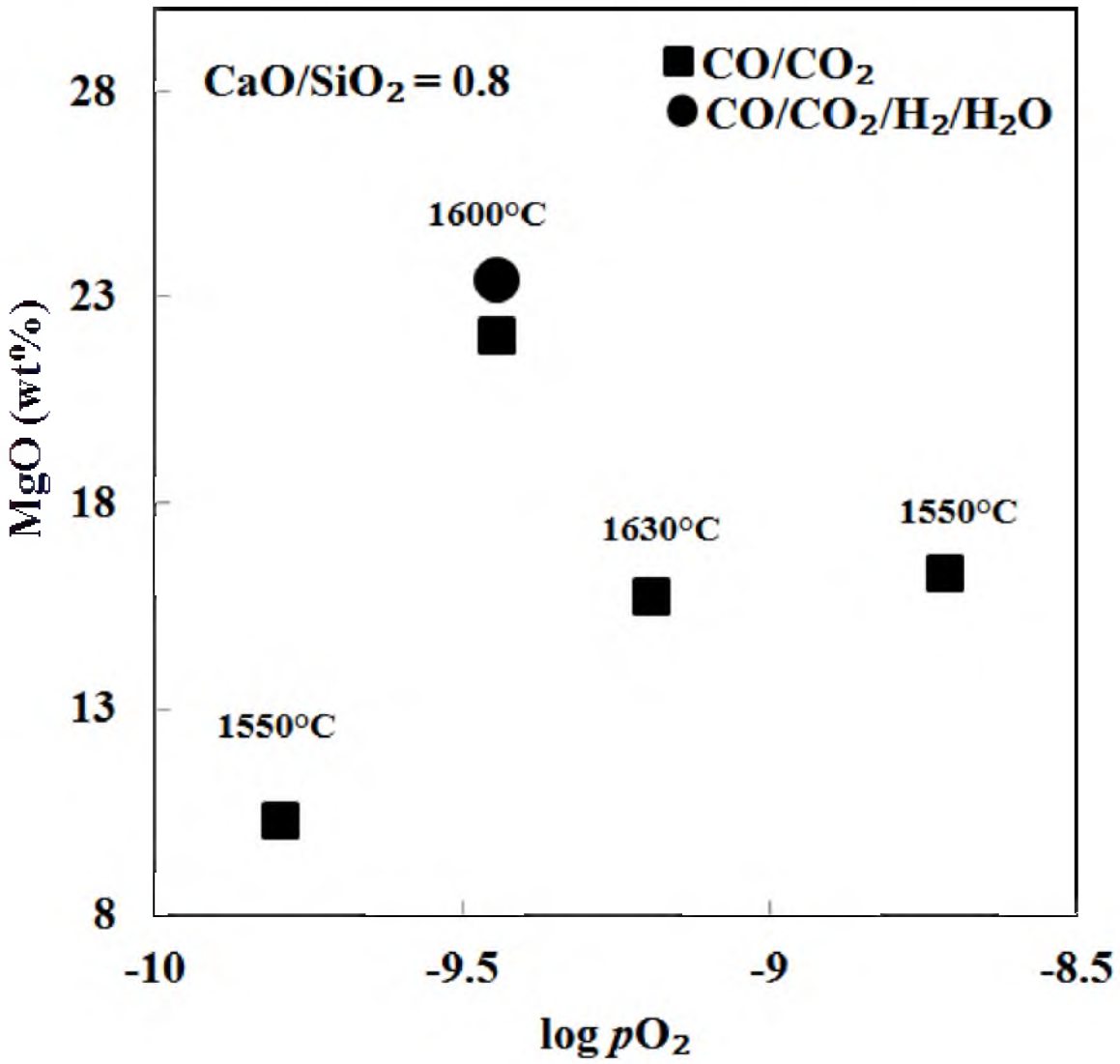

Figure 7-20. The effect of gas composition on MgO solubility at different pO_2 and temperature values for slags with wt% CaO/ wt% SiO_2 of 0.8 and pH_2O of 0 and 0.1 atm in CO/CO_2 and $H_2/H_2O/CO/CO_2$, respectively.

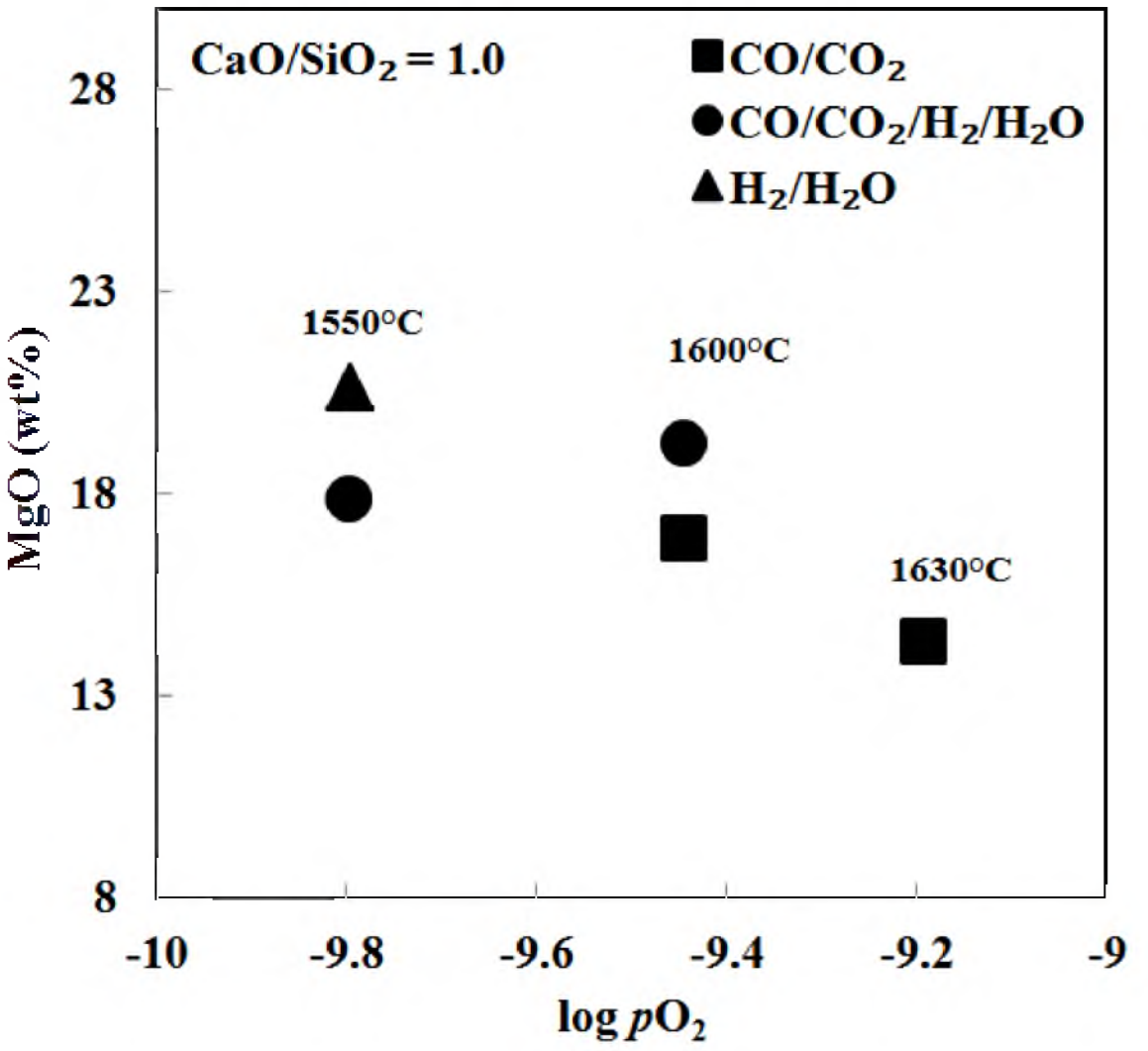

Figure 7-21. The effect of gas composition on MgO solubility at different pO_2 and temperature values for slags with wt% CaO/ wt% SiO_2 of 1.0 and pH_2O of 0, 0.1, and 1.0 atm in CO/CO_2, $H_2/H_2O/CO/CO_2$, and $H_2/H_2O/CO$, respectively.

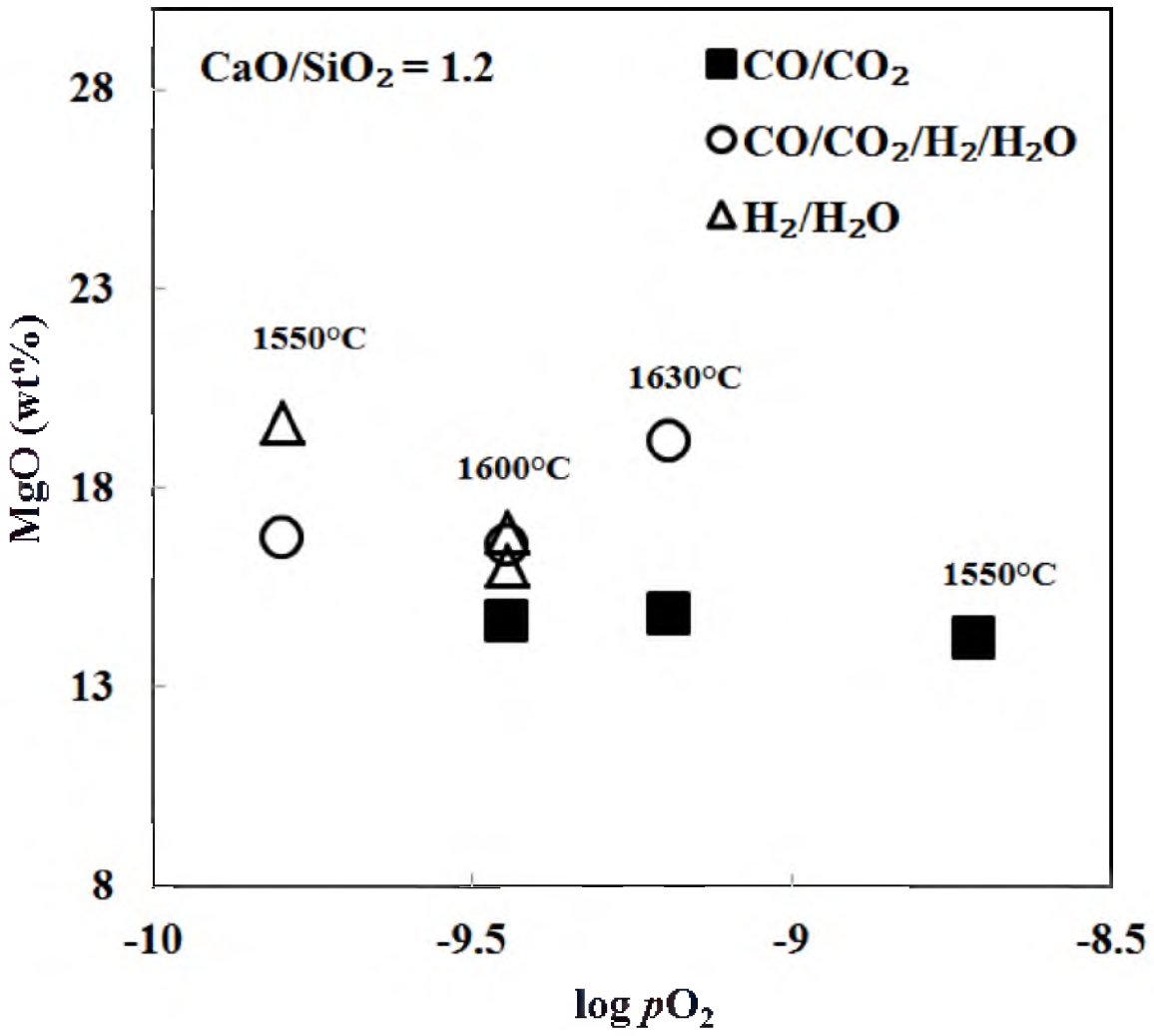

Figure 7-22. The effect of gas composition on MgO solubility at different pO_2 and temperature values for slags with wt% CaO/ wt% SiO_2 of 1.2 and pH_2O of 0, 0.1, and 1.0 atm in CO/CO_2, $H_2/H_2O/CO/CO_2$, and $H_2/H_2O/CO$, respectively.

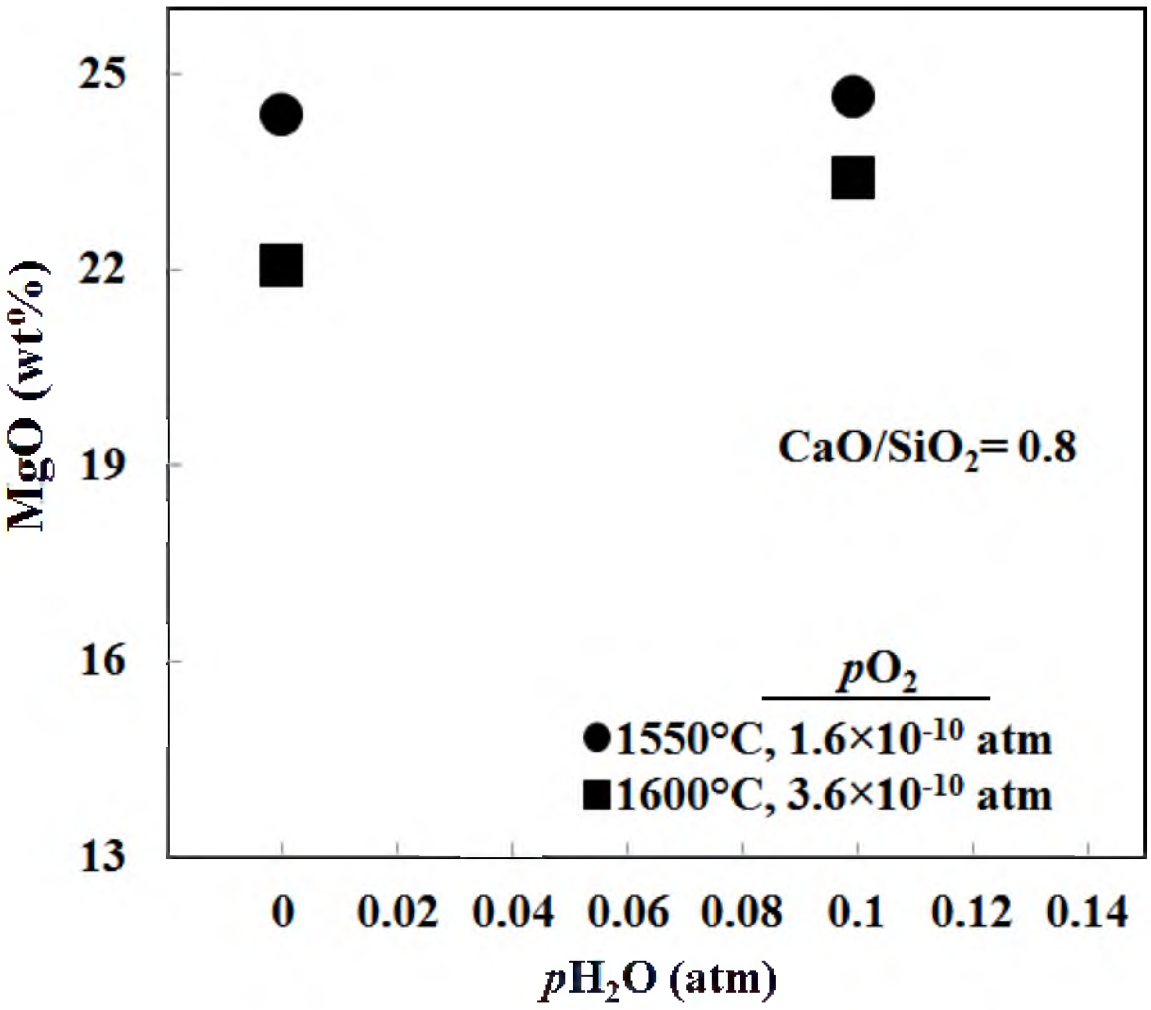

Figure 7-23. The effect of water content in the gas on MgO solubility at wt% CaO/ wt% SiO_2 of 0.8 at different temperatures and pO_2.

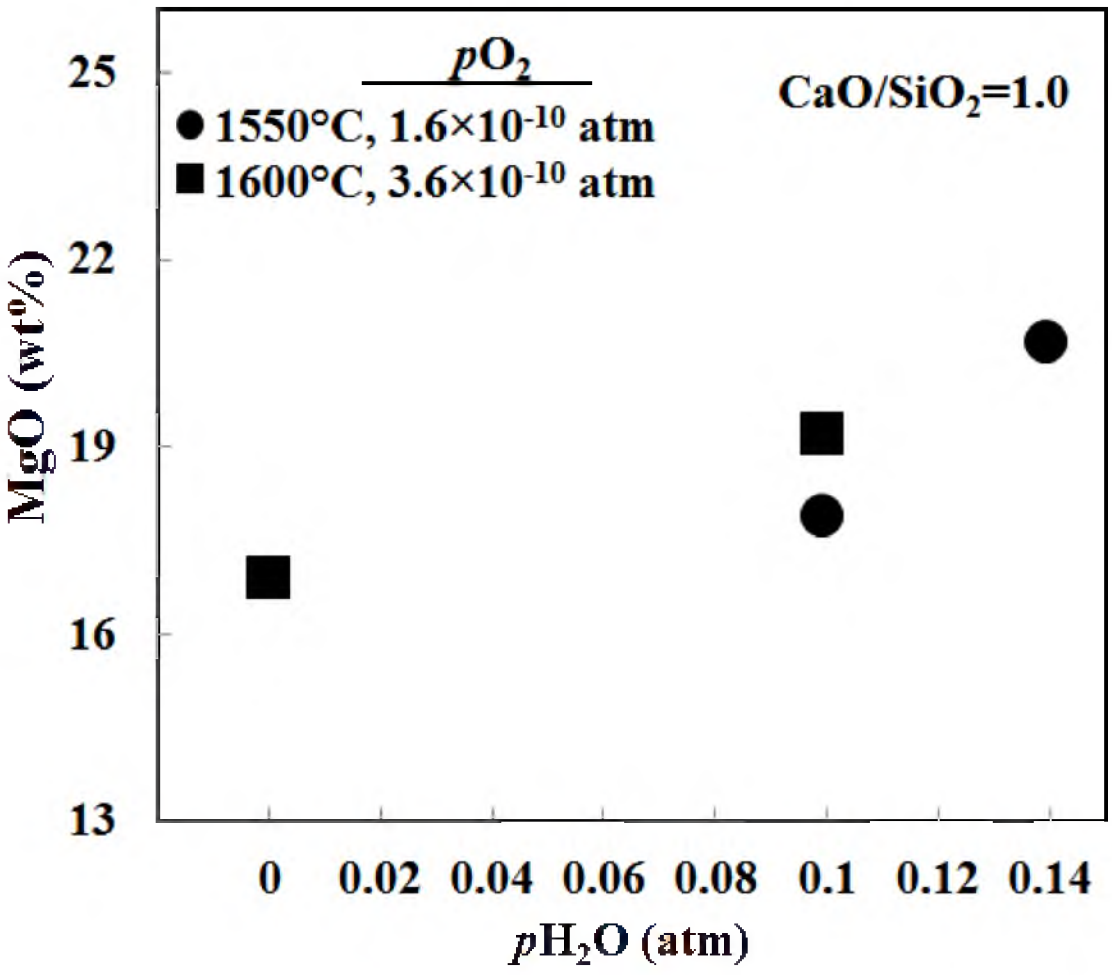

Figure 7-24. The effect of water content in the gas on MgO solubility at wt% CaO/ wt% SiO_2 of 1.0 at different temperatures and pO_2.

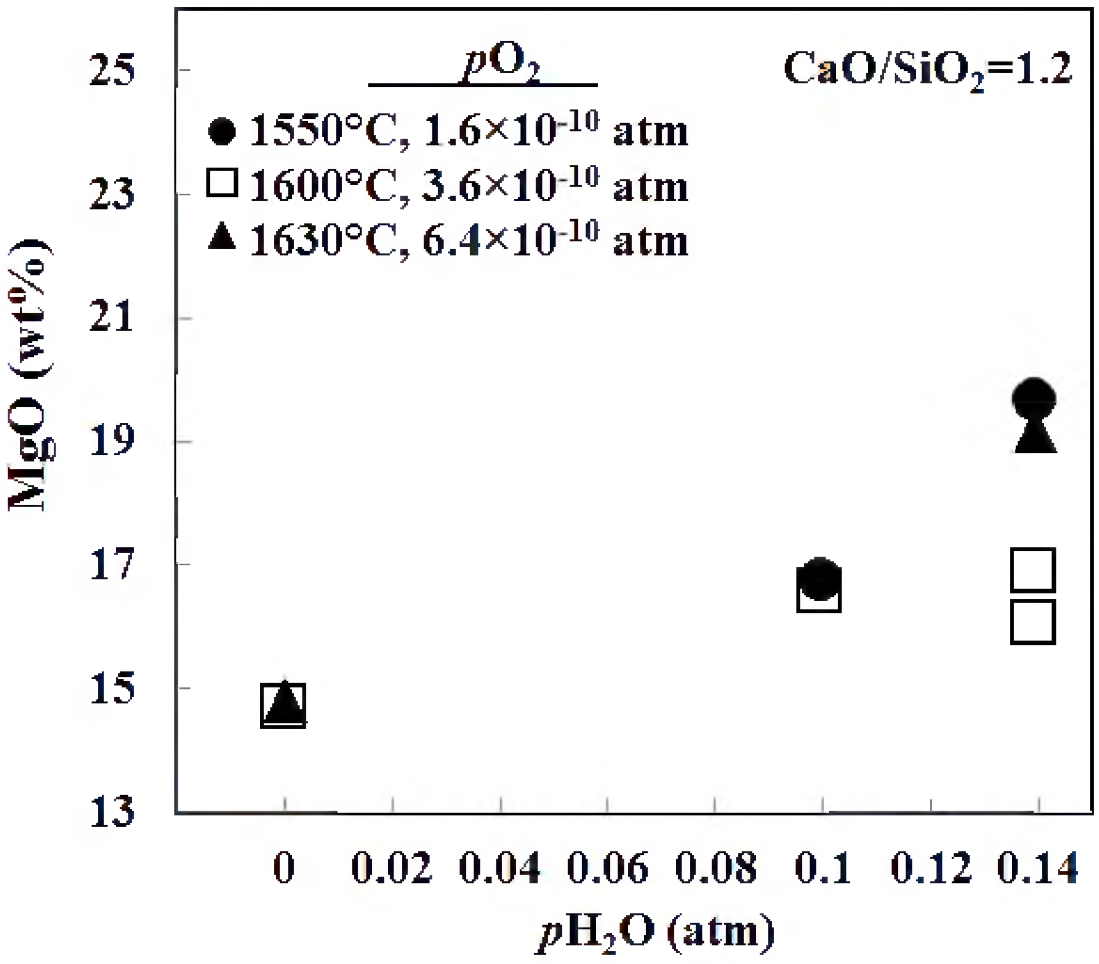

Figure 7-25. The effect of water content in the gas on MgO solubility at wt% CaO/ wt% SiO_2 of 1.2 at different temperatures and pO_2.

wt% CaO/ wt% SiO_2 in the range of 0.8 to 1.2, and under $pO_2 = 2\times10^{-10}$~2×10^{-9} atm, the average MgO wt% was found to be 18 (10.2~26.2), 18 (16.1~20.7), and 20 (16.6~24.6) under CO/CO_2 (blast furnace, BF), H_2/H_2O (H_2 conditions), and $CO/CO_2/H_2/H_2O$ (natural or coal gas, NG/CG), respectively. Figure 7-26 presents a comparison of the effect of gas atmosphere on the average MgO solubility relative to the CO/CO_2 (BF) conditions.

7. 4. 5. Estimation of MgO Solubility in the Slag

Bergman[2] developed a correlation to calculate MgO saturation contents in complex slag based on the magnesia capacity, $C_{Mg^{2+}}$, and the saturation oxygen content in iron, [O wt%], which is as follows:

$$(MgO\ wt\%) = 1.397\ C_{Mg^{2+}}\ (1-4.354[O\ wt\%]) \qquad (7\text{-}8)$$

where

$$C_{Mg^{2+}} = \frac{(Mg^{2+}\ wt\%)}{a_{MgO}} \qquad (7\text{-}9)$$

and a_{MgO} is the activity of MgO present as magnesiowustite. This correlation could not be tested against the results of the current work due to the unavailability of [O wt%] analysis data. On the other hand, Park[4] formulated an empirical correlation based on the data obtained from $CaO\text{-}MgO\text{-}Fe_2O_3\text{-}FeO\text{-}SiO_2\text{-}MnO\text{-}Al_2O_3$ slags at 1600C under ambient

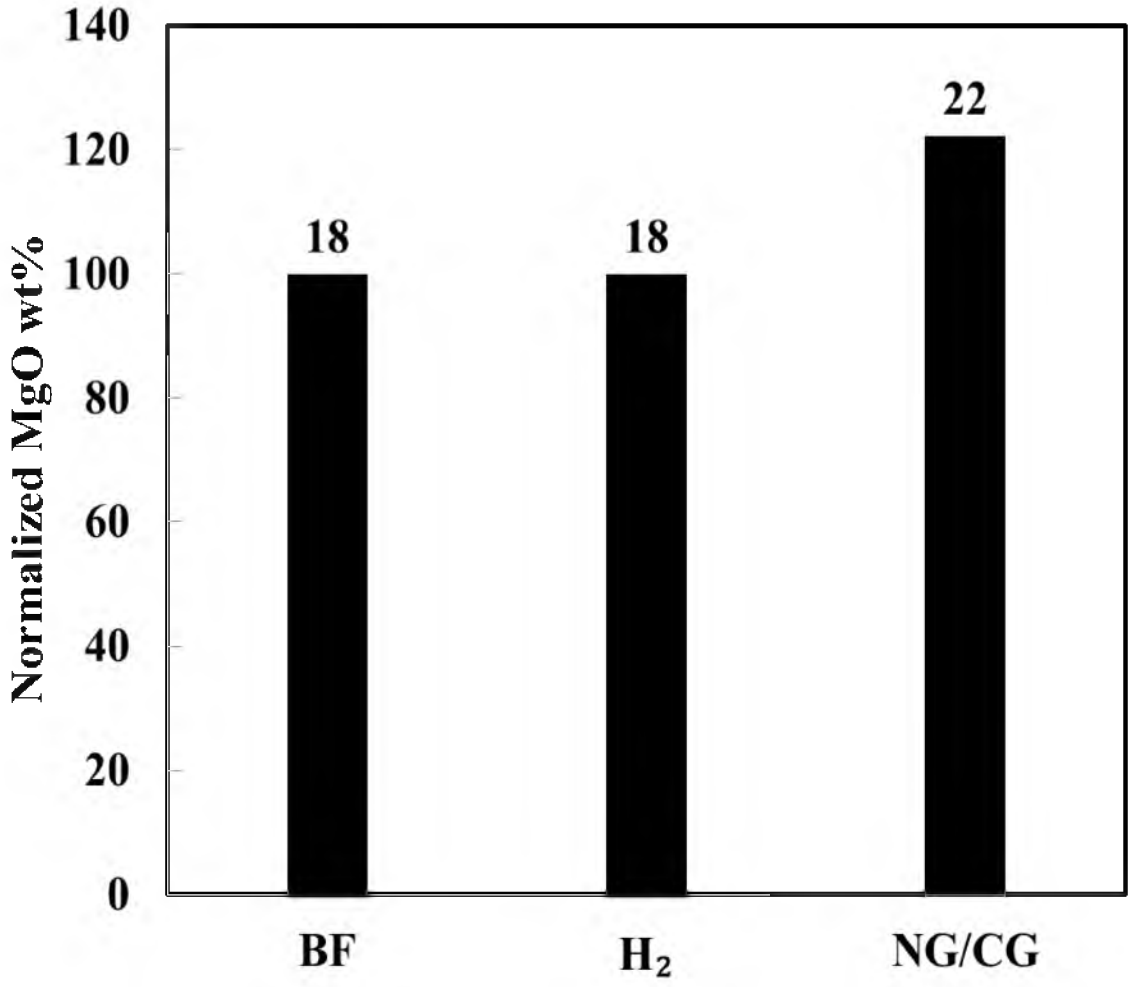

Figure 7-26. The impact of the type of reductant gas on MgO solubility in the slag. The labels show average MgO wt%.

air. This correlation was obtained by the regression with X = (CaO wt%) + 0.45(Fe_2O_3 wt% + FeO wt%) + 0.55(MnO wt%) as follows:

$$(MgO\ wt\%) = 0.00816X^2 - 1.404X + 62.31 \qquad (7\text{-}10)$$

Figure 7-27 shows the calculated MgO solubility by the Park's[4] correlation, eq 7-10, versus the observed values in the current work under H_2/H_2O in the temperature range 1550 to 1650°C. It is seen that Park's correlation overestimated MgO content in the slag, which is attributed to the empirical nature of the correlation and accordingly its reliance on the slag composition, which has significant Fe_2O_3 and MnO contents, and the gas atmosphere, ambient air. Thus, a separate correlation was developed to estimate MgO solubility under the current experimental conditions. The following correlation, eq 7-11, was developed based on the linear regression of the experimental data obtained from the current experiments under H_2/H_2O atmosphere as:

$$(MgO\ wt\%) = 91.4 - 0.43\ (FeO\ wt\%) - 0.54(CaO\ wt\%) - \frac{9.34\times10^4}{T(K)} \quad (r^2=0.86) \qquad (7\text{-}11)$$

The above correlation was found to adequately predict MgO solubility in multicomponent slags with FeO content in the range 1-50, CaO/SiO_2 of 0.4-1.6, and temperature range of 1550-1650°C. Correlation 7-11 has been tested on data of Liu *et al.*[15] and Suito and Inoue[9] that satisfy the aforementioned conditions. The calculated MgO solubility is in good agreement with the experimentally obtained MgO solubility, as

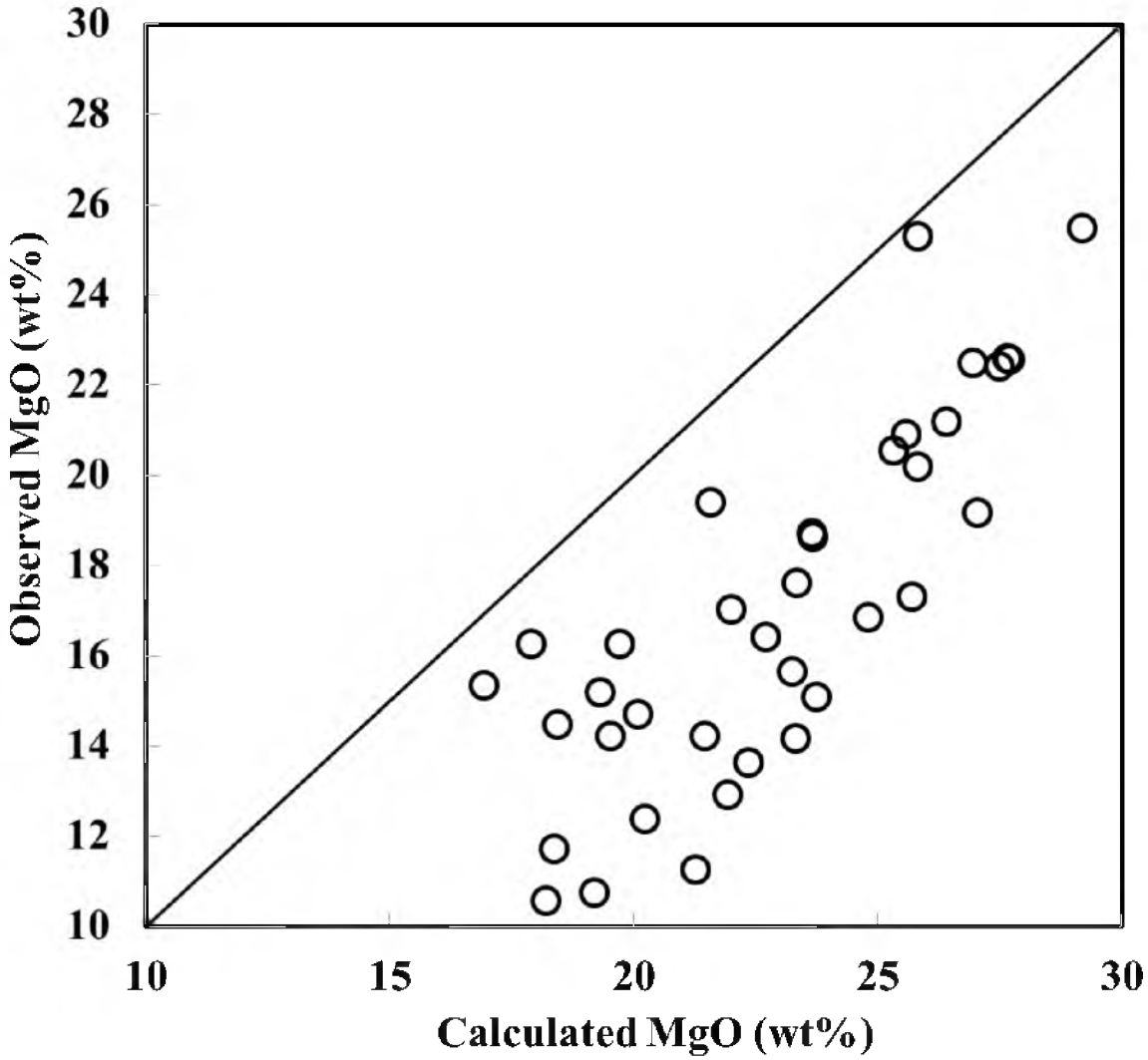

Figure 7-27. Comparison of the calculated and the observed MgO wt% in the present work (under H_2/H_2O).

presented in Figure 7-28, which also shows the current work results. The MgO solubility was correlated to temperature and B′, as follows:

$$(MgO\ wt\%) = 103.4 - 0.41B' - \frac{1.41\times10^{5}}{T(K)} \quad (r^2=0.80) \qquad (7\text{-}12)$$

7. 5. Conclusions

The solubility of MgO in MgO-CaO-FeO-Al_2O_3-SiO_2-P_2O_5-MnO slags was studied, in the temperature range 1550-1650°C, with wt% CaO/ wt% SiO_2 of 0.8 to 1.4, and under pO_2 = 10^{-10}~10^{-9} atm under H_2/H_2O atmosphere to represent the case of using H_2 as a reductant of iron ore concentrate in the flash ironmaking technology. MgO solubility was found to decrease with basicity, which was defined as: B' = (wt% CaO+0.7×wt% Fe_tO+0.59×wt% MnO)-(0.5×wt% SiO_2+0.6×wt% Al_2O_3). The content of FeO in the slag also was found to decrease MgO solubility. MgO was also found to increase with temperature. The following correlation was developed to correlate MgO solubility to the slag composition and temperature:

$$(MgO\ wt\%) = 91.4 - 0.43\ (FeO\ wt\%) - 0.54(CaO\ wt\%) - \frac{9.34\times10^{4}}{T(K)}$$

This correlation was found to fairly well predict MgO solubility in multicomponent slags with FeO content in the range 1-50, CaO/SiO_2 of 0.4-1.6, and temperature range of 1550-1650°C. Also, MgO solubility was correlated to temperature and B′, as follows:

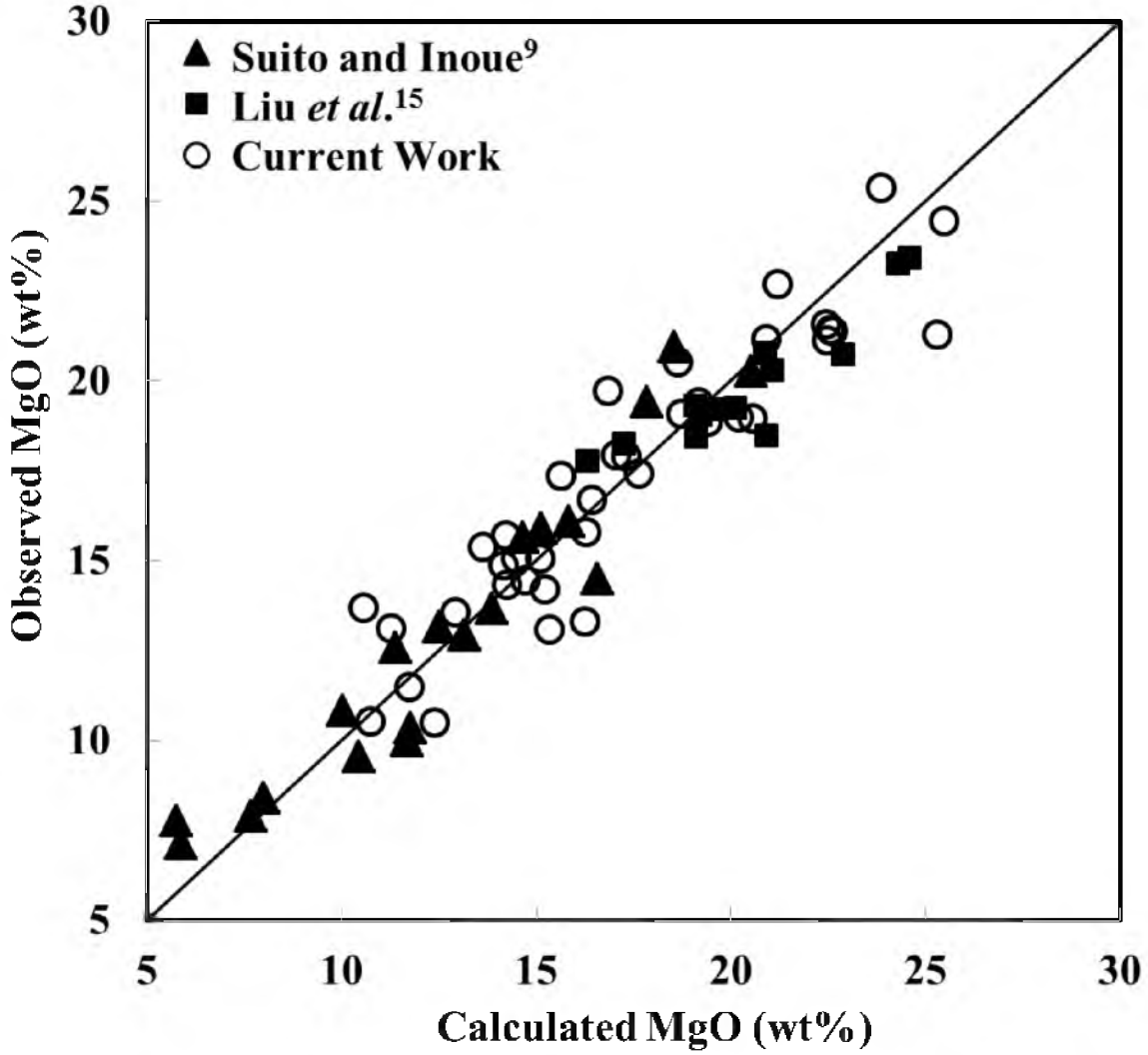

Figure 7-28. Comparison of the calculated and the observed MgO wt% in the present work (under H_2/H_2O) as wells as others' work in the temperature range 1550 to 1650°C using the developed correlation, eq 7-11.

$$(MgO\ wt\%) = 103.4 - 0.41B' - \frac{1.41\times10^{5}}{T(K)}$$

The effect of gas atmosphere was also investigated under H_2/H_2O (H_2 reductant), $CO/CO_2H_2/H_2O$ (natural or coal gas, NG/CG), and CO/CO_2 (blast furnace, BF). The representative results used to compare the effect of gas atmosphere was average values of the experiments carried in the temperature range 1550-1630°C, for slags with CaO/SiO_2 rage 0.8 to 1.2, and under $pO_2 = 2\times10^{-10}$~2×10^{-9} atm. It was found that pH_2O in the gas atmosphere tends to increase MgO solubility in the studied slags; and the average MgO solubility in the slag was 18, 18, and 20 wt% under BF, H_2, and NG/CG, respectively.

7. 6. References

(1) Monaghan, B.; Nightingale, S.; Chen, L.; Brooks, G. The dissolution behaviour of selected oxides in $CaO-SiO_2-Al_2O_3$ slags, VII International Conference on Molten Slags Fluxes and Salts, The South African Institute of Mining and Metallurgy, **2004,** pp. 585-594.

(2) Bergman, A. Some aspects on magnesia solubility in complex slags. *Steel Res.* **1989**, *60*, 191-195.

(3) Trömel, G.; Koch, K.; Fix, W.; Grosskurth, N. Effect of magnesium oxide on the equilibriums in the system $Fe-CaO-FeO_n-SiO_2$ and on the sulfur distribution at 1600°C. *Arch. Eisenhuettenw.* **1969**, *40*, 969-978. (In German).

(4) Park, J. M. MgO solubility in BOF slag equilibrated with ambient air. *Steel Res.* **2001,** *72*, 141-145.

(5) Leonard, R. J.; Herron, R. H. Dolomite additions required to saturate BOF slags with magnesium oxide. *Proc. Natl. Open Hearth Basic Oxygen Steel Conf.* **1977**, *60*, 127-133.

(6) Fetters, K. L.; Chipman, J. Equilibria of liquid iron and slags of the system $CaO-MgO-FeO-SiO_2$. *Tech. Publ. - Am. Inst. Min. Metall. Eng.* **1941**, *145*, 95-112.

(7) Kim, S.-M.; Nicholson, P. S.; Lu, W.-K. Attack of magnesite refractories by alumina-containing slags. *Am. Ceram. Soc. Bull.* **1978**, *57*, 652-655.

(8) Shim, J. D.; Ban-Ya, S. The Solubility of Magnesia and Ferric-Ferrous Equilibrium in Liquid $Fe_tO-SiO_2-CaO-MgO$ Slags. *Tetsu-to-Hagane (J. Iron Steel Inst. Jpn.)* **1981,** *67*, 1735-1744.

(9) Suito, H.; Inoue, R. Manganese equilibrium between molten iron and MgO-saturated $CaO-Fe_tO-SiO_2-MnO$ slags. *Trans. Iron Steel Inst. Jpn.* **1984,** *24*, 257-265.

(10) Suito, H.; Inoue, R.; Takada, M. Phosphorus distribution between liquid iron and MgO saturated slags of the system $CaO-MgO-FeO_x-SiO_2$. *Trans. Iron Steel Inst. Jpn.* **1981,** *21*, 250-259.

(11) Schürmann, E.; Kolm, I. Mathematical description of magnesia saturation in complex steelmaking slags in equilibrium with liquid iron. *Steel Res.* **1986,** *57*, 7-12.

(12) Selin, R. Studies on the MgO solubility in complex steelmaking slags in equilibrium with liquid iron and distribution of phosphorus and vanadium between slag and metal at mgo saturation. Part I. Reference system $CaO-FeO^*-MgO_{sat}-SiO_2$. *Scand. J Metall.* **1991,** *20*, 279-299.

(13) Selin, R., Studies on the magnesia solubility in complex steelmaking slags in equilibrium with liquid iron and distribution of phosphorus and vanadium between slag and metal at mgo saturation. Part II. The total system including $Al2O_3$, SiO_2, and TiO_2. *Scand. J. Metall.* **1991**, *20*, 318-328.

(14) Park, J. M.; Lee, K. K. Reaction equilibria between liquid iron and CaO-Al_2O_3-$MgO_{sat.}$-SiO_2-Fe_tO-MnO-P_2O_5 slag. *Steelmaking Conf. Proc.* **1996,** *79*, 165-171.

(15) Liu, S. H.; Fruehan, R.; Morales, A.; Ozturk, B. Measurement of FeO activity and solubility of MgO in smelting slags. *Metall.Trans. B* **2001**, *32*, 31-36.

(16) Jung, S. M.; Min, D. J.; Rhee, C. H. Solubility of MgO in CaO-SiO_2-MnO slags. *ISIJ Int.* **2007,** *47*, 1823-1825.

(17) Jung, S. M.; Min, D. J.; Rhee, C. H. Solubility of MgO in new ironmaking process-typed slags. *ISIJ Int.* **2007,** *47*, 1718-1722.

(18) Jung, S. M.; Min, D. J. The effect of Fe_tO content on MgO solubilities in lime-based slags. *ISIJ Int.* **2010,** *50*, 1632-1636.

(19) Demidov, K. N.; Klimov, A. V.; Borisova, T. V., Evaluation of MgO solubility in slag during converter-melting blowing. *Stal'* **2010**, 19-21 (In Russian).

(20) Mohassab-Ahmed, M. Y.; Sohn, H. Y. (University of Utah). Method and device for digestion of materials in a microwave oven. U.S. Patent Application No. 61/651, 789, Unpublished (filing date May 25, 2012).

(21) Mohassab-Ahmed, M. Y.; Sohn, H. Y.; Kim, H. G., Sulfur distribution between liquid iron and magnesia-saturated slag in H_2/H_2O atmosphere relevant to a novel ironmaking technology. *Ind. Eng. Chem. Res.* **2012,** *51*, 3639-3645.

(22) Mohassab-Ahmed, M. Y.; Sohn, H. Y.; Kim, H. G., Phosphorus distribution between liquid iron and magnesia-saturated slag in H_2/H_2O atmosphere relevant to a novel ironmaking technology. *Ind. Eng. Chem. Res.* **2012,** *51*, 7028-7034.

(23) Suito, H.; Inoue, R. Thermodynamic considerations on manganese equilibria between molten iron and Fe_tO-MnO-MO_X slags (MO_X = $PO_{2.5}$, SiO_2, $AlO_{1.5}$, MgO, CaO). *Trans. Iron Steel Inst. Jpn.* **1984,** *24*, 301-307.

CHAPTER 8

EFFECT OF GAS PHASE ON THE EQUILIBRIUM DISTRIBUTION OF MANGANESE BETWEEN $CaO-MgO_{sat}-SiO_2-Al_2O_3-FeO-P_2O_5$ SLAG AND MOLTEN IRON

8. 1. Introduction

Manganese content in the steel influences various critical properties. It is known that a low manganese content is essential for enhancing the deep drawability, especially in ultralow carbon steels. On the other hand, manganese improves steel hardenability. Therefore, controlling and adjusting the manganese content in the hot metal and steel is always a prerequisite in iron and steelmaking processes. As part of the effort to develop a new eco-friendly and energy-saving flash ironmaking process at the University of Utah, the effect of the type of gas atmosphere on manganese distribution between slag and metal has been studied. This study is the first effort to study the effect of H_2O in H_2O-containg atmospheres on the distribution of manganese between molten iron and slag, whereas the previous work was all devoted to BF and steelmaking conditions where CO/CO_2 or inert atmospheres was used. In the technology under development, H_2, natural gas, or coal gas is the fuel and reducing agent in the process of producing iron from iron

ore concentrates. One potential route in the proposed technology is to collect the metal as a molten bath where the gas, slag, and molten iron should be equilibrated with each other. The current research was conducted to answer the question: "Does the type of gas mixture used to control the oxygen partial pressure (pO_2) affect the equilibrium distribution of Mn between slag and molten iron with the temperature and slag, starting slag composition, and pO_2 held constant?" For this objective, the distribution of Mn has been investigated between molten iron and MgO-saturated CaO-FeO-Al_2O_3-SiO_2-MnO (0.2-0.8 wt%)-P_2O_5 (0.1-0.9 wt%) slags in the temperature rage 1550 to 1650°C under CO/CO_2, H_2/H_2O, and $CO/CO_2/H_2/H_2O$ atmospheres using the experimental and analysis methods described elsewhere.[1, 2, 3]

8. 2. Thermodynamic Considerations

The following equilibrium is a common reaction used to describe the Mn transfer from molten iron to slag:[4]

$$FeO_{(l)} + \underline{Mn} = MnO_{(l)} + Fe \qquad \Delta G° = -123300 + 56.1T\ (J/mol) \quad (8\text{-}1)$$

The equilibrium constant of reaction 8-1, K_{Mn}, can be expressed as:

$$K_{Mn} = e^{\frac{-\Delta G°}{RT}} = \frac{a_{MnO}}{a_{FeO}.a_{\underline{Mn}}} = \frac{\gamma_{MnO}.X_{MnO}}{\gamma_{FeO}.X_{FeO}.f_{Mn}.[wt\%Mn]} \qquad (8\text{-}2)$$

where γ, X, f_{Mn}, and [wt%Mn] are Raultian activity coefficients of oxides in the slag, mole fraction, manganese Henrian activity coefficient (1 wt%-standard state), and wt% of dissolved Mn in iron, respectively. In this work, [wt%Mn] is in the range 0.04 – 0.15; therefore, f_{Mn} is assumed to be unity. In addition, γ_{FeO} can be calculated from the measured X_{FeO} employing the following equilibrium relationship:[5]

$$Fe_{(l)} + \frac{1}{2}O_{2(g)} = FeO_{(l)} \qquad \Delta G^{\circ}_{FeO} = -225{,}460 + 41.26T \quad (J/mol) \qquad (8\text{-}3)$$

where

$$K_{Fe} = e^{\frac{-\Delta G^{\circ}_{FeO}}{RT}} = \frac{a_{FeO}}{a_{Fe} \cdot pO_2^{1/2}} = \frac{x_{FeO} . \gamma_{FeO}}{a_{Fe} \cdot pO_2^{1/2}} \qquad (8\text{-}4)$$

Therefore, by analyzing for [wt%Mn] and X_{FeO}, the activity coefficient of MnO (γ_{MnO}) was calculated.

The manganese distribution ratio, L_{Mn}, is expressed as:

$$L_{Mn} = \frac{(wt\%\ Mn)}{[wt\%\ Mn]} = \frac{0.77\ (wt\%\ MnO)}{[wt\%\ Mn]} = \frac{X_{MnO}}{[wt\%\ Mn]} \frac{77\ MW_{MnO}}{\sum_{i=1}^{n} MW_{A_i} . X_i} \qquad (8\text{-}5)$$

with (wt% A), [wt% A], MW_A, and n referring to the wt% of A in slag, the wt% of A in metal, molecular weight of A, and number of oxides in the slag, respectively. From eqs 8-2 and 8-4, L_{Mn} can be expressed as:

$$L_{Mn} = \frac{a_{FeO} \cdot f_{Mn}}{\gamma_{MnO}} \left(\frac{77\, K_{Mn} \cdot MW_{MnO}}{\sum_{i=1}^{n} MW_{A_i} \cdot X_i} \right) \qquad (8\text{-}6)$$

8. 3. Results

The chemical analysis and the experimental conditions are presented in Table 8-1. The equilibrium gas compositions are previously listed in Chapter 2. The effect of temperature, slag composition, and gas type on the distribution of manganese will be discussed.

8. 3. 1. The Effect of Temperature on L_{Mn}

It was found that L_{Mn} decreases with temperature, as Figure 8-1 shows, regardless of the type of gas atmosphere in contact with the slag in pO_2 range 1.6×10^{-10} to 1.9×10^{-9} atm. The scatter in the results is attributed to the variation in FeO content. A similar behavior has been reported by Suito and Inoue,[5, 8] Zhu *et al.*,[9] and Meraikib.[6] They also reported the negative dependence on temperature of the equilibrium ratio [wt% MnO/(wt% FeO.wt% Mn)], which is directly proportional to L_{Mn} at constant FeO content.

8. 3. 2. The Effect of Basicity on L_{Mn}

Due to the basic nature of MnO, γ_{MnO} will increase with basicity at the same temperature and slag composition. This relationship has been proved by the work of Suito and Inoue,[8] in the study of MgO-saturated CaO-Fe_tO-SiO_2-P_2O_5 ($\leq$ 3wt%)-MnO (2-5 wt%) in the temperature range 1550 to 1650°C. In their study, they observed that the

Table 8-1. The chemical analysis of slags and the experimental conditions of the present work

Sample	Gas	T (°C)	pO_2	CaO/ SiO_2	FeO (wt%)	MgO (wt%)	CaO (wt%)	Al_2O_3 (wt%)	SiO_2 (wt%)	γ_{FeO}	L_{Mn}
R10	$CO/CO_2/H_2/H_2O$	1550	1.9×10^{-9}	0.8	21.7	24.6	20.3	13.0	25.5	4.5	3.4
R19		1550	1.6×10^{-10}	0.8	10.1	24.4	26.2	16.3	34.8	3.0	4.8
R20		1550	1.6×10^{-10}	1	9.8	17.9	30.7	8.4	31.8	2.8	3.8
R21		1550	1.6×10^{-10}	1.2	10.8	16.8	33.5	18.8	29.8	2.7	8.1
R22		1600	3.6×10^{-10}	0.8	13.0	23.4	26.0	15.7	32.3	2.2	3.0
R23		1600	3.6×10^{-10}	1	12.7	19.2	30.0	17.0	30.9	2.2	2.8
R24		1600	3.6×10^{-10}	1.2	12.4	16.6	32.8	17.2	28.6	2.2	3.6
R27		1630	6.4×10^{-10}	1.2	11.2	19.2	30.1	17.0	30.5	2.5	1.9
R46	CO/CO_2	1550	1.6×10^{-10}	0.8	35.5	10.2	24.5	13.9	22.8	0.7	4.7
R48		1550	1.6×10^{-10}	1.2	16.9	26.2	26.3	15.0	23.6	1.6	4.4
R49		1600	3.6×10^{-10}	0.8	14.7	22.1	25.7	15.2	31.9	1.9	3.2
R50		1600	3.6×10^{-10}	1	16.9	16.9	28.5	15.2	29.4	1.6	7.7
R51		1600	3.6×10^{-10}	1.2	15.3	14.7	30.7	16.6	26.7	1.7	11.6
R52		1630	6.4×10^{-10}	0.8	13.7	15.7	24.7	23.4	32.9	2.0	11.6
R53		1630	6.4×10^{-10}	1	14.6	14.3	28.0	17.0	36.4	1.9	3.9
R54		1630	6.4×10^{-10}	1.2	26.4	14.8	25.2	14.3	27.4	1.0	4.4
R74	H_2/H_2O	1550	1.6×10^{-10}	1	9.9	20.7	34.9	5.1	27.8	2.6	6.1
R75		1550	1.6×10^{-10}	1.2	9.6	19.7	31.2	17.1	32.1	2.8	3.7
R78		1600	3.6×10^{-10}	1.2	10.5	16.1	33.7	17.7	29.5	2.5	5.0
R'78		1600	3.6×10^{-10}	1.2	9.5	16.9	33.8	18.1	29.6	2.8	3.6

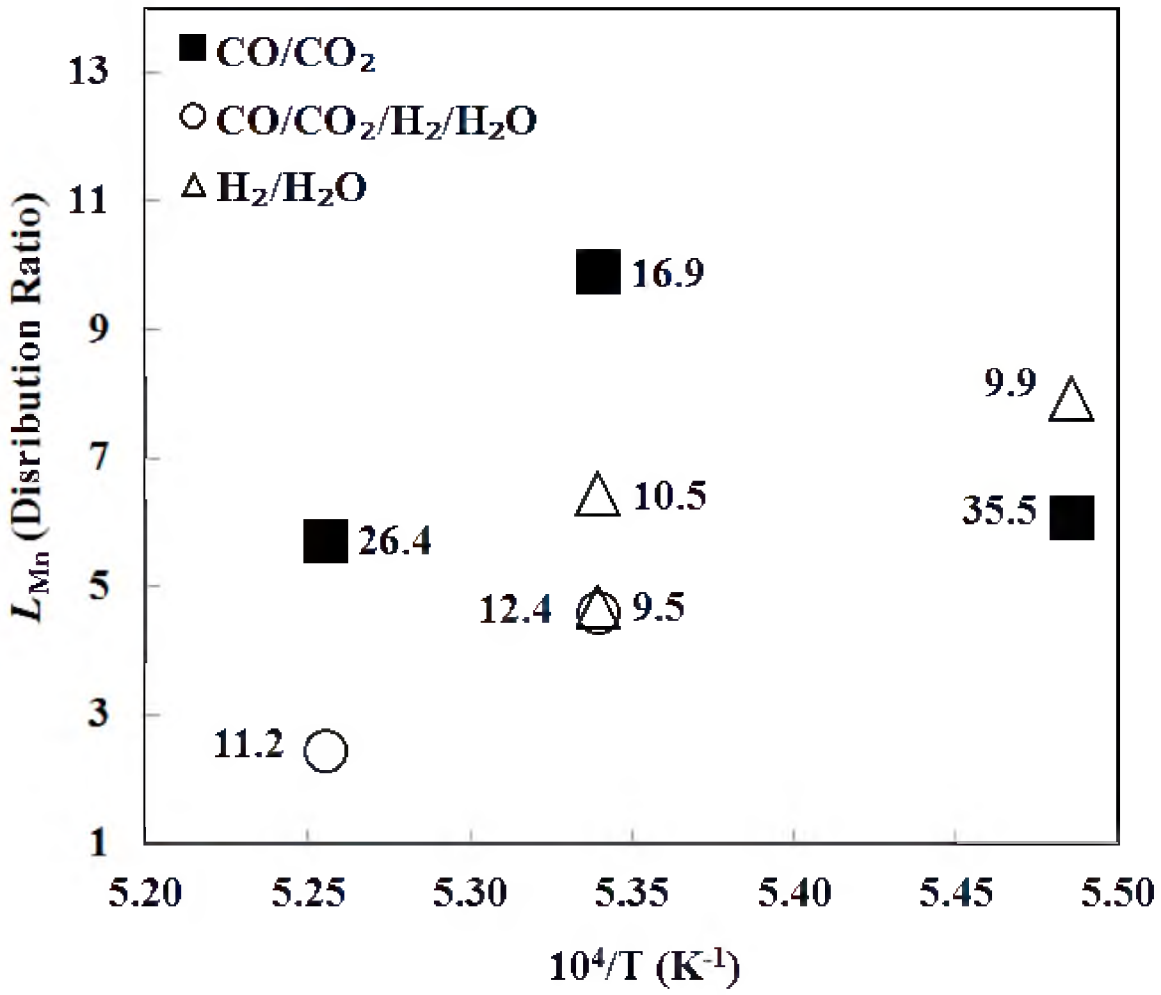

Figure 8-1. The impact of temperature on L_{Mn} at equilibrium under pO_2 range 1.6×10^{-10} to 1.9×10^{-9} atm and pH_2O range of 0.0 to 0.4 atm (the corresponding pH_2O values of each point are listed in Tables 2-4 and 2-7). The labels are FeO wt%.

logarithm of the ratio [wt% MnO/(wt% FeO.wt% Mn)] decreases with basicity (expressed as (wt% CaO+0.3wt% MgO)/(wt% SiO_2+wt% P_2O_5)) at a given temperature. Their basicity rage was 0.01 through 9.0. Park and Lee[10] studied manganese distribution in a MgO saturated CaO-SiO_2-Al_2O_3-Fe_tO-P_2O_5-MnO in the temperature range ~1560 to ~1660°C. They observed that the ratio $\gamma_{MnO}/\gamma_{Fe_tO}$ and the equilibrium quotient (wt% FeO)[wt% Mn]/(wt% MnO) showed positive correlation with basicity ((wt% CaO+wt% MgO)/(wt% SiO_2+0.3wt% Al_2O_3)) in the rage of ~2.3 to ~4.2 in slags with relatively constant FeO contents. Turkdogan[11] also presented data of daily average blast furnace runs and found that the ratio [wt% Mn]/(wt% MnO) increased with basicity (wt% CaO+wt% MgO)/(wt% SiO_2) in the range ~1.2 to ~1.6. Meraikib[6] investigated the data of an electric arc furnace to study the thermodynamics of Mn distribution. He found that γ_{MnO} increases with basicity (wt% CaO)/(wt% SiO_2) in the range ~1.5 to 3.0 at 1550 to 1650°C. Recently, Zhu *et al.*[9] studied the equilibrium distribution of Mn between CaO-SiO_2-Al_2O_3-Fe_tO-P_2O_5-MnO slags with liquid silver in an iron crucible in the temperature range 1300 to 1400°C. They reported that L_{Mn} decreases with the ratio (wt% CaO)/(wt% SiO_2), from 0.3 to 2.3, at constant temperature and FeO content under Ar atmosphere.

In the current study, a narrower basicity range, (wt% CaO)/(wt% SiO_2) = 0.8 – 1.2, was employed to represent the ironmaking conditions. Figure 8-2 shows the effect of slag basicity on L_{Mn} at different temperatures and pO_2. It can be seen that the influence of basicity is not as pronounced as in the work of Suito and Inoue,[8] Park and Lee,[10] Meraikib,[6] and Zhu *et al.*,[9] which is likely to be due to the narrow range in the current study. It is noted that the L_{Mn} changes only slightly when basicity changes from 0.8 to

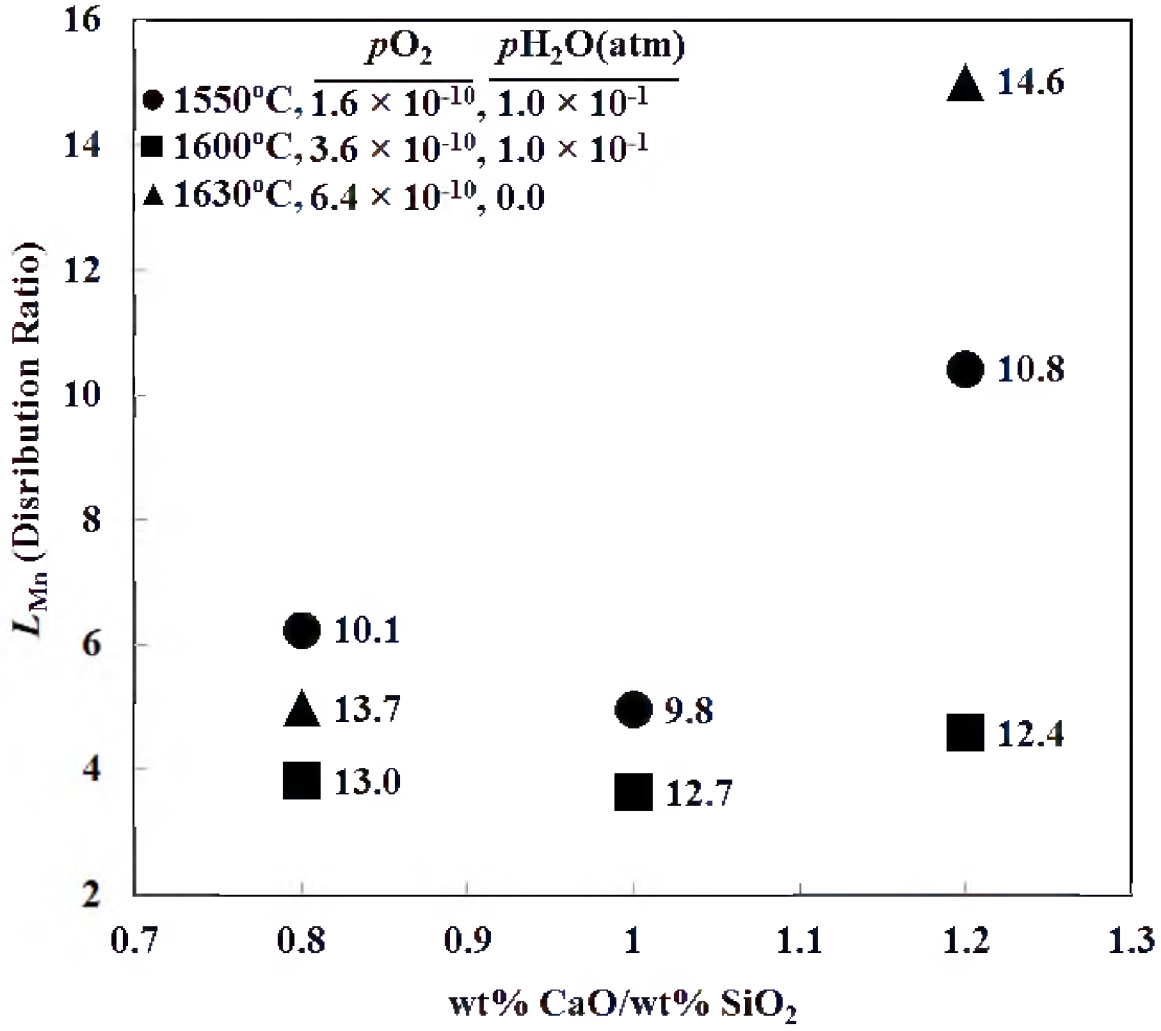

Figure 8-2. The influence of CaO/SiO_2 on the distribution ration of manganese, L_{Mn}, at different temperatures and pO_2. The gas atmosphere was $CO/CO_2/H_2/H_2O$ and CO/CO_2 for samples at 1550-1600°C and 1630°C, respectively. The labels indicate FeO wt%.

1.0 regardless of the temperature and the gas atmosphere, whereas it increase sharply above 1600°C when basicity changes from 1.0 to 1.2. This scatter is attributed to the difference in FeO contents, as shown in Figure 8-2. To further interpret that response of L_{Mn} to basicity, one should investigate the impact of basicity on γ_{FeO} as well as on γ_{MnO}. Figure 6-6 (in Chapter 6) shows that γ_{FeO} depends weakly on basicity in the studied slags regardless of the gas type and temperature. Figure 8-3 was prepared to present the γ_{MnO}as a function of CaO/SiO_2. It is noted that at 1550 and 1600°C (FeO = 12.4-13.0 wt%), γ_{MnO}stayed approximately the same as basicity changed from 0.8 to 1.0, whereas it decreased significantly when basicity increased from 1.0 to 1.2, whereas in samples at 1600°C (FeO = 14.7-16.9 wt%), γ_{MnO} decreased with the increase of basicity. On the other hand, at 1630°C, γ_{MnO} increased with the increase of basicity from 0.8 to 1.0. The reason of this increase at 1630°C is not clear at this point. Ohta and Suito[12] determined γ_{MnO} in CaO-SiO_2-Al_2O_3-MnO(< 10 wt%)-Fe_tO(< 3 wt%) slags equilibrated with molten iron at 1600°C in an $A1_2O_3$ or CaO crucible. They concluded that γ_{MnO} increased with CaO. That discrepancy with the previously reported observations could be attributed to the lower FeO content in the work of Ohta and Suito.[12]

8. 3. 3. The Effect of FeO on L_{Mn}

The influence of FeO content in the slag on L_{Mn} at the three studied temperatures is shown in Figure 8-4. It can been seen that L_{Mn} increases with FeO wt% in the slag at any given temperature regardless of the gas atmosphere. Suito and Inoue[8] reported a similar trend. Park and Lee[10] found that increasing Fe_tO content in their slag, CaO-MgO_{sat}-SiO_2-Al_2O_3-Fe_tO-P_2O_5-MnO, decreases γ_{MnO}. Jung[13] also reported that

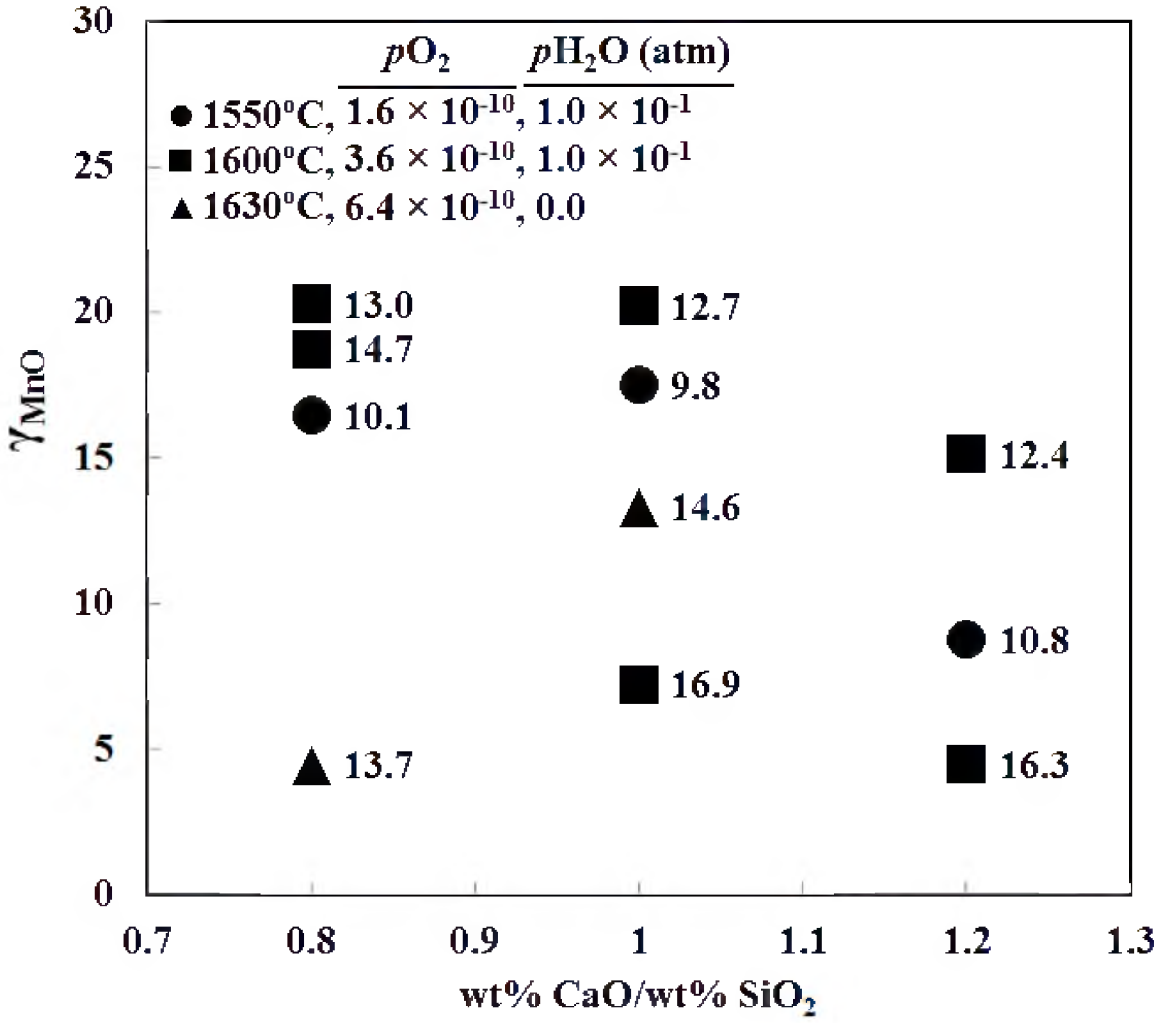

Figure 8-3. The effect of CaO/SiO_2 on γ_{MnO} at constant temperatures at various temperatures and pO_2. The gas atmosphere was $CO/CO_2/H_2/H_2O$ and CO/CO_2 for samples at 1550-1600°C and 1630°C, respectively. The labels indicate FeO wt%.

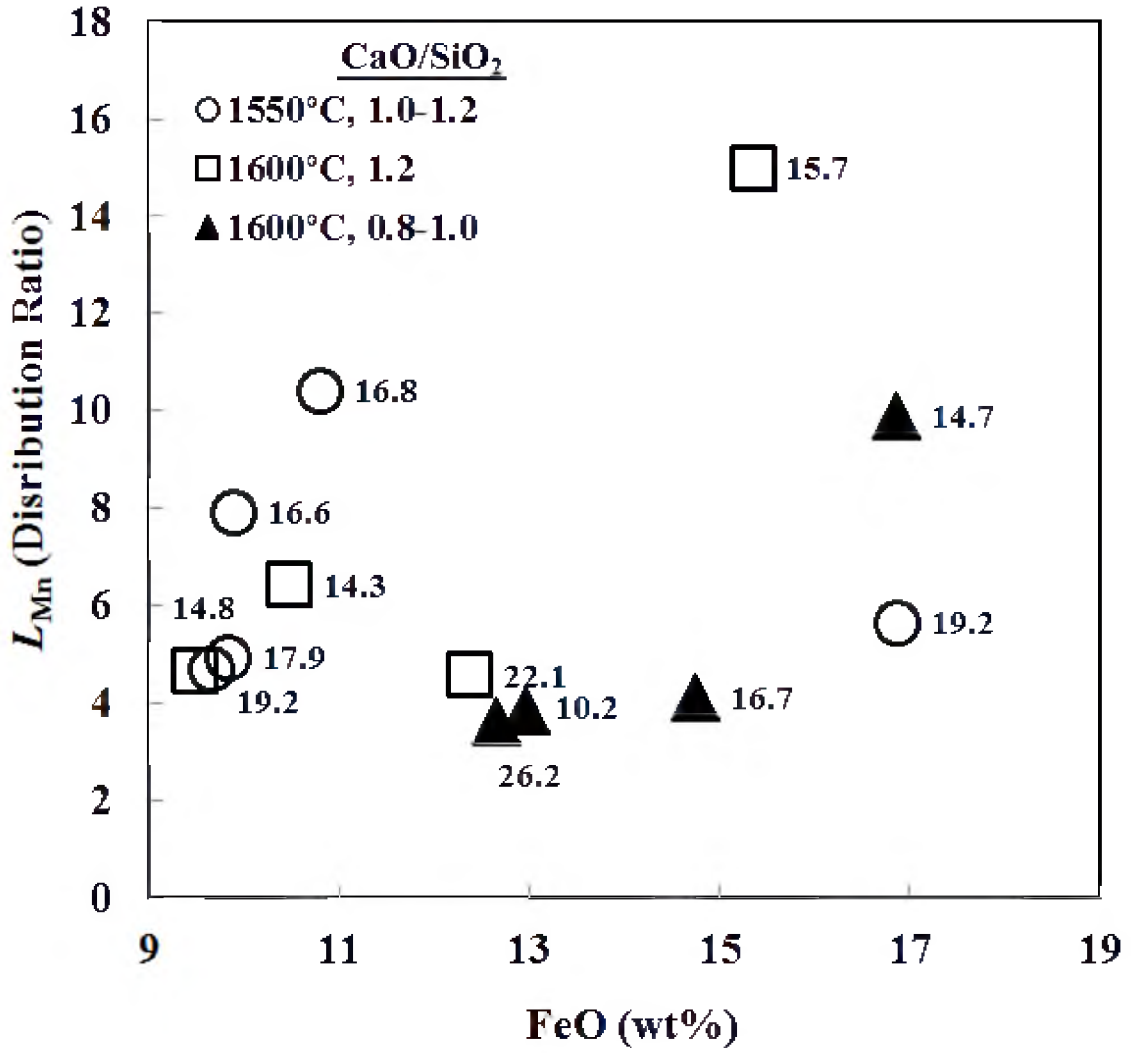

Figure 8-4. The effect of FeO content on L_{Mn} at given temperatures and CaO/SiO_2. The samples at 1550 and 1600°C were conducted under $CO/CO_2/H_2/H_2O$ and CO/CO_2 gas atmospheres, respectively. The labels represent MgO wt% in the slag, which causes the scatter in the data.

γ_{MnO} decreases with an increase in Fe_tO wt% in a CaO-SiO_2-Fe_tO-MgO slag. All above-mentioned observations are consistent with the trend shown in Figure 8-4. It is worth pointing out that L_{Mn} increases with the decrease of γ_{MnO} according to eq 8-6.

At a constant temperature for a given slag composition, γ_{MnO} increases almost linearly with γ_{FeO}, as Figures 8-5 – 8-7 show. Park and Lee[10] obtained the correlation: $\frac{\gamma_{MnO}}{\gamma_{Fe_tO}} = 0.188\,B'' + 0.048$ at 1600°C where B'' = (wt% CaO + wt% MgO)/(wt% SiO_2 + 0.3wt% Al_2O_3). Moreover, Jung[13] found that γ_{MnO} increases with increasing γ_{FeO}. The current results are consistent with both findings.

8. 3. 4. The Effect of the Type of Gas Atmosphere on L_{Mn}

The rank of slags at a given temperature and composition with respect to γ_{FeO} was found to be: CO/CO_2 < $CO/CO_2/H_2/H_2O$ < H_2/H_2O, as discussed in Chapter 6. Also the interaction coefficient of H_2O on γ_{FeO}, $\varepsilon_{FeO}^{H_2O}$, was proved to be positive. Since γ_{FeO} has a linear correlation with γ_{MnO}, the order of slags with respect to γ_{MnO}should be the same as that for γ_{FeO}. That should translate into this order with respect to L_{Mn}: CO/CO_2 > $CO/CO_2/H_2/H_2O$ > H_2/H_2O, which is proven true in Figures 8-8 – 8-10 with the exception of the slags at log pO_2 of -9.8 and 1550°C, the reason for which is not clear at this point. Figures 8-11 and 8-12 supports the previous findings where L_{Mn} was found to decrease with an increase in pH_2O.

For the slag compositions investigated, MgO-saturated CaO-FeO-Al_2O_3-SiO_2-MnO (0.2-0.8 wt%)-P_2O_5 (0.1-0.9 wt%), in the temperature range 1550-1600°C, with CaO/SiO_2 rage 0.8 to 1.2, and under $pO_2 = 2\times10^{-10}$~2×10^{-9} atm, the average L_{Mn} was

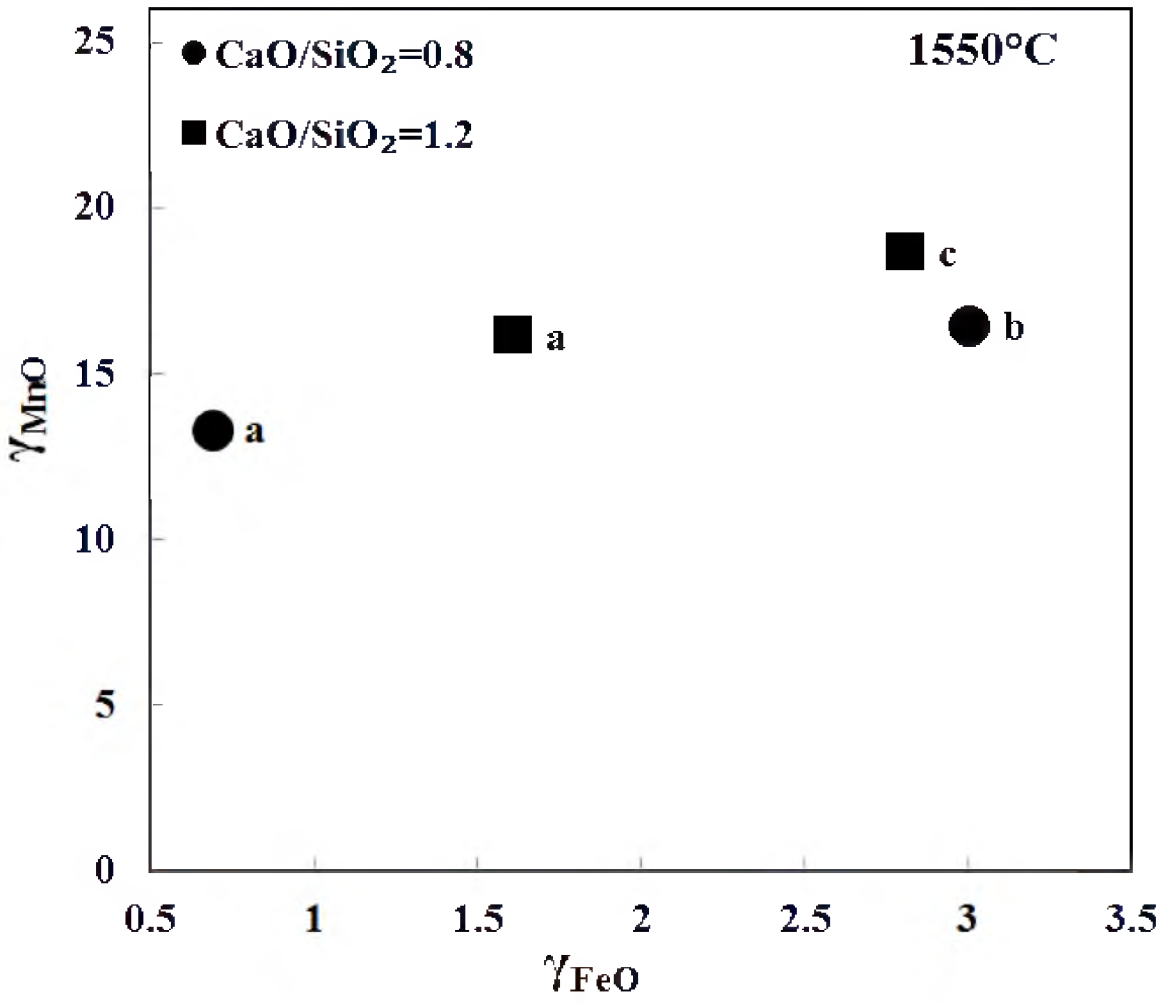

Figure 8-5. The dependence of γ_{MnO} on γ_{FeO} at 1550°C for given CaO/SiO_2. The labels a, b, and c represent CO/CO_2, $H_2/H_2O/CO/CO_2$, and H_2/H_2O atmospheres, respectively.

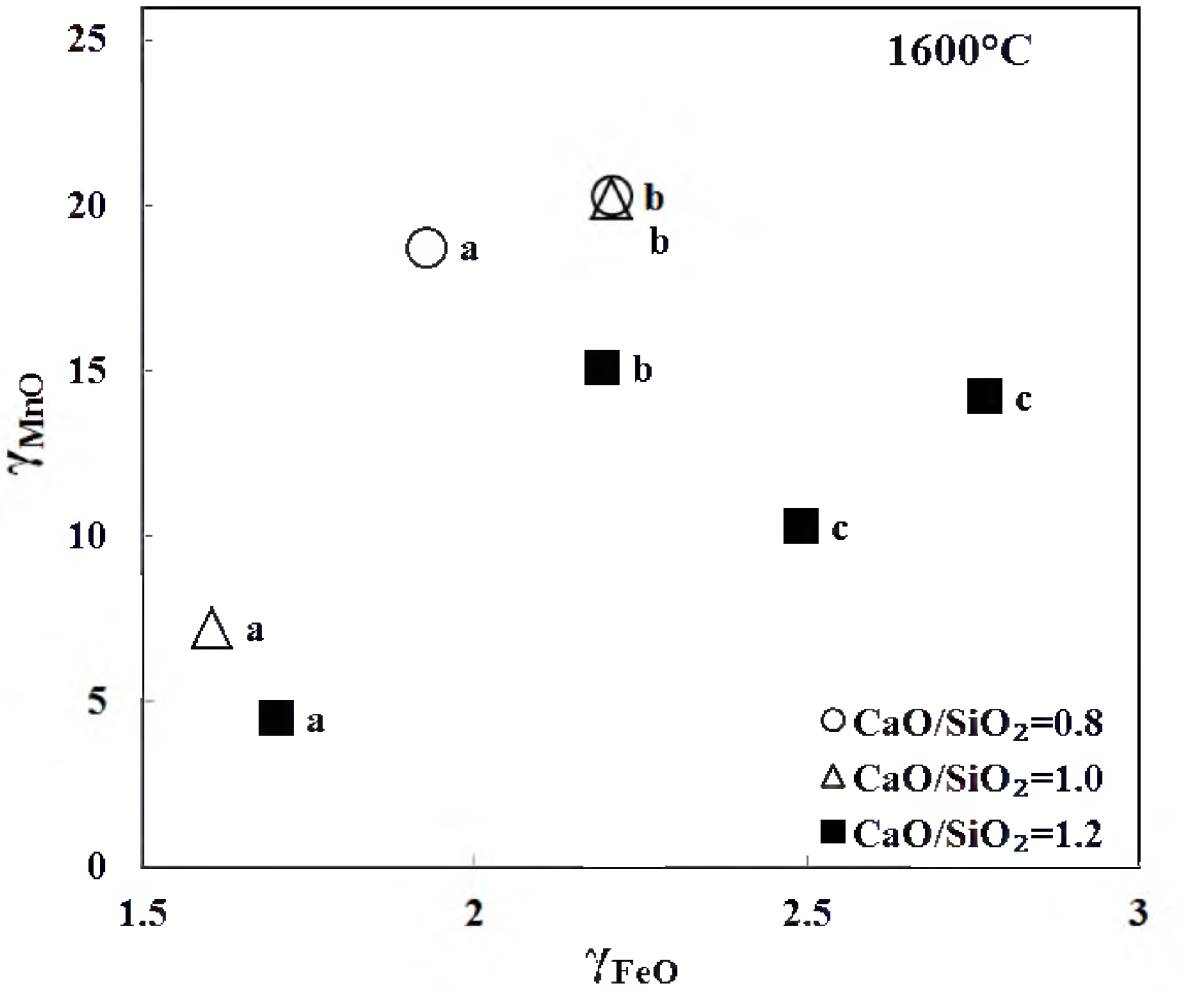

Figure 8-6. The dependence of γ_{MnO} on γ_{FeO} at 1600°C for given CaO/SiO_2. The labels a, b, and c represent CO/CO_2, $H_2/H_2O/CO/CO_2$, and H_2/H_2O atmospheres, respectively.

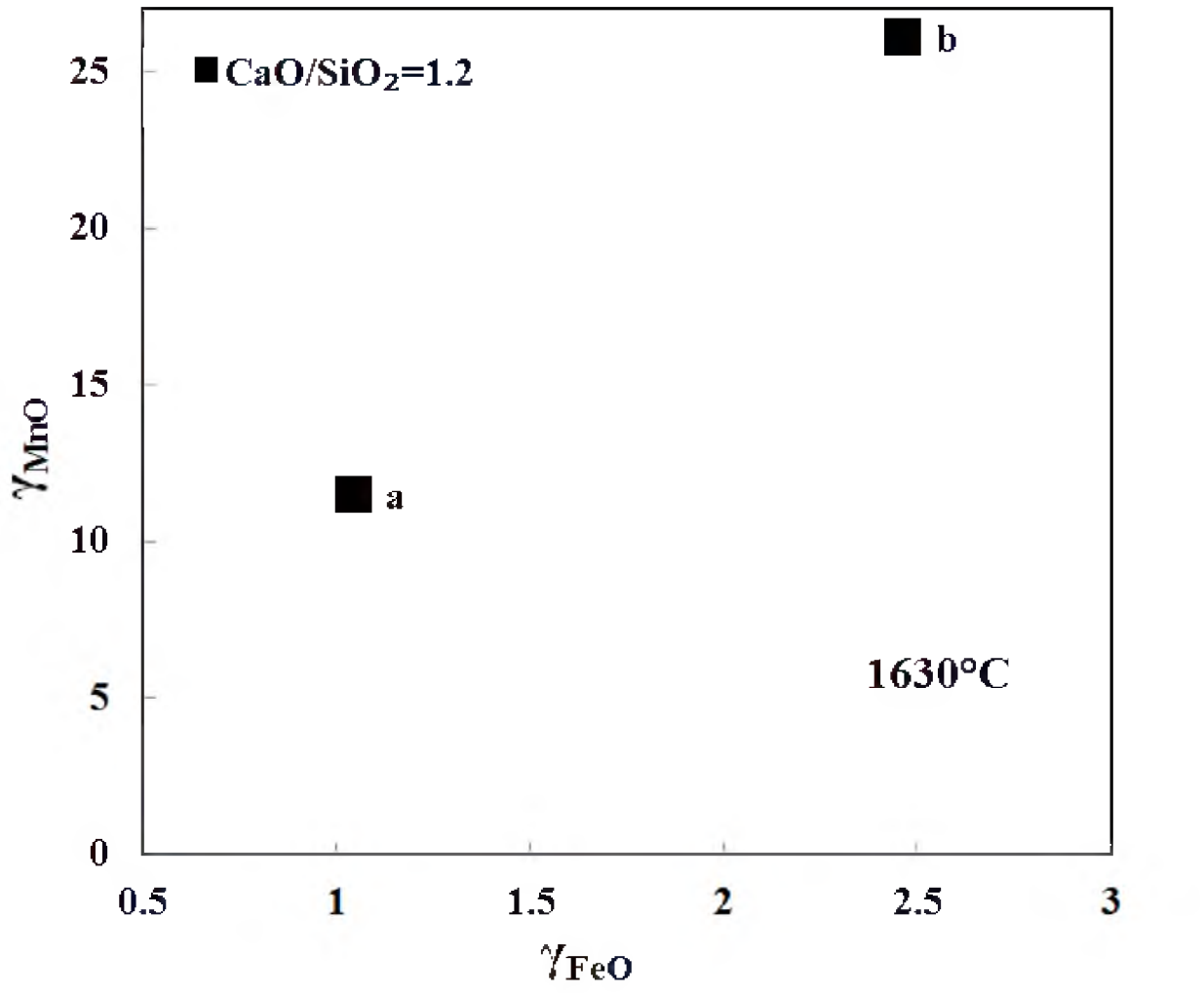

Figure 8-7. The dependence of γ_{MnO} on γ_{FeO} at 1630°C and CaO/SiO_2=1.2. The labels a, and b represent CO/CO_2 and $H_2/H_2O/CO/CO_2$, respectively.

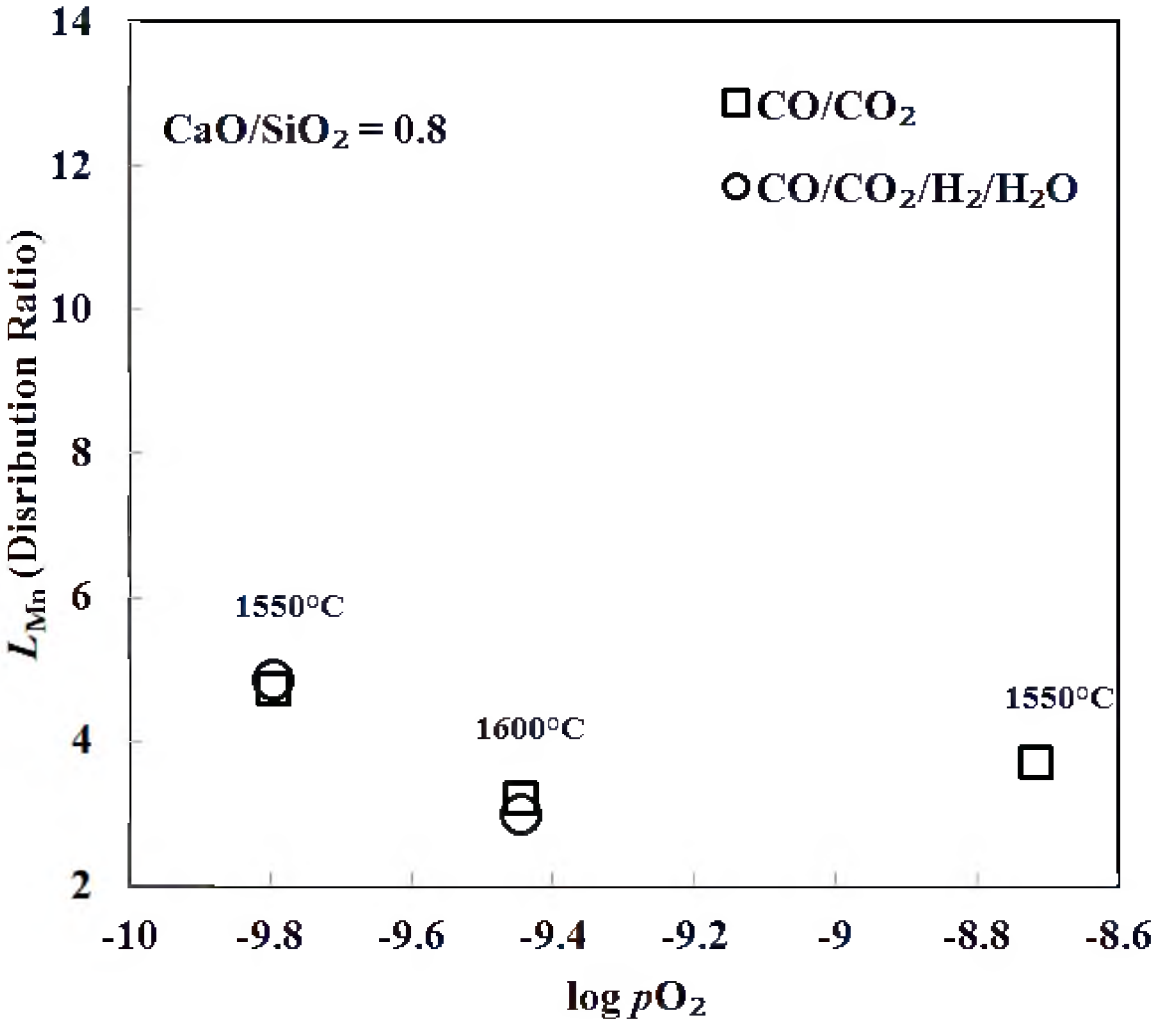

Figure 8-8. The effect of gas composition on L_{Mn} at at different pO_2 and temperature values for slags with wt% CaO/wt% SiO_2 of 0.8 and pH_2O of 0 and 0.1 atm in CO/CO_2 and $H_2/H_2O/CO/CO_2$, respectively.

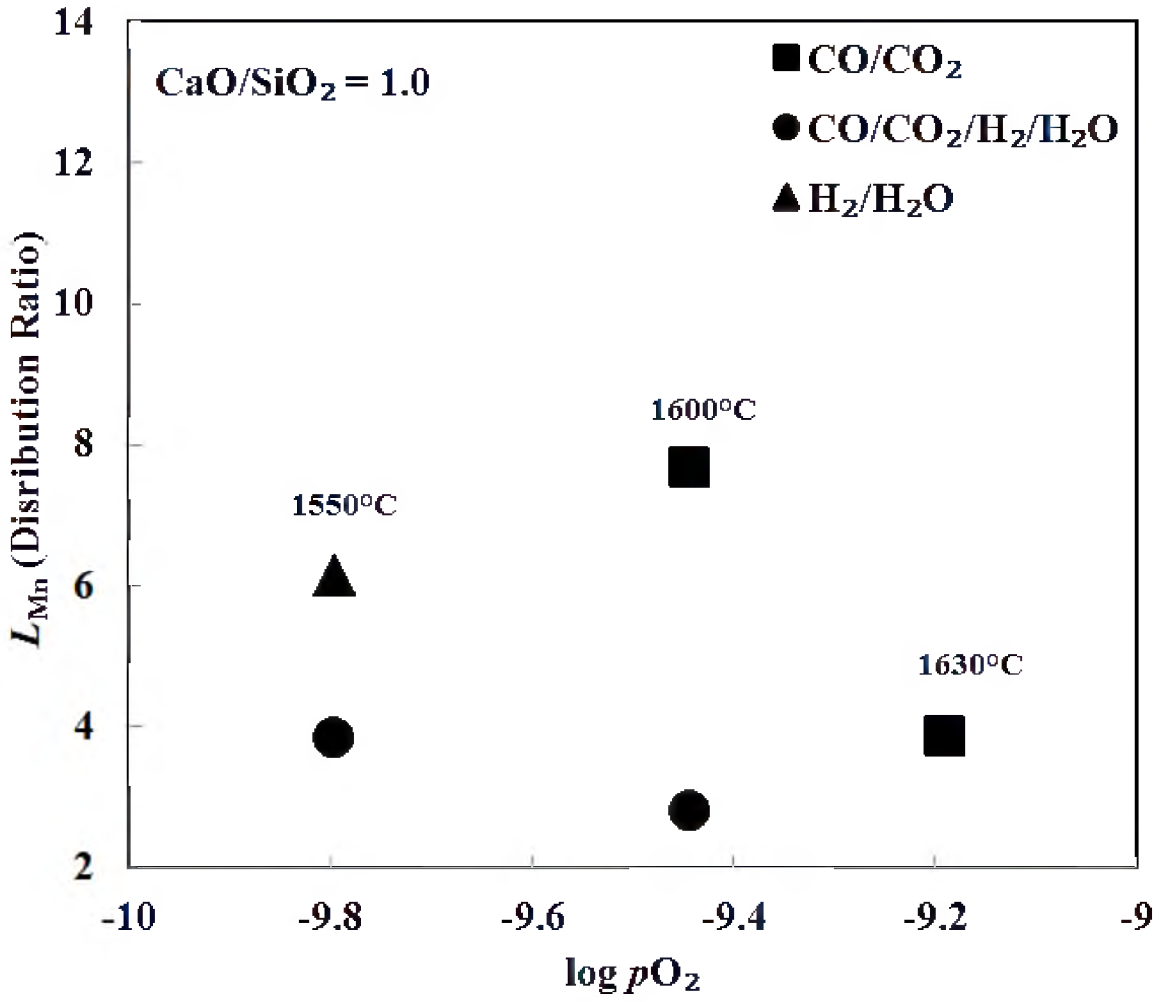

Figure 8-9. The effect of gas composition on L_{Mn} at different pO$_2$ and temperature values for slags with wt% CaO/wt% SiO$_2$ of 1.0 and pH$_2$O of 0, 0.1, and 1.0 atm in CO/CO$_2$, H$_2$/H$_2$O/CO/CO$_2$, and H$_2$/H$_2$O/CO, respectively.

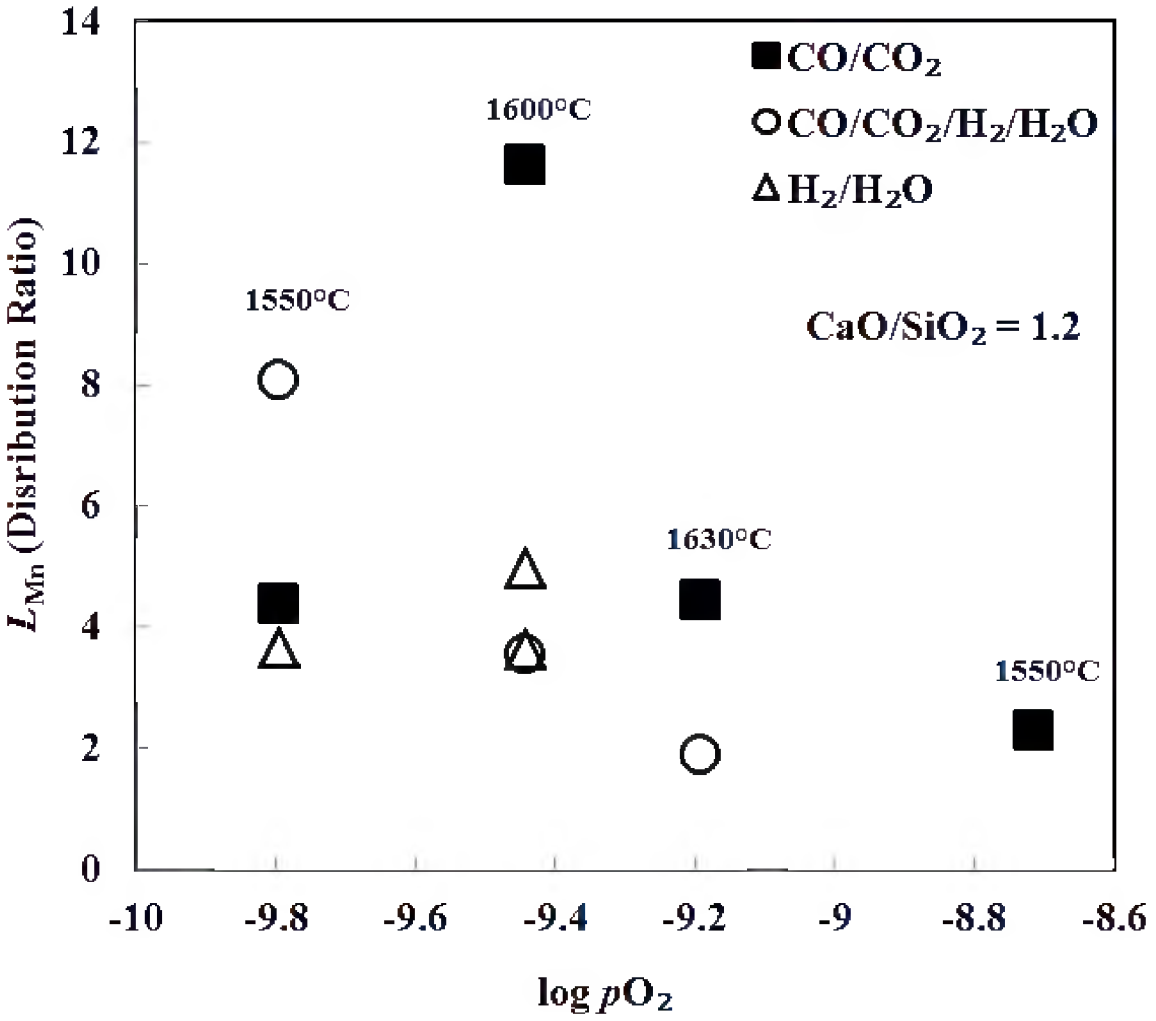

Figure 8-10. The effect of gas composition on L_{Mn} at different pO_2 and temperature values for slags with wt% CaO/wt% SiO_2 of 1.2 and pH_2O of 0, 0.1, and 1.0 atm in CO/CO_2, $H_2/H_2O/CO/CO_2$, and $H_2/H_2O/CO$, respectively.

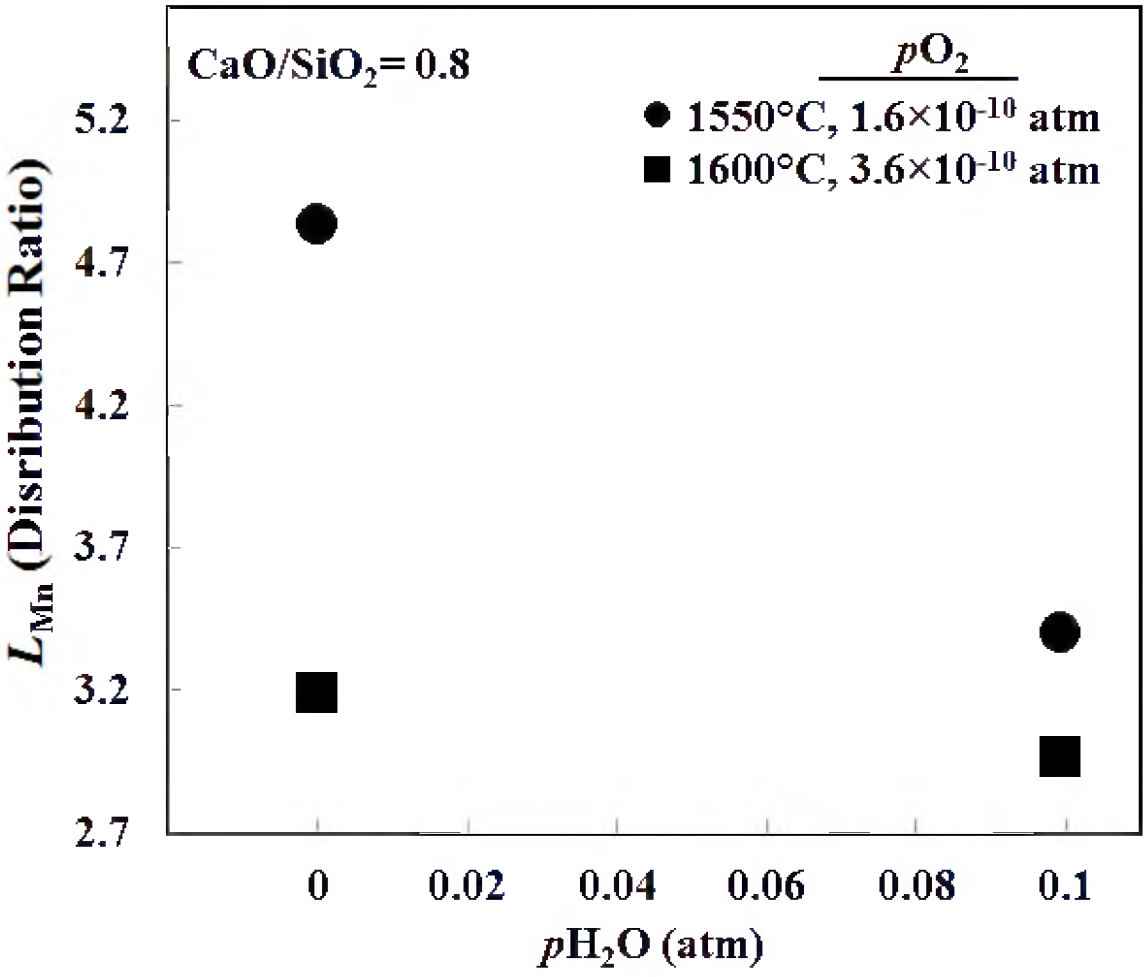

Figure 8-11. The effect of water content in the gas on L_{Mn} at wt% CaO/wt% SiO_2 of 0.8 at different temperatures and pO_2.

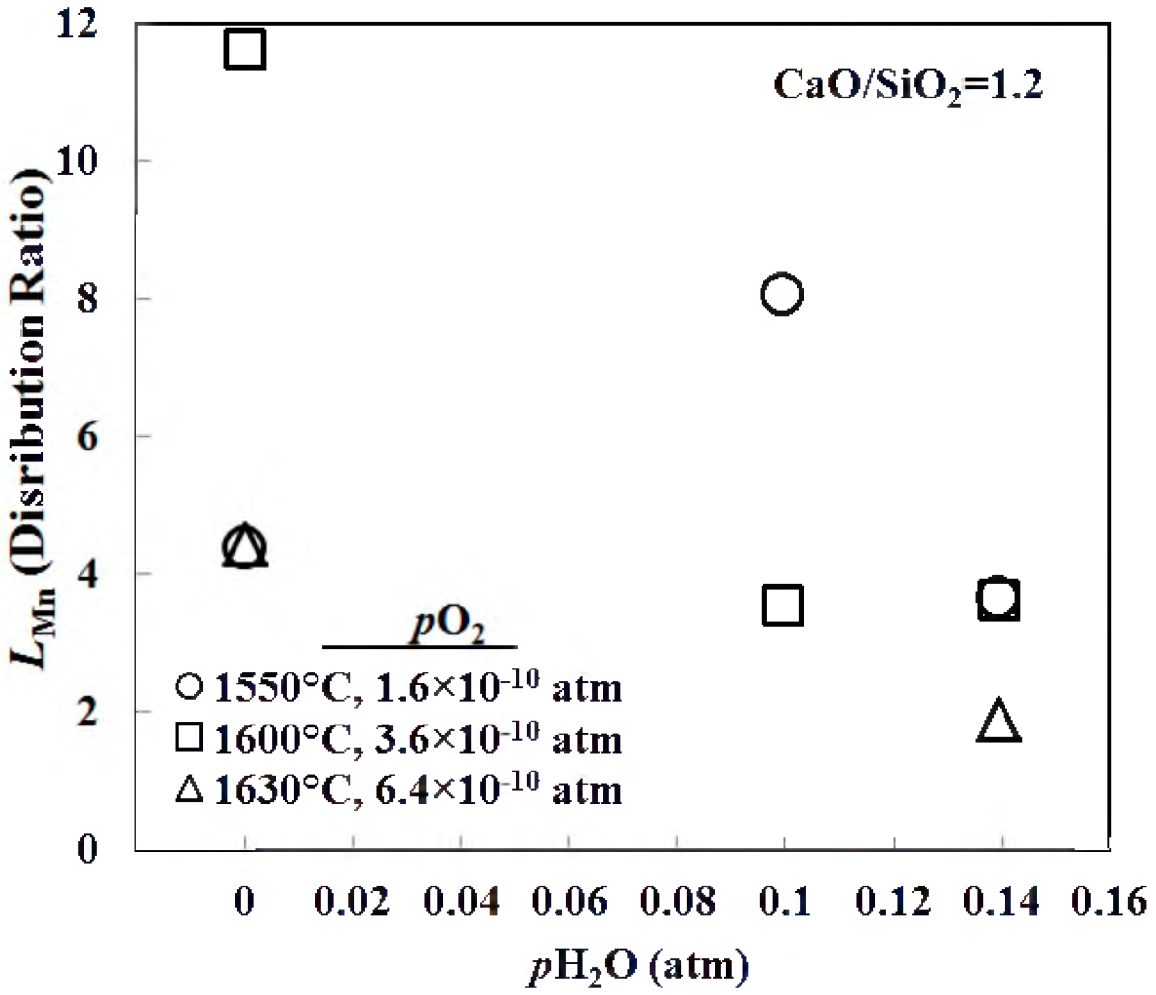

Figure 8-12. The effect of water content in the gas on L_{Mn} at wt% CaO/wt% SiO_2 of 1.2 at different temperatures and pO_2.

found to be 4 (2.8~8.1), 5 (3.6~6.1), and 6 (3.2~11.6) under $CO/CO_2/H_2/H_2O$, H_2/H_2O, and CO/CO_2, respectively.

8. 4. Blast Furnace versus the Flash Ironmaking Technology

In the flash ironmaking process, manganese comes only from the ore, which has an approximately 0.2 wt% manganese content.[14] In the current blast furnace process, coke is another source of manganese in addition to the ore, containing an average of 0.07 wt% manganese.[14] The wt% of Mn in iron is related to L_{Mn} by the following relationship obtained from materials balance:

$$[wt\%Mn]=\frac{t}{(a\cdot L_{Mn})+1}\times 100 \qquad (8\text{-}7)$$

where

$[wt\%Mn]$: manganese weight percentage in produced iron

t : total manganese input per ton of iron

a : slag/metal mass ratio

In the flash ironmaking process, L_{Mn} = 4 and 5 ($CO/CO_2/H_2/H_2O$ and H_2/H_2O, respectively) versus 6 in the case of CO/CO_2. The total Mn input t = 3.40, 3.68 kg/ton iron in the flash and BF process, respectively, considering a typical coke-to-iron ratio of 0.4 in the BF. Applying the same slag/metal ratio of 0.3 as in BF, the Mn content in the iron produced by the flash process would be ~ 0.14 and 0.15 wt% under H_2/H_2O (H_2 conditions) and $CO/CO_2/H_2/H_2O$ (natural/coal gas, NG/CG, conditions), whereas the hot

metal produced under CO/CO_2 would be about 0.13 %. The values of L_{Mn} and [wt% Mn] under the three gas atmospheres are normalized against the BF (CO/CO_2) and compared in Figure 8-13.

8. 5. Conclusions

For the slag compositions investigated, MgO-saturated CaO-FeO-Al_2O_3-SiO_2-MnO (0.2-0.8 wt%)-P_2O_5 (0.1-0.9 wt%), in the temperature range 1550-1600°C, with wt% CaO/wt% SiO_2 rage 0.8 to 1.2, and under $pO_2 = 2\times10^{-10}$~2×10^{-9} atm, the average L_{Mn} was found to be 4, 5, and 6 under $CO/CO_2/H_2/H_2O$ (natural/coal gas, NG/CG), H_2/H_2O (H_2 reductant), and CO/CO_2 (blast furnace, BF), respectively. In other words, L_{Mn} under H_2 and NG/CG conditions is 29 and 43% less than under the BF conditions. Therefore, water in the gas atmosphere depresses L_{Mn}.

When an ore with Mn content of 0.2 wt% is fed into three routes in addition to coke with 0.07 wt% Mn , which was added at the ratio of 0.4 coke-to-hot metal, in the case of the BF conditions, the hot metal produced by the BF, NG/CG, and H_2 is expected to contain 0.13, 0.14, and 0.15 wt% Mn, respectively. That is H_2 and NG/CG are expected to produce hot metal with 17 and 25% more Mn than in the BF conditions.

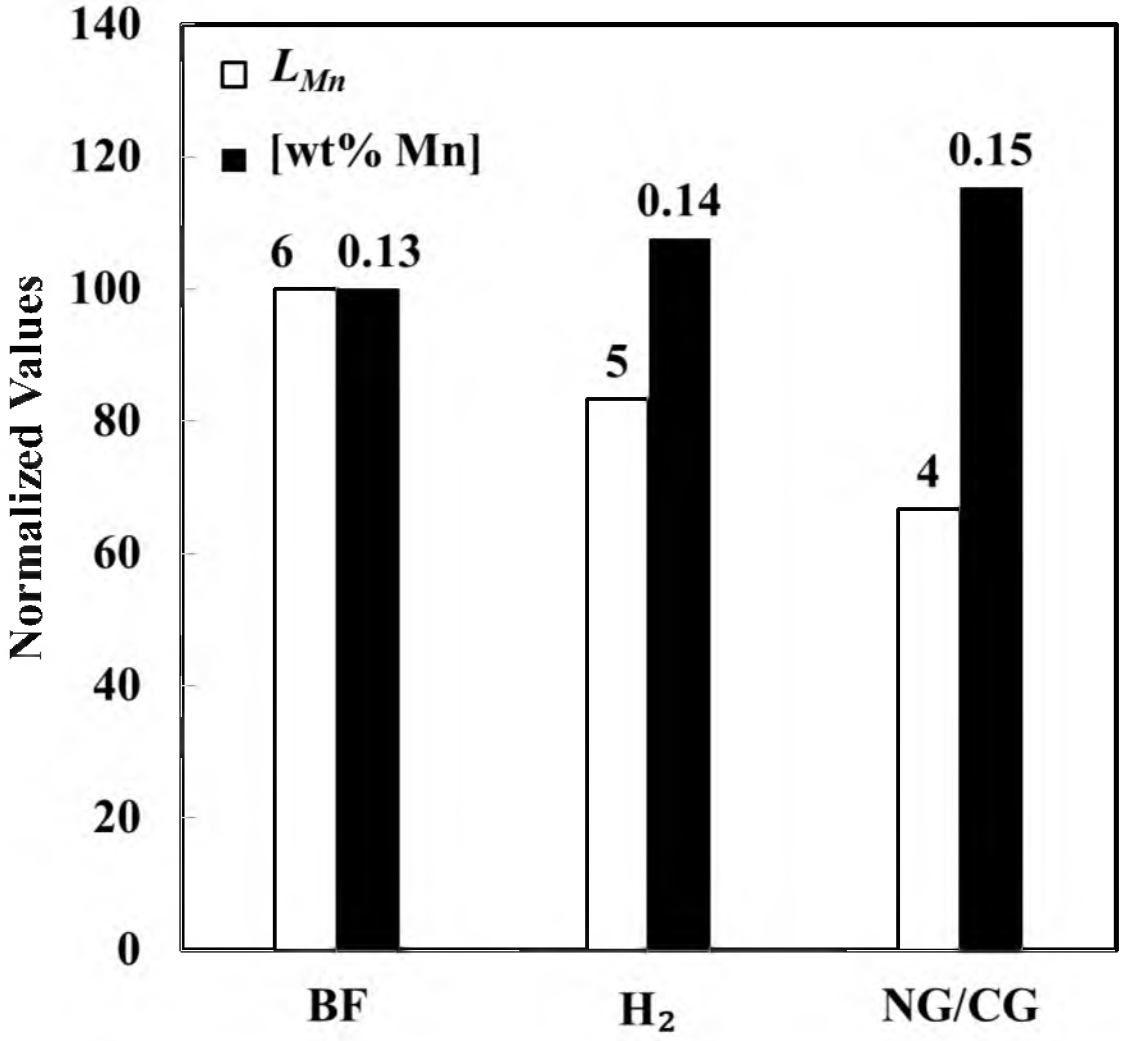

Figure 8-13. The effect of the type of reductant gas on L_{Mn}. The labels show the values of L_{Mn} and [wt% Mn].

8. 6. References

(1) Mohassab-Ahmed, M. Y.; Sohn, H. Y. (University of Utah). Method and device for digestion of materials in a microwave oven. U.S. Patent Application No. 61/651, 789, Unpublished (filing date May 25, 2012).

(2) Mohassab-Ahmed, M. Y.; Sohn, H. Y.; Kim, H. G., Sulfur distribution between liquid iron and magnesia-saturated slag in H_2/H_2O atmosphere relevant to a novel ironmaking technology. *Ind. Eng. Chem. Res.* **2012,** *51*, 3639-3645.

(3) Mohassab-Ahmed, M. Y.; Sohn, H. Y.; Kim, H. G., Phosphorus distribution between liquid iron and magnesia-saturated slag in H_2/H_2O atmosphere relevant to a novel ironmaking technology. *Ind. Eng. Chem. Res.* **2012,** *51*, 7028-7034.

(4) The Japan Society for the Promotion of Science. *Steelmaking Data Sourcebook*. The 19th Committee on Steelmaking; Gordon and Breach Science, New York **1988**.

(5) Taylor, C.; Chipman, J. Equilibria of liquid iron and simple basic and acid slags in a rotating induction furnace. *Trans. AIME* **1943,** *154*, 228-247.

(6) Suito, H.; Inoue, R. Manganese equilibrium between molten iron and MgO-saturated CaO-Fe_tO-SiO_2-MnO slags. *Trans. Iron Steel Inst. Jpn.* **1984,** *24*, 257-265.

(7) Meraikib, M. Manganese distribution between a slag and a bath of molten sponge iron and scrap. *ISIJ Int.* **1993,** *33*, 352-360.

(8) Suito, H.; Inoue, R. Thermodynamic considerations on manganese equilibria between molten iron and Fe_tO-MnO-MO_X slags (MO_X = $PO_{2.5}$, SiO_2, $AlO_{1.5}$, MgO, CaO). *Trans. Iron Steel Inst. Jpn.* **1984,** *24*, 301-307.

(9) Zhu, C.; Li, G.; Chen, Z.; Ma, G.; Liu, J. Manganese Distribution Equilibrium between CaO–Fe_tO–SiO_2–MnO–P_2O_5–(Al_2O_3) Slags and Carbon Saturated Iron. *ISIJ Int.* **2008,** *48*, 123-129.

(10) Park, J. M.; Lee, K. K. Reaction equilibria between liquid iron and CaO-Al_2O_3-$MgO_{sat.}$-SiO_2-Fe_tO-MnO-P_2O_5 slag. *Steelmaking Conf. Proc.* **1996,** *79*, 165-171.

(11) Turkdogan, E. T., Physicochemical aspects of reactions in ironmaking and steelmaking processes. *Trans. Iron Steel Inst. Jpn.* **1984,** *24*, 591-611.

(12) Ohta, H.; Suito, H. Activities of SiO_2 and Al_2O_3 and activity coefficients of Fe_tO and MnO in CaO-SiO_2-Al_2O_3-MgO slags. *Metall. Trans. B* **1995,** *26*, 295-303.

(13) Jung, S. M. Equilibria of manganese and sulfur between liquid iron and CaO-SiO_2-Fe_tO-MgO-MnO slags saturated with $2CaO \cdot SiO_2$ and MgO. *ISIJ Int.* **2003,** *43*, 216-223.

(14) Habashi, F. *Handbook of Extractive Metallurgy*, Vol. I, Wiley-VCH, Weinheim, **1997**, 53.

CHAPTER 9

CONCLUSIONS AND FUTURE WORK

9. 1. The Chemistry of the Slag

In this chapter, CO/CO_2, H_2/H_2O, and $CO/CO_2/H_2/H_2O$ will be referred to as blast furnace (BF), hydrogen (H_2), and natural gas/coal gas (NG/CG), respectively.

Based on the spectroscopic and XRD analyses in addition to NBO/T (non-bridging oxygen per tetradra; the higher this ratio, the lower the polymerization degree) calculations, H_2O stabilizes the more polymerized silicates anions rather than the depolymerized monomers. It was found that for the investigated slags at 1550°C, the H_2 and NG/CG exhibits BO (bridging oxygen; the higher the BO, the higher the polymerization degree) of 55 and 9 % more than the BF, whereas for the ratio NBO/T of both showed ~ 35% less than in the BF. Therefore, it can be concluded that the higher the water content in the gas atmosphere, the more polymerized the silicates in the slag. In the following sections, the effect of this phenomenon on the quality of the produced iron, the loss of iron in the form of FeO, and MgO solubility will be summarized. The representative results were based on the average obtained using slag MgO-saturated CaO-FeO-Al_2O_3-SiO_2-MnO (0.2-0.8 wt%)-P_2O_5 (0.1-0.9 wt%), in the temperature range 1550-1600°C, with CaO/SiO_2 rage 0.8 to 1.2, and under $pO_2 = 2\times10^{-10} \sim 2\times10^{-9}$ atm.

The comparisons are based on an ore with on materials balance using iron ore with approximately 0.02, 0.6, 0.2 wt% S, P, and Mn, respectively, in addition to coke (in the BF) having average contents of 0.9, 0.03, 0.07 wt% S, P, and Mn, respectively. The coke-to-metal ration used in the case of the BF was 0.4. In addition to the difference in S input between the Sohn process and the blast furnace, another important difference is the volatilization of ~30 and 25 wt% S and P during the downward flight of the particles in the reactor shaft in the latter process, which was also considered in the calculations. The same slag/metal weight ratio was 0.3 in all the three routes.

9. 1. 1. Sulfur Distribution Ratio (L_S) and Content in the Hot Metal

H_2O causes the highest L_S of all the other reducing agents. H_2 showed 400% (L_S = 5.0) enhancement in L_S, whereas NG/CG exhibited 130% (2.3) improvement compared with the BF (1.0).

9. 1. 2. Phosphorus Distribution Ratio (L_P) and Content in the Hot Metal

Under the H_2 (L_P = 9) and NG/CG (17) conditions, L_P was 50 and 6 % less than in the BF (18) conditions, respectively. Based on materials balance calculations, the hot metal produced by H_2 ([wt% P] = 0.12) and NG/CG (0.07) would have 25 and 56 % less P than in the BF conditions (0.16). The typical pig iron has ~ 0.2 wt% P. Therefore, the Sohn process is expected to produce hot metal with a lower need for dephosphorization in the steelmaking step.

9. 1. 3. Manganese Distribution Ratio (L_{Mn}) and Content in the Hot Metal

Water in the gas atmosphere depresses L_{Mn}. It was found that L_{Mn} under H_2 (L_{Mn} = 5) and NG/CG (4) conditions is 29 and 43% less than under the BF (7) conditions, respectively. In other words, if the same ore is fed into three routes and by applying material balance, the H_2 (0.15 wt% Mn) and NG/CG (0.14) are expected to produce hot metal with 24 and 41% more Mn than in the BF conditions. The typical pig iron, however, has Mn content 0.9-2.5 wt%; hence, the Sohn process is anticipated to minimize the need for demanganization for low Mn content steels.

9. 1. 4. FeO Content and MgO Solubility in the Slag

One of the advantages of the H_2O in the gas atmosphere is that it increases the activity coefficient of FeO in the slag and accordingly lowers the FeO content. It was found that the FeO content in the slag of H_2 (FeO wt% = 10) and NG/CG (11) is 37 and 31% less than in the BF (16) conditions, respectively. In the typical BF process, the FeO content in the slag is ~1 -1.5 wt% due to the lower temperature (<1550°C).

An empirical correlation was formulated using linear regression to adequately predict γ_{FeO} under H_2/H_2O in slags:

$$\log \gamma_{FeO} = -3.0623 X_{FeO} - 3.1421 X_{CaO} - 2.5068 X_{MgO} + 2.1957 \ (r^2 = 0.72) \quad (9\text{-}1)$$

That correlation fairly well predicts the γ_{FeO} in slags similar to that studied.

On the other hand, the average MgO solubility under the NG/CG (MgO wt% 22) was 22 % higher than in the BF (18) conditions, whereas MgO solubility showed no change under H_2 (18) relative to the BF.

To correlate magnesia solubility to basicity, the available basicity indices were tested but found to provide poor correlations with MgO solubility. Therefore, the following expression was developed based on the MgO solubility data of the current work (under H_2/H_2O) to express slag basicity index:

$$B' = (wt\%\ CaO + 0.7 \times wt\%\ Fe_tO + 0.59 \times wt\%\ MnO) - (0.5 \times wt\%\ SiO_2 + 0.6 \times wt\%\ Al_2O_3) \quad (9\text{-}2)$$

which accounted for the differences in slag composition in the previous and the present work and allowed the comparison between the current and previous work. This basicity index yielded an adequate correlation of MgO solubility, as follows:

$$(MgO\ wt\%)_{saturation} = 103.4 - 0.41B' - \frac{1.41 \times 10^5}{T(K)} \quad (9\text{-}3)$$

Moreover, the following correlation was developed, using the MgO solubility data of the current work (under H_2/H_2O), to correlate MgO solubility to the slag composition and temperature:

$$(MgO\ wt\%)_{saturation} = 91.4 - 0.43\ (FeO\ wt\%) - 0.54(CaO\ wt\%) - \frac{9.34 \times 10^4}{T(K)} \quad (9\text{-}4)$$

This correlation was found to fairly well predict MgO solubility in multicomponent slags with FeO content in the range 1 - 50, CaO/SiO_2 of 0.4 - 1.6, and temperature range of 1550 - 1650°C.

9. 2. Future Work

Water was found to have a pronounced effect on the chemistry of the slag as well as the involved equilibrium reactions. A research is planned to determine the optimum slag composition as well as the temperature for the Sohn ironmaking process. Therefore, it is recommended to further investigate the following topics:

- The effect of the type gas atmosphere on the distribution of Si between slag and molten iron.
- The effect of H_2O on the carbon content in hot metal produced with natural gas or coal gas.
- Experimental determination of the activity coefficient of MgO and FeO in magnesiowustite phase in addition to the equilibrium saturation ratio of magnesiowustite/silicate and the impact of H_2O in the gas atmosphere on them.
- Development of a calibrated analytical method to quantify the different Q-species in the slag.
- Experimental determination of the effect of H_2O content on the slag viscosity.